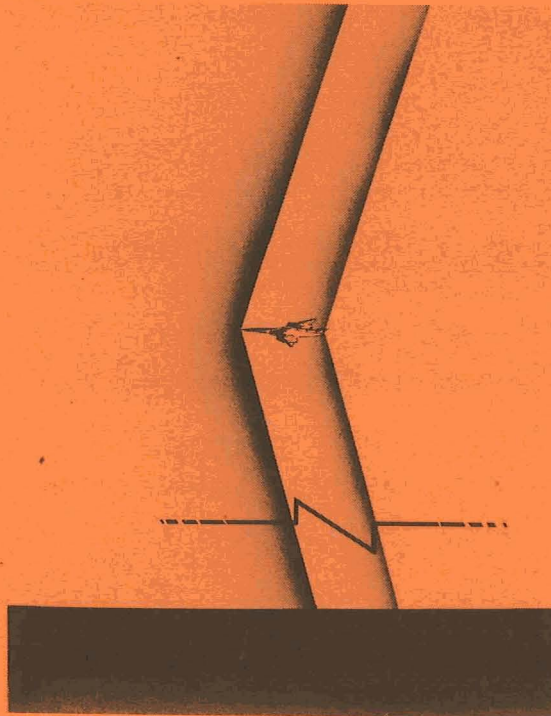


NASA Conference Publication 3172

High-Speed Research: Sonic Boom

Volume I



*Proceedings of a conference held at
Langley Research Center
Hampton, Virginia
February 25-27, 1992*

(NASA-CP-3172) HIGH-SPEED
RESEARCH: SONIC BOOM, VOLUME 1
(NASA) 195 p.

522297

N92-33874
--THRU--
N92-33886
Unclas

H1/05 0118044

NASA

NASA Conference Publication 3172

High-Speed Research: Sonic Boom

Volume I

*Compiled by
Christine M. Darden
Langley Research Center
Hampton, Virginia*

Proceedings of a conference sponsored by the
National Aeronautics and Space Administration,
Washington, D.C., and held at
Langley Research Center
Hampton, Virginia
February 25–27, 1992



National Aeronautics and
Space Administration
Office of Management
Scientific and Technical
Information Program

1992

Preface

Volume I

The purpose of this workshop was to provide a forum for government, industry and university participants in the sonic boom element of NASA's High Speed Research Program to present and discuss important technology issues related to that element. The workshop sessions were divided into atmospheric propagation, acceptability studies and configuration design and operation--the three concurrent research areas within the sonic boom program. Attendance at the workshop was by invitation only.

This volume of the workshop proceedings includes papers on atmospheric propagation and acceptability studies. The papers on atmospheric propagation generally cover studies in the development of molecular relaxation models and atmospheric turbulence models and their incorporation into sonic boom signature propagation algorithms. Experimental flight programs to measure sonic booms are also described. Papers on the acceptability include results of experimental studies on humans in a sonic boom simulator and quantification of vibrations caused by sonic booms.

PRECEDING PAGE BLANK NOT FILMED

CONTENTS

Preface	iii
-------------------	-----

VOLUME I

ATMOSPHERIC PROPAGATION

The Pekeris Problem, and the Interior of the Pulsating Sphere, First Success of Exact Ray Theory, and 'What Rays?'	1
Gerry L. McAninch	
A Numerical Model for Sonic Boom Propagation through an Inhomogeneous, Windy Atmosphere	7
Leick D. Robinson	
Wave Equations and Computational Models for Sonic Boom Propagation through a Turbulent Atmosphere	31
Allan D. Pierce	
Simulations of Sonic Boom Ray Tube Area Fluctuations for Propagation through Atmospheric Turbulence Including Caustics Via a Monte Carlo Method	49
Victor W. Sparrow and Allan D. Pierce	
Analysis of Sonic Boom Data to Quantify Distortions of Shock Profiles	63
Thomas A. Gionfriddo	
The Effect of Turbulence on the Loudness of Minimized Sonic Boom Signatures	77
Kenneth J. Plotkin	
Model Experiment to Study the Effect of Turbulence on Risetime and Waveform of N Waves	97
Bart Lipkens and David T. Blackstock	
Steady State Risetimes of Shock Waves in the Atmosphere	109
Richard Raspet, Henry Bass, Lixin Yao, and Wenliang Wu	
Lateral Spread of Sonic Boom Measurements From US Air Force Boomfile Flight Tests	117
J. Micah Downing	
Preliminary Results from the White Sands Missile Range Sonic Boom Propagation Experiment	137
William L. Willshire, Jr. and David W. DeVilbiss	

ACCEPTABILITY STUDIES

Subjective Loudness Response to Simulated Sonic Booms	151
Jack D. Leatherwood and Brenda M. Sullivan	
Evaluation of Human Response to Structural Vibration Induced by Sonic Boom	171
L. C. Sutherland and J. Czech	

THE PEKERIS PROBLEM, AND THE INTERIOR OF THE PULSATING SPHERE, FIRST SUCCESS OF EXACT RAY THEORY, AND 'WHAT RAYS?'

Gerry L. McAninch
NASA Langley Research Center
Hampton, Va.

SUMMARY

This paper presents what is probably the first application of exact ray theory to provide nontrivial exact solutions of the Helmholtz equation. First the Pekeris problem is considered, this is followed by consideration of the problem of the field maintained within a uniformly pulsating sphere. In the Pekeris problem an iterative solution provides the exact solution on the second iteration, in the second problem it is shown that the exact ray theory eliminates the focus of the geometric theory.

INTRODUCTION

In reference [1], a new theory of the Helmholtz equation is developed. The theory provides the concept of exact rays, which are the channels along which the disturbance energy is actually conveyed. It is established in ref. [1] that these exact rays and the rays of the geometric theory of the Helmholtz equation may be vastly different.

However, the development and discussion of the theory as presented in ref. [1] suffer from a major defect. That is that no use of the theory to obtain a solution of the Helmholtz equation is given. The usefulness of the theory as "...a method for representing and displaying the acoustic field.", which is how it is portrayed in the work of Foreman, is of no small consequence. Yet, it would be nice if the theory were also a predictive tool.

In the following is presented what must be considered as the first real success of the exact ray theory, its application to the solution of two nontrivial propagation problems. In both cases the solution of the problem by the geometric theory fails. The reasons for this failure, and the success of the exact ray theory are discussed.

EXACT RAY THEORY

In ref. [1], solutions of the Helmholtz equation

$$\nabla^2 \Psi + k^2 N^2 \Psi = 0 \quad (1)$$

of the form

$$\Psi = \psi e^{ik\Theta} \quad (2)$$

are sought, with the equation

$$k^2[|\nabla\Theta|^2 - N^2]\psi + \nabla^2\psi + ik[2\nabla\psi \cdot \nabla\Theta + \psi\nabla^2\Theta] = 0 \quad (3)$$

obtained through substitution of equation (2) into Equation (1), split into its real and imaginary parts under the constraint that both ψ and Θ be real. This provides the coupled system of equations:

$$2\nabla\psi \cdot \nabla\Theta + \psi\nabla^2\Theta = 0 \quad (4)$$

$$k^2[|\nabla\Theta|^2 - N^2]\psi + \nabla^2\psi = 0 \quad (5)$$

for the unknown functions ψ and Θ . Equation (5) may be written in the form:

$$|\nabla\Theta|^2 = N^2 + \frac{\nabla^2\psi}{k^2\psi} \quad (6)$$

which proves convenient for later discussion.

AN ITERATIVE SOLUTION PROCEDURE FOR THE EXACT RAY EQUATIONS

An approach to the solution of Equations (4) and (6) is to solve the system iteratively, with the first iteration being provided by letting $\psi = \text{constant}$ in Equation (6). Thus the first iteration is essentially the geometric theory:

$$|\nabla\Theta_0|^2 = N^2 \quad (7)$$

$$2\nabla\psi_0 \cdot \nabla\Theta_0 + \psi_0\nabla^2\Theta_0 = 0 \quad (8)$$

with the higher order iterations obtained by solving the system of equations:

$$|\nabla\Theta_m|^2 = N^2 + \frac{\nabla^2\psi_{m-1}}{k^2\psi_{m-1}} \quad (9)$$

$$2\nabla\psi_m \cdot \nabla\Theta_m + \psi_m\nabla^2\Theta_m = 0 \quad (10)$$

for $m=1,2,3,\dots$

The approximate solution obtained on the m^{th} iteration will be represented in the form:

$$\Psi_m = \psi_m e^{ik\Theta_m} \quad (11)$$

THE PEKERIS PROBLEM

The solution of Equation (1) for a point source located at $(x,y,z) = (0,0,\beta)$ in a medium with sound speed given by $c(z) = az$, as obtained by C. L. Pekeris [2] by the method of eigenfunction expansion, is:

$$\Psi = \frac{2(\beta z)^{1/2}}{R_1 R_2} \text{Exp}\left\{2i\left[\left(\frac{\omega}{a}\right)^2 - \frac{1}{4}\right]^{1/2} \text{Arctanh}\left(\frac{R_1}{R_2}\right)\right\} \quad (12)$$

where:

$$R_1 = [x^2 + y^2 + (\beta - z')^2]^{1/2} \quad (13)$$

$$R_2 = [x^2 + y^2 + (\beta + z')^2]^{1/2} \quad (14)$$

Translating the coordinate system from directly below the source on the plane where $c = 0$ to the source allows the solution given in Equation (12) to be written in the form:

$$\Psi = \frac{2(1 + \epsilon z)^{1/2}}{\epsilon R_1 R_2} \text{Exp}\{ik[1 - (\frac{\epsilon}{2k})^2]^{1/2} [(\frac{2}{\epsilon}) \text{Arctanh}(\frac{R_1}{R_2})]\} \quad (15)$$

In this coordinate system:

$$R_1 = [x^2 + y^2 + z^2]^{1/2} \quad (16)$$

$$R_2 = [x^2 + y^2 + (z + \frac{2}{\epsilon})^2]^{1/2} \quad (17)$$

and the quantity ϵ is defined through the relationship:

$$c(z) = c_0(1 + \epsilon z) \quad (18)$$

Thus:

$$N = \frac{1}{1 + \epsilon z} \quad (19)$$

ITERATIVE SOLUTION OF EXACT RAY THEORY

That the solutions of Equations (7) and (8) are given by:

$$\Theta_0 = (\frac{2}{\epsilon}) \text{Arctanh}(\frac{R_1}{R_2}) \quad (20)$$

$$\Psi_0 = \frac{2(1 + \epsilon z)^{1/2}}{\epsilon R_1 R_2} \quad (21)$$

is easily verified by direct substitution into the governing equations. Further, that :

$$\frac{\nabla^2 \Psi_0}{k^2 \Psi_0} = -\frac{\epsilon^2 N^2}{4k^2} \quad (22)$$

is also easily verified. Hence Equation (9) becomes:

$$|\nabla \Theta_1|^2 = N^2 \{1 - \frac{\epsilon^2}{4k^2}\} \quad (23)$$

for $m=1$. Use of the fact that

$$|\nabla \Theta_0|^2 = N^2 \quad (24)$$

allows this to be written as:

$$|\nabla \Theta_1|^2 = |\nabla \Theta_0|^2 \{1 - \frac{\epsilon^2}{4k^2}\} \quad (25)$$

Hence,

$$\Theta_1 = [1 - \frac{\epsilon^2}{4k^2}]^{1/2} \Theta_0 \quad (26)$$

Now consider Equation (10) for $m = 1$,

$$2\nabla \Psi_1 \cdot \nabla \Theta_1 + \Psi_1 \nabla^2 \Theta_1 = 0 \quad (27)$$

which may be written as

$$[1 - \frac{\epsilon^2}{4k^2}]^{1/2} [2\nabla \Psi_1 \cdot \nabla \Theta_0 + \Psi_1 \nabla^2 \Theta_0] = 0 \quad (28)$$

through use of Equation (26). Thus

$$2\nabla\psi_1 \cdot \nabla\Theta_0 + \psi_1 \nabla^2\Theta_0 = 0 \quad (29)$$

or

$$\psi_1 = \psi_0 \quad (30)$$

Therefore, on the second iteration the solution may be written as:

$$\Psi_2 = \frac{2(1 + \epsilon z)^{1/2}}{\epsilon R_1 R_2} \text{Exp}\{ik[1 - (\frac{\epsilon}{2k})^2]^{1/2} [(\frac{2}{\epsilon}) \text{Arctanh}(\frac{R_1}{R_2})]\} \quad (31)$$

Further iterations are not required, this is in fact the exact solution.

THE PULSATING SPHERE

In the following it is suggested that if the exact rays are, in fact, the channels along which the disturbance energy is conveyed, then, if there is no net energy flux there are no rays. This rather simple thought provides some rather startling results when applied to the determination of the disturbance field within a uniformly pulsating sphere.

ANALYSIS

In the following the refractive index will be taken as depending only on the radial coordinate r . Now consider the disturbance field maintained within a sphere of radius a , centered on $r = 0$, which is pulsating uniformly with harmonic velocity $U_0 e^{-i\omega t}$. Observing that there can be no net energy flux through any point within the sphere, it is proposed that no ray field can exist within the sphere. Therefore, it must be true that:

$$\Theta = \text{constant} \quad (32)$$

throughout the region of interest.

This simple observation leads to some interesting conclusions. First consider the eiconal equation of the geometric theory, which becomes simply:

$$N^2 = 0 \quad (33)$$

implying that the geometric theory fails. The exact ray theory eiconal equation becomes:

$$N^2 + \frac{\nabla^2 \psi}{k^2 \psi} = 0 \quad (34)$$

In either case the transport equation becomes:

$$0 = 0 \quad (35)$$

Equation (34) is nothing more than the Helmholtz equation; however, it is now known that ψ is a real quantity. Further, the geometry of the problem is such that the solution can depend on r only. Note however, that the geometric theory, as usually applied, essentially forces \hat{r} to be normal to a constant phase surface, hence along the rays, whereas the exact ray theory shows that \hat{r} lies along a surface of constant phase!

Equation (34) may be written as:

$$\frac{1}{r^2} \left\{ \frac{\partial}{\partial r} \left[r^2 \frac{\partial \psi}{\partial r} \right] \right\} + k^2 N^2 \psi = 0 \quad (36)$$

and solved for analytic $N(r)$.

DISCUSSION AND CONCLUSIONS

The analysis of the Pekeris problem through use of the exact ray theory has provided the exact solution on the second iteration. If this problem were solved by the geometric theory only a single term of an infinite series would be obtained at each order. Further, each of these terms would be secular in Θ , the coordinate along the ray.

The failure of the geometric theory can be traced to its inability to determine the correct phase speed. The success of the exact ray theory in this problem may be attributed to the presence of the term $\frac{\nabla^2 \psi}{k^2 \psi}$ in the exact ray eiconal equation, and the subsequent correct determination of the phase speed.

The analysis of the pulsating sphere problem, provided above, has shown that the exact ray theory developed in ref. [1] may be applied directly to determine the disturbance field in a case for which the geometric theory has a focus. The exact ray theory eliminates the focus through the simple expedient of eliminating the rays. The argument may be expressed in the form:

There is no net energy flux --> there are no rays --> there can be no caustic.

Overall then, the analysis of the two problems considered above indicates that often the errors of the geometric theory may best be resolved by considering the equations in the form of the exact ray theory, Equations (4) and (5), rather than analyzing the equations of the geometric theory. In particular, the pulsating sphere problem indicates that the geometric theory is poorly formulated for problems for which there is no net energy flux through some point or points within the region of interest.

REFERENCES

1. Foreman, Terry L.: An exact ray theoretical formulation of the Helmholtz equation. Journal of the Acoustical Society of America, vol. 86, No. 1, July 1989.
2. Pekeris, C. L.: Theory of Sound Propagation in a Half-Space of Variable Sound Velocity Under Conditions of Formation of a Shadow Zone. Journal of the Acoustical Society of America, vol. 18, No. 2, Oct. 1946.

A NUMERICAL MODEL FOR SONIC BOOM PROPAGATION THROUGH AN INHOMOGENEOUS, WINDY ATMOSPHERE*

Leick D. Robinson
Applied Research Laboratories
The University of Texas at Austin
Austin, TX

SUMMARY

The ZEPHYRUS computer model calculates sonic boom distortion during propagation through the atmosphere. The model includes the effects of nonlinear distortion, attenuation, dispersion, and wind. Trial runs with the model indicate that, in general, stable shocks have not formed when the sonic boom reaches the ground. Also, the rise time of the lead shock may strongly depend on the overall waveform shape, and may be significantly increased by purely dispersive effects when matching occurs between the rise time and the characteristic oxygen molecular relaxation time.

INTRODUCTION

The ZEPHYRUS computer model has been developed by the author to calculate sonic boom distortion during propagation through a "real" atmosphere. The atmosphere is modeled as inhomogeneous and stratified, with a nonuniform, stratified wind field. A three-dimensional ray theory is used to generate the ray paths associated with the sonic boom shock front produced by a supersonic aircraft. In this, self-refraction is ignored and assumed to be important only in describing the propagation along the rays. The ray model is fully three-dimensional in that no inherent symmetry is assumed in the wave front shape.

* Work was supported by NASA Langley Research Center Contract N00039-88-C-0043, Task 5-1-1, and Contract N00039-91-C-0082, Task 05A1-001.01, as well as IR&D support at Applied Research Laboratories, The University of Texas at Austin.

The distortion along the ray paths is computed by a modified Pestorius algorithm (ref. 1) which includes the effects of weak shock theory along with attenuation and dispersion due to a thermoviscous medium with oxygen and nitrogen molecular relaxation. Propagation through reflections and weak (line-like) caustics is allowed. The effects of turbulence are not included in the current model. A more detailed discussion of the theory underlying this model may be found in ref. 2.

THEORETICAL BASIS

Thompson (ref. 3) used the theory of characteristic forms and curves of systems of differential equations to derive the ray path equations for a moving medium. This method provides a simpler, more straightforward derivation of the equations than that provided by the traditional approach which utilizes the eikonal equation. This method is easily extendable to non-steady state atmospheric models, in which the atmospheric parameters have some time dependence. The discussion of this theory by Courant and Hilbert (ref. 4) is excellent, although, in this author's opinion, often overlooked by researchers due to the mathematical and notational density of its presentation.

We may define a spatial function $x(t; \phi, t_0)$ where variations in time t for constant ray launch parameters (ϕ, t_0) generate individual rays in the ray family. We introduce the function $\Psi(x)$, where $\{\Psi(x) = t; t \text{ constant}\}$ describes the wavefront at time t and thus $\Psi(x(t; \phi, t_0)) = t$. The slowness vector \mathbf{p} may be defined by

$$\mathbf{p} = |\mathbf{p}| \hat{\mathbf{n}} = \nabla \Psi \quad (1)$$

where

$$|\mathbf{p}| = \frac{1}{c_0 + \mathbf{W} \cdot \hat{\mathbf{n}}} \quad (2)$$

and where $\hat{\mathbf{n}}$ is the wavefront normal, and c_0 and \mathbf{W} are the local small signal sound speed and the local wind velocity, respectively.

The ray path equations are given by

$$\frac{d\mathbf{x}}{dt} = \frac{\mathbf{W}(1 - \mathbf{W} \cdot \mathbf{p}) + c_0^2 \mathbf{p}}{(1 - \mathbf{W} \cdot \mathbf{p})} \quad (3)$$

and

$$\frac{d\mathbf{p}}{dt} = - \sum_{i=1}^3 p_i \nabla W_i - \nabla c_0 |\mathbf{p}| \quad (4)$$

We define the infinitesimal cross-sectional ray tube area as

$$A = \frac{\left(\frac{\partial \mathbf{x}}{\partial \phi} \times \frac{\partial \mathbf{x}}{\partial t_0} \right) \cdot \frac{\partial \mathbf{x}}{\partial t}}{\left| \frac{\partial \mathbf{x}}{\partial t} \right|} \quad (5)$$

hereafter referred to in short as the ray tube area.

The lossless nonlinear transport equation may be derived without resorting to the wave equation by transforming the hydrodynamic equations into the retarded time domain and then successively eliminating all terms containing acoustic variables other than the acoustic overpressure. The resulting equation is

$$\frac{\partial}{\partial s} \left[\frac{P'^2 |A|}{\Omega \rho_0} \left| \mathbf{q} + \frac{\mathbf{W}}{c_0^2} \right| \right] - \frac{2|A|\beta P'^2 P'_{,t}}{\rho_0^2 c_0^4} = 0, \quad (6)$$

$$\Omega = 1 - \mathbf{W} \cdot \mathbf{p}$$

where s is the distance along the ray path, P' is the acoustic overpressure, ρ_0 is the medium density, \mathbf{q} is the slowness vector in the rest frame of the medium, and β is the parameter of nonlinearity, usually assumed to have the value 1.2 in air.

We make the following variable transformations:

$$\Pi = KP' \quad (7)$$

where

$$K = \sqrt{\frac{|A| \rho_{0s} c_{0s}}{|A_s| \rho_0 \Omega} \left| \mathbf{q} + \frac{\mathbf{W}}{c_0^2} \right|} \quad (8)$$

and

$$\frac{dZ}{ds} = \sqrt{\frac{|A_s| \beta^2 \rho_{0s} c_{0s}^5 \Omega^3}{|A| \beta_s^2 \rho_0 c_0^8 \left| \mathbf{q} + \frac{\mathbf{W}}{c_0^2} \right|^3}} \quad (9)$$

The values ρ_{0s} , c_{0s} , A_s , and β_s represent the initial values of the medium density, small signal sound speed, ray tube area, and coefficient of nonlinearity.

If the initial waveform is sinusoidal, the shock formation "distance" in Z is

$$Z_{\text{shock}} = \frac{\rho_{0s} c_{0s}^3 t_{\text{char}}}{2\pi \beta_s \Pi_s} \quad (10)$$

where t_{char} is the period of the sine wave and Π_s is the peak transformed overpressure of the initial waveform (see, for example, ref. 5).

We will transform from Z to a dimensionless distance coordinate

$$\sigma = \frac{Z}{Z_{\text{shock}}} \quad (11)$$

and normalize Π to a dimensionless value

$$Y = \frac{\Pi}{\Pi_s} \quad (12)$$

Eq. 6 becomes

$$\frac{\partial Y}{\partial \sigma} - \frac{\tau Y Y_{t'}}{2\pi} = 0 \quad (13)$$

For more general problems, we will set t_{char} to a "characteristic" time of the signal. For instance, with N-waves we will set t_{char} to be the initial duration of the N-wave.

Note that although $\partial Z/\partial s$ becomes infinite if the ray tube area becomes zero (the occurrence of a caustic), $Z(s)$ will remain well-behaved and finite as long as $\partial A/\partial s$ is non-zero. This is true for line-like "weak" caustics, but not point-like "strong" caustics.

Eq. 13 is in the same form as the lossless Burgers' equation in retarded time coordinates,

$$\frac{\partial P}{\partial x} - \frac{\beta P P_{t'}}{\rho_0 c_0^3} = 0 \quad (14)$$

Thus, techniques for solving Burgers' equation may now be applied to the current problem. Specifically, we may now employ the Pestorius algorithm. This algorithm separately applies the effects of nonlinear distortion and atmospheric absorption. The nonlinear distortion is advanced along the ray path over a series of successive steps. At appropriate intervals, the propagation is halted, the waveform is transformed into the frequency domain, and the accumulated attenuation is applied. The wave is transformed back into the time domain, and the cycle begins again. The updated standard atmospheric absorption model from ref. 6 is used to calculate the attenuation and dispersion coefficients.

RESULTS

Comparisons with Known Results

Stable Step Shocks -- Viscosity Only

The nonlinear motion of a plane wave in a viscous medium without molecular relaxation effects is described by Burgers' equation, which is, in retarded time coordinates:

$$P'_{x'} - \frac{\beta P' P'_{t'}}{\rho_0 c_0^3} = A_{iv} P'_{t't'} \quad (15)$$

where the attenuation coefficient α is related to A_{iv} by

$$\alpha = A_{iv} \omega^2 = 4\pi^2 A_{iv} f^2 \quad (16)$$

at frequency f .

Eq. 15 has the exact solution

$$P' = \frac{P_{\infty}}{2} \left[1 + \tanh \left(\frac{t'}{\tau} - \frac{x'}{v\tau} \right) \right] \quad (17)$$

where P' asymptotically approaches the value of P_{∞} with increasing t' and τ and v are given by

$$\tau = \frac{4A_{iv}\rho_0 c_0^3}{\beta P_{\infty}} \quad (18)$$

$$v = -\frac{2\rho_0 c_0^3}{\beta P_{\infty}} \quad (19)$$

This waveform represents a stable shock solution which does not change shape as it propagates.

Since the rise time is the time between 10% and 90% of P_{∞} , it is related to τ in this solution by

$$t_{rt} = \ln(9) \tau \quad (20)$$

A modified initial waveform that consisted of Eq. 17 truncated after a sufficiently long time interval was used as the input, with a sampling density such that the time separation between data points in the waveform array was 1 millisecond and

$$P_{\infty} = 200 \text{ Pa}$$

$$\rho_0 = 1.0 \text{ kg/m}^3$$

$$c_0 = 300 \text{ m/s}$$

$$\beta = 1.2$$

For purposes of testing the model, values of A_{iv} were imposed to give theoretical stable shock rise times of 100.0, 10.0, and 1.0 msec; these values do not represent a physically realistic atmosphere. Figs. 1 through 3 give the rise times as a function of propagation distance. The sawtooth pattern in the rise time plots is due to the Pestorius algorithm. Each "tooth" represents the completion of one attenuation step, which increases the rise time. Between successive applications of attenuation, the nonlinear effects cause the rise time to steadily decrease as the lead shock steepens. Thus, the numerical solution oscillates between over- and under-estimation of the rise time. For 100.0 and 10.0 msec rise times, we see that the numerical result eventually oscillates around a midpoint at the exact solution. Since the nonlinear steps are always applied first in the Pestorius algorithm, the initial waveform will undershoot the *numerically* stable solution until the wave has propagated a characteristic "stable shock formation" distance.

As we see in Fig. 3, when the rise time is reduced to 1.0 msec, the sampling resolution, the rise portion of the shock is no longer sufficiently resolvable in our data. The attenuation is thus no longer of sufficient strength to overcome the nonlinear steepening and discontinuous shocks form between successive attenuation steps. In this regime, the sampling density would have to be increased in order to obtain reliable rise time information.

For 100.0 and 10.0 msec rise times, Figs. 4 and 5 show the initial waveform and the waveforms immediately before and after the applications of attenuation that occur at various distances. Note that the numerical code not only predicts the correct displacement, but at each distance the generated waveforms completely bracket the exact solution.

Stable Shock Formation

A waveform consisting of a step function of arbitrary shape will generally tend toward the stable shock solution as it propagates. It is important to ascertain that ZEPHYRUS not only generates the correct stable solution, but its rate of formation as well. The stable shock formation in the presence of only viscous attenuation may be obtained analytically to good approximation by the following analysis. The effects on the rise time of thermoviscous attenuation and nonlinear distortion are considered separately, and then combined under the assumption that both effects are locally small and so any interaction terms may be ignored.

First, consider only thermoviscous effects. If we start with a step function at $x = 0$

$$f(t') = \begin{cases} 0, & t' < 0 \\ P_{\infty}, & t' \geq 0 \end{cases} \quad (21)$$

then $f(t', x)$ becomes

$$f(t', x) = \frac{P_{\infty}}{\sqrt{4\pi A_{IV} x}} \int_0^{\infty} e^{-(t'-\tau)^2/4A_{IV} x} d\tau = \frac{P_{\infty}}{2} \left[1 + \operatorname{erf}\left(\frac{t'}{\sqrt{4A_{IV} x}}\right) \right] \quad (22)$$

By interpolation from tabulated values for the error function (erf), the rise time t_{rt} (defined as 10% to 90% of P_{∞}) is given by

$$t_{rt} = 2 (0.906) \sqrt{4A_{IV} x} = 3.624 \sqrt{A_{IV} x} \quad (23)$$

Thus,

$$\frac{dt_{rt}}{dx} = \frac{3.624 \sqrt{A_{IV}}}{2\sqrt{x}} = \frac{(3.624)^2 A_{IV}}{2t_{rt}} \quad (24)$$

Since the shape of the error function has the same general shape and character as other sufficiently smooth step functions, such as the hyperbolic tangent, we make the assumption that this equation will be a good approximation for the effects of the attenuation on the rise time for more general waveforms.

From the Earnshaw solution for the lossless Burgers' equation (ref. 7), we have that the effect of the nonlinear distortion on the rise time is

$$\frac{dt_{rt}}{dx} = - \frac{(0.8)\beta P_{\infty}}{\rho_0 c_0^3} \quad (25)$$

We shall combine these two effects into a single equation:

$$\frac{dt_{rt}}{dx} = \frac{(3.624)^2 A_{iv}}{2t_{rt}} - \frac{(0.8)\beta P_{\infty}}{\rho_0 c_0^3} \quad (26)$$

In order to estimate the validity of our approximation, we may compare this with the stable shock solution. The propagation is in equilibrium when the right side is zero, or when

$$t_{rt0} = \frac{(3.624)^2 A_{iv} \rho_0 c_0^3}{2\beta(0.8)P_{\infty}} = 8.21 \frac{A_{iv} \rho_0 c_0^3}{\beta P_{\infty}} \quad (27)$$

The analytically exact stable shock solution yields a rise time of

$$t_{rt0} = \ln(9) \frac{4A_{iv} \rho_0 c_0^3}{\beta P_{\infty}} = 8.79 \frac{A_{iv} \rho_0 c_0^3}{\beta P_{\infty}} \quad (28)$$

Clearly, the two results agree fairly closely.

Eq. 26 has the solution

$$\xi = -\eta - \ln(1 - \eta) \quad (29)$$

where

$$x = \frac{t_{rt0} \xi \rho_0 c_0^3}{(0.8)\beta P_{\infty}} \quad (30)$$

and

$$t_{rt} = \eta t_{rt0} \quad (31)$$

In Fig. 6, this solution is plotted along with the numerical result produced by ZEPHYRUS (with molecular relaxation effects turned off) with excellent agreement. The exact value for t_{rt0} from Eq. 28 was used rather than the approximate value produced by Eq. 27.

Figs. 1 through 6 indicate that, as long as the model sampling is sufficiently fine to resolve the lead shock, we may interpolate between the extremes of the "sawtooth" function to find the actual rise time.

Hayes Program Result

For trials in a realistic atmosphere, the values for the atmospheric profiles are taken from the 1962 standard atmosphere (ref. 8). In this initial case, the atmosphere is at rest; i.e., the wind velocity is zero at all altitudes. Figs. 7, 8, and 9 show the ray paths from the lower portion of the ray cone produced for an aircraft traveling at Mach 2.0 at an altitude of 16,764 meters (55,000 feet) in the direction of the x-axis.

In the ongoing work at the Advanced Vehicles Division at NASA Langley, there are a variety of designs considered for the High-Speed Civil Transport. The initial waveform we have used is a typical predicted sonic boom signature calculated for one such proposed design in the vicinity of the aircraft. This waveform was calculated for the direction directly below the aircraft, and so the

ray with the shortest path to the ground was chosen from the ray fan displayed in Figs. 7, 8, and 9. This waveform will be used in most of the remaining discussion.

The Hayes program has been used for many years to predict sonic boom amplitudes (ref. 9). The Hayes program does not include attenuation effects, but only models the nonlinear distortion. In order to compare the output of ZEPHYRUS with the Hayes result, the attenuation effects were turned off and the resulting solution computed. The comparison is displayed in Fig. 10. Shown is the normalized pressure amplitude $Y(t')$. This eliminates the effects of geometric spreading and variation of atmospheric inhomogeneities, and allows us to observe the effects of nonlinear distortion alone.

The final result agrees well with the result obtained from the Hayes program. The discrepancy in the tail shock is due to the fact that the initial calculated waveform actually contained a small, slowly dying "tail." This was included in the Hayes prediction, but truncated in our model to save computer time, since we were primarily interested in the behavior of the lead shock.

Humidity Effects

Figs. 11 and 12 show the same propagation with the full nonlinear and attenuation effects turned on, for the cases of 0% and 50% relative humidity at the ground. The general wave shape is unchanged, but the attenuation produces rounding at the shock, and, near the ground, was able to unshock the waveform. The asymmetry of the rounding at the shock, most evident in the case of dry air near the ground, is due to the effects of dispersion. Comparison of Figs. 11 and 12 indicates that the effects of attenuation are strongly dependent on humidity.

The rise times predicted at ground level are 0.35 ms at 50% humidity, and 4.5 ms at 0% humidity. This agrees well with sonic boom measurements, as does the very strong dependence of rise time on humidity that is displayed (see, for example, ref. 10).

Lack of Stable Shock Formation

Figs. 13 and 14 show the plots of rise time at 0% and 50% relative ground humidity. A vertical line is placed at the location of the ground reflection. At low altitudes, the attenuation is dominated by the molecular relaxation effects, producing large rise times near the ground where the

attenuation effects are strongest and the nonlinear effects are weakest. It may be noted that the peak rise time does not actually occur at the point of reflection. The attenuation continues to spread out the shock after the reflection in this region. This indicates that a stable lead shock has not formed at the point of ground reflection. Thus, rise time calculations based on theoretical, steady state solutions are unlikely to obtain the correct value for the rise time observed at the ground for actual sonic boom measurements.

Multiple Rise Time Peaks at 50% Relative Ground Humidity

Fig. 14 for the rise time at 50% humidity displays an interesting phenomenon in which the rise time displays a second peak at the mid-level altitudes. The same behavior is observed on both the downward and the upward reflected paths.

The strongest dispersion in the phase velocities occurs at the relaxation frequency. Fig. 15 shows that the oxygen and nitrogen frequencies increase extremely rapidly in the middle altitudes. At these altitudes, the oxygen relaxation frequency lies within the region of the frequency spectrum of the waveform which dominates the characteristics and shape of the lead shock and so effects the rise time strongly. This results in the increase in rise time in this region.

At upper and lower altitudes, the relaxation frequency moves out of the region of the frequency spectrum significant to the shock characteristics, and so the dispersion begins to affect the waveform less strongly. Thus, the rise time is reduced once the wave has passed out of this region.

Wind Effects

The ZEPHYRUS model is capable of modeling propagation in a windy atmosphere. In order to examine the effects of wind on the received sonic boom, the rather extreme case of propagation through a jet stream was considered. Fig. 16 displays the wind profile shape of a typical jet stream. The wind profile data were adapted from a paper by McLean (ref. 11). Figs. 17 and 18 demonstrate the effects of the jet stream on the ray paths.

The calculated received waveform and rise time are shown in Figs. 19 and 20. Since the longest rise times are observed at low humidities, a relative ground humidity of 0% was chosen in

order to magnify the effects of the jet stream. The presence of the jet stream clearly has a minimal effect on the results, indicating that in sonic boom modeling, large-scale horizontal wind effects may be ignored for most investigations.

Dependence on Waveform Shape

It has been proposed that observed rise times primarily depend on the magnitude of the lead shock, modeled as a simple step shock, and that the shape of the remaining waveform is relatively unimportant (ref. 12). In order to investigate this, the initial waveform displayed in the previous figures was modified to include a portion of constant overpressure immediately behind the initial shock. This was propagated at 0% relative ground humidity, so that the long rise time would magnify any observable effects. The results are displayed in Fig. 21.

The amplitude of the initial waveform was reduced so that the lead shock amplitude of the received waveform at ground level would be comparable to the results of Fig. 11. The observed rise time along the ray path is displayed in Fig. 22. Interpolation yields a rise time at the ground of approximately 12.5 msec, over twice that observed in the previous waveform. Thus, waveform shape clearly may have a strong influence on the rise time.

Rise Time Definition

The structure of the leading shocks observed in Figs. 11 and 21 suggests that the definition and utility of "rise time" used in the modern literature may have to be re-evaluated. The shocks observed in these figures consist of nearly vertical portions that are strongly rounded only at the very top. Clearly, the upper rounding accounts for nearly the entire rise time. Thus, the single "rise time" quantity is incapable of correctly indicating the extremely rapid increase in amplitude at the leading edge of the shock. Careless use of the "rise time" value in current loudness algorithms may lead to very misleading results.

CONCLUSIONS

The ZEPHYRUS propagation model incorporates a number of physical effects into a single model. Trials with the ZEPHYRUS model have yielded several significant results.

First, simple "stable step shock" solutions are generally not adequate for rise time prediction. Stable shocks have not formed at ground level, and thus the rise time will depend on the ray path history. In addition, the rise time depends on the waveform shape behind the shock.

Second, the dispersion due to molecular relaxation may have a strong direct influence on the rise time. This occurs when the characteristic relaxation time closely matches the rise time.

Finally, simple loudness algorithms which use only rise time and shock amplitude may be inadequate. The lead shock typically has a highly asymmetric structure that is not adequately characterized by the rise time and shock amplitude alone.

REFERENCES

1. Pestorius, F. M: *Propagation of Plane Acoustic Noise of Finite Amplitude*, ARL-TR-73-23, Applied Research Laboratories, The University of Texas at Austin, AD 778 868, August 1973.
2. Robinson, Leick D.: *Sonic Boom Propagation through an Inhomogeneous, Windy Atmosphere*, Ph.D. dissertation, The University of Texas at Austin, December 1991.
3. Thompson, Robert J.: Ray Theory for an Inhomogeneous Moving Medium. *J. Acoust Soc. Am.*, vol. 51, 1972, pp. 1675-1682.
4. Courant, R.; and Hilbert, D.: *Methods of Mathematical Physics*, Interscience, New York, 1962, Vol. II, Chap. VI, pp. 577-618.
5. Pestorius, 1973.
6. Bass, H. E.; Sutherland, L. C.; and Zuckerwar, A. J.: Atmospheric absorption of sound: Update. *J. Acoust. Soc. Am.*, vol. 88, no. 4, Oct. 1990, pp. 2019-2021.
7. Earnshaw, S.: *On the Mathematical Theory of Sound*, Phil. Trans. Roy. Soc. London, vol. 150, 1860, pp. 133-148.
8. *U.S. Standard Atmosphere, 1962*, U.S. Government Printing Office, December 1962.
9. Hayes, W. D.; Haefeli, R. C.; and Kularud, H. E.: *Sonic Boom Propagation in a Stratified Atmosphere, with Computer Program*, NASA-CR1299, April 1969.
10. Pierce, Allan D.; and Sparrow, Victor W.: Relaxation and Turbulence Effects on Sonic Boom Signatures. *First Annual High-Speed Research Workshop*, Williamsburg, Va., May 14-16, 1991.

11. McLean, George S., Jr.: The Jet Stream Profile and Associated Turbulence. *Air Force Surveys in Geophysics No. 140*, Geophysics Research Directorate, AFCRL, March 1962.
12. Kang, Jongmin: *Nonlinear Acoustic Propagation of Shock Waves Through the Atmosphere with Molecular Relaxation*, Ph.D. Dissertation, The Pennsylvania State University, May 1991.

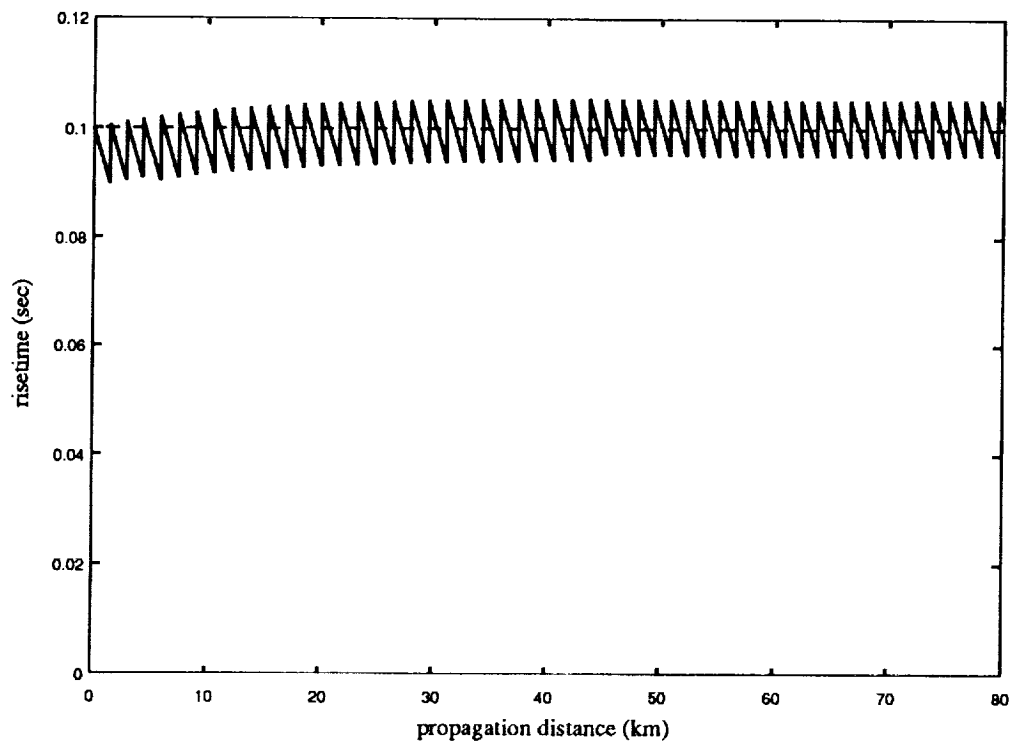


Figure 1. Stable shock rise time (100ms).

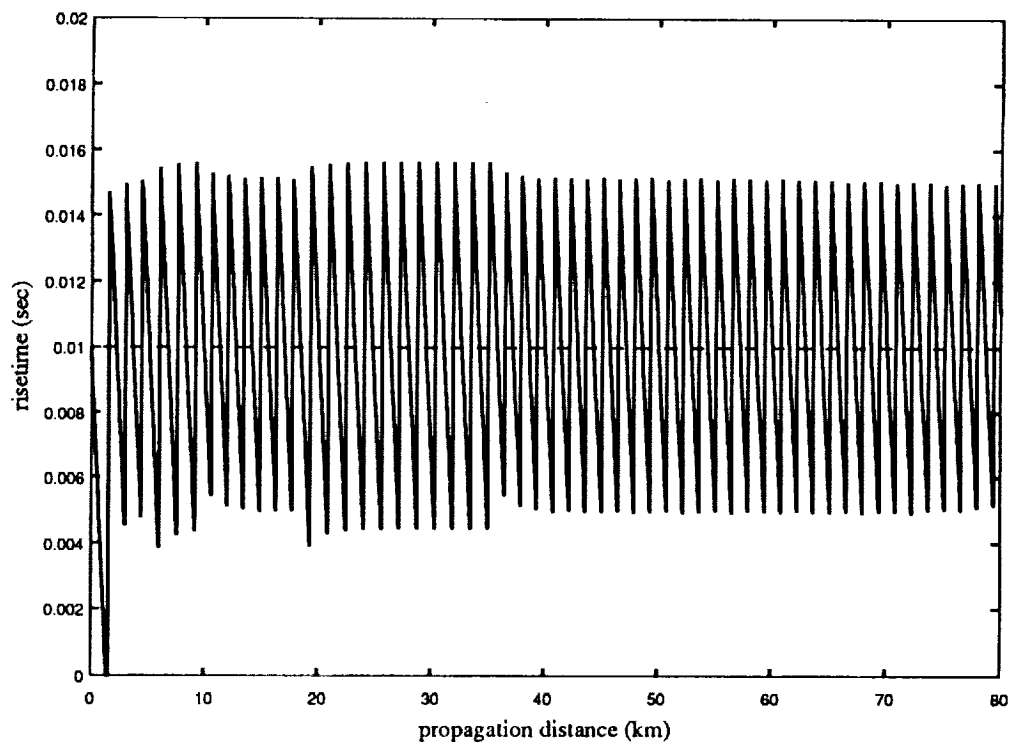


Figure 2. Stable shock rise time (10ms).

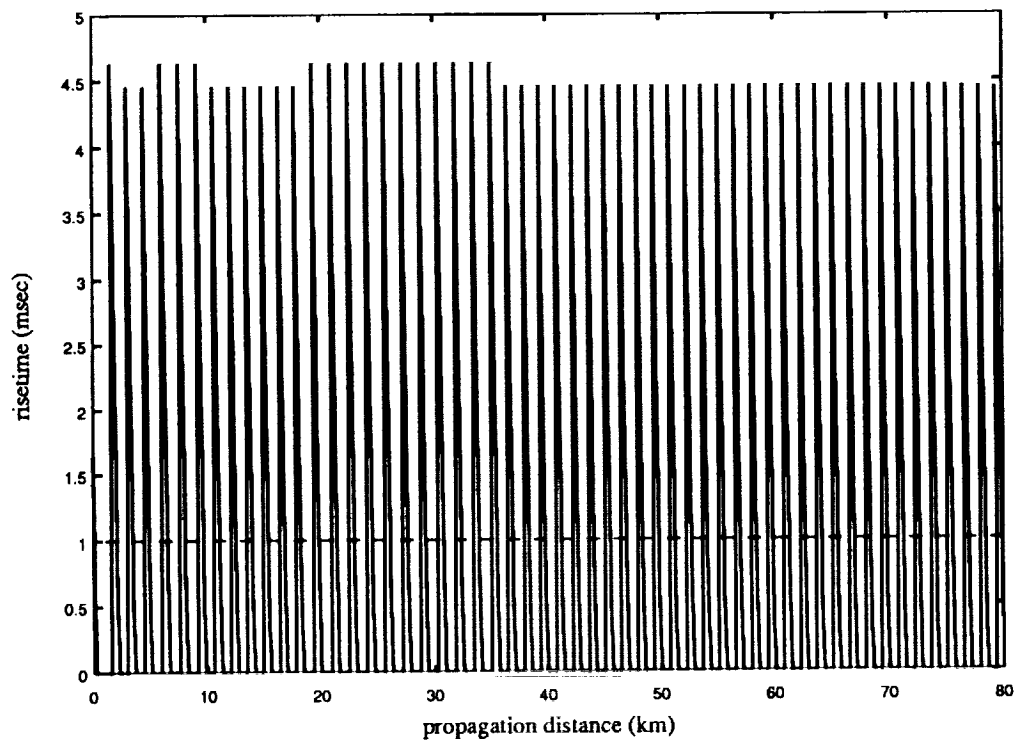


Figure 3. Stable shock rise time (1ms).

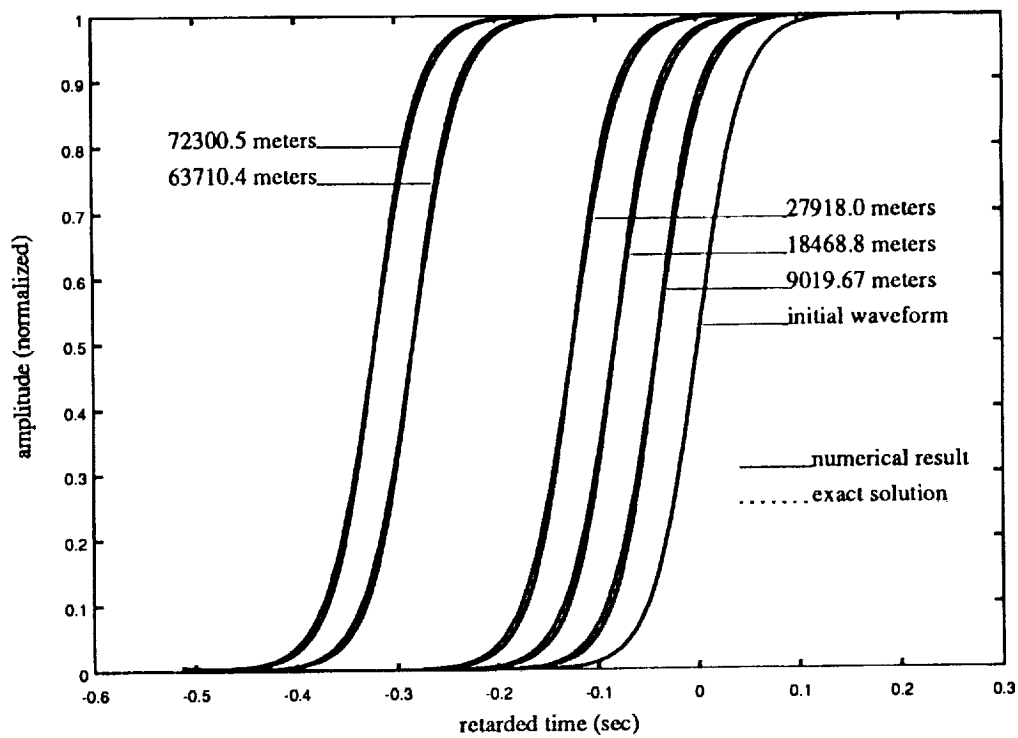


Figure 4. Stable shock waveforms (100 ms rise time).

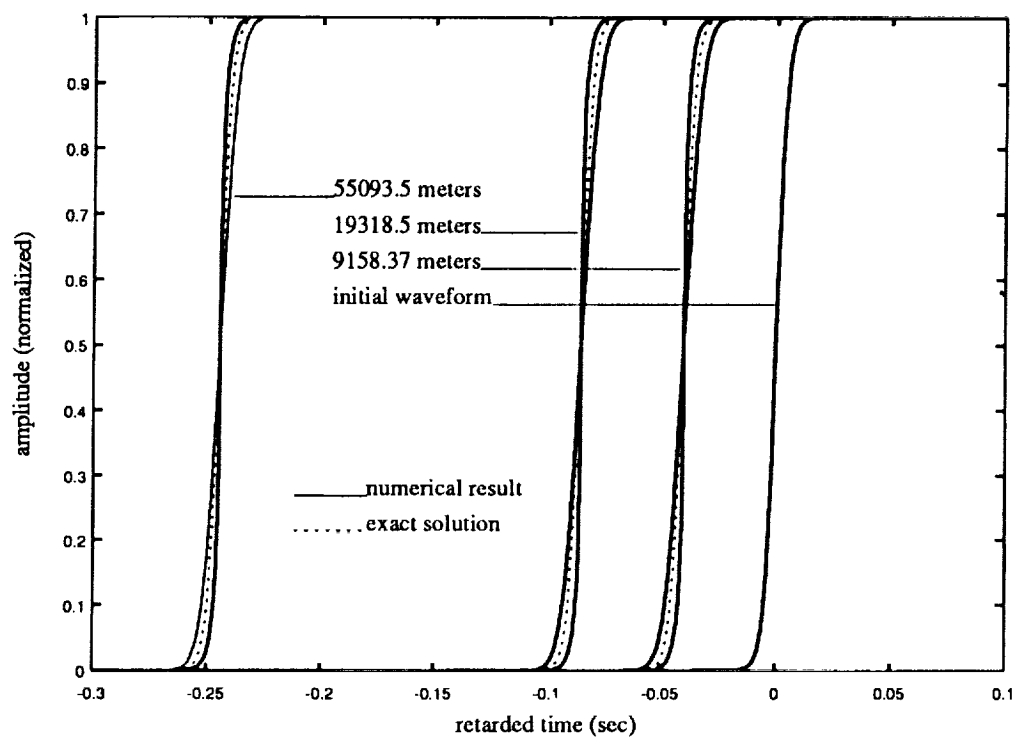


Figure 5. Stable shock waveforms (10ms rise time).

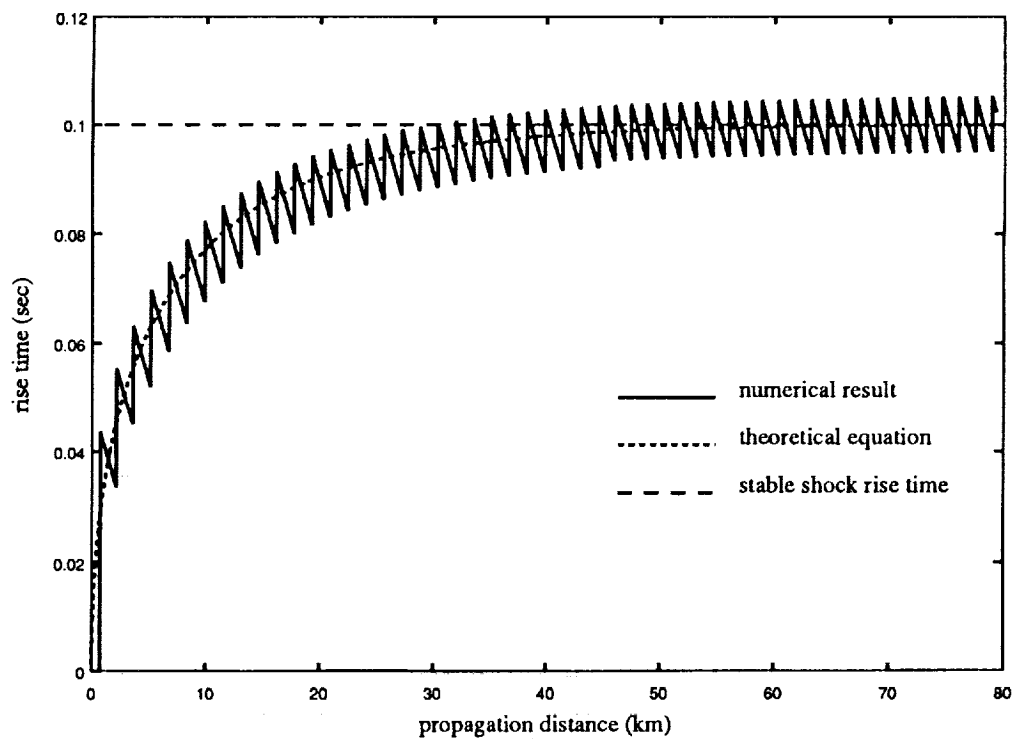


Figure 6. Stable shock formation, no molecular relaxation.

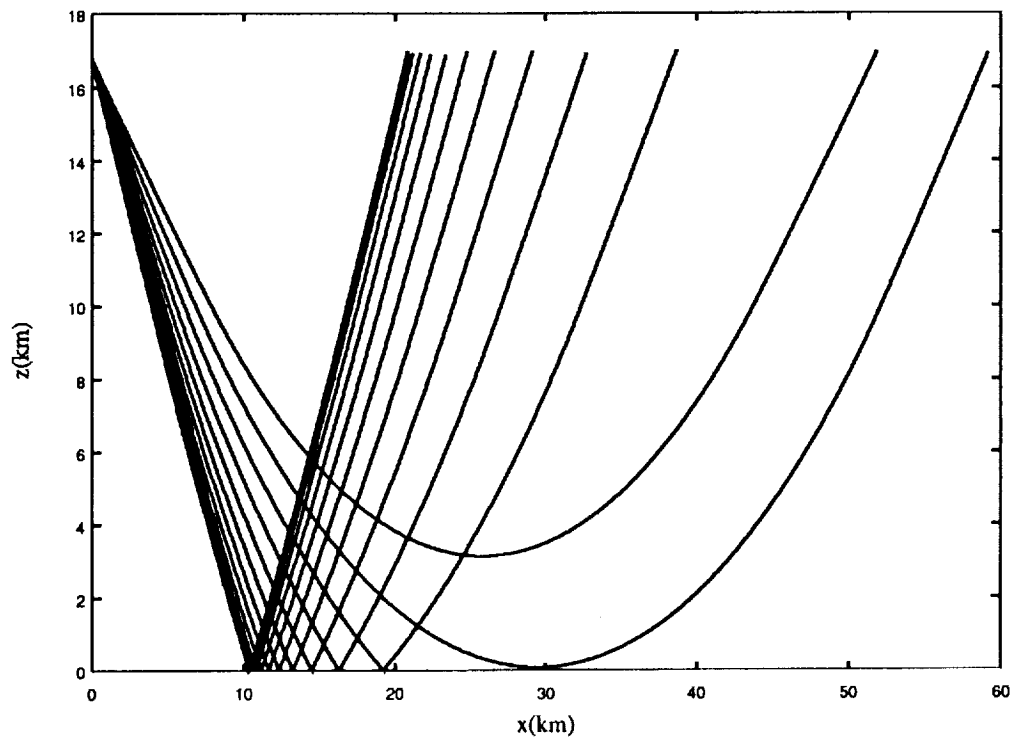


Figure 7. Ray fan, standard atmosphere (x vs. z)

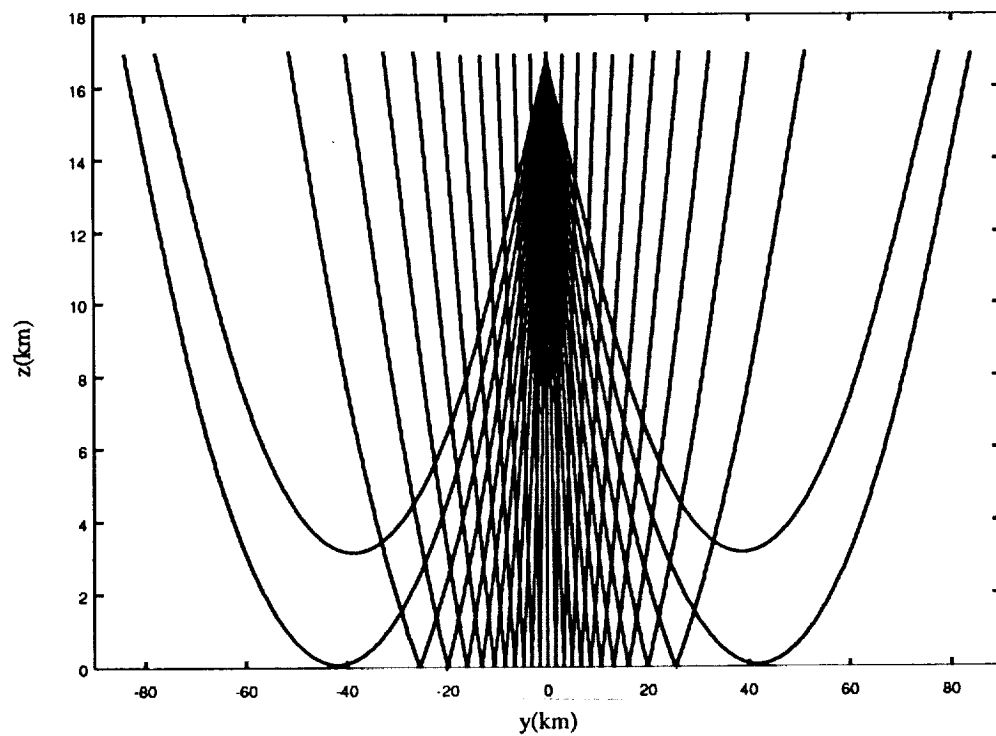


Figure 8. Ray fan, standard atmosphere (y vs. z)

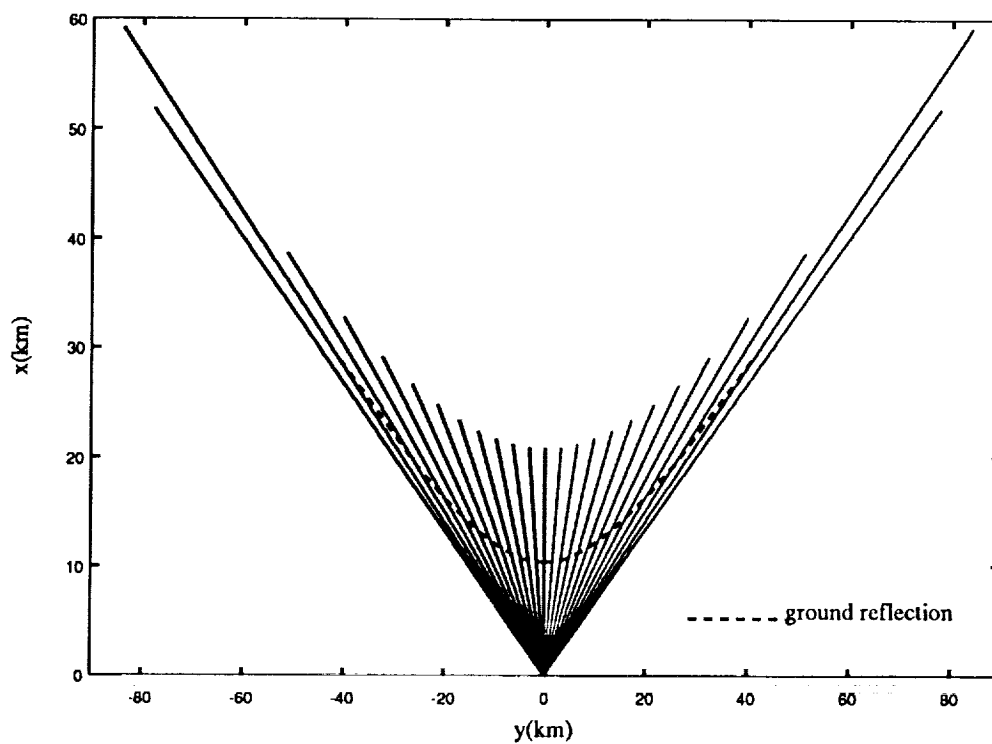


Figure 9. Ray fan, standard atmosphere (x vs. y).

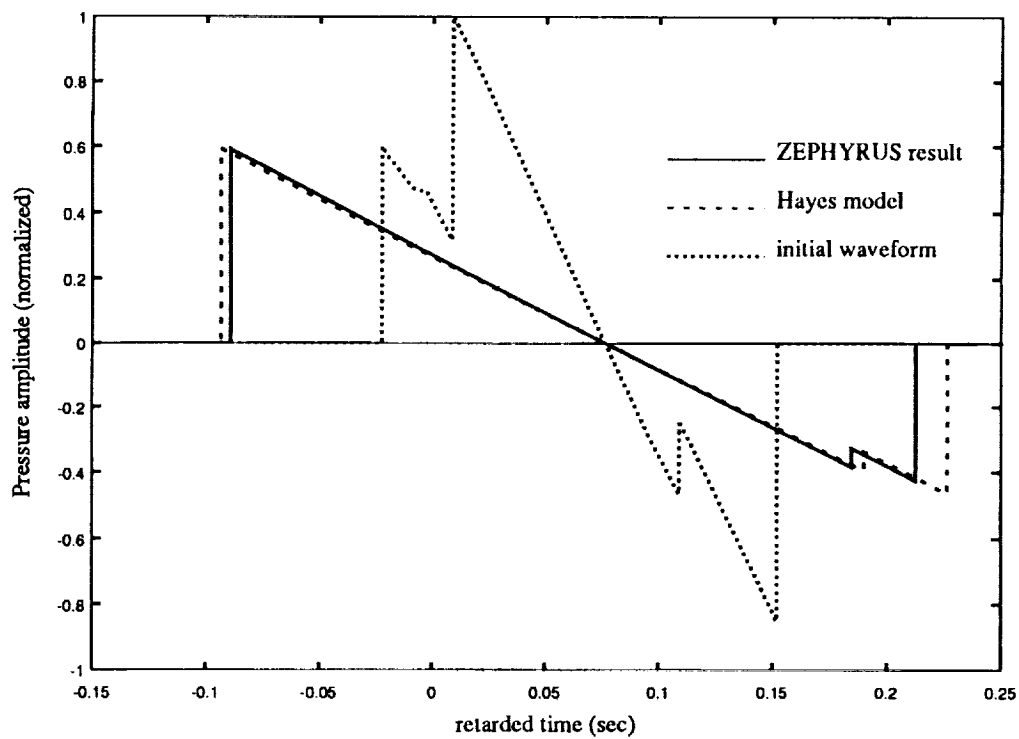


Figure 10. Comparison with the Hayes program.

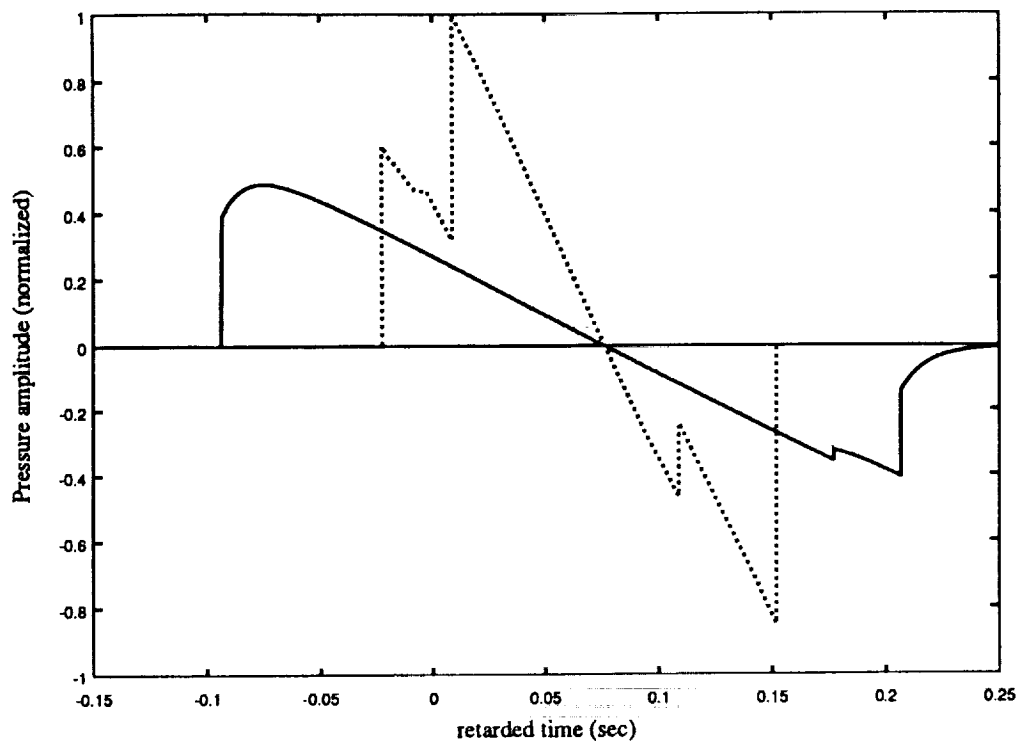


Figure 11. Sonic boom waveform (0% relative humidity at ground).

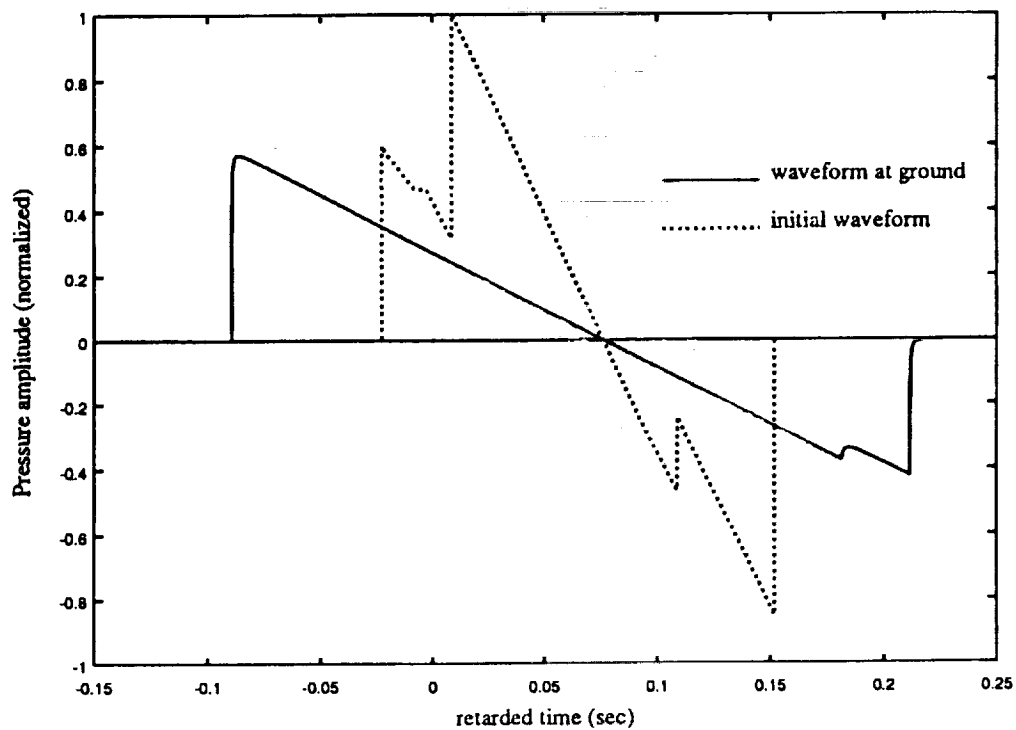


Figure 12. Sonic boom waveform (50% relative humidity at ground).

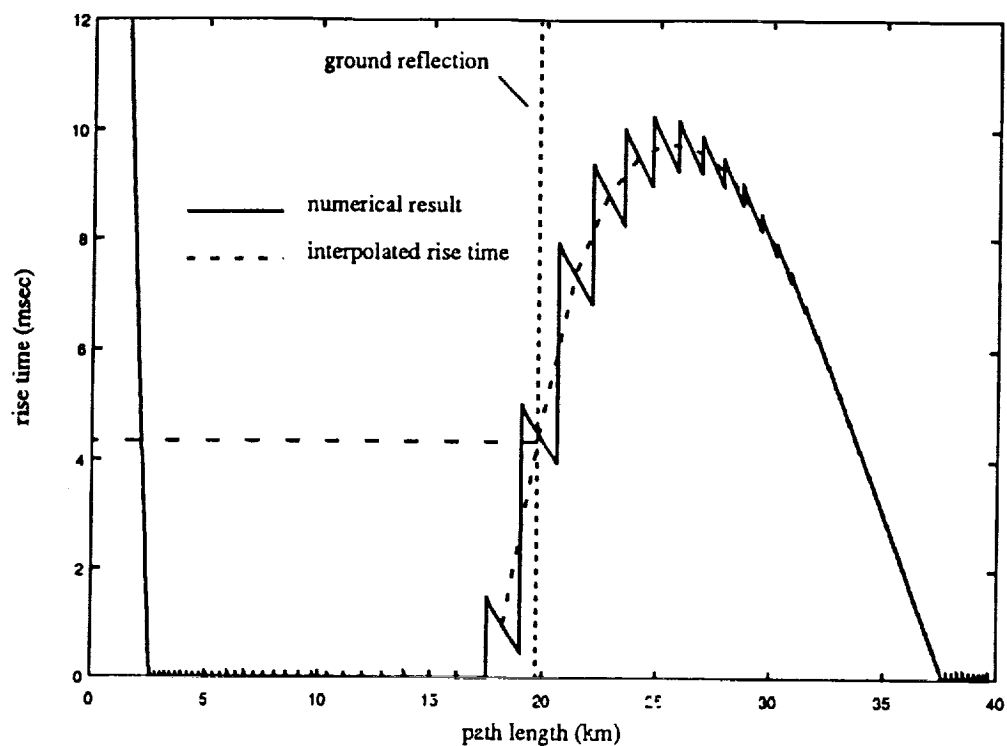


Figure 13. Rise time (0% relative humidity at ground).

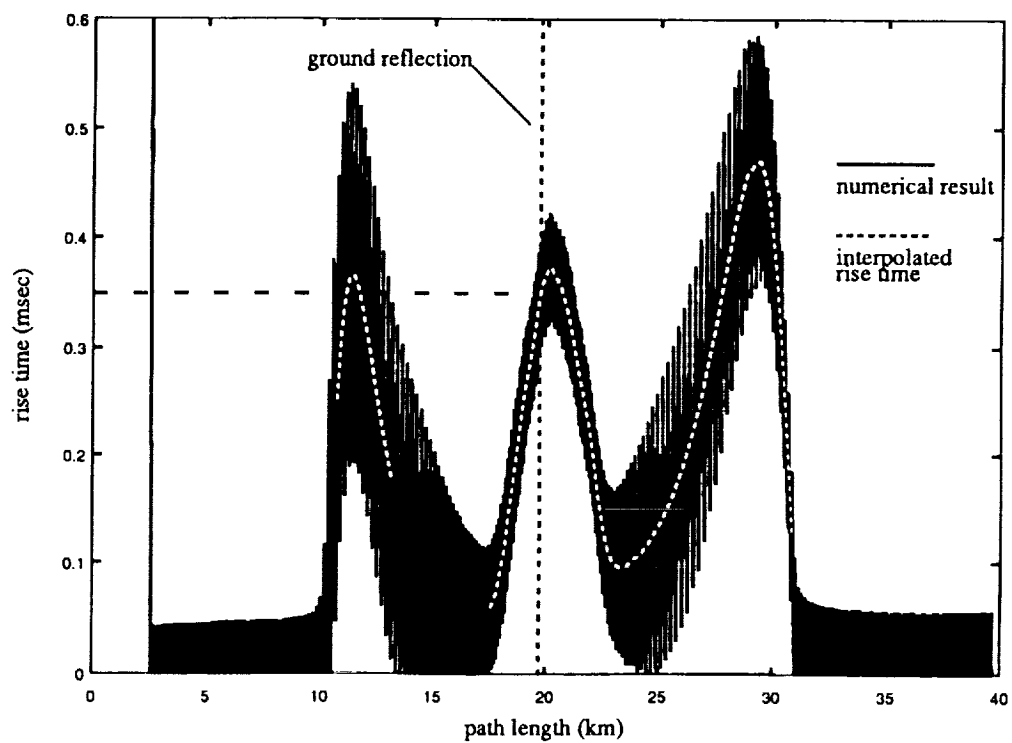


Figure 14. Rise time (50% relative humidity at ground).

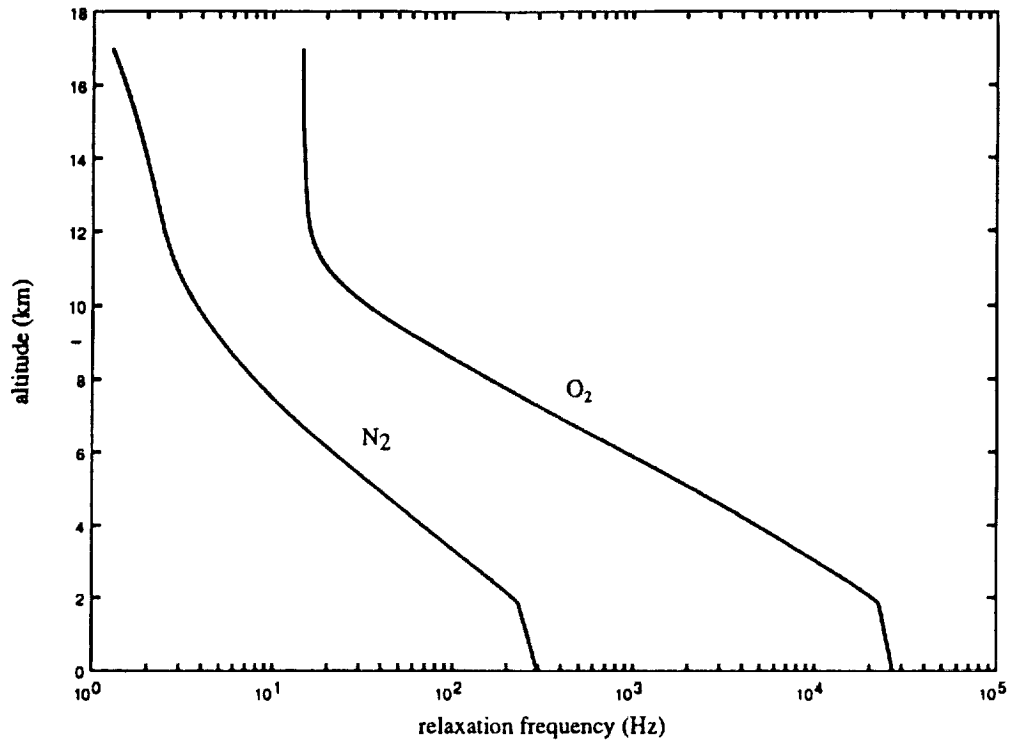


Figure 15. O_2 and N_2 relaxation frequencies (50% relative humidity at ground).

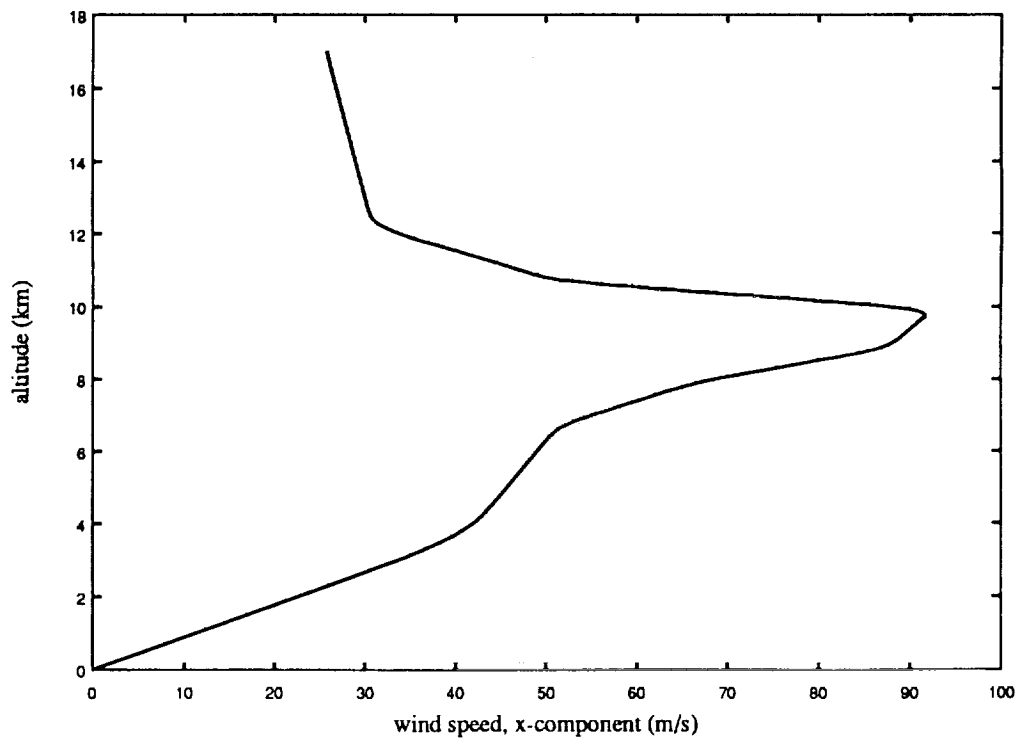


Figure 16. Typical jet stream.

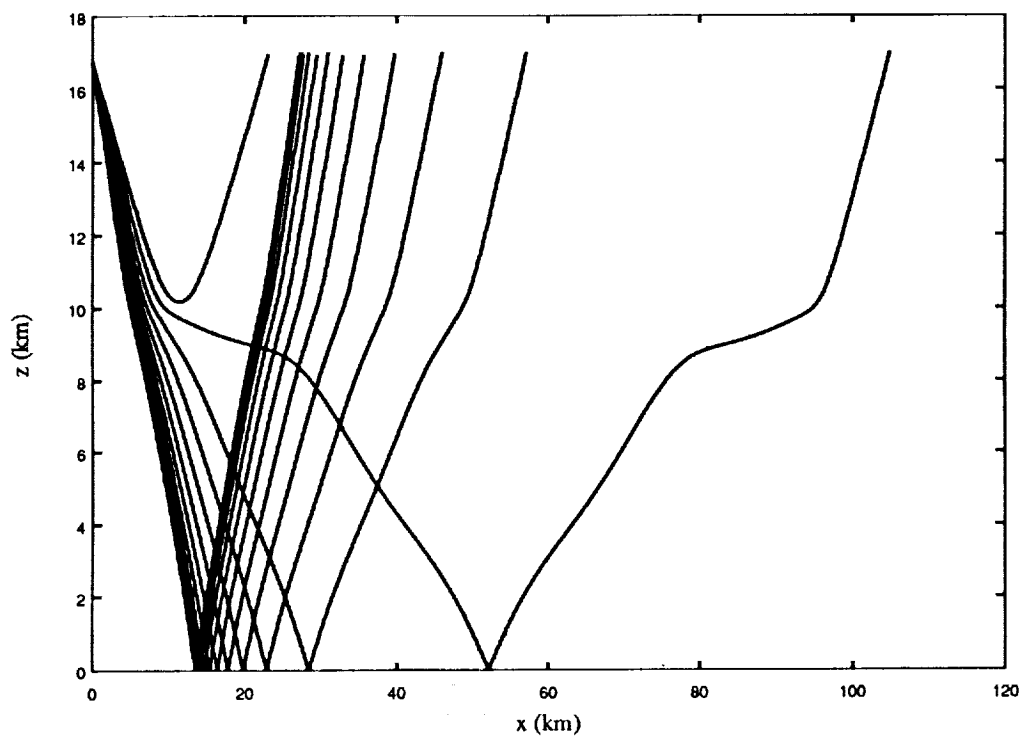


Figure 17. Ray fan through a jet stream (x vs. z).

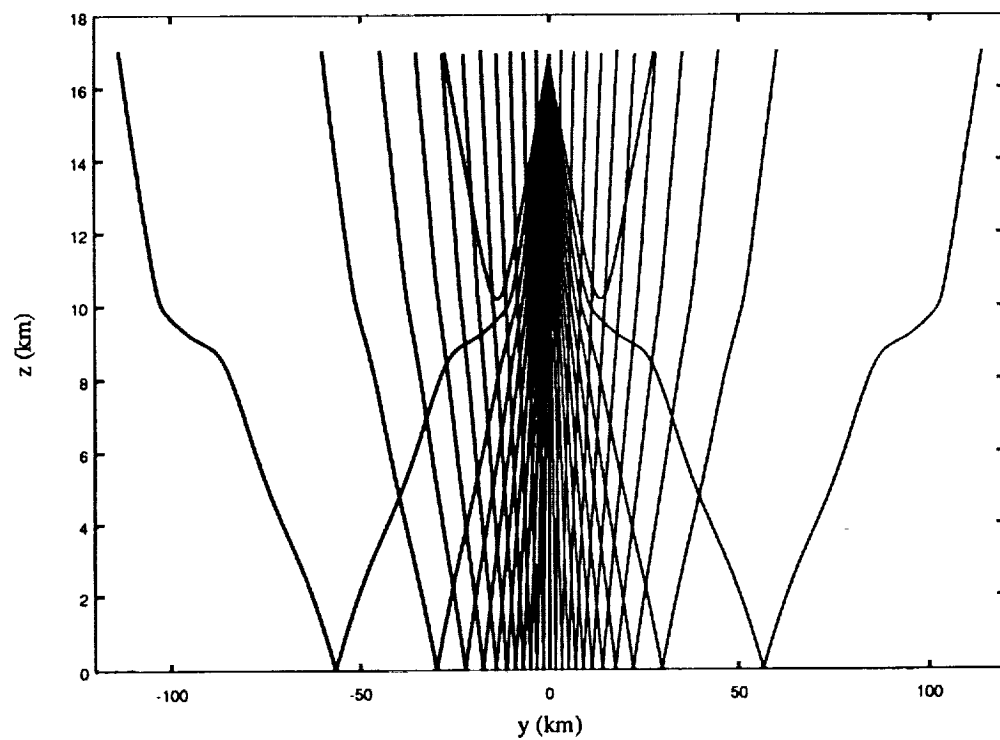


Figure 18. Ray fan through a jet stream (y vs. z)

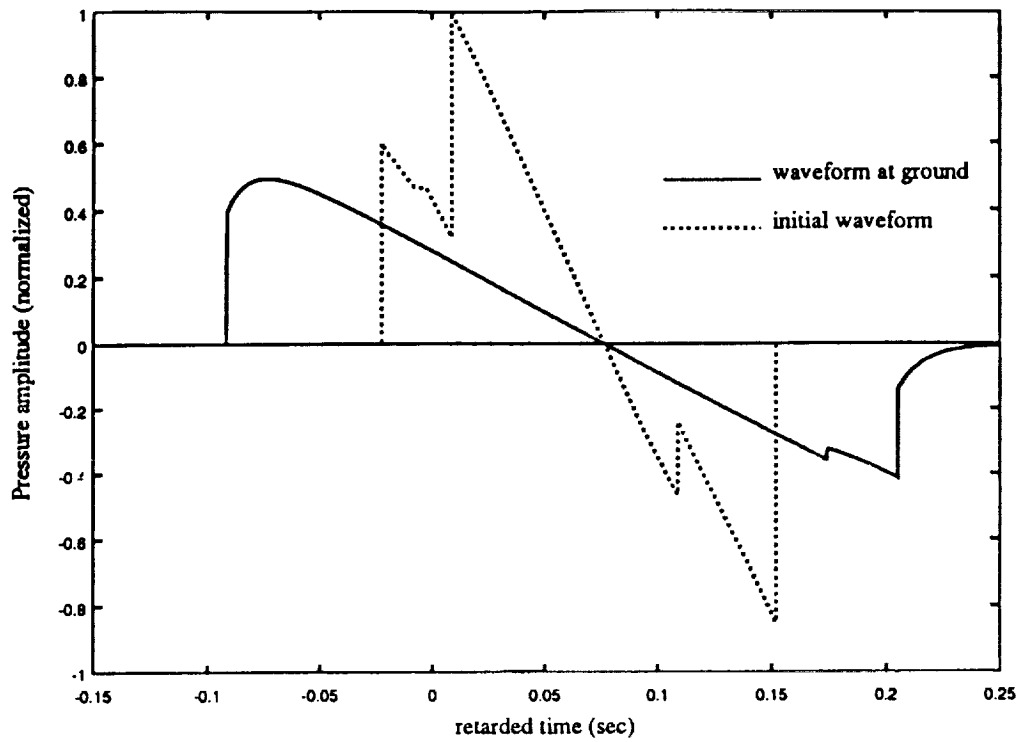


Figure 19. Sonic boom waveform at ground after passage through jet stream.

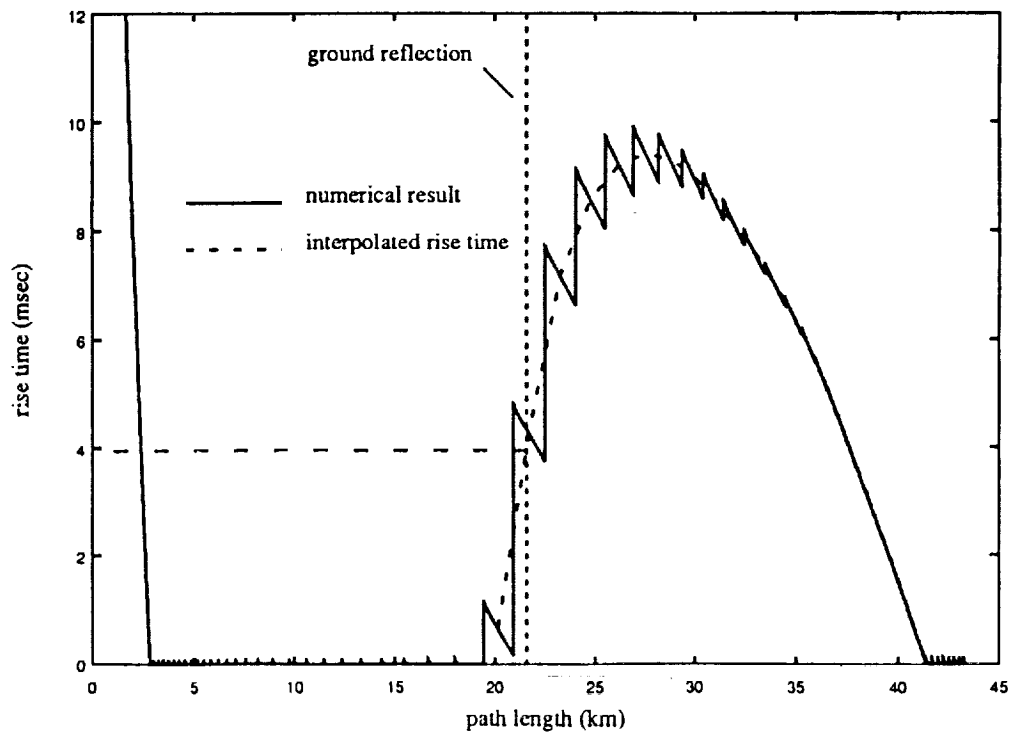


Figure 20. Rise time during passage through jet stream (0% relative humidity at ground).

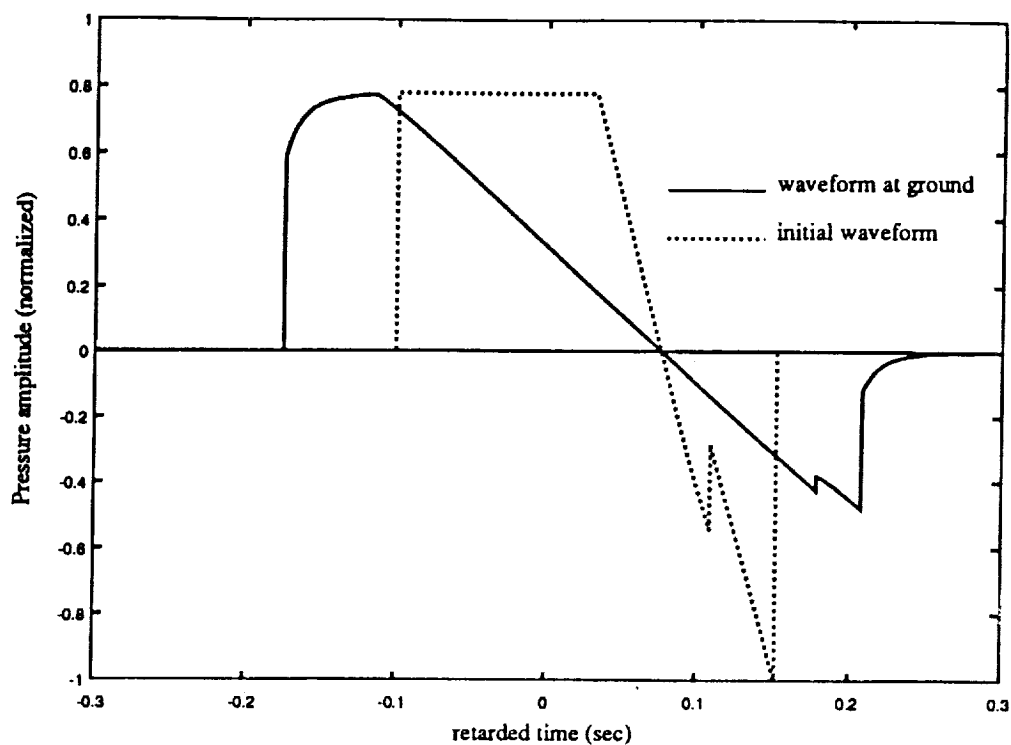


Figure 21. Modified waveform (0% relative humidity).

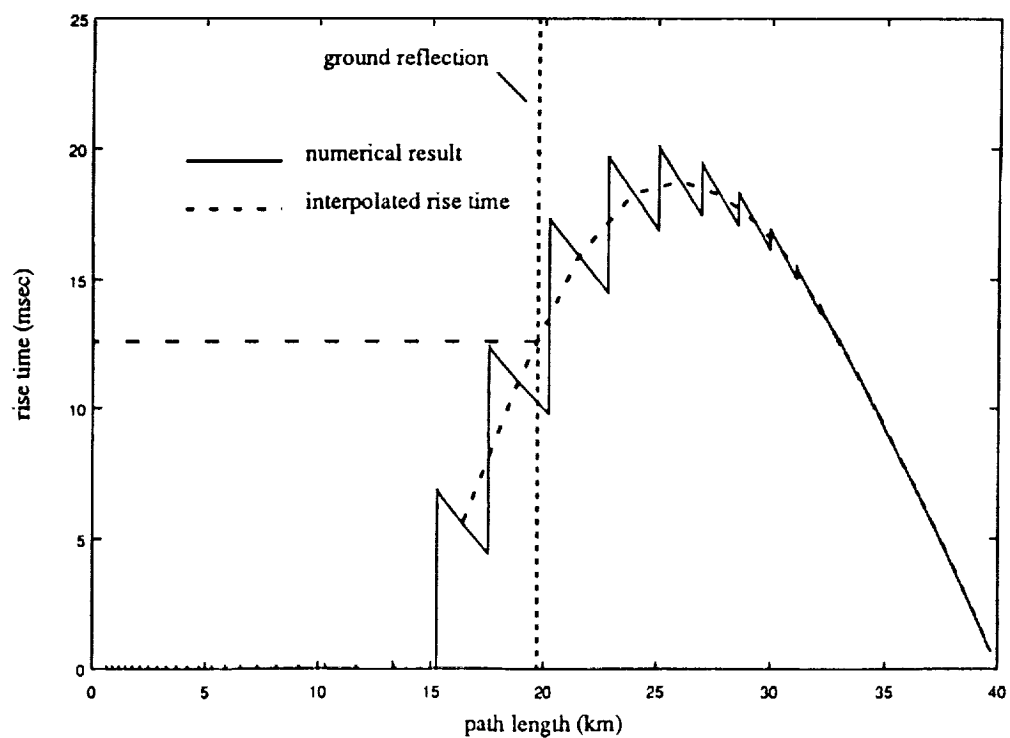


Figure 22. Rise time for modified waveform (0% relative humidity at ground).

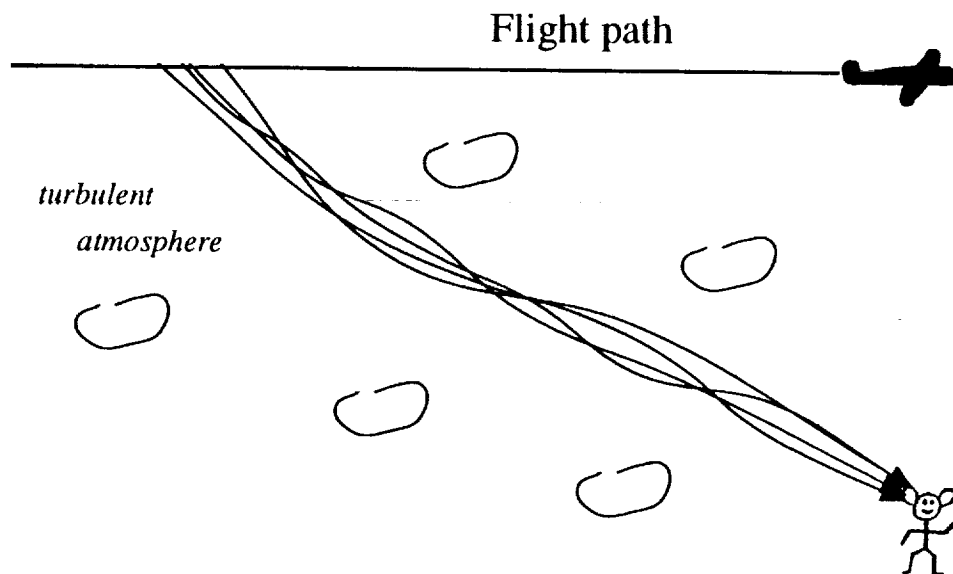
WAVE EQUATIONS AND COMPUTATIONAL MODELS FOR
SONIC BOOM PROPAGATION THROUGH A TURBULENT ATMOSPHERE*

Allan D. Pierce
College of Engineering Division of the
Graduate Program in Acoustics
and
Department of Mechanical Engineering
157 Hammond Building
The Pennsylvania State University
University Park, PA 16802

SUMMARY

The improved simulation of sonic boom propagation through the real atmosphere requires greater understanding of how the transient acoustic pulses popularly termed sonic booms are affected by atmospheric turbulence. The present paper describes a nonlinear partial differential equation that can be used to simulate the effects of smaller-scale atmospheric turbulence on sonic boom waveforms. The equation is first order in the time derivative and involves an extension of geometrical acoustics to include diffraction phenomena. Various terms in the equation are explained in physical terms. Such terms include those representing convection at the wave speed, diffraction, molecular relaxation, classical dissipation, and nonlinear steepening. The atmospheric turbulence enters through an effective sound speed, which varies with all three spatial coordinates, and which is the sum of the local sound speed and the component of the turbulent flow velocity projected along a central ray that connects the aircraft trajectory with the listener.

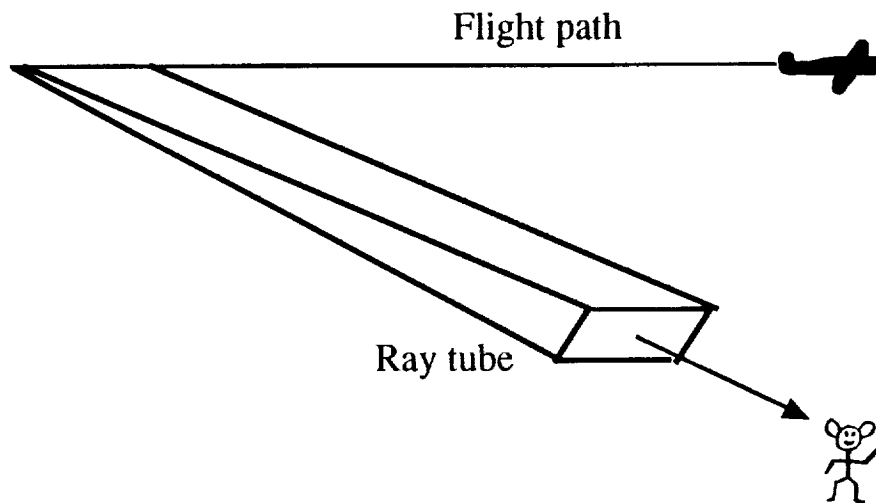
* Work done under NASA Grant NAG-1-947.



*Rays connecting
aircraft trajectory and listener*

- *multiplicity* caused by *turbulence*
- *all* such rays *closely spaced*
- *arrive* within an
interval of a *few milliseconds*
(10 to 30)

Ray acoustics have intrinsic difficulties for the simulation of the effects of turbulence on sonic boom propagation. When small-scale turbulence is taken into account, many rays can connect the flight trajectory and any given listener location on the ground. Such rays, however, are closely intertwined and can arrive within a very small time interval.



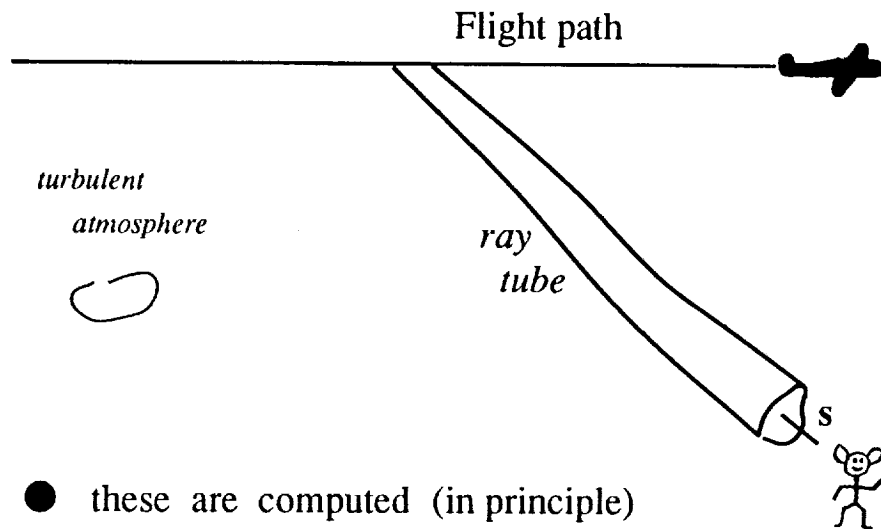
*If you could **average turbulence**
over length scales
of order of 100 m,*

then

- *only one ray connects
aircraft trajectory and listener*
- *energy (more precisely, wave action)
travels down ray tube*

The multiplicity of rays is expected to disappear if the turbulence is ignored, or if one takes the atmosphere to be perfectly stratified. The absence of multipaths is also expected if one averages out the smaller-scale turbulence. Just how gross this averaging must be is a matter of conjecture, but one anticipates that an averaging out of scales less than 100m will be adequate.

Concepts of a *central ray*
and of a *nominal ray tube*



- these are computed (in principle)
leaving out the *fine-scale turbulence*

First approximation is

$$p = B(s) f(t, s)$$

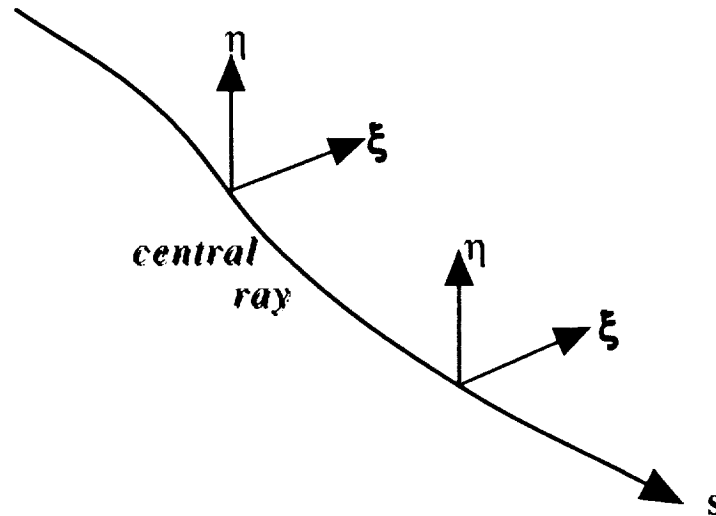
where

$B(s)$ = Blokhintzev amplitude factor, adjusting
continuously with s
to "conserve" wave action flux
along ray tube

$f(t, s)$ = "normalized" waveform,
distorting with
increasing propagation distance

The theory in the present paper begins with the premise that ray acoustics is a good departure point for developing a simulation model that includes the fine-scale turbulence. One conceives of one out of many rays that connects the trajectory with the listener and refers to it as the central ray. It and the associated nominal ray tube can be found by use of a model that ignores fine-scale turbulence.

Conceptual framework for simulating the effects of fine-scale turbulence



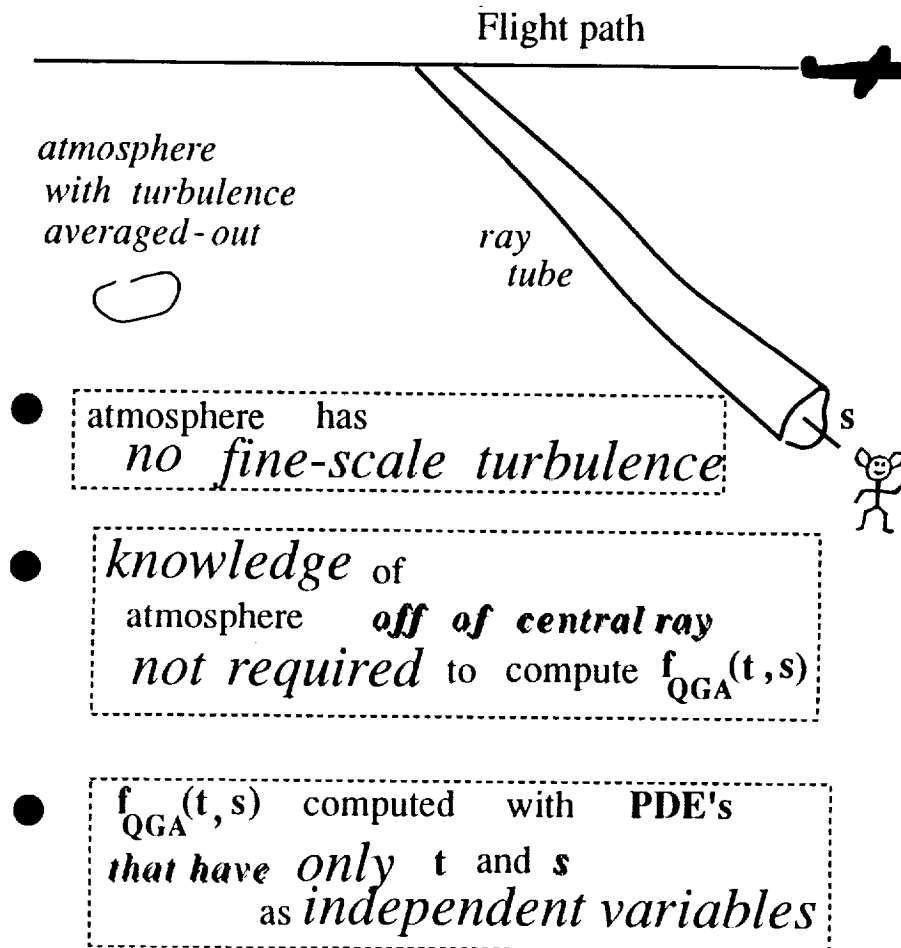
local curvilinear coordinate system
 s, ξ, η

- s = distance along central ray
- central ray is
line $\xi=0, \eta=0$
- directions of $\nabla \xi$ and $\nabla \eta$ *not necessarily*
constant along central ray

To consider the distortion of sonic boom waveforms by small-scale turbulence, one needs to explicitly consider physical processes that take place off of the central ray. To do such, one needs to introduce an appropriate curvilinear coordinate system. One has some latitude in choosing the coordinate mapping, but the central ray should be the line along which the other two coordinates are identically zero.

Quasi-geometrical acoustics (QGA)

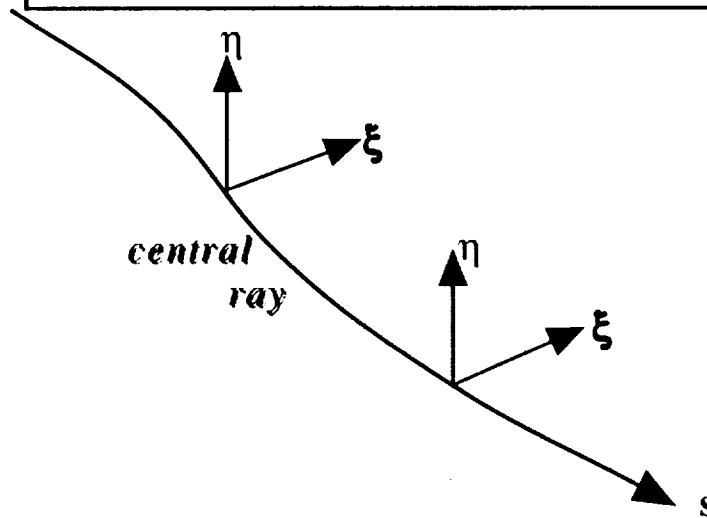
$$p_{QGA} = B_{QGA}(s) f_{QGA}(t, s)$$



The commonly used theory of sonic boom propagation based on the concept of rays is here termed quasi-geometrical acoustics because it contains some ingredients such as nonlinear steepening and stretching of waveforms that are not ordinarily associated with geometrical acoustics. One can still use some results in a broader framework that takes small-scale turbulence into account.

Suggested modification
for *turbulent atmosphere* (TA)

$$p_{TA} = B_{QGA}(s) f_{TA}(t, s, \xi, \eta)$$



- same $B_{QGA}(s)$, computed *leaving out*
fine-scale turbulence

- *knowledge* of atmosphere in
"general vicinity" of central ray
required to compute $f_{TA}(t, s, 0, 0)$

- $f_{TA}(t, s, \xi, \eta)$ computed with PDE's
having t, s, ξ, η as independent variables

The suggested modified theory makes use of the same Blokhintzev amplitude factor (which can be regarded as being roughly proportional to the inverse of the square root of the ray tube area) that emerges in the geometrical acoustics of an inhomogeneous medium. The propagation of the waveform shape, however, is regarded as a three-dimensional, rather than a one-dimensional, phenomenon.

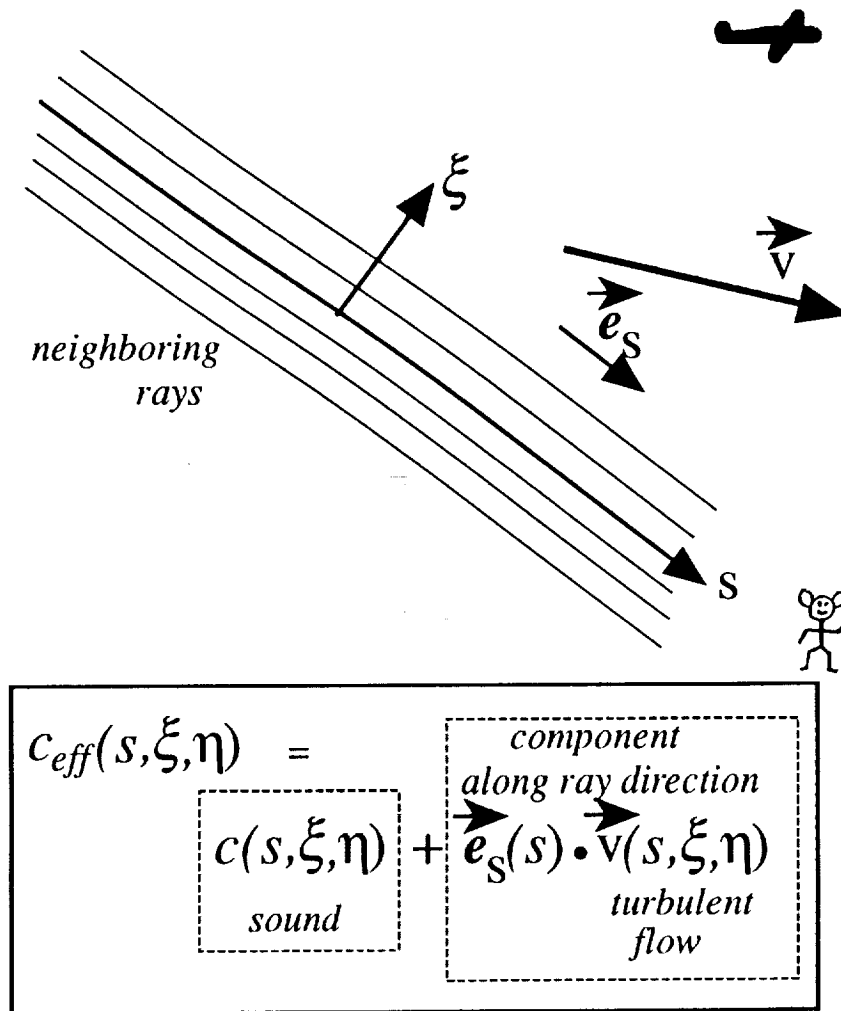
$$p_{TA} = B_{QGA}(s) f_{TA}(t, s, \xi, \eta)$$

What affects propagation
of $f_{TA}(t, s, \xi, \eta)$?

- *convection* at **effective wave speed**
- ξ, η *dependence*
of **effective wave speed**
- *nonlinear* steepening
- classical *dissipation* processes
shear viscosity
bulk viscosity
thermal conductivity
- *relaxation* of
internal molecular vibrations
oxygen O_2
nitrogen N_2
- *diffraction*

The propagation of the waveform shape factor through a turbulent atmosphere is known from other analyses to be affected by a multitude of physical effects. Those of which the author is currently aware are listed above. Relaxation, for example, has been shown to have a substantial effect on sonic boom rise times, although it appears that turbulence effects are the major contributor.

Effective sound speed



An important simplification in the theory is the incorporation of fluid flow associated with turbulence into an effective sound speed, this being the speed at which waves propagate along the ray tube direction. An intrinsic simplification is that no distinction is made between the direction along the central ray and the direction normal to the wavefront associated with the central ray.

$$\frac{\partial f_{TA}}{\partial t} + \left[\text{CONVECTION TERM} \right] + \left[\text{SEVERAL OTHER TERMS} \right] = 0$$

The Convection Term:

$$\left[\text{CONVECTION TERM} \right] = c_{\text{eff}} \frac{\partial f_{TA}}{\partial s}$$

$$\begin{aligned} c_{\text{eff}} &= c_{\text{eff}}(s, \xi, \eta) \\ &= c(s, \xi, \eta) + v_{\parallel}(s, \xi, \eta) \end{aligned}$$

coupling of convection

at different values of ξ and η
arises because of the
diffraction term.

The partial differential equation developed here for propagation of the waveform shape function through a turbulent atmosphere is deliberately chosen to be of first order in the time differentiation. Here the most important of the several terms is exhibited. The convection term incorporates the tendency for the wave to “locally” move with the effective sound speed.

$$\frac{\partial f_{\text{TA}}}{\partial t} + \left[\text{CONVECTION TERM} \right] + \left[\text{DIFFRACTION TERM} \right] + \left[\text{SEVERAL OTHER TERMS} \right] = 0$$

The Diffraction Term:

$$\begin{aligned} & \left[\text{DIFFRACTION TERM} \right] \\ &= -\frac{c_{\text{eff}}(s)}{2} \left\{ \frac{\partial^2}{\partial \xi^2} + \frac{\partial^2}{\partial \eta^2} \right\} \int_s^\infty f_{\text{TA}}(t, s', \xi, \eta) ds' \end{aligned}$$

Upper limit on integral can be replaced by *any point* ahead of the wave onset

The diffraction term couples propagation along various lines parallel to the central ray and explicitly involves differentiation with respect to transverse coordinates. It is analogous to similar terms that occur in the parabolic equation (PE) for constant frequency propagation, in the NPE developed by McDonald and Kuperman, and in the KZB equation developed in the Soviet Union.

Heuristic Derivation

Diffraction Term

$$\frac{\partial^2 f}{\partial t^2} - c^2 \left\{ \frac{\partial^2}{\partial s^2} + \nabla_T^2 \right\} f \approx 0$$

$$\left\{ \frac{\partial}{\partial t} - c \frac{\partial}{\partial s} \right\} \left\{ \frac{\partial}{\partial t} + c \frac{\partial}{\partial s} \right\} f \approx c^2 \nabla_T^2 f$$

But $f \approx f(s - ct)$, so

$$\frac{\partial}{\partial t} \approx -c \frac{\partial}{\partial s}$$

$$-2c \frac{\partial}{\partial s} \left[\left\{ \frac{\partial}{\partial t} + c \frac{\partial}{\partial s} \right\} f \right] \approx c^2 \nabla_T^2 f$$

and the bracketed quantity vanishes at $s = \infty$, so

$$\left\{ \frac{\partial}{\partial t} + c \frac{\partial}{\partial s} \right\} f \approx \frac{c}{2} \int_s^\infty \nabla_T^2 f \, ds$$

RHS is the negative of the diffraction term

Although a more nearly rigorous derivation of the diffraction term may be possible, a heuristic derivation is more useful as it is less prone to conceptual errors and yields insight into the nature of the approximations entailed. The derivation here is for quasi-one-dimensional propagation in the $+s$ -direction through a homogeneous medium, with the 3-D wave equation taken as a starting point.

$$\begin{aligned} & \frac{\partial f_{TA}}{\partial t} + [\text{CONVECTION TERM}] \\ & + [\text{NONLINEAR STEEPENING TERM}] \\ & + [\text{SEVERAL OTHER TERMS}] = 0 \end{aligned}$$

Nonlinear correction for wave speed:

$$c_{\text{eff}} \frac{\partial}{\partial s} \rightarrow [c_{\text{eff}} + \beta v_{\text{ac}}] \frac{\partial}{\partial s}$$

[NONLINEAR STEEPENING TERM]

$$\begin{aligned} & = \beta v_{\text{ac}} \frac{\partial f_{TA}}{\partial s} \\ & = \beta \frac{B_{QGA}}{\rho c} f_{TA} \frac{\partial f_{TA}}{\partial s} \end{aligned}$$

Recall that $p_{TA} = B_{QGA} f_{TA}$

while $v_{\text{ac}} = p_{\text{ac}} / \rho c$ ***for a plane traveling wave***

The manner in which nonlinear steepening is incorporated into the theory parallels that of the textbook derivation of the inviscid Burgers' equation. Two nonlinear effects, the increase of sound speed with increasing pressure and the additional convection of the wave by the fluid velocity increment associated with the wave itself, contribute to the term. The parameter β is 1.2 for air.

$$\begin{aligned} & \frac{\partial f_{TA}}{\partial t} + [\text{CONVECTION TERM}] \\ & + [\text{MOLECULAR RELAXATION TERMS}] \\ & + [\text{SEVERAL OTHER TERMS}] = 0 \end{aligned}$$

***Transition from
equilibrium sound speed to frozen sound speed:***

$$c_{\text{eff}} \frac{\partial f_{TA}}{\partial s} \rightarrow c_{\text{eff}} \frac{\partial f_{TA}}{\partial s} + \sum_{\nu} (\Delta c)_{\nu} \frac{\partial f_{\nu}}{\partial s}$$

*molecular
relaxation
terms*

where

$$f_{\nu} + \tau_{\nu} \frac{\partial f_{\nu}}{\partial t} \approx \tau_{\nu} \frac{\partial f_{TA}}{\partial t}$$

or

$$f_{\nu} - c\tau_{\nu} \frac{\partial f_{\nu}}{\partial s} \approx -c\tau_{\nu} \frac{\partial f_{TA}}{\partial s}$$

are appropriate relaxation equations

Molecular relaxation can be regarded as the tendency for the energy associated with internal vibrations to be frozen in the limit of high frequency. When this happens to the oxygen molecules, an increment $(\Delta c)_1$ is added to the sound speed. The internal variable f_1 is equal to f_{TA} when the vibrational energies are frozen, but equal to zero when these energies adiabatically adjust to thermal equilibrium with the temperature carried by the sound wave.

— PSUPE —

The PSU Propagation Equation

$$\begin{aligned} & \frac{\partial f_{\text{TA}}}{\partial t} + c_{\text{eff}} \frac{\partial f_{\text{TA}}}{\partial s} + \beta \frac{B_{\text{QGA}}}{\rho c} f_{\text{TA}} \frac{\partial f_{\text{TA}}}{\partial s} \\ & - \frac{c(s)}{2} \left\{ \frac{\partial^2}{\partial \xi^2} + \frac{\partial^2}{\partial \eta^2} \right\} \int_s^\infty f_{\text{TA}}(t, s', \xi, \eta) ds' \\ & + \sum_\nu (\Delta c)_\nu \frac{\partial f_\nu}{\partial s} - \delta \frac{\partial^2 f_{\text{TA}}}{\partial s^2} = 0 \end{aligned}$$

Seek solution to initial value problem:

at time t_0 one specifies:

$$f_{\text{TA}}(t_0, s, \xi, \eta)$$

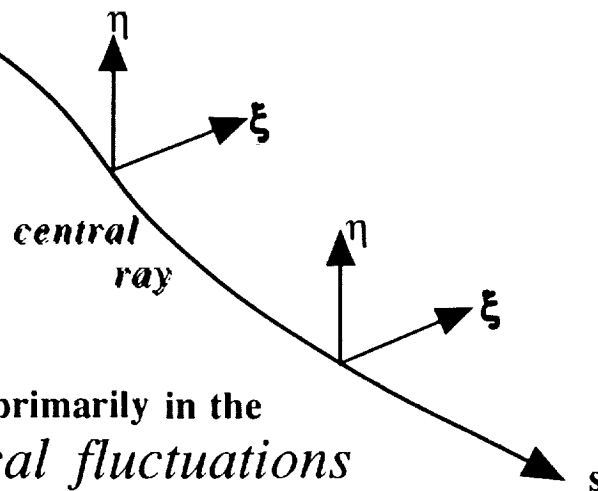
for “all” values of s, ξ, η

and one “marches” forward in time

The overall nonlinear partial equation proposed for studying the effects of fine-scale atmospheric turbulence on sonic boom waveforms is exhibited here. Giving it the acronymic name PSUPE is with tongue in cheek. Pronounce it as if you had a lisp and were trying to say “soup.” (But it is not duck soup!) The last term is the classical dissipation term, a familiar feature of Burgers’ equation.

Turbulence enters into the model through

$$c_{\text{eff}}(s, \xi, \eta) = c(s, \xi, \eta) + v_{\parallel}(s, \xi, \eta)$$



- interest is primarily in the *statistical fluctuations* in the waveforms
- *not necessary* to seek detailed simulation
- *computational problems* can be *formidable*
- seek all possible additional *simplifications*

The model involves turbulence through the dependence of the effective sound speed on position. It is anticipated that one will rarely know the momentary state of turbulence sufficiently well that an accurate simulation for a specific case would be desired. Rather one will seek to use the equation to relate statistical properties of the waveforms to statistical properties of the turbulence.

Simplifications regarding atmosphere and turbulence

Turbulence enters into the model through

$$c_{\text{eff}}(s, \xi, \eta) = c(s, \xi, \eta) + v_{\parallel}(s, \xi, \eta)$$

*central
ray*

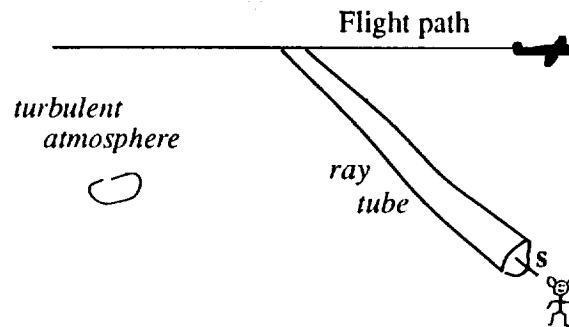
- $$c(s, \xi, \eta) = c_0 + \Delta c(s, \xi, \eta)$$

$$v_{\parallel}(s, \xi, \eta) = \Delta v_{\parallel}(s, \xi, \eta)$$
- $\Delta v_{\parallel}(s, 0, 0) = 0 \quad \Delta c(s, 0, 0) = 0$
- partial derivatives are zero along central ray
- Δv_{\parallel} is a cartesian component of a
homogeneous isotropic gaussian
random vector field with zero mean

Tentatively, the general simplifications listed here seem adequate for initial exploration of the statistical variations of sonic boom waveforms. It is the small-scale turbulence that is important, so it appears unwarranted to try to include large scale phenomena. The effective sound speed along the central ray is taken as constant and the deviations from that value at adjacent points are regarded as adhering to the simplest model of homogeneous isotropic turbulence with all joint probability density functions being gaussian.

Issues

- Does PSUPE include all relevant physics?
- Can we leave any terms out?
- How does one actually accomplish the numerics?
- Can one squeeze out some analytical results with no or minimal numerics?
- Are relevant turbulence scales in Kolmogoroff inertial subrange?



Things should be as simple as possible, but not simpler.

--- A. Einstein

Here are some issues that are believed to be worthy of consideration by the broader acoustic propagation community. The quotation is from memory; Einstein may have phrased it slightly differently. Whether the emphasis was on the *as simple as possible* or on the *not simpler* is unknown, but in any event it is a good philosophy to live by.

SIMULATIONS OF SONIC BOOM RAY TUBE AREA FLUCTUATIONS FOR
PROPAGATION THROUGH ATMOSPHERIC TURBULENCE INCLUDING CAUSTICS
VIA A MONTE CARLO METHOD*

Victor W. Sparrow
and
Allan D. Pierce
Graduate Program in Acoustics
157 Hammond Building
The Pennsylvania State University
University Park, PA 16802

SUMMARY

This paper outlines a theory which gives statistical predictions for how often sonic booms propagating through the earth's turbulent boundary layer will encounter caustics given the spectral properties of the atmospheric turbulence. The theory is simple but approximately accounts for the variation of ray tube areas along ray paths. This theory predicts that the variation of ray tube areas is determined by the product of two similar area factors, $\Psi(x)$ and $\Phi(x)$, each satisfying a generic harmonic oscillator equation. If an area factor increases the peak acoustic pressure decreases, and if the factor decreases the peak acoustic pressure increases. Additionally, if an area factor decreases to zero and becomes negative the ray has propagated through a caustic, which contributes a phase change of 90° to the wave. Thus it is clear that the number of times that a sonic boom wave passes through a caustic should be related to the distorted boom waveform received on the ground. Examples are given based on a characterization of atmospheric turbulence due to the structure function of Tatarski as modified by Crow.

INTRODUCTION

The National Aeronautics and Space Administration soon will decide whether it is technically and environmentally feasible for the United States to begin building a new supersonic transport aircraft. A critical design criteria for such an airplane is to minimize its sonic boom noise impact. Because the atmosphere is not homogeneous, but is a turbulent medium, we are concentrating on studying the propagation of sonic booms in a statistical sense.

* Work done under NASA Grant NAG-1-947.

The perceived loudness of sonic booms has been roughly linked to the magnitude of the initial shock amplitude of a sonic boom waveform, as well as to the rise time of this initial shock amplitude.¹ Through the process of focusing and defocusing in a turbulent medium, spikes can appear near both the initial rise phase and trailing rise phase of a sonic boom.² One question which needs to be answered statistically, therefore, is how often can one expect such spikes to occur?

The purpose of this paper is to outline a new theory for the propagation of acoustical waves through a turbulent medium. In the next section, the ray equations for an inhomogeneous moving media are developed in which the turbulence is taken as small and the solutions developed as a power series in the small amplitude of the turbulence. In section two, a Monte Carlo type simulation is introduced, by which one can generate representations of the effects of the turbulence. Section three gives a particular autocorrelation function to characterize the atmospheric turbulence. This autocorrelation function is based on the interpolation structure function of Crow. Section four presents some example calculations, and section five gives some conclusions and points to future work.

1. FORMULATION OF THE MODEL EQUATIONS

In the following it will be assumed that all acoustic waves will travel along one ray path, which will be called the central ray. Also to make the mathematical development tractable, a coordinate system will be used which follows along the central ray. See Fig. 1. Here x will be the distance along the central ray, and y and z are distances from the central ray in orthogonal coordinates. The vector \vec{e}_{ray} is the unit vector pointing along the central ray.

Because of the effect of turbulence, it is necessary to define an effective speed of sound which incorporates the vector $\vec{v}_{\text{turbulent}}$ which represents the ambient velocity of the air during the passage of the sound. The effective sound speed here is defined

$$c_{\text{eff}}(x, y, z) = c_{\text{actual}} + \vec{e}_{\text{ray}} \cdot \vec{v}_{\text{turbulent}} \quad (1)$$

where c_{actual} is the actual speed of sound.

Near the central ray, one can expand the effective speed of sound into a power series in the orthogonal coordinates y and z . Keeping only the terms of second order,

$$\begin{aligned} c_{\text{eff}}(x, y, z) \approx & c_{\text{eff}}(x, 0, 0) \\ & + \frac{\partial c_{\text{eff}}}{\partial y} y + \frac{\partial c_{\text{eff}}}{\partial z} z \\ & + \frac{1}{2} \frac{\partial^2 c_{\text{eff}}}{\partial y^2} y^2 + \frac{\partial^2 c_{\text{eff}}}{\partial y \partial z} yz + \frac{1}{2} \frac{\partial^2 c_{\text{eff}}}{\partial z^2} z^2 . \end{aligned} \quad (2)$$

To simplify the analysis, it will be assumed that

$$\frac{\partial^2 c_{\text{eff}}}{\partial y \partial z} = 0 . \quad (3)$$

This assumption, in effect, causes the y and z axes to twist along the central ray, but decouples the problem such that the c_{eff} is a simple function of y plus a simple function of z .

Because the amplitude of the acoustic wave is controlled by the focusing or defocusing of ray tube areas, the amplitude along the central ray will be proportional to the inverse of the square root of the ray tube area. The ray tube area is the product of the ray tube height in the y direction and of the ray tube width in the z direction. Each of these factors can be predicted by a purely two-dimensional ray tracing model, since it has been assumed that the y and z coordinates have been decoupled.

The ray equations for the two dimensional model are

$$\frac{dx}{d\tau} = c \cos \theta \quad (4)$$

$$\frac{dy}{d\tau} = c \sin \theta \quad (5)$$

and

$$\frac{d\theta}{\tau} = \frac{\partial c}{\partial x} \sin \theta - \frac{\partial c}{\partial y} \cos \theta . \quad (6)$$

Here the flow is taken into account in the speed of sound $c = c_{\text{eff}}$, and the angle θ is measured from the x axis. The variable τ is time.³

Take the variable η to denote a ray path relatively near the x axis; see Fig. 2. In the figure η is in the same direction as y , and the ray path $\eta = 0$ would be a straight line. Now assume that along the x axis, where $c = c(x, 0)$, that

$$\frac{\partial c}{\partial y} = 0 \quad (7)$$

and

$$\frac{\partial c}{\partial x} = 0 . \quad (8)$$

However, further assume that $\partial^2 c / \partial y^2$ does vary along the x axis. With these assumptions, the ray tracing Eqs. (4), (5), and (6) yield the following equations giving the variation with respect to η :

$$\frac{d}{d\tau} \left(\frac{\partial x}{\partial \eta} \right) = 0 \quad (9)$$

$$\frac{d}{d\tau} \left(\frac{\partial y}{\partial \eta} \right) = c_0 \frac{\partial \theta}{\partial \eta} \quad (10)$$

and

$$\frac{d}{d\tau} \left(\frac{\partial \theta}{\partial \eta} \right) = - \left(\frac{\partial^2 c}{\partial y^2} \right)_{y=0} \frac{\partial y}{\partial \eta} . \quad (11)$$

Eqs. (10), (11), and (4), along the x axis, may be combined to yield a linear ordinary differential equation in x ,

$$\frac{d^2}{dx^2} \left(\frac{\partial y}{\partial \eta} \right) = - \frac{1}{c_0} \left(\frac{\partial^2 c}{\partial y^2} \right)_{y=0} \frac{\partial y}{\partial \eta} . \quad (12)$$

Eq. (12) will serve as a model equation for the rest of this paper. It can be rewritten as

$$\frac{d^2 \Psi}{dx^2} + f(x) \Psi = 0 \quad (13)$$

where

$$\Psi = \frac{\partial y}{\partial \eta} \quad (14)$$

and

$$f(x) = \frac{1}{c_0} \left(\frac{\partial^2 c}{\partial y^2} \right)_{y=0} . \quad (15)$$

Given the physically intuitive initial conditions that

$$\Psi = 1 \quad \text{and} \quad \frac{d\Psi}{dx} = 0 \quad (16)$$

at $x = 0$, the ODE (12) can be solved via straightforward numerical procedures for a given $f(x)$.

Similarly, for the z direction one can derive an ODE

$$\frac{d^2 \Phi}{dx^2} + g(x) \Phi = 0 \quad (17)$$

where

$$\Phi = \frac{\partial z}{\partial \eta} \quad (18)$$

and

$$g(x) = \frac{1}{c_0} \left(\frac{\partial^2 c}{\partial z^2} \right)_{z=0} \quad (19)$$

with similar initial conditions. As noted earlier, the amplitude of the ray is proportional to the square root of the area of the ray tube, and combining the solutions to both ODEs (13) and (17) the ray amplitude will be proportional to $(\Psi \Phi)^{-1/2}$.

2. MONTE CARLO NUMERICAL SIMULATION

Figure 3 schematically shows how a statistical solution to Eq. (13) may be found. Given some ensemble of the function $f(x)$, one can take one particular $f(x)$ and generate the corresponding $\Psi(x)$ by numerically solving Eq. (13). By repeating this process with other particular $f(x)$'s, one can generate an ensemble of the $\Psi(x)$. It is then possible to perform standard statistical analyses on the properties of the $\Psi(x)$ giving insight into the nature of propagation through turbulence.

For the particular model stated here, $f(x)$ will be assumed to be a real homogeneous random function with zero ensemble mean,

$$\langle f(x) \rangle = 0 \quad , \quad (20)$$

and with auto-correlation function

$$\langle f(x)f(x + \Delta) \rangle = R(\Delta) \quad . \quad (21)$$

To pick the $f(x)$'s in a statistically representative way, $f(x)$ will be given by the Fourier series

$$f(x) = \sum_{n=-\infty}^{\infty} a_n e^{i2\pi n x/W} \quad (22)$$

over a long interval W . Here it is assumed that the coefficients a_n for negative n are complex conjugates of those for positive n since $f(x)$ is a real valued function. Further it is assumed that the a_n 's for positive n are statistically independent and their real and imaginary parts are all statistically independent.

Since computationally the sum in Eq. (22) cannot be taken from $-\infty$ to ∞ , the approximate expression

$$f(x) = \sum_{n=-N}^N a_n e^{i2\pi n x/W} \quad (23)$$

will be used. Here N is a large integer, which will be specified later. In this approximation one can find that

$$R(\Delta) = \sum_{n=-N}^N |a_n|^2 e^{-i2\pi n \Delta/W} \quad (24)$$

By approximating this expression as a Fourier transform, and taking the inverse transform, one has the approximation

$$\langle |a_n|^2 \rangle = \frac{1}{W} \int_{-\infty}^{\infty} R(\Delta) e^{-i2\pi n \Delta/W} d\Delta \quad (25)$$

Now it will be assumed that the real and imaginary parts of the a_n have a zero mean and are gaussian distributed,

$$\langle (\text{Re}(a_n))^2 \rangle = \langle (\text{Im}(a_n))^2 \rangle = \frac{1}{2} \langle |a_n|^2 \rangle . \quad (26)$$

To pick a representative $\text{Re}(a_n)$ from the gaussian ensemble we simple equate

$$\text{Re}(a_n) = q \langle |a_n|^2 \rangle^{1/2} \quad (27)$$

where q is a gaussian deviate.

Once the realization of turbulence $f(x)$ has been synthesized from knowing the a_n , ODE (13) can be integrated numerically to find $\Psi(x)$. Recall that it is this function $\Psi(x)$ and the similar function $\Phi(x)$ that determine the ray tube areas. Since (13) is a second order differential equation, it is easy to integrate by breaking it into a system of two first order equations:

$$\left\{ \begin{array}{l} \frac{d}{dx}(\Psi) = \Psi' \\ \frac{d}{dx}(\Psi') = -f(x)\Psi \end{array} \right\} \quad (28)$$

The appropriate initial conditions for this integration are $\Psi(x) = 1$ at $x = 0$ and $\Psi'(x) = 0$ at $x = 0$. Physically this means the ray tube has a scaled initial area of 1 and is neither increasing nor decreasing in area with distance. If there were no turbulence, $f(x)$ would be identically zero for all x , and $\Psi(x)$ would remain 1 for all x .

3. A PARTICULAR AUTOCORRELATION FUNCTION

Once the autocorrelation function $R(\Delta)$ has been specified, the function $f(x)$ can be synthesized via Eqs. (23) and (25). In this section we specify one type of autocorrelation function due to the isotropic turbulence theory of Tatarski.⁴ Expanding our definition for $R(\Delta)$,

$$\begin{aligned} R(\Delta) &= \langle f(x)f(x+\Delta) \rangle \\ &= \left\langle \frac{1}{c_0^2} \left(\frac{\partial^2 c(x)}{\partial y_1^2} \right)_{y_1=0} \frac{1}{c_0^2} \left(\frac{\partial^2 c(x+\Delta)}{\partial y_2^2} \right)_{y_2=0} \right\rangle \end{aligned} \quad (29)$$

Further, since v_x is stationary one can show

$$R(\Delta) = \frac{-1}{2c_0^2} \left\{ \frac{\partial^2}{\partial y_1^2} \frac{\partial^2}{\partial y_2^2} \left\langle (v_x(x, y_1, 0) - v_x(x + \Delta, y_2, 0))^2 \right\rangle \right\}_{\substack{y_1=0 \\ y_2=0}} \quad (30)$$

The squared quantity above corresponds to the $D_{xx}(\vec{r})$ structure function of Tatarski. Here the vector \vec{r} can be readily decomposed into components parallel and perpendicular to the coordinate system of the central ray as $\vec{r} = \Delta \vec{e}_x + (y_2 - y_1) \vec{e}_y$. Through rewriting the $D_{xx}(\vec{r})$ function in terms of $D_{rr}(|\vec{r}|)$, taking the indicated derivatives, and using the Crow's interpolation structure function⁵ in this expression, a simple autocorrelation function is obtained:

$$\begin{aligned} R(\Delta) &= \langle f(x)f(x+\Delta) \rangle \\ &= \frac{1}{L^4} \frac{1 + \frac{1}{6}(\Delta/l_0)^2}{\left(1 + (\Delta/l_0)^2\right)^{8/3}} \end{aligned} \quad (31)$$

where L is a convenient constant given by

$$\frac{1}{L^4} = \frac{24}{c_0^2} \frac{\epsilon^{3/2}}{(15\nu)^{5/2} C^{3/2}} \quad (32)$$

Here l_0 is the smallest length scale of the turbulence. Crow's interpolation structure function has correct limits for both the cases where $|\vec{r}| \ll l_0$ and where $|\vec{r}| \gg l_0$. The other constants in this expression are the kinematic viscosity ν , the energy dissipated per unit mass and per unit time ϵ , and the Kolmogorov constant C which is approximately 1.9. The kinematic viscosity of air is approximately 1.525×10^{-5} m²/s. Given the structure function for the wind velocity $C_v^2 = C\epsilon^{2/3}$ about 0.07, from the work of Brown and Hall⁶, a reasonable value for ϵ is 10^{-2} m²/s. Hence from Tatarski's expression for l_0 ,

$$l_0 = \sqrt[4]{\frac{(15C\nu)^3}{\epsilon}}, \quad (33)$$

a representative value for l_0 in the turbulent boundary layer near the earth's surface is $l_0 \approx 0.0096$ m.

4. SOME EXAMPLE CALCULATIONS

The particular $R(\Delta)$ of the previous section resembles a delta function, see Fig. 4. Its Fourier transform equal to $\langle |a_n|^2 \rangle$ in Eq. (25) will be a very smooth function, nearly a constant. Hence, instead of directly computing this Fourier transform, one can solve Eq. (25) via a numerical integration for certain specific n , and then use interpolation between the numerically integrated values to find $\langle |a_n|^2 \rangle$ for any n . Because the integrand of Eq. (25) is even, one may express this equation as

$$\langle |a_n|^2 \rangle = \frac{2l_0}{WL^4} \int_0^\infty \frac{1 + (u^2/6)}{[1 + u^2]^{8/3}} \cos(2\pi n l_0 u / W) du \quad (34)$$

This equation was numerically integrated with the upper limit of integration taken so large as to keep the sum accurate to four significant digits. Here W was taken to be 320. m, with $l_0 =$

0.0096 and $L = 0.32$. Some sample results of this numerical integration, via the Mathematical symbolic manipulation package ⁷ are given in Table I.

Table I.

n	$\langle a_n ^2 \rangle$
0	.003908
100	.003908
200	.003906
300	.003903
400	.003899
500	.003895
600	.003890
700	.003884
800	.003877
900	.003869
1000	.003861

From Eq. (27), given the $\langle |a_n|^2 \rangle$, one needs only q to synthesize the a_n and thus $f(x)$. In our calculations the q were generated via the standard Box-Muller transformation.⁸ Since $f(x)$ is real, Eq. (23) may be rewritten as

$$f(x) = a_{R0} + \sum_{n=1}^N 2a_{Rn} \cos(2\pi nx/W) - 2a_{In} \sin(2\pi nx/W) \quad (35)$$

where a_{Rn} and a_{In} are the real and imaginary parts of a_n , respectively.

As reported at the end of the last section, the turbulence theory of Tatarski and Crow indicates that the smallest scale of the turbulence is on the order of 1 centimeter. Therefore if one keeps W the "period" of turbulence 320. m as above, then N in Eq. (35) will need to be 32,000 to account for all of the turbulent length scales. Figure 5 shows one realization of $f(x)$ plotted with the range going from 0 to 2. m only. As can be seen, the function oscillates randomly and often, although only two meters has been plotted. When this $f(x)$ is integrated to obtain $\Psi(x)$ the integration step size must be very small because of the rapid variations in $f(x)$.

Figure 6 shows six realizations of $\Psi(x)$ integrated from six realizations of $f(x)$, all having the same spectral properties. One of the rays is diverging, three are staying about the same, and two are converging. These two converging rays decrease and become negative indicating that they are going through caustics. It is surprising that the rays have gone through a caustic so quickly after only 1 meter of propagation.

After some analysis one can attribute this phenomenon to the nature of our synthesized $f(x)$, and to the lack of any dissipative mechanisms in the present model. The smallest length scale, or equivalently turbule size, involved in $f(x)$ is approximately 1 centimeter. Recent experimental results, however, have pointed out that realistic length scales for atmospheric turbulence are on the order of one meter near the ground and ten or more meters at heights of tens of meters.⁹⁻¹¹ Thus when a sonic boom propagates through the earth's planetary boundary layer, the boom will generally encounter turbules on the order of 10 meters or larger.

One can simulate this experimental result by truncating the Fourier series, Eq. (35), with a smaller N . For example, by picking $N = 32$ the smallest length scale in (35) will be 10 m. Figure 7 shows one realization of $f(x)$ if the Fourier series is truncated with $N = 32$. Figure 8 shows five realizations of the $\Psi(x)$ given five $f(x)$'s with $N = 32$, and the distance in meters at which a caustic would develop has been increased slightly. Thus, in the present model realistic realizations of the spectral properties of the turbulence still lead to predictions of caustics occurring every few meters.

We attribute this result to the inherent dissipationless formulation of the model presented here. If the model had included some absorption processes, the tendency for the amplitude to spike would be less pronounced, and caustics would occur less often.

5. CONCLUSIONS AND FUTURE WORK

This paper has presented a new model for the stochastic simulation of sound propagation through a turbulent medium using perturbation calculations of rays and ray-tube areas. For realistic realizations of atmospheric turbulence the model predicts that sonic booms will spike up with the occurrence of caustics in only a couple of meters on average. A large ensemble of runs needs to be performed to provide detailed statistics on the occurrence of caustics. The present model lacks any dissipative mechanisms and this property limits the ability to make any predictions which could be compared with experiments. The model does, however, show that sonic booms propagating through atmospheric turbulence do have a strong tendency to exhibit spikes, agreeing with some of the predictions of Ref. 2. In the future the model presented in this paper will be extended to include the atmospheric absorption effects such as classical dissipation and molecular relaxation dissipation.

REFERENCES

1. Shepherd, Kevin P.; and Sullivan, Brenda M.: *A Loudness Calculation Procedure Applied to Shaped Sonic Booms*. NASA TP-3134, 1991.
2. Pierce, Allan D.: Spikes on sonic-boom pressure waveforms. *J. Acoust. Soc. Am.* vol. 44, no. 4, 1968, pp. 1052–1061.
3. Pierce, Allan D.: *Acoustics: An Introduction to Its Physical Principles and Applications*. Acoustical Society of America, Woodbury, NY, 1989, p. 375.

4. Tatarski, V. I.: *Wave Propagation in a Turbulent Medium*. Trans. by Silverman, R. A.; McGraw-Hill, New York, 1961. Reprinted by Dover, New York, 1967.
5. Crow, S. C.: Distortion of sonic bangs by atmospheric turbulence. *J. Fluid Mech.* vol. 37, no. 3, 1969, pp. 529–563.
6. Brown, Edmund H.; and Hall, Jr., Freeman F.: Advances in Atmospheric Acoustics. *Rev. Geophys. and Space Phys.* vol. 16, no. 1, 1978, pp. 47–110.
7. Wolfram, Stephen: *Mathematica, A System for Doing Mathematics by Computer*. Addison Wesley, New York, 1988.
8. Press, William H.; Flannery, Brian P.; Teutolsky, Saul A.; and Vetterling, William T.: *Numerical Recipes: The Art of Scientific Computing, Fortran Version*. Cambridge, New York, 1989, pp. 202–203.
9. Johnson, Mark A.; Raspet, Richard; and Bobak, Michael T.: A turbulence model for sound propagation from an elevated source above level ground. *J. Acoust. Soc. Am.* vol. 81, no. 3, 1987, pp. 638–646.
10. Bass, Henry E.; Bolen, Lee N.; Raspet, Richard; McBride, Walton; and Noble, John: Acoustic propagation through a turbulent atmosphere: Experimental characterization. *J. Acoust. Soc. Am.* vol. 90, no. 6, 1991, pp. 3307–3313.
11. McBride, Walton; Bass, Henry E.; Raspet, Richard; and Gilbert, Kenneth E.: Scattering of sound by atmospheric turbulence: A numerical simulation above a complex impedance boundary. *J. Acoust. Soc. Am.* vol. 90, no. 6, 1991, pp. 3314–3325.

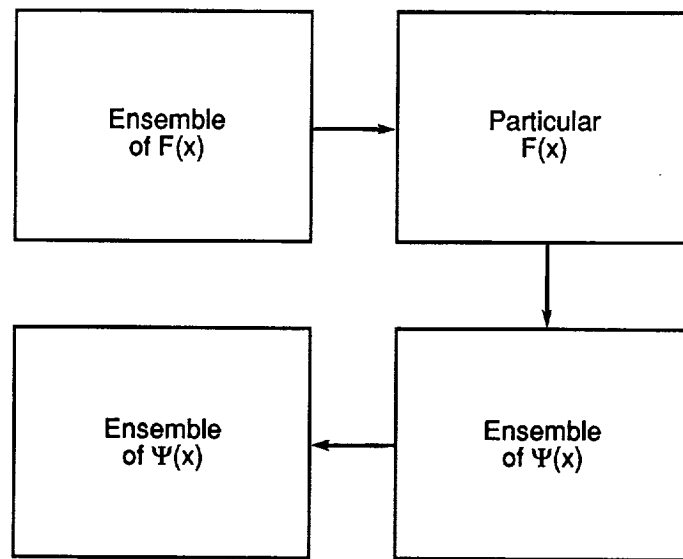


Figure 3. Monte Carlo approach to realizing an ensemble of the $\Psi(x)$ functions.

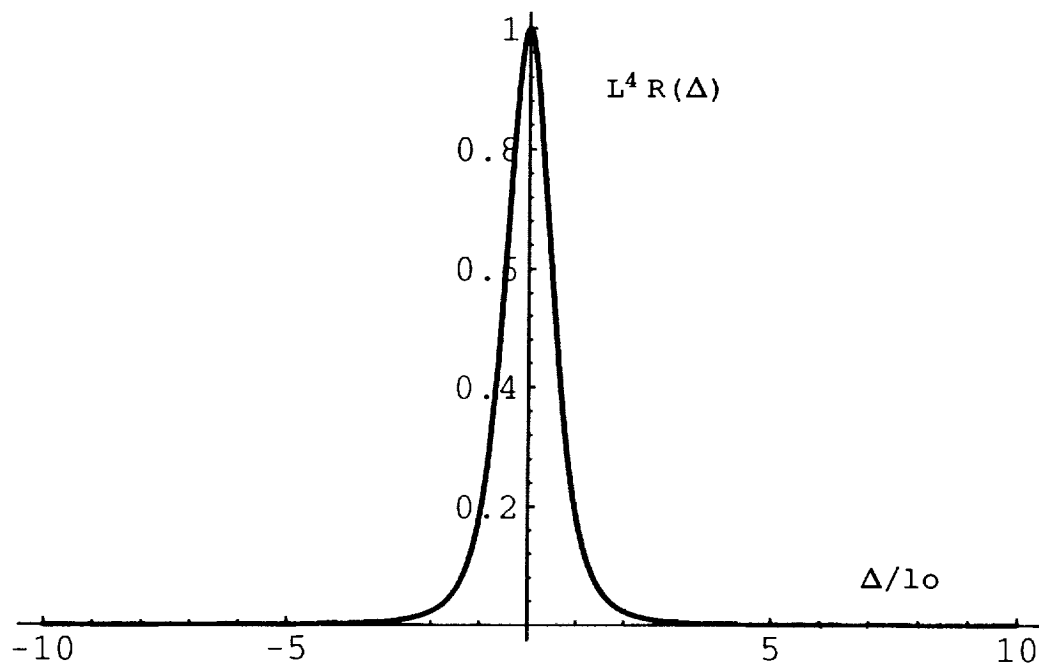


Figure 4. The particular autocorrelation function $R(\Delta)$ employed in the analysis, based on the interpolation structure function of Crow.

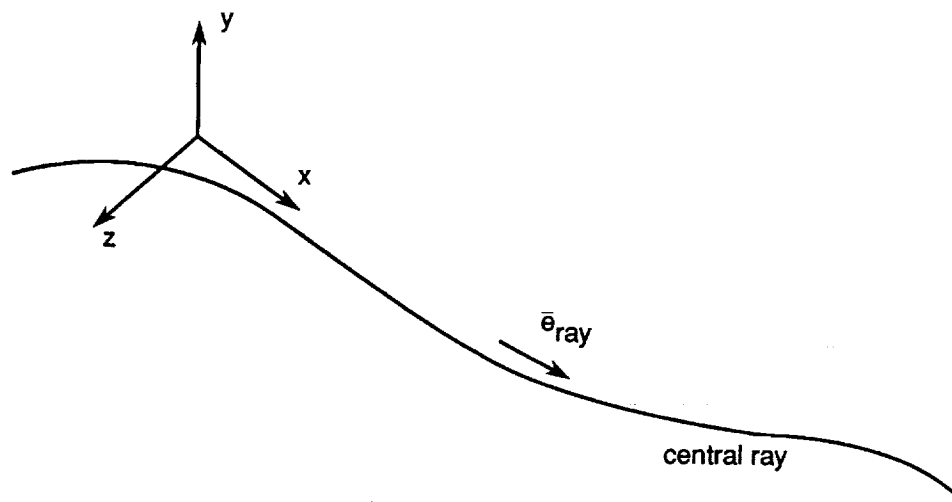


Figure 1. Coordinate system. The x axis is aligned with the direction of propagation regardless of how the ray twists and turns.

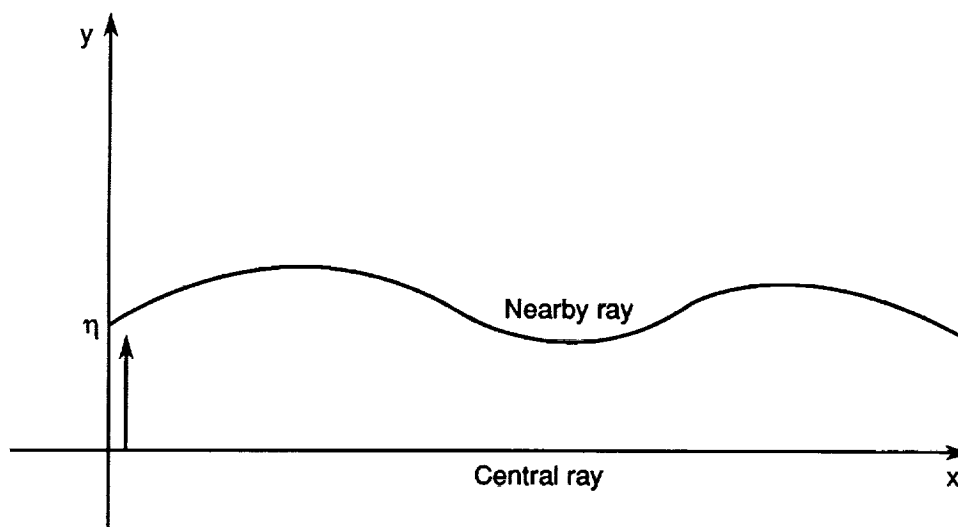


Figure 2. The variable η represents a ray path close to the central ray.

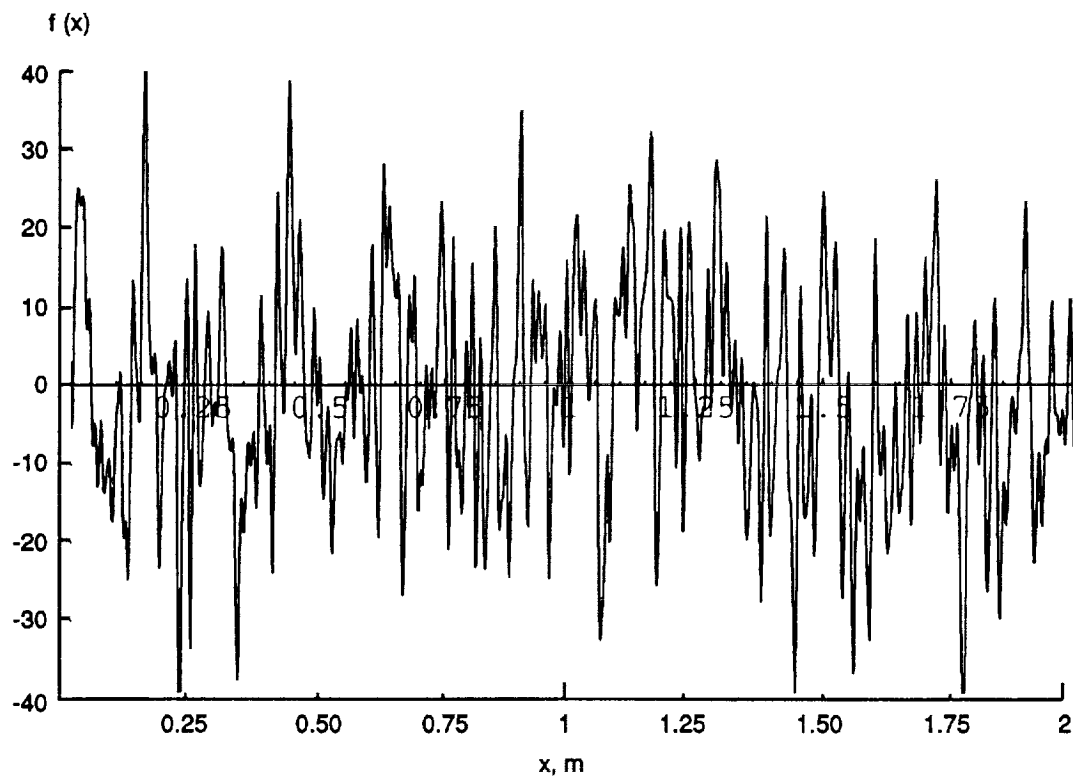


Figure 5. A typical realization of $f(x)$ over two meters, $N = 32,000$.

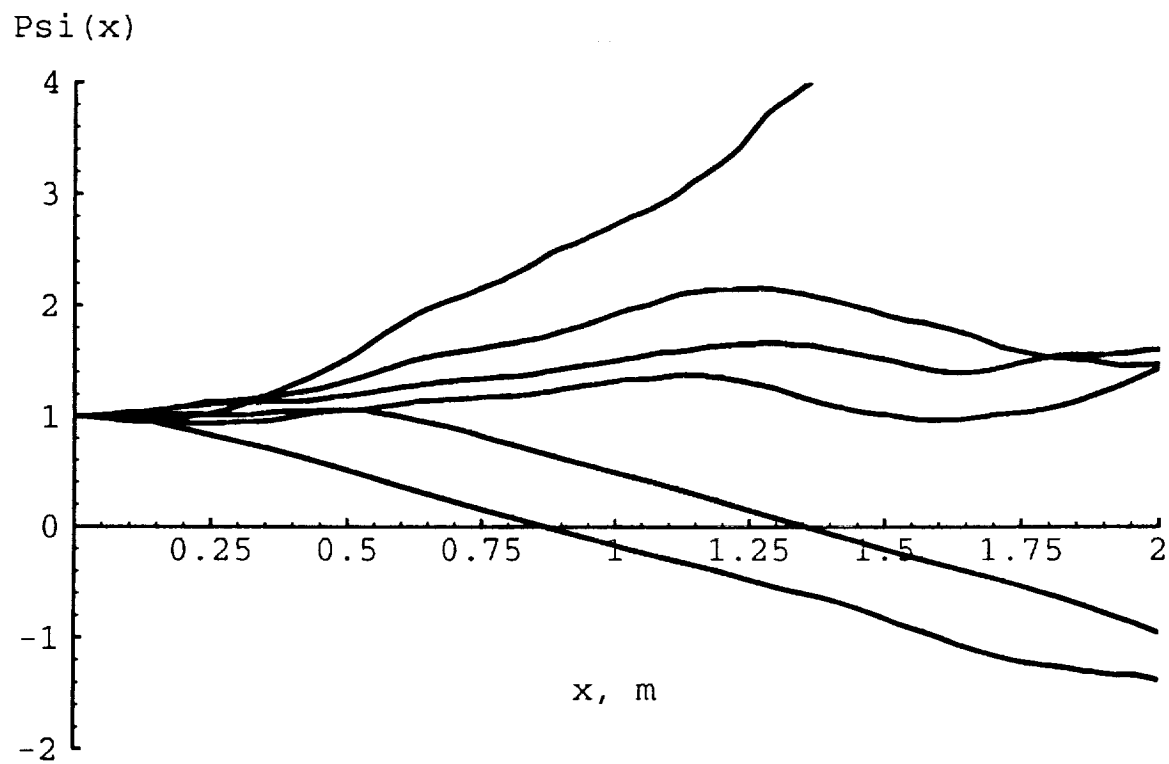


Figure 6. Realizations of $\Psi(x)$ over two meters, $N = 32,000$.

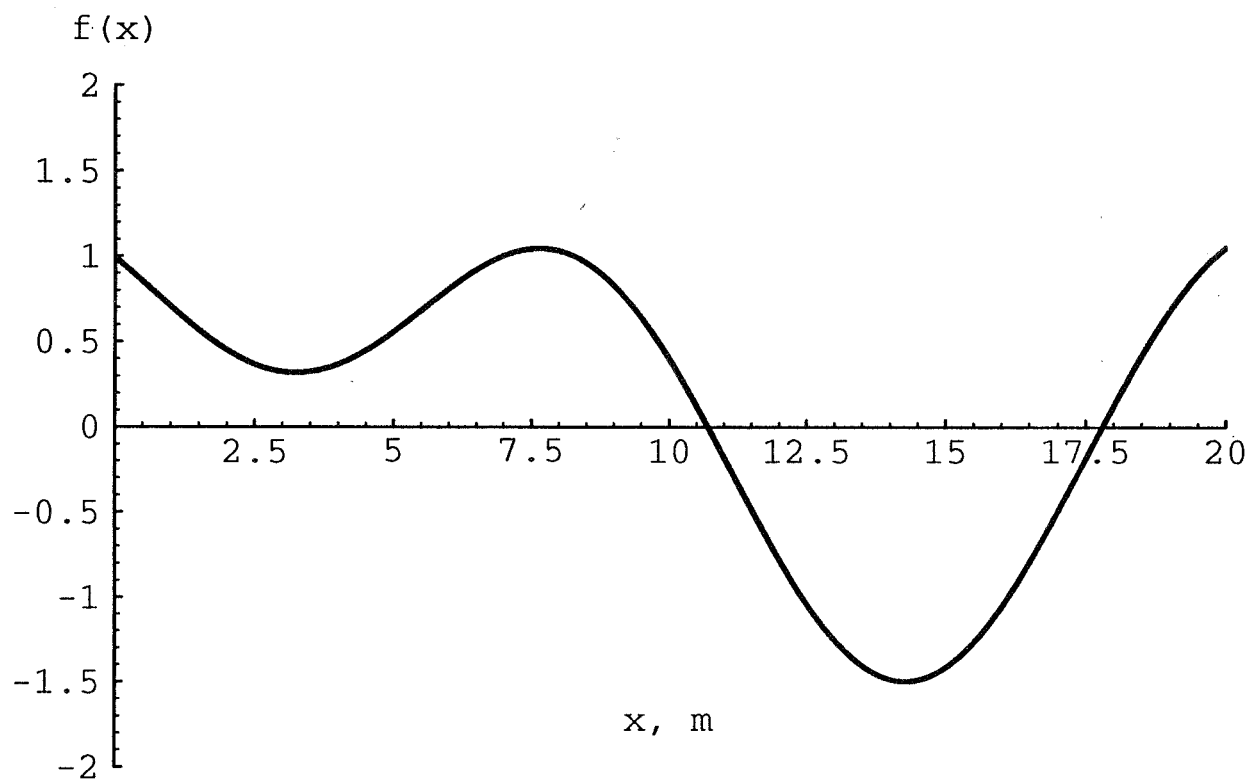


Figure 7. A typical realization of $f(x)$ over twenty meters, $N = 32$.

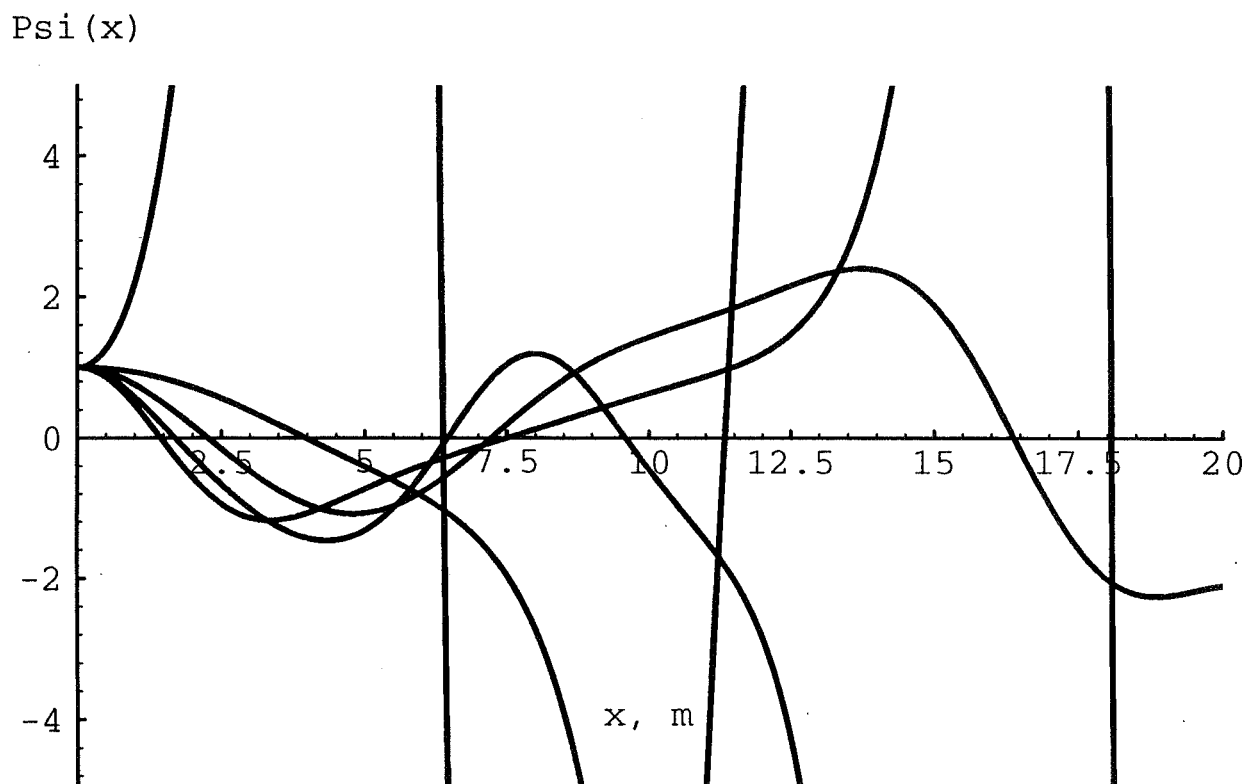


Figure 8. Realizations of $\Psi(x)$ over twenty meters, $N = 32$. The curve that increases initially and leaves the figure recrosses the $\Psi(x) = 0$ line at ranges of 6.4, 11.3, and 18.0 m. The other curves that leave the figure do not reappear.

ANALYSIS OF SONIC BOOM DATA TO QUANTIFY DISTORTIONS OF SHOCK PROFILES

Thomas A. Gionfriddo
Graduate Program in Acoustics
117 Applied Science Building
The Pennsylvania State University
University Park, PA 16802

SUMMARY

Researchers at Penn State have been examining some sonic boom waveforms recorded during overflights by the Air Force which have become available to NASA and its contractors. The quality of the digitized data and the supporting meteorological data was such that one could test the applicability of molecular relaxation theories. In the late sixties it had been supposed that the finite rise times in the absence of turbulence had neglected the vibrational relaxation of nitrogen molecules. Bass *et al.*¹ have demonstrated that molecular relaxation definitely gives the correct order of magnitude of the observed rise times. However, the Air Force data in conjunction with the recent steady-state shock profile model theory of Kang and Pierce² give the first opportunity to make a detailed quantitative assessment of the molecular relaxation hypothesis.

Currently an investigation is ongoing to establish a method of quantifying the distortion of a sonic boom wave from a classic N-wave shape using the Air Force data taken at Edwards AFB in 1987. Using the premise that energy will be conserved approximately for a sonic boom wave both before and after the boom passes through the Earth's turbulent boundary layer, a classic undistorted waveform is constructed from the distorted signature received at the ground. A correlation between the mean-squared deviation of the distorted and undistorted waveforms and the distance the boom travels through the turbulence is sought.

* Work done under NASA Grant NAG-1-947.

EXPERIMENTAL SONIC BOOM DATA

Sonic boom data used in the following studies was obtained from United States Air Force flights in the Mojave Desert during the period from July 31 thru August 7, 1987. The pressure waveforms at the ground were recorded by Boom Event Analyzer Recorder (BEAR) systems along a linear array perpendicular to the flight track (see Fig. 1). The array of thirteen BEARs permitted measurement of the lateral spread of sonic booms out to twelve miles on one side and six miles on the other. This project provides a data set of approximately 500 digitized booms from forty-four flights and nine aircraft. Meteorological data consisting of temperature, humidity, and wind speed profiles were also obtained in conjunction with the aircraft flyovers.

The BEAR devices consist of a piezoelectric microphone in an inverted mount configuration and digital analyzer/recorder unit. The microphone faces a steel base plate with 2mm separation distance, and two windscreens enclose the tent-shaped assembly. The BEAR systems are installed and calibrated at the desired locations prior to the flyovers and generally left unattended for the duration of the tests. The analyzer/recorder unit continually samples the microphone voltage input at a rate of 8kHz, and saves any signal it considers to be a sonic boom based on a series of voltage level and duration thresholds. Sonic boom events are saved to a RAM (Random Access Memory) cartridge. The RAM cartridges are collected after the flights and the data is transferred to more permanent storage on a micro-computer. The frequency response of the BEAR is reported to be reliable from 0.5Hz to 2.5kHz³. Good low-frequency response is vital for accurate recording of the sonic boom waveshape, which typically has a fundamental frequency component in the range of 5-10Hz (100-200ms in time)⁴.

A visual sort procedure was applied to the Mojave Desert waveforms, to categorize by waveform shape. Seven categories were established: Classic N, double-peaked, multi-peaked, rounded, peaked, messy, and U-wave (see Fig. 2). Some of the data files were found unusable due to premature recording truncation by the BEAR units.

I. MOLECULAR RELAXATION MODEL

The rise times of the experimental data from the August 5 flights in the Mojave Desert are seen to be inversely proportional to the steady state shock overpressure and serve as a measure of the early shock structure of the sonic boom (see Fig. 3). Rise times of two to three ms are typical for overpressures in the range of 30-100 pas-

cals. Rise time as used for Kang's molecular relaxation model is defined as the time for the acoustic pressure to increase from 10% to 90% of the steady-state shock overpressure value. The *steady state* shock overpressure is loosely related to the maximum overpressure of the waveform. The molecular relaxation theory, which incorporates a steady-state version of Burger's equation, requires monotonically increasing waveforms. Most experimental sonic boom data do not monotonically increase during the rise phase, therefore a set of six rules which determine the effective peak overpressure were developed and applied to the experimental data to validate the comparison between the molecular relaxation theory and real data⁵.

The molecular relaxation model is based on the augmented Burger's equation, i.e., Burger's equation with nonlinear steepening, thermal viscosity, and molecular relaxation terms⁶.

$$\frac{\partial p}{\partial t} + c \frac{\partial p}{\partial x} + \text{NST} + \text{TVT} + \text{MRT} = 0 \quad (1)$$

The augmented Burger's equation is coupled with the relaxation equation (Eq. 2) for oxygen and nitrogen processes in the Earth's atmosphere (τ_ν is relaxation time)⁷.

$$p_\nu + \tau_\nu \frac{\partial p_\nu}{\partial t} = \tau_\nu \frac{\partial p}{\partial t} \quad (2)$$

Some assumptions are made for the model to be valid: shocks are weak (typically 300 pascals maximum), molecular relaxation (N_2 and O_2 processes) is important only during the rise phase of the sonic boom, the rise phase structure is determined solely by the peak overpressure of the shock and the local properties of the atmosphere, and the rise phase is much shorter in time duration than the positive phase of the shock.

The shock is then modeled as a frozen profile. The steady-state version of Burger's equation is used to predict a theoretical rise phase using asymptotic and numerical solution methods according to the numerical technique suggested in Fig. 4. It is noted that O_2 relaxation is important in the early rise phase and N_2 relaxation is dominant in the later rise phase⁸.

Using this molecular relaxation theory to determine a rise phase profile based on the meteorological conditions at the Mojave Desert site, it was determined that the theory did not adequately explain the rise time⁹. Theoretical predictions for rise time versus steady-state shock overpressure form a lower bound for experimental data points (see Fig. 5). Experimental rise times are typically two to five times longer than the theory would predict. Approximately 10% of the experimental data is seen to agree well with the rise phase generated by the theory (see Fig. 6). However, molecular relaxation does not satisfactorily predict the correct rise phase profile in the majority of the cases (see Fig. 7). It is suspected that turbulence is the mechanism responsible for the discrepancy in the rise time and early shock structure.

II. QUANTIFYING THE DISTORTION IN SONIC BOOM SIGNATURES

Classification of the sonic boom data by the amount of distortion from an N-wave shape is accomplished by tabulating the mean squared deviation between a recorded boom and an ideal N-wave. An ideal N-wave in the discrete time domain is constructed using

$$p_{ideal}[n] = p_{max,i} \frac{2}{T_i} \left(t_{0,i} + \frac{T_i}{2} - \frac{n}{f_s} \right) \quad t_{0,i} \leq t \leq t_{0,i} + T_i \quad (3)$$

where $p_{max,i}$ is the peak overpressure of the ideal boom waveform; T_i is the duration of the ideal N-wave (time from maximum to minimum overpressure); $t_{0,i}$ is the start time of the ideal waveform, relative to the start of data acquisition of the recorded boom; and f_s is the sample rate in hertz (see Fig. 8). The ideal boom is symmetric about the time axis, i.e., lift effects are not considered in the ideal boom.

The question of how a recorded waveform and its ideal N-wave counterpart should be superimposed to yield meaningful results is of importance to the success of this distortion quantification method. If the duration of the ideal N-wave is much larger or much smaller than the recorded wave, or superimposed incorrectly, the deviation between the two waveforms may be very large and an unreliable estimate of the distortion in the recorded boom.

For a recorded classic N-wave, it is desired to have a corresponding ideal N-wave which closely matches—resulting in minimal mean square deviation for similar N-waves. In this analysis, a recorded boom and its ideal N-wave contain the same total energy. Energy for an acoustic waveform is defined as

$$\int_{t=t_{start}}^{t_{end}} p^2(t) dt \quad \text{for continuous time} \quad (4)$$

$$\frac{1}{f_s} \sum_{n=n_{start}}^{n_{end}} p^2[n] \quad \text{for discrete time} \quad (5)$$

Where f_s is the sample rate in Hz, p is the acoustic pressure at time t or sample number n . It turns out that for an N-wave as defined in equation (3), the duration and maximum overpressure are related to the total energy (e) of the waveform as in Eq. 6.

$$p_{max,i} = \sqrt{\frac{3e}{T_i}} \quad (6)$$

Energy here is a scaled quantity. In a plane wave the actual energy density is given as $e = p^2/\rho_0 c^2$. The scaling factor $1/\rho_0 c^2$ is omitted in Eqs. (4) and (5)¹⁰.

The next step is determining the proper start and stop times for the ideal N-wave. The term *leading energy ratio* (LER) is here defined as the ratio of the energy accumulated from the start of the recorded sonic boom up to the data sample which contains the maximum positive overpressure to the total energy contained in that boom recording:

$$\text{LER} = \frac{\sum_{n=n_{start}}^{n_{pmax}} p^2[n]}{\sum_{n=n_{start}}^{n_{end}} p^2[n]} \quad (7)$$

Similarly, the *trailing energy ratio* (TER) is the ratio of energy accumulated from the data sample containing the minimum overpressure until the end of the recording, to the total energy:

$$\text{TER} = \frac{\sum_{n=n_{pmin}}^{n_{end}} p^2[n]}{\sum_{n=n_{start}}^{n_{end}} p^2[n]} \quad (8)$$

The LER and TER are determined from those recorded booms most closely resembling the N-shape (members of the classic N waveshape category). An average value of the LER and TER is determined exclusively for each type of aircraft, since it is believed that these values are dependent upon the physical attributes of the aircraft.

Using the average of the LER and TER values, the start and stop time of the ideal N-wave is determined. The ideal wave should start (reach maximum overpressure) at the time when the energy ratio (accumulated energy since the start of the boom recording divided by total energy of the boom) of the recorded boom currently being scrutinized first equals the average LER for that type aircraft. The ideal wave should end (return to ambient pressure) at the time when the energy ratio of the recorded boom equals 1 minus the average TER for that aircraft. After these steps, the duration of the ideal boom is known, and Eq. (6) is used to find the maximum overpressure of the ideal boom. Eq. (3) may then be applied to generate the ideal N-wave.

The mean squared deviation is calculated in discrete-time as shown in Eq. (9). This quantity indicates the amount of distortion in the recorded sonic boom as compared to the ideal N-wave, or the amount of distortion inflicted upon the sonic boom as it

propagates through the turbulent boundary layer to the ground.

$$\text{Mean squared deviation} = \frac{\sum_{n_{start}}^{n_{end}} (p_{ideal}[n] - p_{recorded}[n])^2}{\sum_{n_{start}}^{n_{end}} p_{ideal}^2[n]} \quad (9)$$

A few examples of sonic boom data and the associated ideal N-waves resulting from the above procedure are shown. In the first example, classic N data is used (see Fig. 9). The mean-squared deviation for this shape signature is typically on the order of 0.01. The following example shows a rounded signature having a mean-squared deviation of approximately 0.3 (see Fig. 10). The third plot shows a signature that is apparently buried in background noise or is the superposition of several wavefronts (see Fig. 11). This type of data is deemed unusable. The current method of calculating waveform distortion is intended to be applied to waveforms that somewhat resemble the classic N shape; this includes all the waveshape categories mentioned earlier except for some messy signatures. The mean-squared deviation measurement is believed to be invalid for multiple-shock signatures and those signatures buried in background noise of significant magnitude as compared to the maximum overpressure.

To reach the objective of this analysis, the mean-squared deviation is compared to the amount of turbulence through which the shock travels. Experimental evidence has shown the turbulent boundary layer to be the region where the most distortion occurs in sonic boom signatures¹¹. A typical turbulent boundary layer height of 3000 feet (0.568 mi.) is used. Using a two-dimensional approximation to the actual propagation path (see Fig. 12), the path length through the turbulent region is found in terms of aircraft altitude (A) and lateral ground distance from the flight track to the receiver (D) as:

$$\text{TBL path length} = \frac{0.5682 \text{ mi.}}{\cos \phi} \quad (10)$$

where $\phi = \tan^{-1}(\frac{D}{A})$ is the angle between the downward vertical and the straight line connecting the aircraft to the receiving microphone. The path length increases as lateral distance from the flight track increases, though the dependence on lateral distance becomes less significant as airplane altitude increases.

The mean-squared deviation is seen to correlate well with the turbulent boundary layer path length for the F-18 aircraft data (see Fig. 13). The six F-18 flights occurred over a three hour period on August 6, from 7:44 to 10:48 AM local time. The flyovers ranged in altitudes from 2.5 to 8.2 miles, and Mach numbers from 1.08 to 1.43. A linear regression was performed on the F-18 data resulting in a high correlation coefficient of 0.77. The linear fit is shown in the figure. This plot and the results from other aircraft flights (having lower correlation) seem to indicate that the waveform distortion is a function of the path length through the turbulence. The analysis method is still in the developmental stage and further refinements are expected in the future.

REFERENCES

1. Bass, H. E.; Ezell, J.; Raspet, R.: Effect of vibrational relaxation on rise times of shock waves in the atmosphere. *J. Acoust. Soc. Am.* vol. 74, no. 5, 1983, pp. 1514–1517.
2. Kang, J.; Pierce, A. D.: The effect of molecular relaxations on the propagation of sonic booms, recent developments in air and structure-borne sound and vibration. Auburn Univ., Auburn, Alabama, March 1990, pp. 97–104.
3. Lee, Robert A.; Mazurek, Doug; Price, Dale; Crabill, Monty; Palmer, Barbera: *Boom Event Analyzer Recorder (BEAR): System description*. AAMRL-TR-89-035, Aug. 1989.
4. Hilton, David A.; and Newman, Jr., James W.: Instrumentation techniques for measurement of sonic-boom signatures. *J. Acoust. Soc. Am. Suppl.* vol. 39, 1966, pp. S31–S35.
5. Kang, J.: *Nonlinear acoustic propagation of shock waves through the atmosphere with molecular relaxation*. A thesis in mechanical engineering, The Pennsylvania State University, May 1991, pp. 151–152.
6. Ibid. p. 30.
7. Ibid. chapter 4.
8. Ibid. p. 102.
9. Ibid. pp. 173–176.
10. Pierce, A. D.: *Acoustics: An Introduction to Its Physical Principles and Applications*. Acoustical Society of America, Woodbury, NY, 1989, p. 39.
11. Garrick, I. E.; and Maglieri, D. J.: *A summary of results on sonic-boom pressure-signature variations associated with atmospheric conditions*. NASA TN D-4588, May 1968, pp. 22–23.

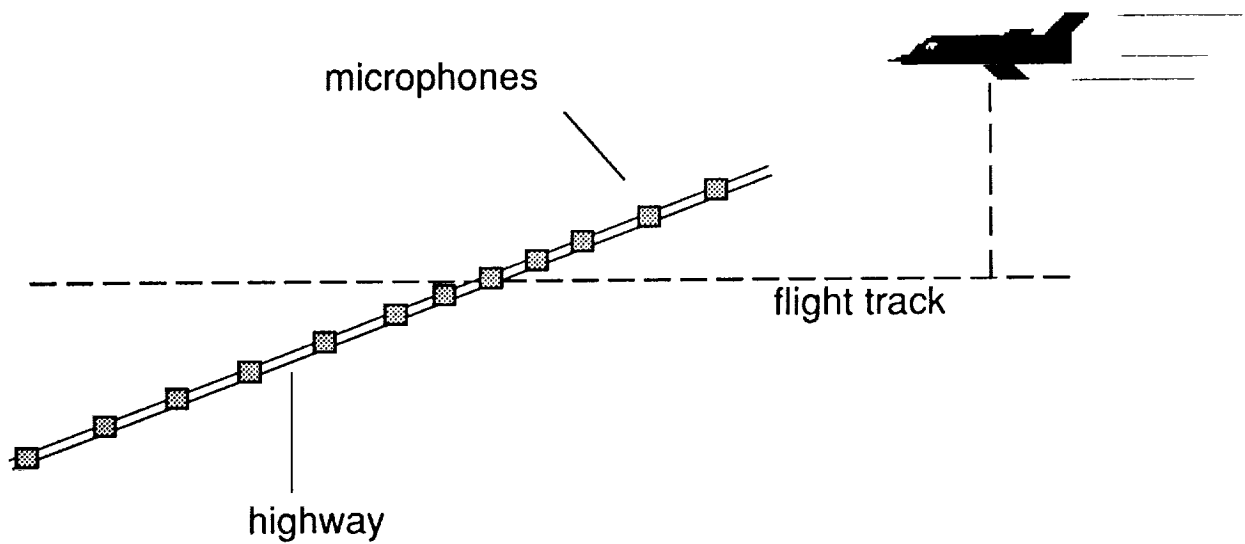


Figure 1. Schematic of sonic boom recording project conducted by the United States Air Force in the Mojave Desert, July 31 - August 7, 1987.

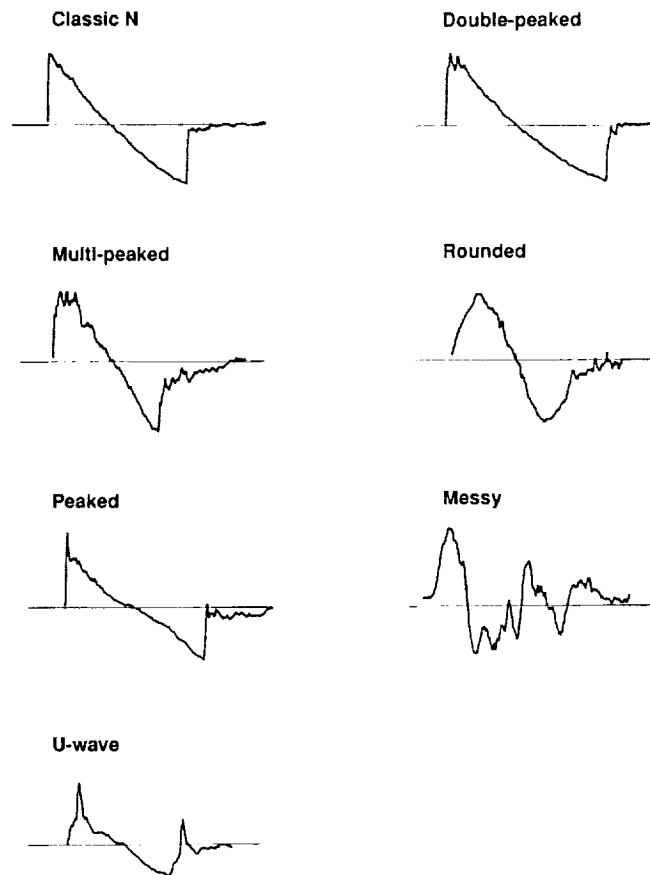


Figure 2. Examples of sonic boom signature classification categories.

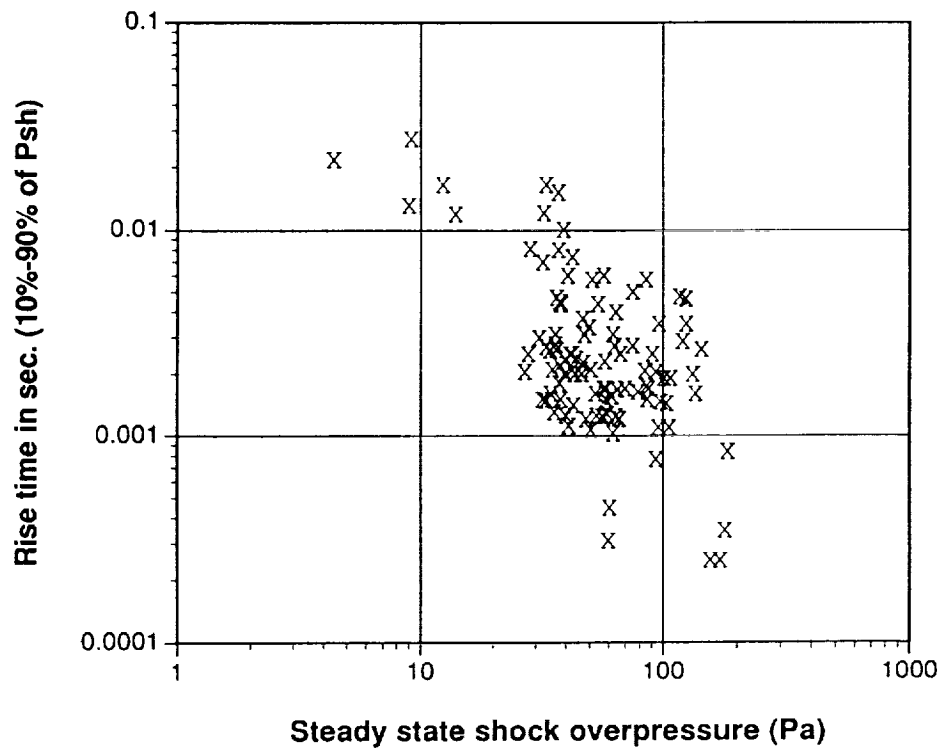


Figure 3. Rise times of recorded sonic booms versus steady state shock overpressure.

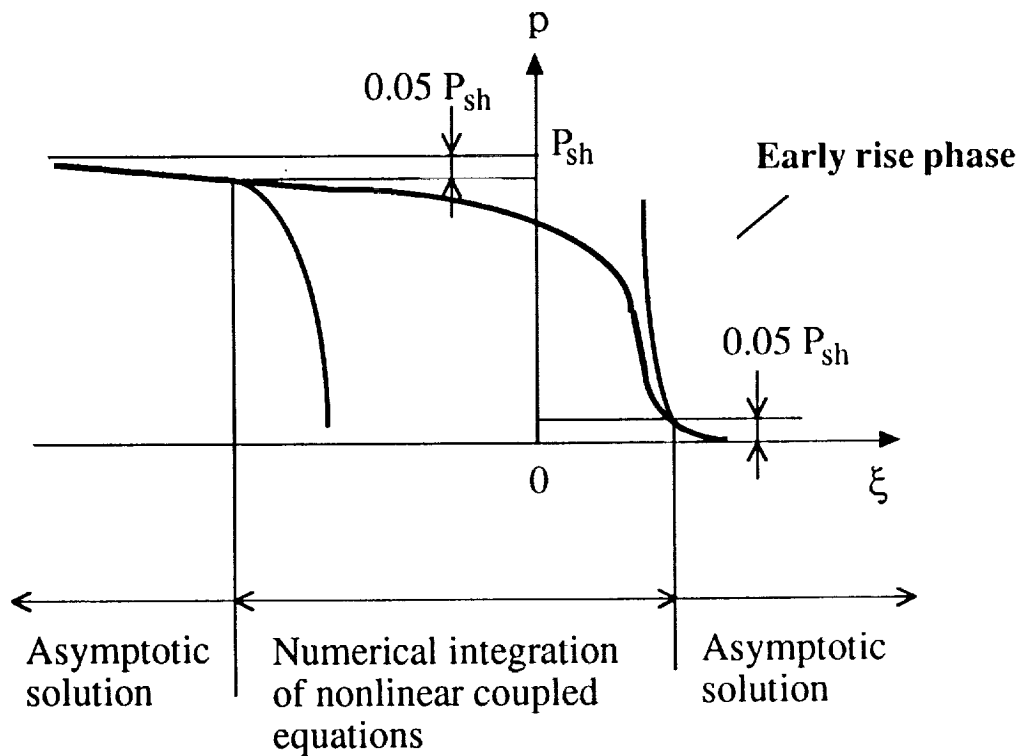


Figure 4. The theoretical rise phase predicted from molecular relaxation theory is determined using a combination of asymptotic and numerical solution methods.

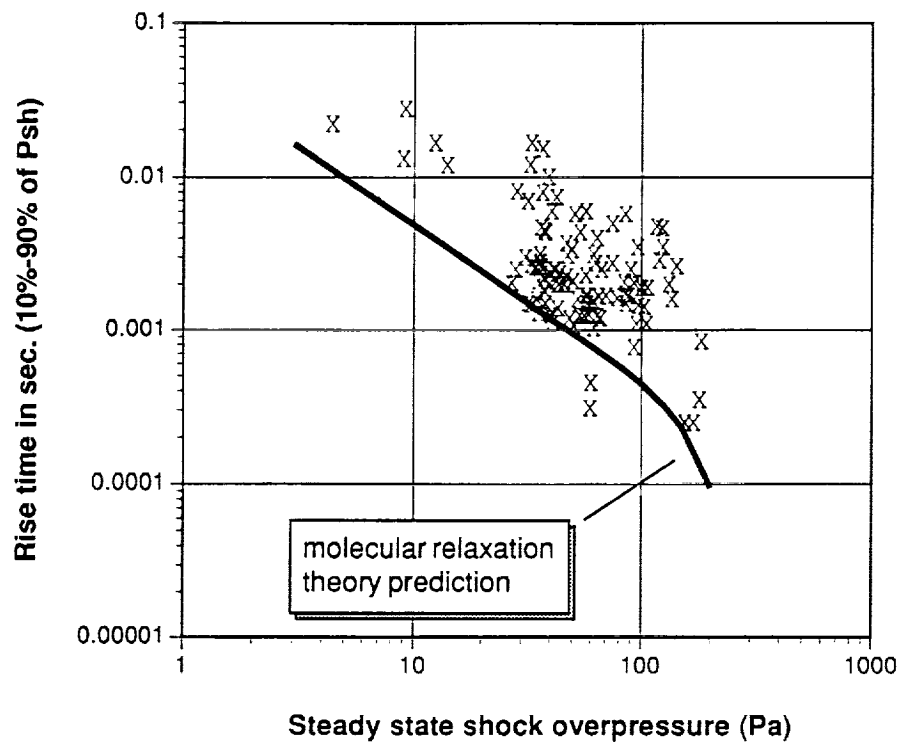


Figure 5. Rise times of recorded sonic booms versus steady state shock overpressure, as compared to the molecular relaxation model.

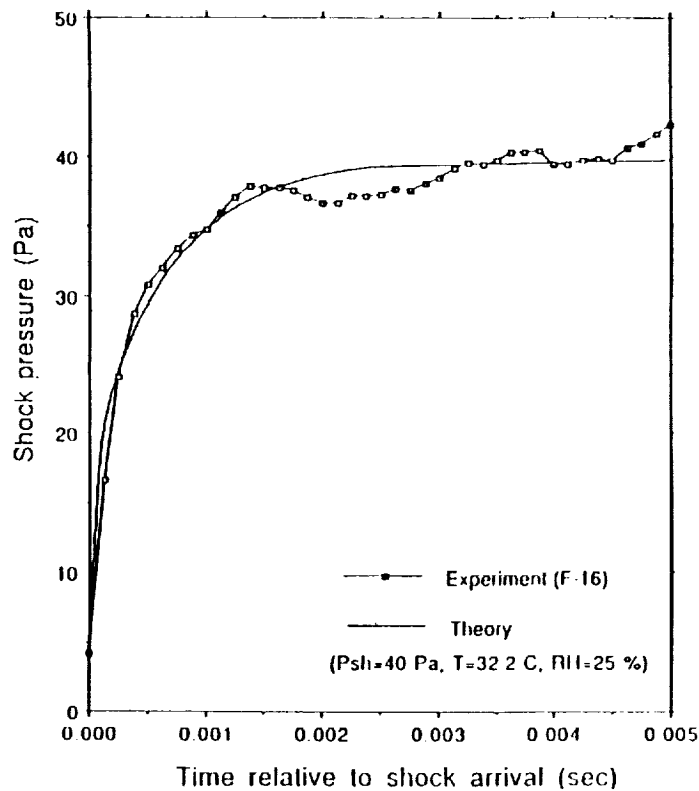


Figure 6. Example of good agreement between actual rise phase and rise phase predicted by the molecular relaxation theory.

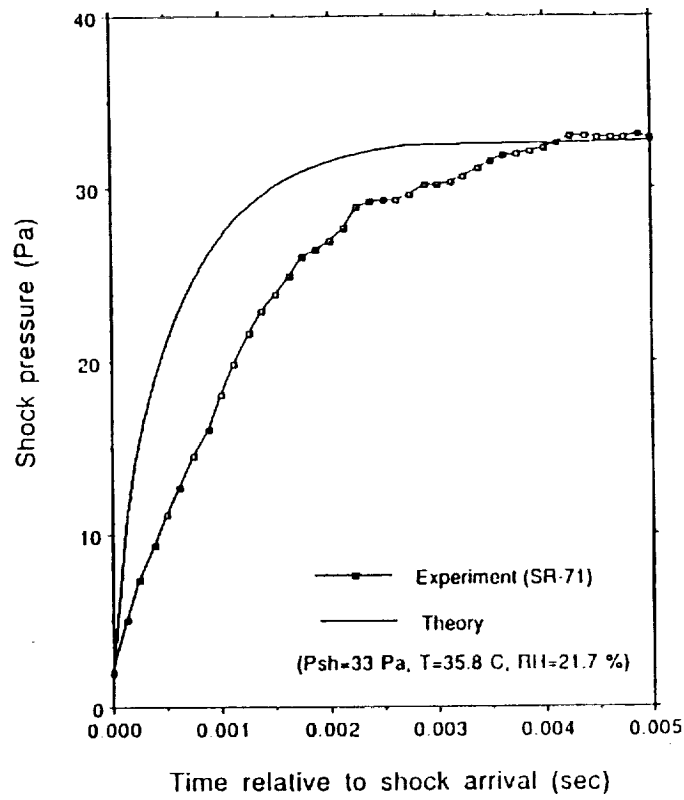


Figure 7. Example of poor agreement between actual rise phase and rise phase predicted by the molecular relaxation theory.

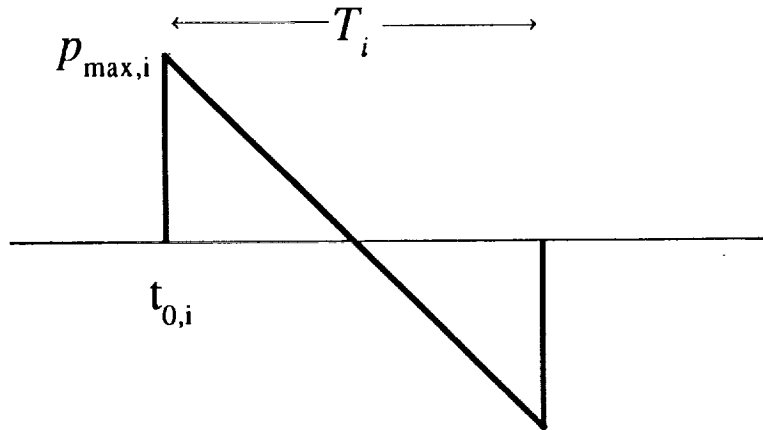


Figure 8. Ideal N waveform (acoustic pressure versus time) used in signature distortion analysis.

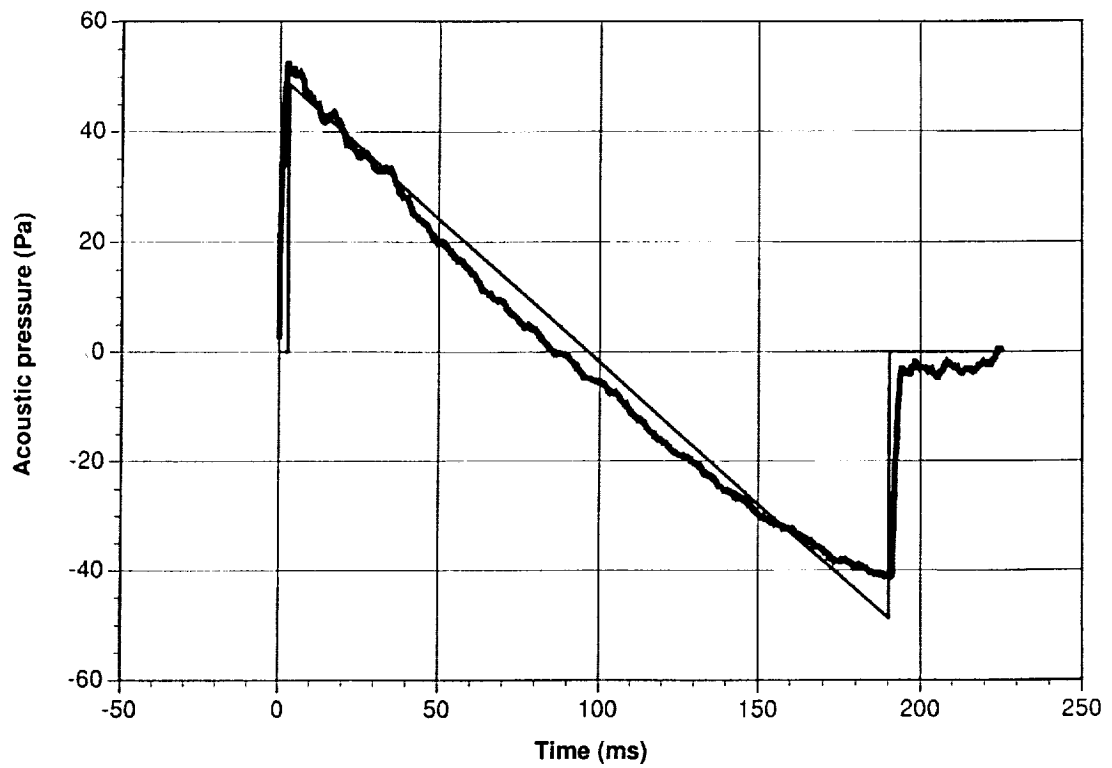


Figure 9. Example of classic N-shaped sonic boom (thick line) having small deviation from ideal N wave (thin line).

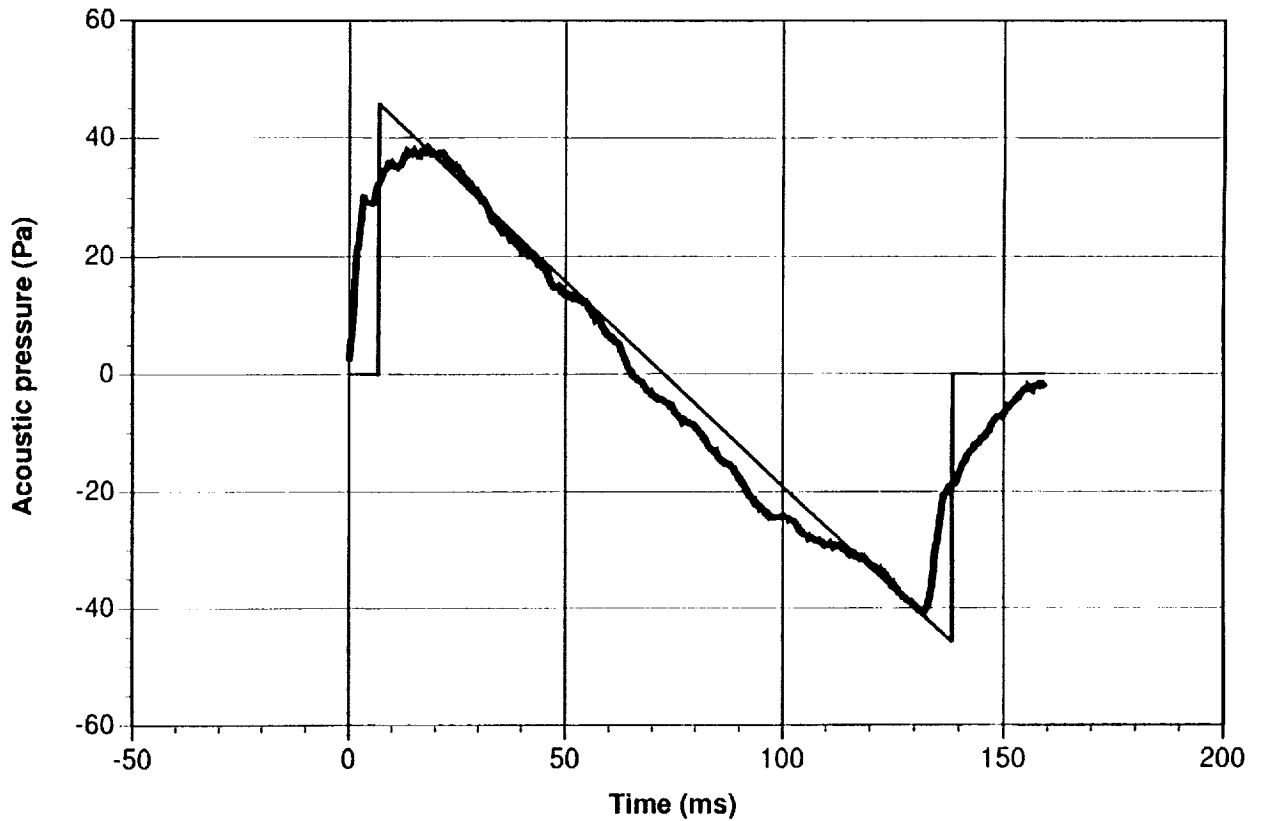


Figure 10. Example of classic N-shaped sonic boom (thick line) having considerable deviation from ideal N wave (thin line).

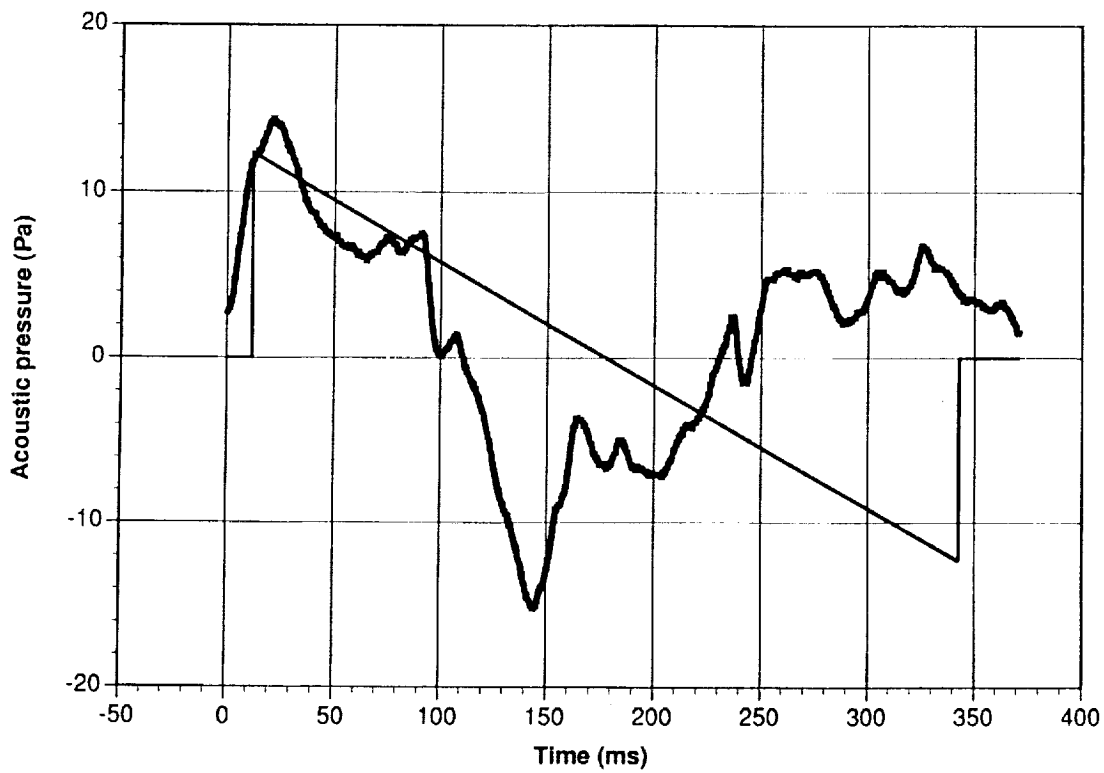


Figure 11. Example of sonic boom data that is unusable for mean-squared deviation analysis.

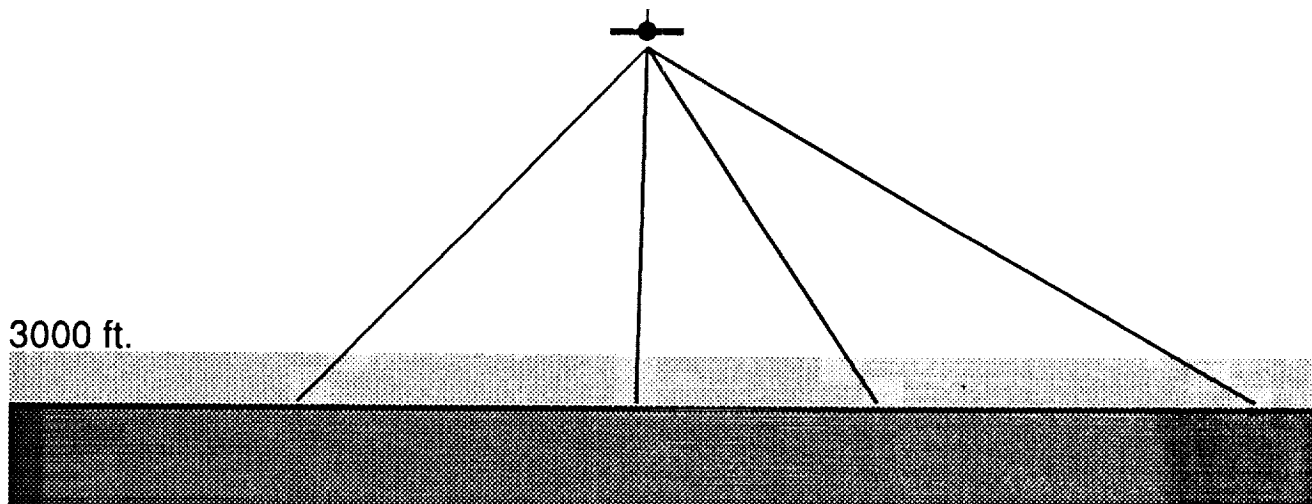


Figure 12. Illustration of turbulent boundary layer (shaded region); the path length approximation used in the mean-squared deviation analysis is the portion of the straight ray path within the turbulent boundary layer.

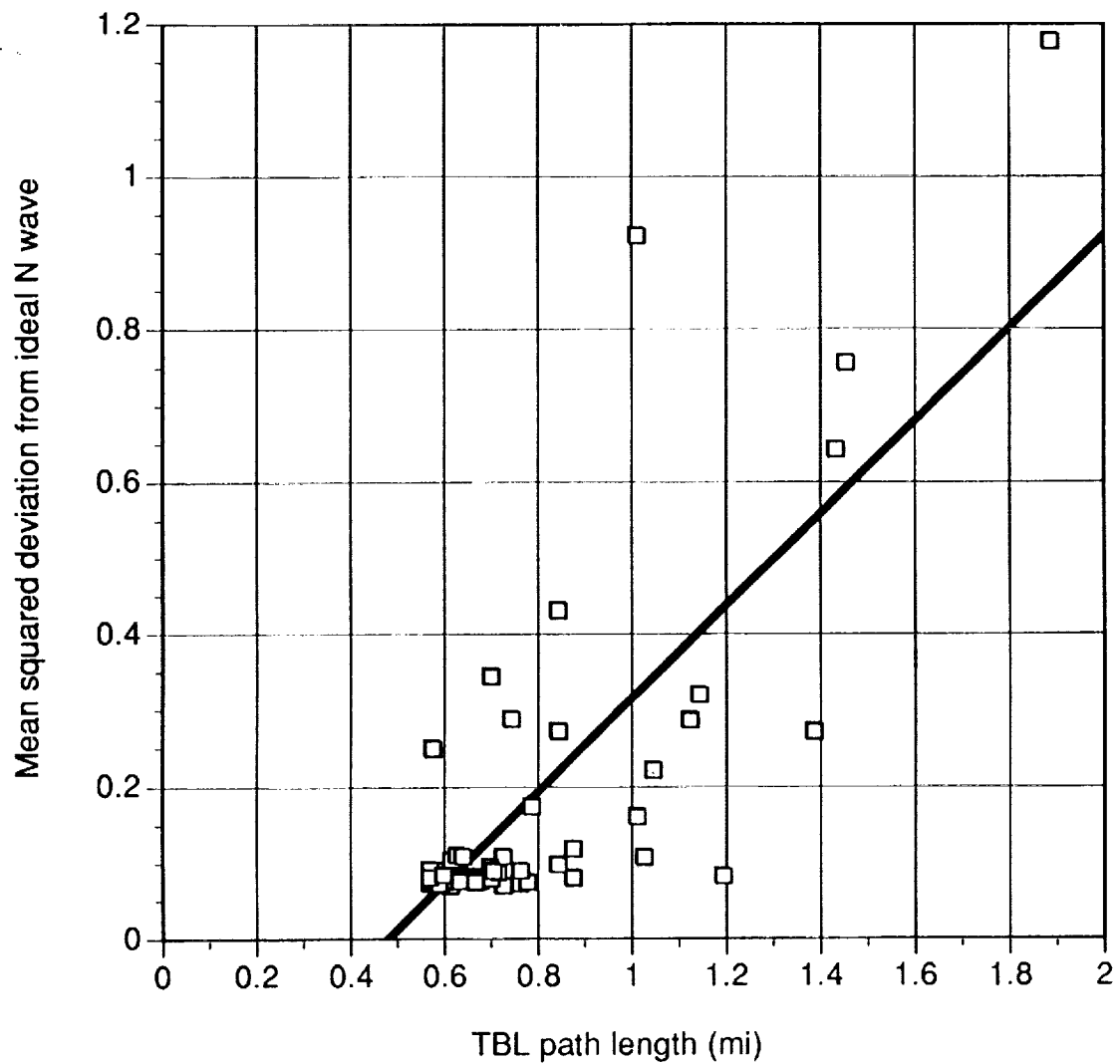


Figure 13. Mean squared deviation versus turbulent boundary layer path length for F18 aircraft with linear regression fit shown by solid line (correlation coefficient = 0.77).

THE EFFECT OF TURBULENCE ON THE LOUDNESS OF
MINIMIZED SONIC BOOM SIGNATURES

Kenneth J. Plotkin
Wyle Laboratories
2001 Jefferson Davis Highway
Arlington, Virginia 22202

INTRODUCTION

An important issue for shaped minimized sonic booms is whether turbulence-induced distortions will adversely affect the benefits gained by shaping. This question has been considerably simplified by two recent results. The first is the finding that the loudness of sonic booms is well quantified by loudness.¹ The second is that loudness of a shaped boom is dominated by the shock waves.² The issue is now the effect of turbulence on weak (1 psf or less) sonic booms. Since it is clear that molecular relaxation effects have a significant effect on shock structure and loudness,³ turbulence effects must be examined in conjunction with relaxation-thickened shocks. This analysis must be directed toward loudness calculations, and include all pertinent mechanisms.

SHOCK MECHANISMS AND DOMAIN

The following four mechanisms are significant:

1. Molecular relaxation absorption, which thickens shocks and reduces high-frequency content. The current standard values⁴ of absorption are used in this paper.
2. Non-linear steepening (aging), which steepens shocks and generates high-frequency energy.
3. First-order scattering, which distorts the region immediately following the shock, generating the "spiky fine structure". The theory of Crow⁵ is extended and used in this analysis.
4. Second-order scattering, which thickens shocks. While this is still the subject of controversy, we employ the theory of Plotkin and George.⁶

For the sake of simplicity, calculations in this paper are performed for the following basic conditions:

- Shock overpressure of 1 psf, including ground reflection; corresponds to 0.5 psf before reflection. This is the greatest shock pressure which is credible for minimized booms. Weaker shocks are thicker, and are less sensitive to most of the mechanisms discussed here.

- A ramp shock structure with a 3 msec rise time. This is a typical rise time for a 1 psf shock without turbulent thickening.
- Fifty percent relative humidity, corresponding to average conditions. Much analysis has been done using 10 percent humidity, which is not uncommon for Edwards Air Force Base test conditions but has absorption much higher than typical across the country.
- Five-thousand-foot propagation distance through a turbulent planetary boundary layer consisting of homogeneous turbulence with intensity 3×10^{-6} and macroscale of 100 feet. This is a very simplified model, but each parameter has typical magnitude and the combinations yield reasonable results when used in the theories of References 5 and 6.

The ramp shock structure noted above is a simple structure often used for generic analysis of boom signatures and spectra. Figure 1, taken from Reference 2, shows an N-wave boom with this shock structure, and the corresponding spectrum. The oft-cited feature of a 12 dB/decade rolloff above $1/\pi f$ corresponds to this structure. Figure 2 shows a shock structure computed from actual molecular relaxation.⁷ A third shock structure which may be considered is a hyperbolic tangent (with thickness based on maximum slope), computed from the Burgers' equation as discussed in Reference 6. Figure 3 shows the spectra of the ramp and tanh shocks, together with the spectrum of a simple step function. There is a considerable difference between the ramp and tanh spectra, even though both have essentially the same thickness. A relaxation shock, as in Figure 2, would have a spectrum somewhere between ramp and tanh. A preliminary review has been made of spectra of measured sonic boom N-waves. This review suggests that the most common spectrum tends to have the high-frequency rolloff corresponding to a ramp shock seen in Figure 1. Spectral properties are important for the current analysis, so the ramp shock structure has been adopted.

ABSORPTION AND STEEPENING MECHANISMS

Shock structure is a balance between dissipation and steepening. It is now well accepted that the basic dissipation for sonic boom shocks is molecular absorption, with turbulence causing an anomalous additional absorption which results in additional random thickening. It is useful to examine the strength of the basic mechanisms, with a goal toward understanding the evolution time of the shock structure reaching the ground.

Figure 4 shows the effect of molecular relaxation alone. We have started with the spectrum of a step function shock, and applied molecular absorption at 50 percent humidity for several propagation distances. Two features are clear:

- The spectral shape resembles that of a tanh shock more than that of a ramp shock. The resemblance is greater for higher absorption or longer propagation distances.
- Even after a considerably long propagation distance, the spectrum has not achieved the shape of a 3 msec thick shock.

The counteracting mechanism is non-linear steepening, for which the propagation speed of a wave is:

$$a_{\infty} \left(1 + \frac{\gamma + 1}{2 \gamma} \frac{\delta p}{p_{\infty}} \right) \quad (1)$$

so that a wave of strength δp advances at a speed increased by $a_{\infty} \frac{\gamma + 1}{2 \gamma} \frac{\delta p}{p_{\infty}}$. For a 1 psf sonic boom (0.5 psf before reflection), the advance speed is 0.22 ft/sec. In the absence of absorption, a shock with a 3 msec rise time would steepen to zero rise time after propagating about 15,000 feet. This is comparable to the thickening time shown above. These distances are long compared to the typical 5,000-foot turbulent layer considered here, so it is quite possible that a steady shock structure does not exist. If the shock is not steady state, it will approach steady state very slowly. A clear extension of this analysis is that the larger features of a boom (duration, low-frequency structure, etc.) will not change during propagation through the final turbulent layer.

LOUDNESS CALCULATIONS

Loudness has been computed in a manner similar to that used by Shepherd *et al.*² and May and Sohn.⁸ The one-third octave band energy spectrum is obtained, then converted into an equivalent sound level spectrum by normalizing via an auditory time constant. There are several opinions as to the best value of the auditory time constant; we have taken 125 msec as used by May and Sohn.⁸ This spectrum is then applied to the Stevens Mark VII loudness calculation.⁹ In this method, the one-third octave band levels are first mapped onto a sone chart, as illustrated in Figure 5. Each contour represents a particular perceived loudness; the corresponding sound level varies with frequency, according to the characteristics of the human ear. A 9 dB increase in level corresponds to a doubling of the sone value. Shown in Figure 5 is the spectrum from a sonic boom analyzed by Johnson and Robinson.¹⁰ The sone values of each one-third octave band are combined as defined in Reference 9, and the total is converted into a level. For the current problem, the issue is which parts of the spectrum have the greatest contribution to the total loudness, and how those parts of the spectrum are affected by turbulence. For the example spectrum in Figure 5, the bands from 63 to 250 Hz are the most important.

Figure 6 shows the spectra from Figure 3, with several sone contours overlaid. The loudness levels for the step, ramp, and tanh shocks are 101, 93, and 90 PLdB, respectively. (Loudness of corresponding N-waves, with two shocks, would be 3 dB higher.) The significant frequencies for loudness are apparent

from the relation between the spectra and the sone curves. There is a dramatic difference between the step function and the thickened shocks, and a lesser (but significant) difference between the two thickened shock structures. It is interesting that the most significant frequencies for loudness are those in the vicinity of the change in slope associated with the finite rise time. Figure 6 clearly identifies the most important frequency range for analysis.

TURBULENT SCATTERING

The first order scattering theory by Crow⁵ successfully explains the spiky fine structure associated with turbulent distortion. Crow's final result for mean square fluctuations p_1 behind a unit step function shock may be written:

$$\begin{aligned}\langle p_1^2 \rangle &= \frac{1}{h^{7/6}} \int_0^\infty x^{5/6} A \epsilon^{2/3}(x) dx \\ &= (h_c/h)^{7/6}\end{aligned}\tag{2}$$

where h = receiver position behind shock
 x = distance back along propagation path
 $\epsilon(x)$ = turbulence dissipation function
 A = constant = 0.702 for velocity turbulence

Using a turbulence model based on a flat plate boundary layer, together with nominal atmospheric wind amplitudes and fluctuations, Crow obtained a value of $h_c = 0.7$ msec. This result agrees with flight test data, albeit with the use of a reasonably estimated turbulence model rather than the actual turbulence during flight tests. Equation (2) is singular at the shock ($h=0$), but this is a consequence of zero rise time; when applied to a finite thickness shock with structure $p_o(t)$, it may be shown⁶ that the perturbations are bounded by:

$$\langle p_1^2 \rangle \leq \int_{-\infty}^h \left(\frac{h-t}{h_c} \right)^{-7/12} \frac{d p_o(t)}{d t} d t \tag{3}$$

Figure 7 shows Equation (3) applied to a tanh shock of thickness T , where it is assumed that $T = h_c$. The maximum rms perturbation in that figure is slightly larger than the shock strength. It may be seen from Equation (3) that the magnitude of the perturbations scales as $(h_c/T)^{7/12}$, so that for $T = 3$ msec and $h_c = 0.7$ msec, the maximum rms perturbation is about 60 percent of shock strength.

Crow's analysis provides estimates of only rms fluctuations, and not spectra, so in its original form it cannot be used to predict effects on loudness. It also does not account for the potential attenuation of

scattered waves by molecular absorption. Absorption and spectral effects can be incorporated into Equation (2) on an *ad hoc* basis as:

$$\langle p_1^2 \rangle = \frac{1}{h^{7/6}} \int_0^\infty G(x) \Phi(f) e^{-\alpha x} dx \quad (4)$$

Equation (4) is formulated on the following basis:

- In Equation (2), the integrand $x^{5/6} A \epsilon^{2/3}(x)$ represents the contribution from a differential layer at distance x behind the shock. The particular form follows from the Kolmogorov spectrum and other aspects of Crow's formulation. The quantity $G(x)$ is a generalization of the original integrand.
- The factor $e^{-\alpha x}$ represents molecular absorption over distance x . This term depends on the frequency content of the scattered waves, and its utility is closely coupled to estimates of the scattered spectrum.
- The factor $\Phi(f)$ represents the spectral distribution of sound scattered from the layer at x . With inclusion of this factor, Equation (4) becomes a prediction of the spectrum of the scattered sound, rather than just of the amplitude.

Inclusion of the spectral term requires a merging of Crow's analysis, which considered scattering of a step function, with traditional scattering analyses of harmonic waves. Crow abandoned harmonic analysis in favor of the step function, which simplified the scattering volume into a "paraboloid of dependence" and thereby made the problem tractable. In the second scattering analysis of Reference 6, it is clear that the regime leading to Equation (1) is equivalent to the regimes studied by Chernov¹¹ and Tatarski¹² for small angle scattering of continuous waves, for which scattered sound is proportional to:

$$\langle |p_1|^2 \rangle \propto k^4 E \left(2k \sin \frac{\theta}{2} \right) \quad (5)$$

where k is the wave number of the sound, θ is the scattering angle, and E is the spectral density (in wave number space) of the turbulence. For a shock with power spectrum $1/k^2$, the scattered energy is proportional to Equation (5) times $1/k^2$. Assuming a Kolmogorov spectrum, the high- and low-frequency limits of Equation (5) are:

$$\langle |p_1|^2 \rangle \propto \begin{cases} k^2 & , \quad k \leq \frac{\pi}{5 L_o \theta} \\ k^{-5/3} \theta^{-11/3} & , \quad k > \frac{\pi}{5 L_o \theta} \end{cases} \quad (6)$$

where L_o is the turbulent macroscale length. (Following the conventions used in Reference 6, the macroscale length is defined as the normalized integral of the correlation function. It is 2/5 the largest eddy size, which corresponds to the low-wavenumber limit of the Kolmogorov subrange.)

Equations (6) give the shape of $\Phi(f)$, provided the scattering angle θ is known. This angle is readily obtained from the geometry of the paraboloid of revolution, as sketched in Figure 8. The paraboloid – which represents the scattering volume associated with the perturbations at position h – has the shock as its directrix and its focus at h . The scattering angle and paraboloid radius are simple functions of x , as indicated in Figure 8. It is straightforward to write the spectral distribution factor as:

$$\Phi(f) = \frac{6}{\pi f_o} \begin{cases} (f/f_o)^2 & , f < f_o \\ (f/f_o)^{-5/3} & , f > f_o \end{cases} \quad (7)$$

where

$$f_o = \frac{a}{10 L_o} \left(\frac{x}{2h} \right)^{1/2}$$

The leading coefficient of $\Phi(f)$ has been selected such that $\int_0^\infty \Phi(f)df = 1$, so that the original amplitude of Crow's solution is preserved. Note that the spectral contribution from the layer at x will have its peak at frequency f_o . The spectral peak at each h will be broadened by the fact that f_o varies with x . It is clear from the paraboloid geometry that f_o increases as h decreases, so that perturbations close to the shock will tend to have higher frequency content than those far from it.

With the inclusion of Equation (7), spectra of scattered sound may be calculated. Figure 9 shows spectra at several locations h , for the nominal propagation conditions discussed earlier. The basic features are as expected: perturbations are larger closer to the shock, and the peak frequency is higher at smaller h . It is interesting that at low frequencies the spectra are somewhat flatter than the 6 dB/octave slope of an N-wave, while at high frequencies the spectra decay faster than the 12 dB/octave slope of a shock. When scattering is significant, the effect on spectra will be an enhancement within the middle frequency range.

The calculation leading to Figure 9 still has the properties that amplitude increases as h decreases, and that perturbations continue to grow as propagation distance increases. The increase with decreasing h is a particular problem because the loudness calculation requires the total spectrum, i.e., integrated over h . Both of these effects can be shown to be associated with waves scattered at very small angles. Scattered waves appear behind the shock because their forward propagation speed is reduced by the cosine of the scattering angle. Recall from Equation (1) that waves behind the shock catch up to it at a rate of

$a_\infty \frac{\gamma+1}{4\gamma} \frac{\Delta p}{p_\infty}$ (Equation (1) less the propagation speed of the shock). For a scattered wave to actually fall

behind the shock, it must be scattered at an angle such that its speed is reduced by at least this amount. This corresponds to:

$$\cos \theta \leq 1 - \frac{\gamma+1}{4\gamma} \frac{\Delta p}{p_\infty} \quad (8)$$

Waves scattered at smaller angles never become distinct; they are immediately absorbed by the shock. Figure 10 shows a calculation similar to that of Figure 9, but excluding the extreme forward scattering identified by Equation (8). The scattered energy is limited at small h , and in fact becomes smaller at h values smaller than shown. With this non-linear coalescence included, it is possible (without further assumptions) to integrate the spectra over h , to obtain the total scattered spectrum. The integrated spectrum is shown in Figure 11. Shown are the results for the nominal 5,000-foot propagation distance, and also for 2,000 and 10,000 feet. The difference between total scattered energy for these three propagation distances is much smaller than if steepening had not been accounted for, and the spectrum reaches an asymptotic limit at larger propagation distances. Losses in the shock are thus a mechanism which puts a finite limit on growth of first scattered waves.

If the spectra in Figure 11 are compared with the the ramp shock spectrum shown in Figures 3 and 6, and considered relative to the sone contours, there is an effective peak in the region which is most significant for loudness of the original shock. (Recall that this region is around the frequency where the 6 dB/octave to 12 dB/octave break associated with the shock thickness occurs.) The scattered waves thus have a potential to increase the loudness of a boom. To quantify this, it is appropriate to consider the loudness of an unperturbed sonic boom and the change if perturbations are superposed.

LOUDNESS OF SONIC BOOMS WITH SCATTERED WAVES

Figure 12 shows the one-third octave spectrum of a 1 psf N-wave, with a duration of 350 msec and a ramp shock structure with 3 msec rise time. Loudness (PLdB) and two other metrics (C- and A-weighted sound exposure level) are indicated on the figure. This spectrum corresponds to the ramp spectrum in Figures 3 and 6, but doubled (two shocks) and with some features associated with the 350 msec signature duration. The spectrum is also normalized with regard to the 0.125 msec auditory response time.

Figure 13 shows the result of superposing the scattered spectrum, Figure 11 (5,000-foot turbulent layer), onto Figure 12. There is an enhancement in the 40 to 300 Hz range, resulting in an increase in loudness of about 2 dB. This increase grows with longer propagation distance, but at a slower rate. The increase would be about 5 dB for a 20,000-foot layer, a substantially longer distance than would occur under real conditions.

This loudness enhancement presumes that the shock structure remains unchanged. Sonic boom shocks propagating through turbulence experience random increases in thickness. The theory of Reference 6 predicts that a steady-state shock, for these conditions, would have a hyperbolic tangent structure with a 12 msec rise time. An actual turbulence-induced shock would be somewhat thinner for two reasons. First, a 5,000-foot layer is not quite long enough for an initially thin shock to achieve this asymptotic structure. Second, the theory of Reference 6 tends to overpredict thicknesses somewhat, since it includes energy at very small angles which is not actually extracted from the shock. It is therefore realistic to consider that turbulence would cause an average thickness in this case of about 6 msec, which is double the molecular absorption-controlled basic rise time.

Figure 14 shows the spectrum and loudness of a 350 msec, 1 psf boom with a shock thickness of 6 msec. Loudness is about 4 dB less than that of the 3 msec rise time boom in Figure 12. This comparison by itself could suggest that random thickening yields a reduction in loudness. However, when the first scattering perturbations are added, the result shown in Figure 15 is a spectrum and level which are very nearly the same as the nominal unperturbed, 3 msec rise time, boom. The net result of this calculation is that the shock thickens, decreasing its loudness, but the energy scattered out of the shock appears as perturbations which increase the loudness by a matching amount. Minor differences in assumptions could cause this balance to differ, so a conclusion cannot be reached as to whether there will be a net increase or decrease in loudness. Earlier discussions regarding non-linear regeneration of high frequencies suggest there will be a net increase, but for the relatively weak shocks associated with minimized booms this generation is not substantial. It is clear, however, that the average change to loudness is substantially less than if only scattered perturbations or only turbulence-induced thickening were considered.

THREE DIMENSIONS AND VARIABILITY

The above discussion, considering the average predictions from scattering perturbation and thickening theories, is effectively a one-dimensional model. There are variations inherent in the process, although only averages were discussed here. There is, however, a potential for greater variation, associated with transverse variability. Scattering is a three-dimensional phenomenon, in which the incident sound is diverted to a different direction. The perturbations following a particular element of shock front do not originate from that element; they are extracted from other, laterally displaced, portions of the shock. Depending on particular turbulent structures, two bounding situations can be postulated:

- The net effects of scattering may be transversely homogeneous. Shock thickening is fairly uniform across the front, and fluctuations are also evenly distributed. There can be local peaked and rounded signatures (as is seen in flight tests) but the effect on loudness is uniform. The net result

would be observed spectra similar to Figure 15, varying only moderately from the original spectrum, Figure 12.

- There may be substantial local variations in scattering. One area of wavefront may pass through a region which causes substantial energy to be scattered from it. This energy may propagate to positions behind elements of wavefront which emerge intact from their local turbulence. The net result is that some wave elements may retain their original thickness but contain perturbations (as in Figure 13), while other elements may be thickened but not have perturbations (as in Figure 14). In this case, a significant spatial variability may increase the effective one-dimensional variability.

Flight tests which exhibited consistent spatial alternation of peaked and rounded signatures¹³ suggest the latter, although definitive conclusions would require analysis of the correlation between perturbation spectra and shock thickness. The recent NASA sonic boom propagation measurements¹⁴ provide an opportunity to examine these extremes. That experiment involved a number of recording positions at close intervals along the flight track, and multiple aircraft passes at short time intervals.

CONCLUSIONS

An analysis has been performed of the effect of turbulence on the loudness of minimized sonic booms. The first scattering theory by Crow⁵ was extended to include molecular absorption and to predict the spectral characteristics of the scattered sound. The effect of non-linear steepening was accounted for in application of the modified theory to low-boom shock waves.

The most important frequencies for loudness were shown to be those controlled by the shock structure, in particular, around the transition between the basic step function spectrum and the higher frequency rolloff associated with the shock. This transition frequency is inversely proportional to shock thickness, which has a minimum associated with molecular relaxation processes and can increase due to turbulence. Scattered waves, which appear as perturbations behind each shock, have spectra whose peaks are generally in this frequency range. There will obviously be variation in loudness, and there is a question of whether there will be an increase or decrease in average loudness.

When linear acoustics is considered, scattering neither creates nor destroys acoustic energy. Any average decrease in loudness due to turbulence-induced thickening will be balanced by an increase due to the perturbations associated with the scattered waves. This balance can be altered by non-linear steepening. Two effects were shown to be significant:

- Because of non-linear steepening, only sound which is scattered at an angle larger than some minimum will actually be scattered out of the shock. This puts two limits on predictions from linear

scattering theory. The first limit is that it eliminates the singularity at the shock front. The second limit is that the amplitude of scattered waves does not indefinitely increase with turbulent layer thickness.

- Non-linear steepening can regenerate high frequencies which were scattered out of the shock. This can potentially increase loudness. However, for minimized booms, non-linear effects are sufficiently weak that this is negligible for typical 5,000-foot or less turbulent layers.

The conclusion of this analysis is that the turbulence will not substantially increase or decrease the average loudness of minimized booms, but can introduce significant variability.

The relative strengths of the balancing mechanisms in the shock waves were examined. The mechanisms are non-linear steepening and absorption by molecular relaxation processes. Considering average humidity conditions, and shock strengths of 1 psf or less (including doubling at the ground), both mechanisms are weak. Each, taken alone, would require a propagation distance in excess of 10,000 feet to double or halve rise time. If the shock is not in an equilibrium state when it enters the lowest 5,000 feet of the atmosphere, it is not likely that an equilibrium structure will evolve in that final layer. The history of the shock from higher altitudes must be established, and this is a potential source of rise time (hence loudness) variability.

An important detail in establishing loudness variability is the transverse spatial uniformity of scattering. It is shown that transverse nonuniformity can add ± 3 dB of variability, in addition to other causes of variation. The recent NASA measurements of sonic boom propagation through turbulence¹⁴ are expected to be very valuable in evaluating this.

References

1. Shepherd, K.P., Sullivan, B.M., Leatherwood, J.D., and McCurdy, D.A., "Sonic Boom Acceptability Studies", First Annual High-Speed Research Workshop, May 14-16, 1991.
2. Shepherd, K.P., and Sullivan, B.M., "A Loudness Calculation Procedure Applied to Shaped Sonic Booms, NASA TP 3134, 1991.
3. Pierce, A.D., "Weaker Sonic Booms may be Considerably More Quiet", Presented at Acoustical Society of America Meeting, November 1989.
4. "American National Standard Method for the Calculation of the Absorption of Sound by the Atmosphere", ANSI S1.26-1978.
5. Crow, S.C., "Distortion of Sonic Bangs by Atmospheric Turbulence", *J. Fluid Mech.*, 37 (3), 529-563, 1969.

6. Plotkin, K.J., and George, A.R., "Propagation of Weak Shock Waves Through Turbulence", *J. Fluid Mech.*, 54 (3), 449-467, 1972.
7. Pierce, A.D., and Sparrow, V.W., "Relaxation and Turbulence Effects on Sonic Boom Signatures", presented at First Annual High-Speed Research Workshop, Williamsburg, VA, May 14-16, 1991.
8. May, D.N., and Sohn, R.A., "Simple Response Metrics for Minimized and Conventional Sonic Booms", *J. Sound Vib.*, 145 (2), 225-238, 1991.
9. Stevens, S.S., "Perceived Level of Noise by Mark VII and Decibels (E)", *J. Acoust. Soc. Am.*, 51 (2), 575-601, 1971.
10. Johnson, D.R., and Robinson, D.W., "The Subjective Evaluation of Sonic Bangs", *Acustica*, 18 241-258, 1967.
11. Chernov, L.A., *Wave Propagation in a Random Medium*, McGraw-Hill, 1960.
12. Tatarski, V.I., *Wave Propagation in a Turbulent Medium*, McGraw-Hill, 1961.
13. Hilton, D.A., Huckel, V., Steiner, R., and Maglieri, D.J., "Sonic Boom Exposures During FAA Community-Response Studies Over a Six-Month Period in the Oklahoma City Area", NASA TN D-2539, 1964.
14. Willshire, W.L., Jr., "Preliminary Results From White Sands Missile Range Experiment", presented at NASA High-Speed Research Sonic Boom Workshop, February 25-27, 1992.

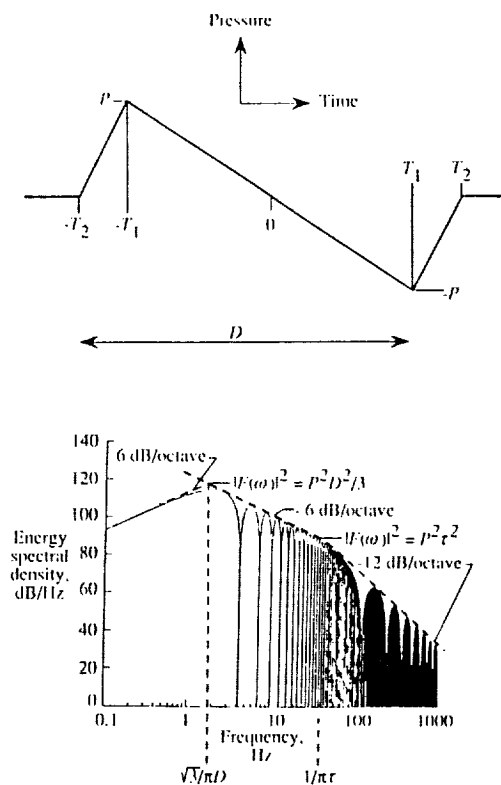
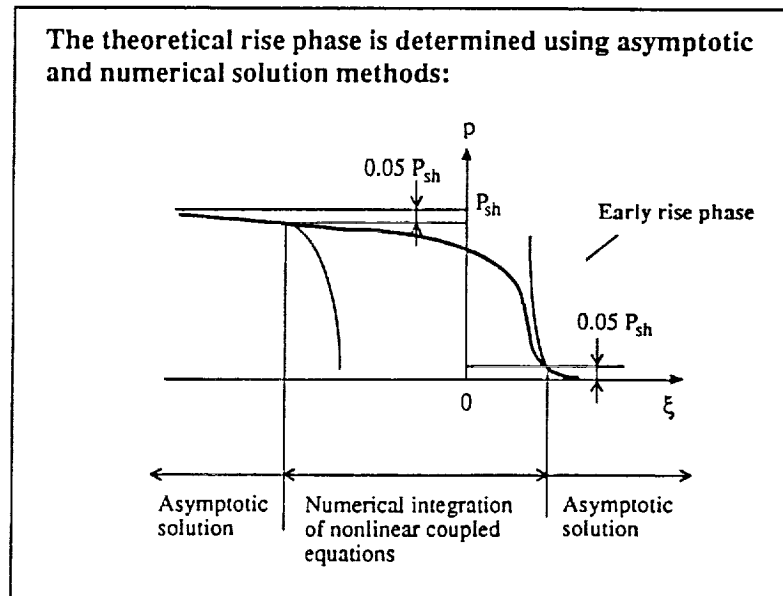


Figure 1. Spectrum of N-wave sonic boom.²



Early rise phase: O_2 relaxation dominates
 Later rise phase: N_2 relaxation dominates

Figure 2. Molecular relaxation shock structure.⁷

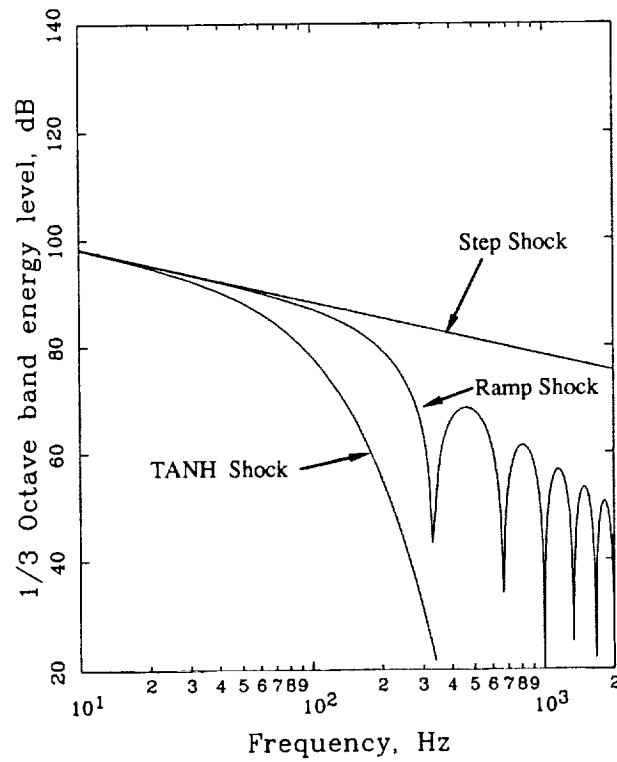


Figure 3. Spectra of step function shock and two shock structures with 3 msec rise times.

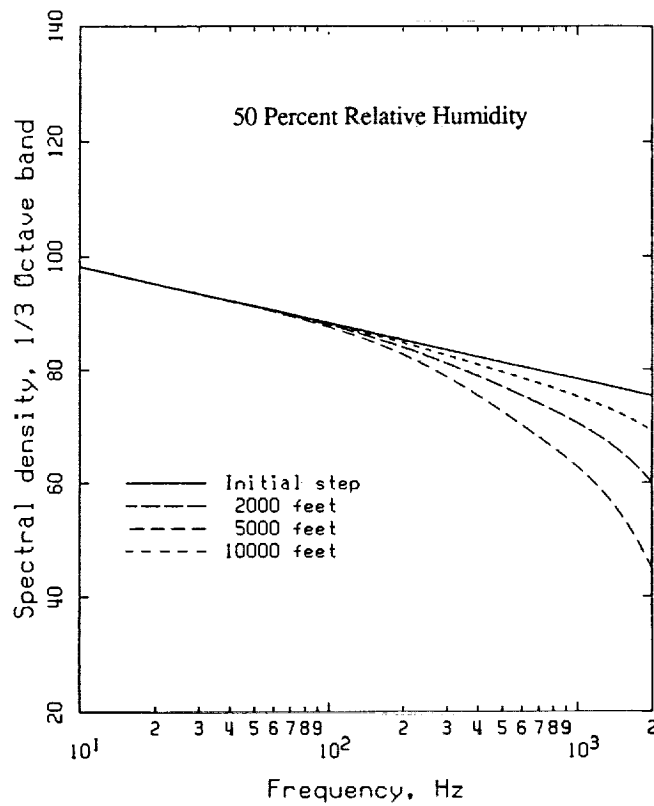


Figure 4. Effect of absorption on spectrum of a step function acoustic wave.

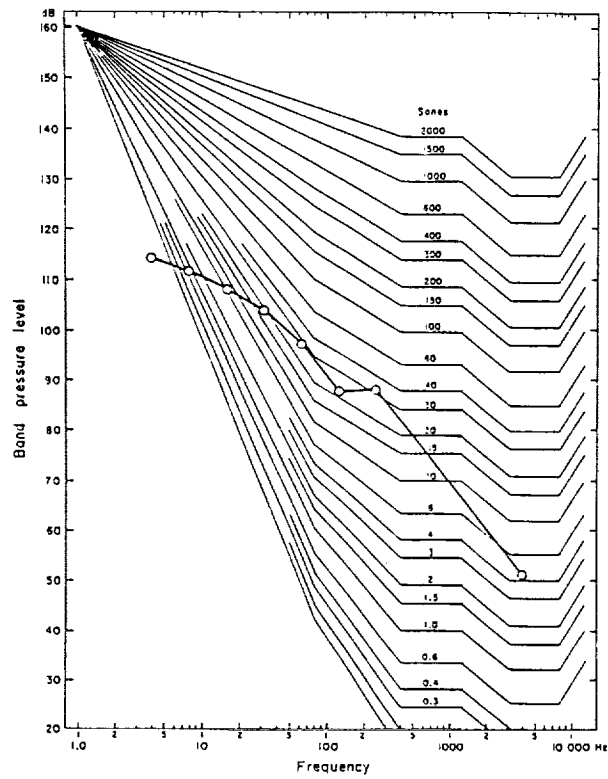


Figure 5. Sone chart for loudness calculation,⁹ with sonic boom spectrum¹⁰ overlaid.

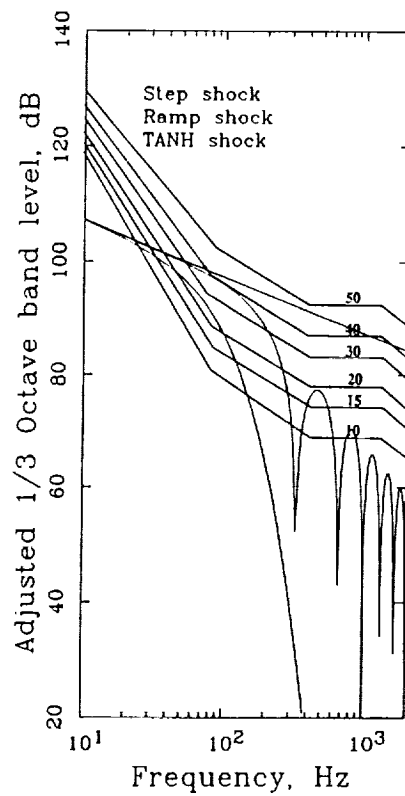


Figure 6. Step, ramp, and tanh shock spectra overlaid on sone chart.

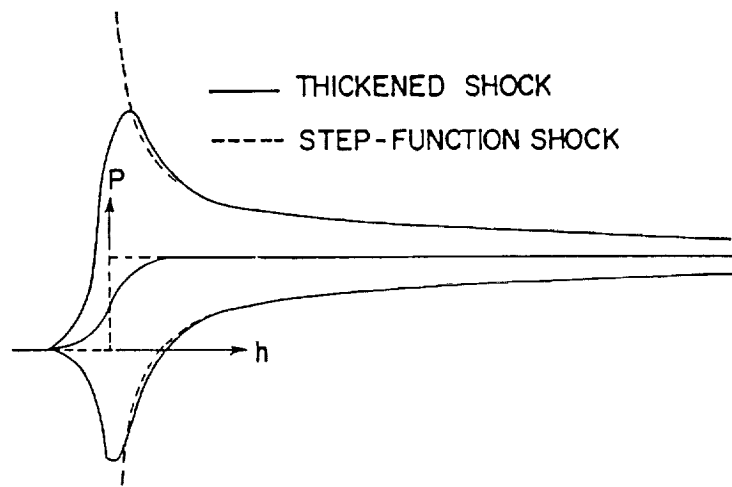
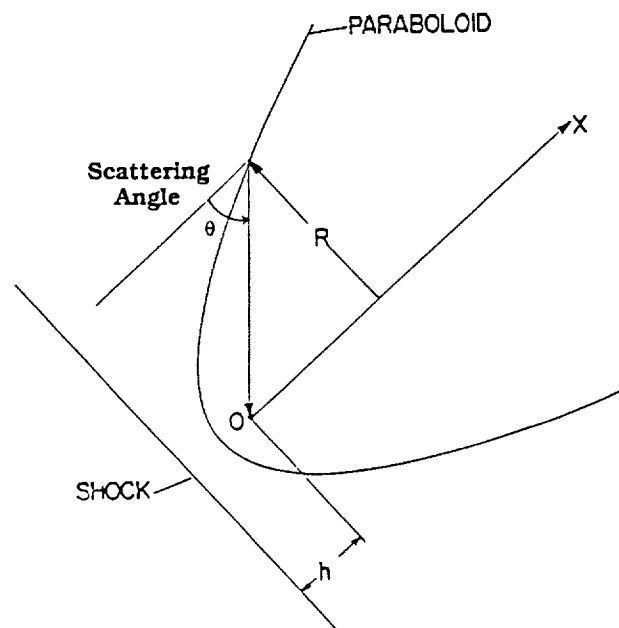


Figure 7. Root-Mean-Square perturbations for a thickened shock of Thickness $T = h_c$ and $(h_c/h)^{7/12}$.



$$R \approx (2hx)^{1/2}$$

$$\theta = (2h/x)^{1/2}$$

Figure 8. Scattering angle from paraboloid of revolution.

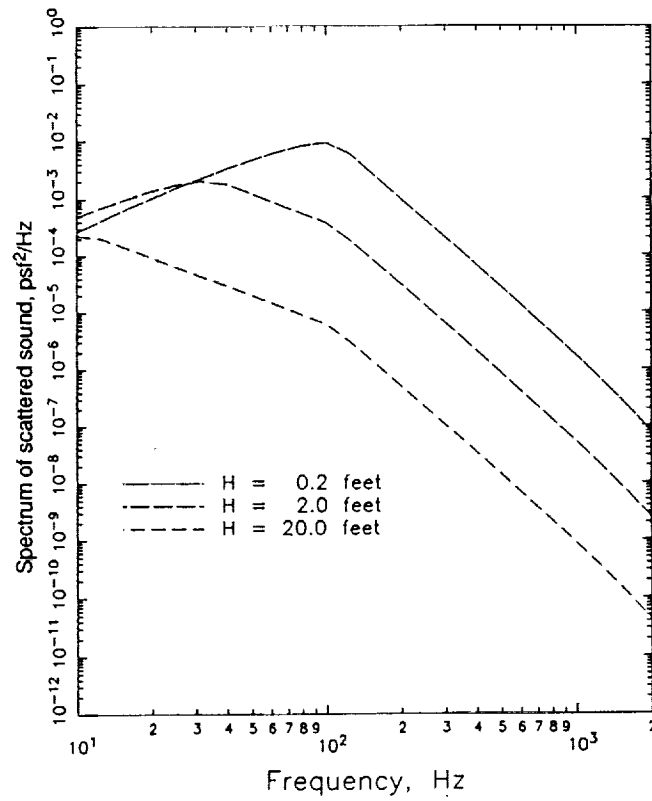


Figure 9. Spectrum of scattered sound at several distances h behind shock front. Linear acoustics.

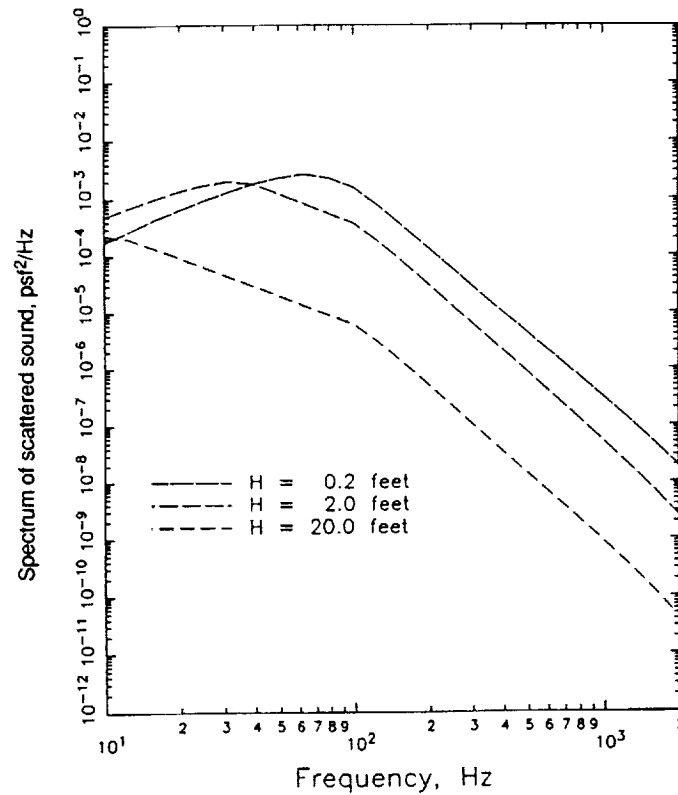


Figure 10. Spectrum of scattered sound at several distances h behind shock front. Non-linear coalescence accounted for, $\Delta p = 1$ psf.

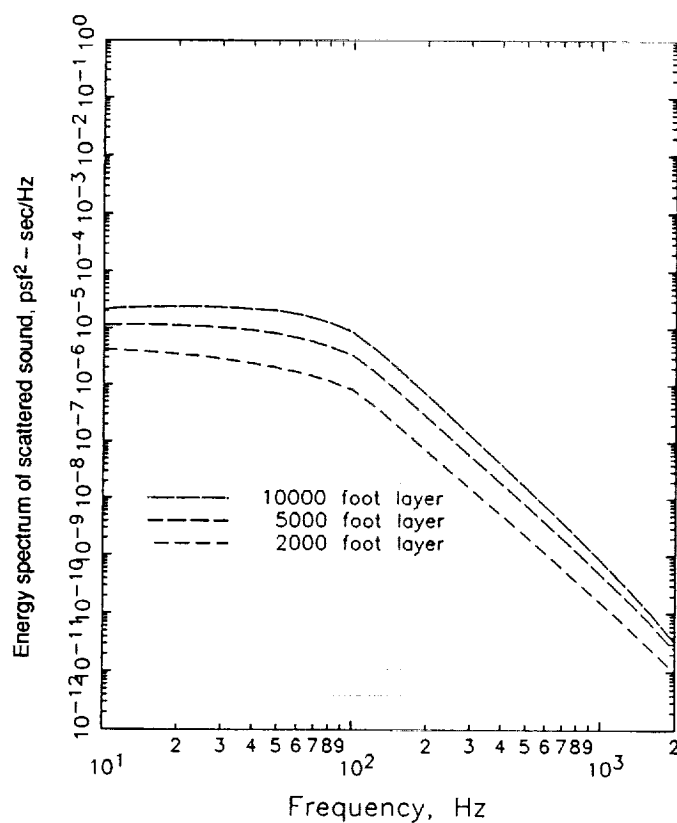


Figure 11. Energy spectrum of scattered sound, several propagation distances.
Non-linear coalescence accounted for, $\Delta p = 1$ psf.

Duration = 350 msec; 3 msec Ramp Shock
No Turbulence

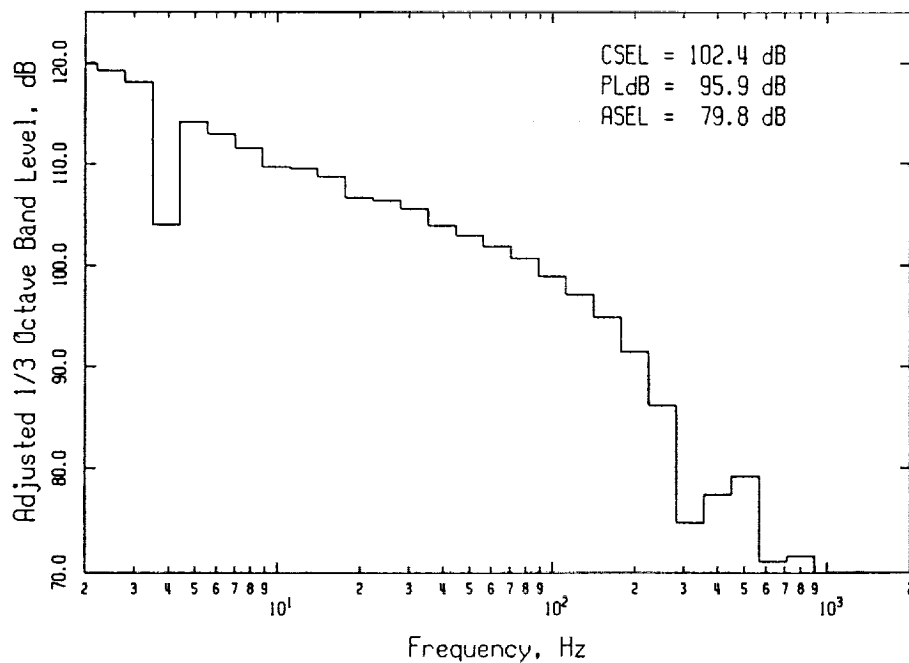


Figure 12. Spectrum of 350 msec, 1 psf, 3 msec rise time N-wave,
no turbulent distortion.

Duration = 350 msec; 3 msec Ramp Shock
Propagation Through 5000 feet of Turbulence

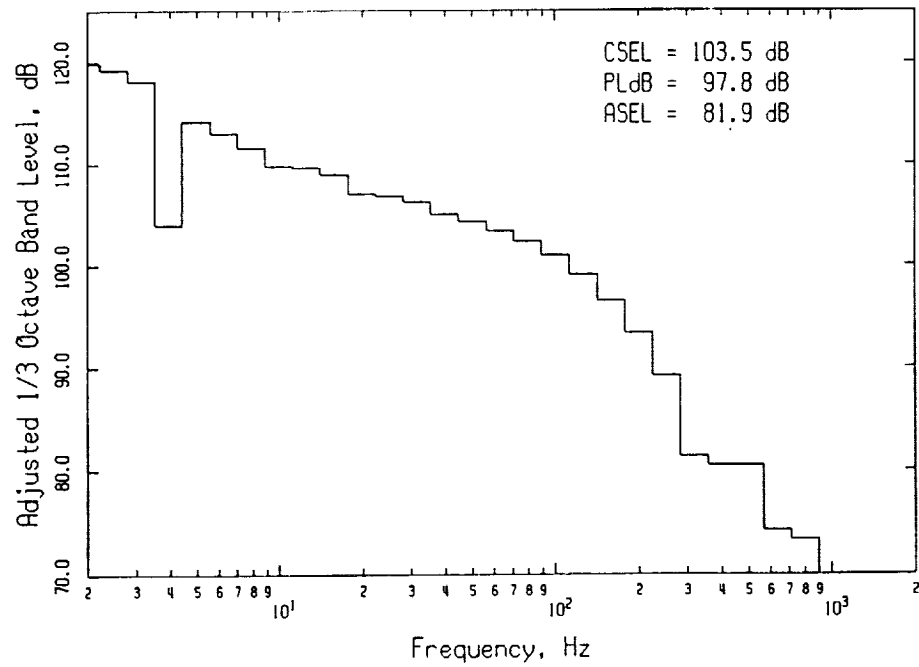


Figure 13. Spectrum of 350 msec, 1 psf N-wave with turbulent distortion, rise time fixed at 3 msec.

Duration = 350 msec; 6 msec Ramp Shock
No Turbulence

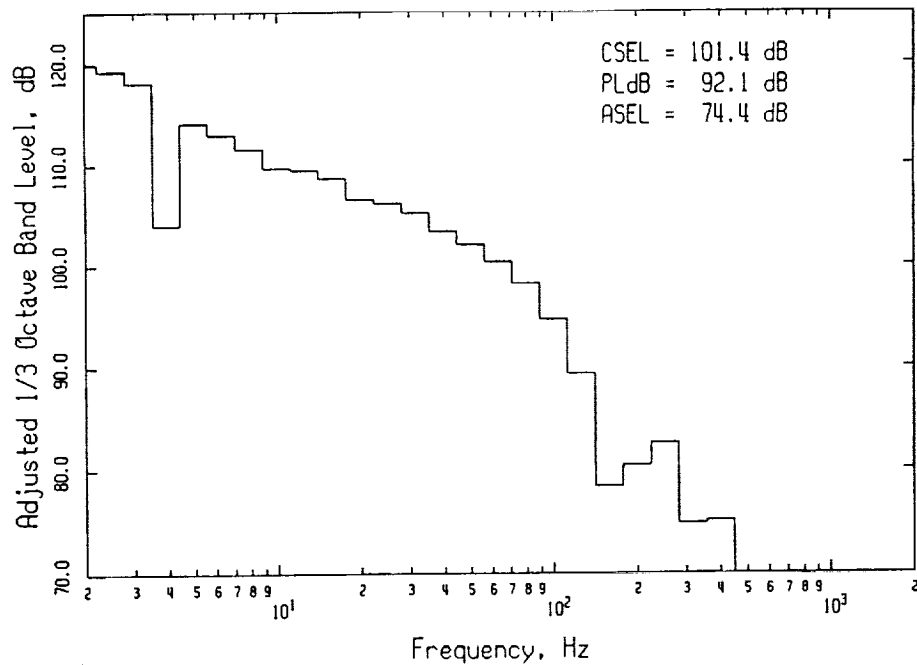


Figure 14. Spectrum of 350 msec, 1 psf N-wave, shock thickened to 6 msec rise time, no turbulent distortion.

Duration = 350 msec; 6 msec Ramp Shock
Propagation Through 5000 feet of Turbulence

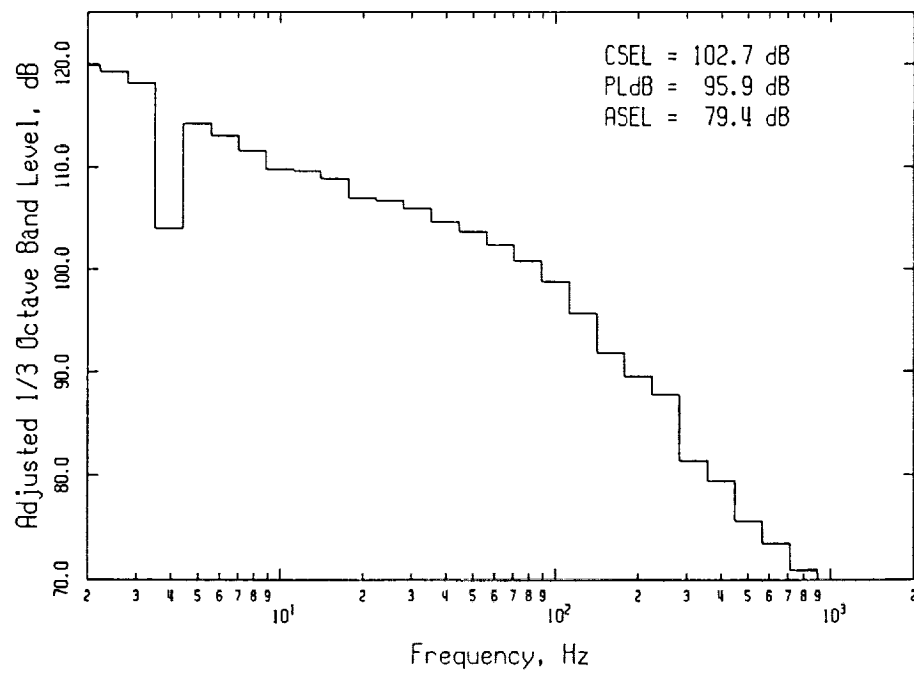


Figure 15. Spectrum of 350 msec, 1 psf N-wave, including turbulent distortion and shock thickened to 6 msec rise time.

MODEL EXPERIMENT TO STUDY THE EFFECT OF TURBULENCE ON
RISETIME AND WAVEFORM OF N WAVES*

Bart Lipkens

Applied Research Laboratories and Mechanical Engineering Department
The University of Texas at Austin
Austin, TX

David T. Blackstock

Applied Research Laboratories and Mechanical Engineering Department
The University of Texas at Austin
Austin, TX

SUMMARY

Typical measured sonic boom rise times are two to five times longer than rise times calculated using molecular relaxation theory. The difference may be due to atmospheric turbulence. A model experiment has been set up to study the influence of turbulence on waveform and rise time of spark-produced N waves. The N waves propagate through turbulence generated by a plane jet. The model turbulence is scaled down from atmospheric turbulence by approximately the same factor as the model N wave is scaled down from the sonic boom. Our experiments show that passage through the turbulence produces a wide variety of changes in the N waveform. Spiked and rounded N waves are observed, and average rise time is increased by a factor of about 2. A tentative observation based on data obtained so far is that rise time is always increased, never decreased, by turbulence.

INTRODUCTION

Sonic boom pressure waveforms have a typical N wave signature in a steady atmosphere (Fig. 1). The important characteristics of the waveform are its peak overpressure Δp , its rise time τ , and its duration T . The rise time[†] and peak overpressure are closely related to the subjective response of people to the sonic boom.¹ Field measurements of sonic booms show that the ground signature is rarely an ideal N wave.² A wide variety of distorted N waves (Fig. 2), from spiked to

*Work supported by NASA Langley Research Center.[†]Rise time is defined as the time portion of the rise phase of the N wave between 10% and 90% of its peak overpressure.

rounded and even double-peaked, is seen. Moreover, observed rise times are two to five times larger than those calculated using molecular relaxation theory.^{3,4} Although it has long been accepted that atmospheric inhomogeneities associated with turbulence are the cause of the waveform variability,⁵ the role of turbulence in increasing rise time is more controversial. The first evidence of wrinkled shock fronts occurred in shadowgraphs taken by Bauer and Bagley⁶ of ballistic shocks propagating through low-speed turbulent wall jets. The bow and tail shocks were broken into a number of lines by the interaction with the jets. Bauer and Bagley interpreted these lines as ripples in a smoothly connected shock front. They also presented a set of oscilloscope pictures, showing the spiking and rounding of the shocks by the turbulence. Plotkin and George⁷ attributed the multiple lines to lagging scattered waves, which provide a possible mechanism for increasing the rise time. Tubb⁸ measured the effect of grid generated turbulence on rise time of a weak shock. He found that, on a statistical average, passage through the turbulence doubled the rise time. The ballistic experiments of Sanai, *et al.*^{9,10} produced schlieren photographs of fold-like shock structure for weak shocks and concave shock fronts for strong shocks. Hall's shadowgraphs¹¹ show shock fronts that are always folded after passage through a higher speed jet. Bass, *et al.*¹² measured N waves produced by supersonic projectiles and did not observe any correlation between measured rise time and the atmospheric turbulence.

Our goal was to construct a model experiment to investigate the effect of turbulence on the waveform, especially rise time and peak overpressure, of N waves.

SCALING OF THE TURBULENCE

In our model experiment the N waves are produced by electrical sparks. Table 1 presents an overview of typical values of rise time, peak overpressure, and duration of sonic booms and spark-produced N waves.

Table 1
Typical Values of Rise Time, Peak Overpressure, and Duration for Sonic Booms and Spark-Produced N Waves

	Sonic Boom	Electrical Spark
Rise Time	1-10 ms	0.5-2 μ s
Duration	100-300 ms	10-30 μ s
Amplitude	30-200 Pa	100-500 Pa

The table shows that the time scale factor relating sonic booms to spark-produced N waves is of order 5,000 to 10,000. The model turbulence has to be scaled down

from the atmospheric turbulence by approximately the same factor. Table 2 shows typical values for the inner and outer length scales and the thickness of atmospheric turbulence. Also shown are the scaled down values for the turbulence in the model experiment.

Table 2
Typical Values of the Turbulence Parameters in the Atmosphere and the
Scaled Down Turbulence for the Model Experiment

	Atmospheric Turbulence	Model Experiment Turbulence
Turbulent boundary layer thickness	1000 m	0.1-0.2 m
Outer length scale	100-200 m	0.01-0.02 m
Inner length scale	10 mm	0.001 mm

The turbulence for the model experiment is generated by a plane jet. The flow facility consists of a 700 watt centrifugal blower, a settling chamber, and a nozzle exit. The jet nozzle is a slit, 0.25 m high and width variable from 0 to 0.1 m. For the results described, the distance between the spark source and the microphone is 0.4 m, of which the jet occupies 0.2 m (i.e., the scaled thickness of the atmospheric turbulent boundary layer). The N waves propagate across the jet at a position about 0.4 m downstream from the nozzle.

Although the sonic boom is a cylindrical wave while a spark-produced N wave is a spherical wave, the difference does not cause any fundamental problems for our investigation. We have also used a parabolic mirror to produce a locally plane wave when it was advantageous to do so.

A more significant difference is the fact that the linear pressure drop between the head and tail shock is much steeper for the spark-produced N wave than for the sonic boom. The typical sonic boom is so long and so weak (the slope of the midsection is of the order of 1 Pa/ms) that the flow field behind the head shock is practically steady. Because the spark-produced N waves are both stronger and much shorter (the slope of its midsection is of the order of 10,000 Pa/ms), the flow behind its head shock is not steady. Although the gross behavior of the two waves is not affected by this difference, the rise time is.^{13,14} Fortunately the ratio of rise time to duration is about the same for both waves.

A very wide band condensor microphone¹⁵ was used in order to accurately measure rise times as short as 0.5 μ s. The construction and calibration of the

microphone and preamplifier are described by Cornet.¹⁶ The signal from the preamplifier is digitized and sent to a Macintosh computer, where all data processing takes place.

RESULTS

The procedure was to make 100 measurements with no turbulence and then 100 measurements with the plane turbulent jet turned on. The rise time and peak overpressure of each individual waveform were computed automatically from the stored signatures. Also computed were average rise time τ_{aver} , average peak overpressure Δp_{aver} , and standard deviation σ for the 100 measurements. Figure 3 shows some typical waveforms for the spherical N wave after passage through the turbulent field. A wide variety of spiked and rounded N waves is shown. Clearly, the distortion of the spark-produced N waves by the turbulent jet is qualitatively the same as the distortion of sonic booms by the atmospheric boundary layer. The distortion is most noticeable in the vicinity of the shocks. Moreover, for each individual N wave the distortion at the tail shock is similar to that of the head shock. In Fig. 4, graphs (a) and (b) compare the peak overpressure, both with and without turbulence, for the 100 measurements. Although variability of Δp is increased enormously by the turbulence ($\sigma_{\Delta p}$ rises from 7 Pa to 61 Pa), Δp_{aver} is not affected very much (190 Pa with turbulence, 166 Pa without). The number of spiked ($\Delta p > \Delta p_{\text{aver}}$) N waves versus the number of rounded ($\Delta p < \Delta p_{\text{aver}}$) N waves is about the same (54 versus 46). Graphs (c) and (d) in Fig. 4 show the comparison of the rise time data. Both average rise time and the variability are significantly increased. In particular, τ_{aver} changes from 0.82 μs (no turbulence) to 1.72 μs (turbulence present), a more than two-fold increase. The corresponding increase in σ_{τ} is 0.05 μs to 0.96 μs . Even more important is that turbulence seems only to increase the rise time, never to decrease it. This can be seen from Fig. 5, which shows cumulative probability curves for both rise time and peak overpressure. The cumulative probability curve compares the rise time and peak overpressure data with the average for no-turbulence N waves. It is seen that none of the turbulence rise time data is smaller than the no-turbulence value of τ_{aver} . Our measurements apparently confirm Pierce's prediction⁴ that turbulence only increases rise time. Experiments with plane N waves showed the same general results. The average rise time increased by a factor of 2.2 and similar distortions were observed in the waveforms of N waves that had propagated through the turbulence.

DISCUSSION and CONCLUSIONS

A model experiment has been carried out to study the effect of turbulence on the waveform and especially the rise time of spark-produced N waves. The results

show that the model turbulence (plane jet) creates the same distortion (spiking and rounding) of the spark-produced N waves as atmospheric turbulence creates on the sonic booms. Similar distortions were observed by Bauer and Bagley.⁶ An important result is that the turbulence seems only to be a shock thickening mechanism, as was proposed by Pierce.⁴ The rise time of each N wave, after passage through the turbulence, is larger than when no turbulence is present. These results apply to spherical N waves as well as to plane N waves. On a statistical average the rise time is doubled after passage through the turbulence, which confirms the results of Tubb⁸ and disagrees with the conclusions of Bass *et al.*¹² The average peak overpressure is about the same as the no-turbulence average peak overpressure. Turbulence greatly increases the variability in rise time and peak overpressure. Future experimental work will include characterizing the strength and length scales of the turbulent field by hot wire anemometry and measuring the effect of acoustic nonlinearities (e.g., healing effect) on the propagation of the N waves.

REFERENCES

1. Sheperd, L. J., and Sutherland, W. W.: Relative Annoyance and Loudness Judgments of Various Simulated Sonic Booms, NASA CR NAS-1-6193 Subcontract B-87017-US, 1967.
2. Maglieri, D. J.: Sonic Boom Flight Research - Some Effects of Airplane Operations and the Atmosphere on Sonic Boom Signatures, in *Sonic Boom Research*, A. R. Seebass, Ed., NASA SP-147, April 1967.
3. Kang, J.: Nonlinear Acoustic Propagation of Shock Waves Through the Atmosphere With Molecular Relaxation, Ph. D. thesis, Pennsylvania State University, May 1991.
4. Pierce, A. D., and Sparrow, V. W.: Relaxation and Turbulence Effects on Sonic Boom Signatures, NASA First Annual High-Speed Research Workshop, Williamsburg, Virginia, 1991.
5. Pierce, A. D., and Maglieri, D. J.: Effects of Atmospheric Irregularities on Sonic-Boom Propagation, *J. Acoust. Soc. Am.* vol. 51, 1972, pp. 702-721 .
6. Bauer, A. B., and Bagley, C. J.: Sonic Boom Modelling Investigation of Topographic and Atmospheric Effects, U. S. Dept. of Transport, Rep. FAA-No-70-10, 1970.
7. Plotkin, K. J., and George, A. R.: Propagation of Weak Shock Waves through Turbulence, *J. Fluid Mech.* vol. 54, 1972, pp. 449-467.
8. Tubb, P. E.: Measured Effects of Turbulence on the Rise Time of a Weak Shock, AIAA Paper 75-543, March 1975.
9. Sanai, M., Toong, T-Y., and Pierce, A. D.: Ballistic Range Experiments on Superbooms Generated by Refraction, *J. Acoust. Soc. Am.*, vol. 59, 1976, pp. 513-519.
10. Sanai, M., Toong, T-Y., and Pierce, A. D.: Ballistic Range Experiments on Superbooms Generated at Increasing Mach Numbers, *J. Acoust. Soc. Am.*, vol. 59, 1976, pp. 520-524.
11. Hall, S. V.: Distortion of Sonic-Boom Pressure Signatures by High-Speed Jets, *J. Acoust. Soc. Am.*, vol. 63, No. 6, June 1978, pp. 1749-1752.
12. Bass, H. E., Layton, B. A., and Bolen, L. N.: Propagation of Medium Strength Shock Waves Through the Atmosphere, *J. Acoust. Soc. Am.*, vol. 82, no. 1, July 1987, pp. 306-310.

13. Orenstein, L. B.: The Rise Time of N Waves Produced by Sparks, Technical Report ARL-TR-82-51, Applied Research Laboratories, The University of Texas at Austin, 5 October 1982 (AD A120817).
14. Honma, H., and Glass, I. I.: Weak Spherical Shock-Wave Transitions of N Waves in Air With Vibrational Excitation, *Proc. R. Soc. Lond. A*, vol. 391, 1984, pp. 55-83.
15. Cheng, S. T. W., Jones, M. R., Blackstock, D. T., and Wright, W. M.: Focusing of an N Wave by an Ellipsoidal Reflector: an Experiment in Air, *J. Acoust. Soc. Am.*, vol. 85, S113, 1989.
16. Cornet, E. P.: Focusing of an N Wave by a Spherical Mirror, Technical Report ARL-TR-72-40, Applied Research Laboratories, The University of Texas at Austin, 19 September 1972 (AD 157035).

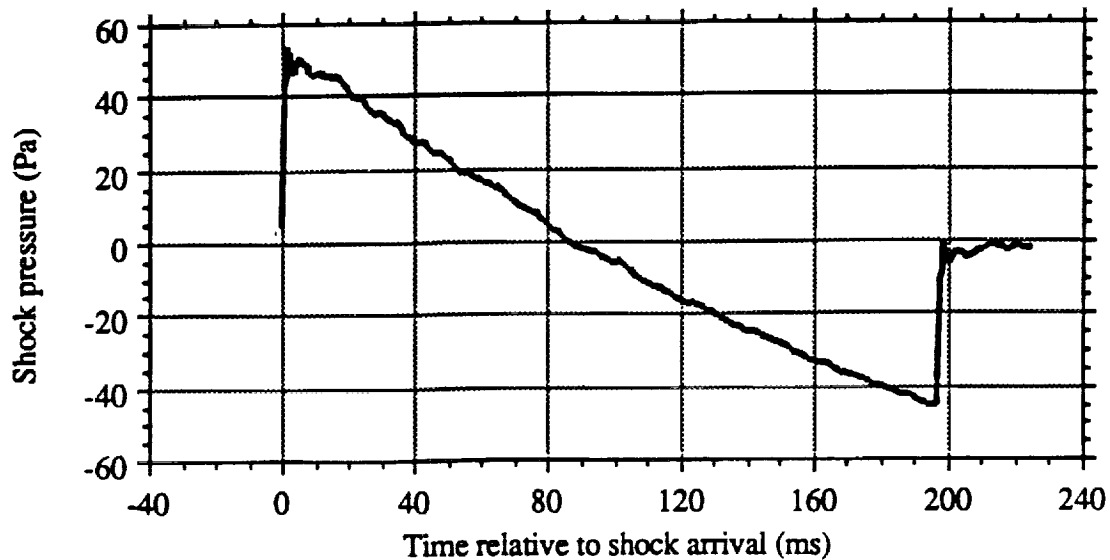


Figure 1. Typical pressure waveform of a sonic boom generated by an SR-71 airplane flying at a Mach number of 2.6 and at an altitude of 20 km: (a) plot of the waveform for its entire duration; (b) detailed profile of the first 8 ms of the waveform (from Kang⁴).

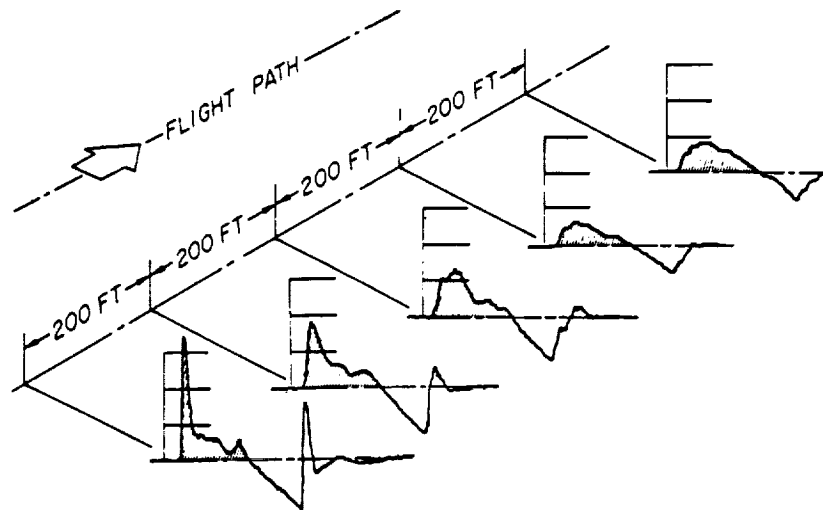


Figure 2. Measured sonic boom pressure signatures at several points on the ground track of a fighter aircraft in steady-level flight at a Mach number of 1.7 and an altitude of 28,000 feet. The change in waveform is attributed to atmospheric inhomogeneities (from Maglieri³).

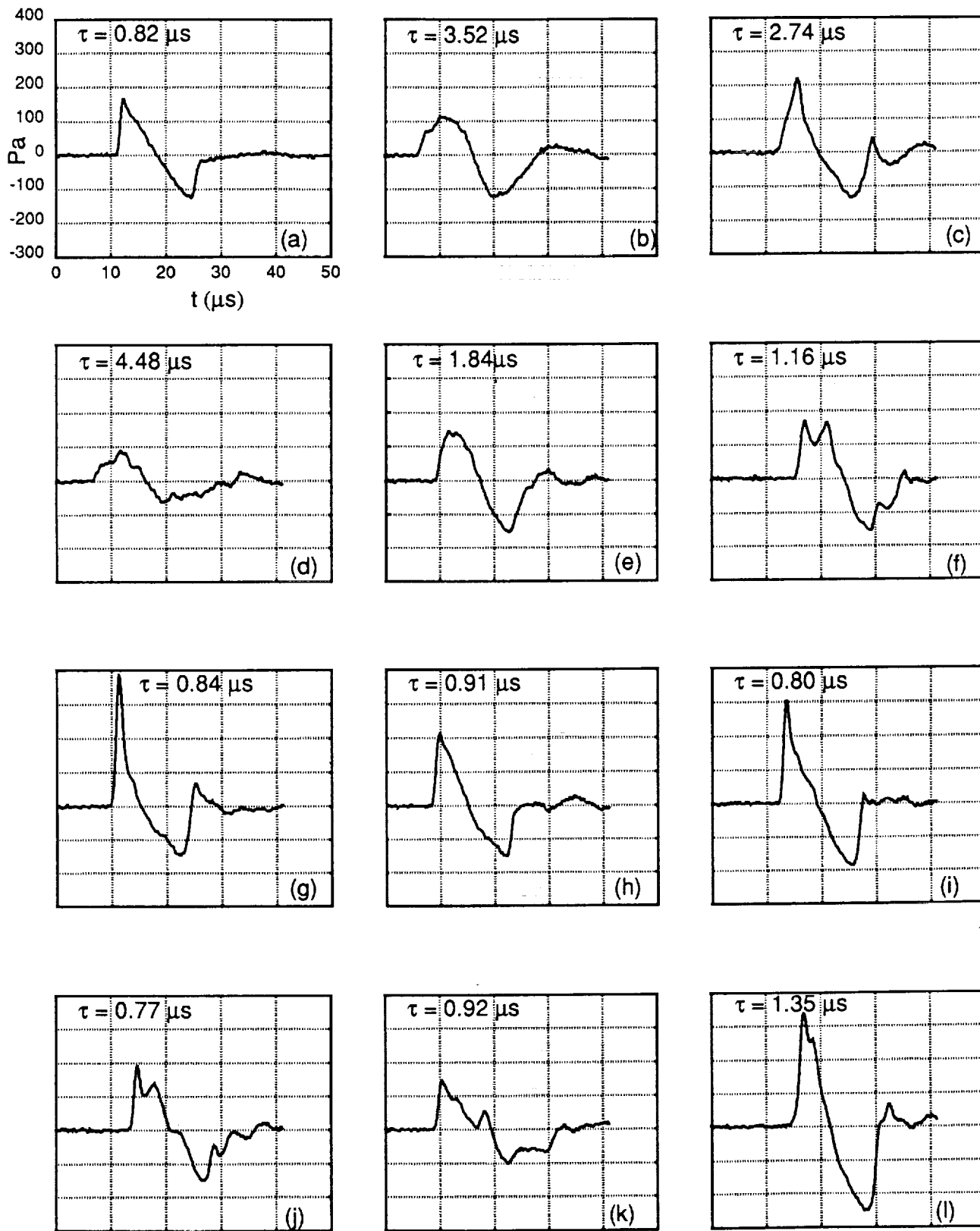


Figure 3. Waveforms of spherical N waves : (a) without turbulence, (b)-(l) with turbulence.

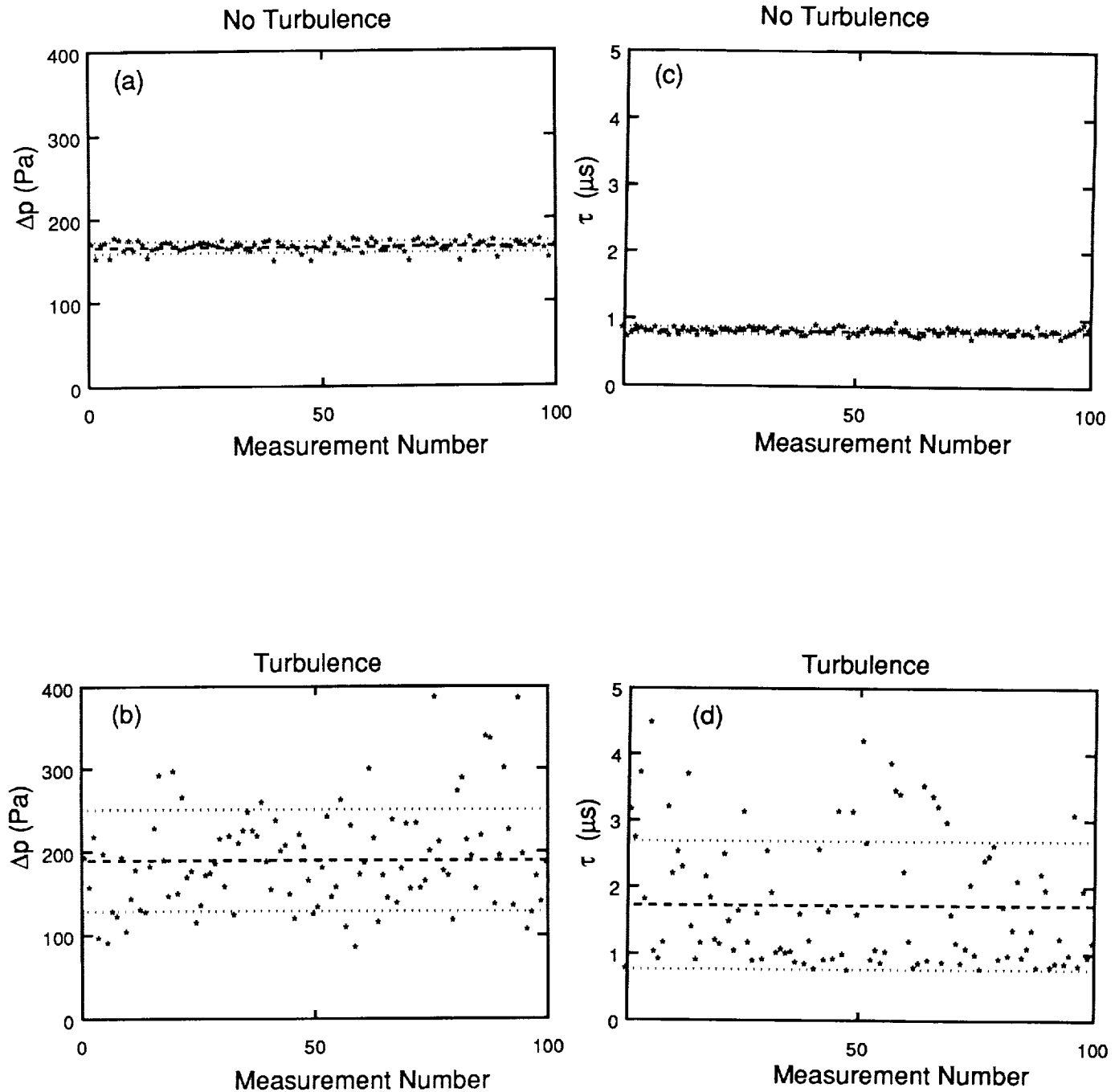


Figure 4. Comparison of peak overpressure, (a)-(b) and rise time, (c)-(d) for 100 N waves with and without turbulence.

--- average value
 average value $\pm \sigma$

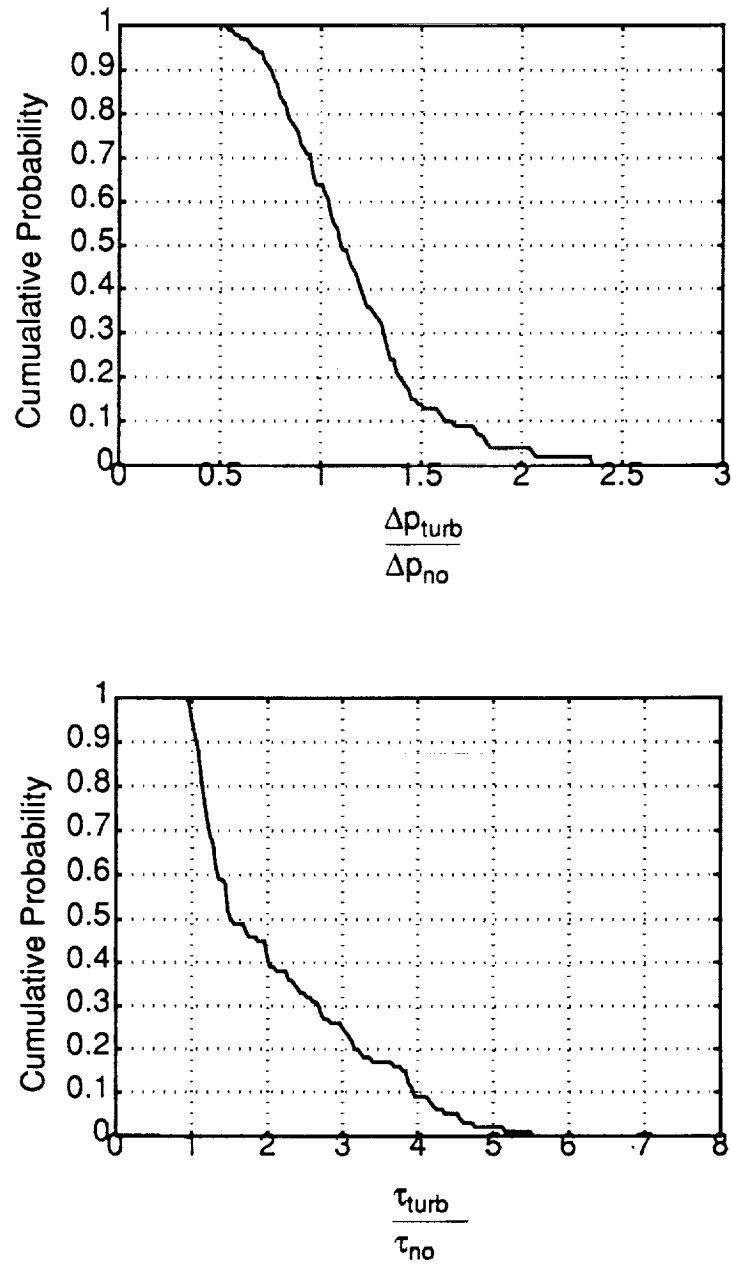


Figure 5. Cumulative probability curve of rise time and peak overpressure.

STEADY STATE RISETIMES OF SHOCK WAVES IN THE ATMOSPHERE

Richard Raspet, Henry Bass, and Lixin Yao

Department of Physics and Astronomy

University of Mississippi

University, MS 38677

Wenliang Wu

Department of Electrical Engineering

University of Mississippi

University, MS 38677

SUMMARY

A square wave shape is used in the Pestorius algorithm to calculate the risetime of a step shock in the atmosphere. These results agree closely with steady shock calculations. The healing distance of perturbed shocks due to finite wave effects is then investigated for quasi-steady shocks. Perturbed 100 Pa shocks require on the order of 1.0 km travel distance to return to within 10% of their steady shock risetime. For 30 Pa shocks the minimum recovery distance increases to 3.0 km. It is unlikely that finite wave effects can remove the longer risetimes and irregular features introduced into the sonic boom by turbulent scattering in the planetary boundary layer.

INTRODUCTION

In a previous paper¹ we compared the risetimes calculated by the enhanced Pestorius^{2,3,4} algorithm with risetimes calculated using the augmented Burger's^{5,6,7} equation under the assumption of a steady step shock. Good agreement was obtained if the N-wave used in the enhanced Pestorius algorithm had a duration on the order of 100 times the risetime.

Sparrow⁸ has applied his numerical method for general finite amplitude wave propagation to the propagation of square pulses as displayed in Fig. 1. These pulse shapes are particularly useful for performing the comparison described in Ref. 1 since the shock front is a better approximation of a steady

shock than a long duration N-wave. In addition, if the calculation is performed without geometric spreading, the shock overpressure will remain constant until the central linear position of the wave is convected to the shock front (see Fig. 1). t_a may be calculated using weak shock consideration as

$$t_a = \frac{\rho c^2 T_0}{4\beta P_0} \quad (1)$$

where P_0 is the overpressure, T_0 is the duration, c is the speed of sound, ρ is the density of air, and $\beta = 1.2$.

We have also used this waveform to investigate the distance a perturbed shock must propagate before its risetime approaches its steady state value. Plotkin and George⁹ suggest that finite wave effects might significantly shorten the risetimes after scattering has initially increased them.

CALCULATIONS

The numerical algorithm which includes vibrational relaxation absorption and dispersion³ was applied to the square wave form displayed in Fig. 1. The initial rise portion of the wave was modeled by a hyperbolic tangent as illustrated in Fig. 2 for the initial wave shape. This rise shape is the solution to the Burger's equation for a steady shock in a non-relaxing media.

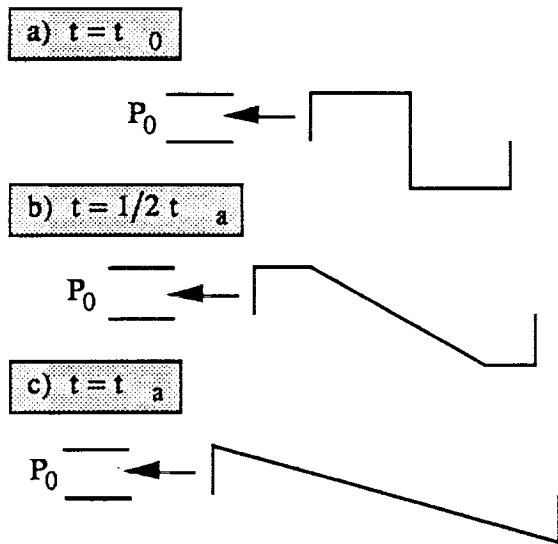


Figure 1. Square shock propagation without geometric spreading.

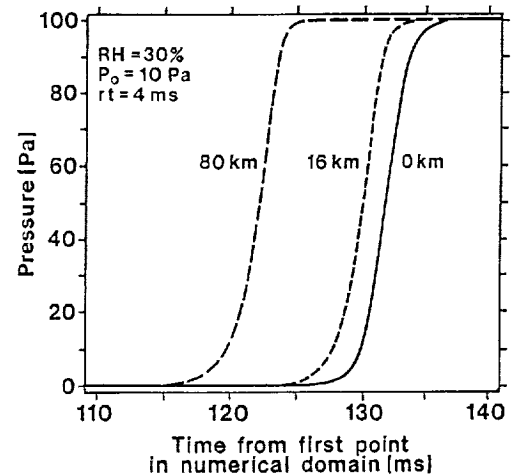


Figure 2. Development of the shock front with distance for a square wave with a 10 Pa overpressure at 295°K and a relative humidity of 30%.

For all calculations the 250 ms duration waveform is embedded in 125 ms of zeroes in front of and behind the pulse to allow for non-linear duration changes and to minimize sampling errors. 8192 points are used to assure that the rise portion of the wave contains sufficient points to model the physical properties accurately. We note that 8192 points were only required for 100 Pa overpressure waves but this number of points was used in all calculations.

RISETIME OF STEADY SHOCKS

The numerical algorithm was started with a hyperbolic tangent rise portion with a best guess risetime for three steady state overpressures (100, 30 and 10 Pa), two relative humidities (30% and 10%) and a temperature of 295°K. These conditions were chosen for comparison with Kang and Pierce's calculations^{6,7} and with our earlier work with non-steady shocks² in the atmosphere. The shocks were propagated until a steady risetime was achieved.

In some cases the wave had to be propagated extreme distances to achieve an equilibrium risetime since the rise shape was quite different from the initial hyperbolic tangent. We will discuss this in more detail in the next section.

Table I contains the risetimes computed from the enhanced Pestorius algorithms with results read from Fig. 5.12 of Kang's dissertation. These values are read from a log-log scale and are only accurate to two significant digits.

Table I. Comparison of rise times computed using a square wave in the enhanced Pestorius algorithm with Kang's steady state calculations.

	Pressure	Risetime (ms)	
		square wave	steady state
<hr/>			
10% Relative Humidity	100 Pa	1.00	1.10
	30 Pa	3.90	4.70
	10 Pa	11.80	13.60
30% Relative Humidity	100 Pa	0.45	0.34
	30 Pa	1.40	1.60
	10 Pa	4.10	4.90

The two results agree within about 20%, confirming the validity of both methods as means of estimating the risetimes of steady shocks. This relatively good agreement is in contrast to the comparison of the steady state risetimes with the risetime of spherically decaying relatively short duration explosion waves calculated using the enhanced Pestorius algorithm. The risetimes of the spherically decaying short duration waves are significantly shorter than the square wave or steady state risetimes.

HEALING DISTANCE OF PERTURBED WAVES

Square pulses were started with a range of risetimes about the equilibrium risetimes listed in Table I. All waves had a hyperbolic tangent rise function. Figure 3 displays the results for 30% relative humidity and 30 Pa overpressure. The pulse started with a 1.5 ms risetime, dips to a lower risetime, then approaches a 1.4 ms risetime. The pulse started at 1.0 ms has a risetime within 0.1 ms of the 1.5 ms risetime pulse after propagating about 2.5 km, while the pulse started at 2.0 ms is within 0.1 ms after 4.0 km.

The healing distance is longer for atmospheric conditions with larger attenuation. The 30 Pa pulses with a 10% relative humidity started with 4.0 ms and 3.5 ms risetimes which agree within 0.1 ms by 10 km; pulses started at 4.5 ms and 4.0 ms are within 0.1 ms at 12 km. The behavior of the risetime versus distance for different starting risetimes is displayed in Fig. 4.

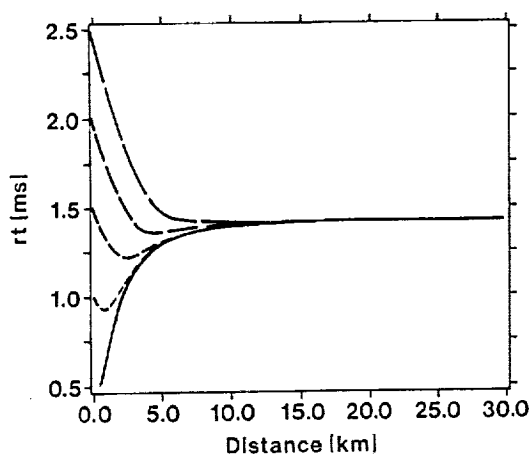


Figure 3. Development of risetime for a 30 Pa overpressure shock wave for $T=295^{\circ}\text{K}$ and a relative humidity of 30%.

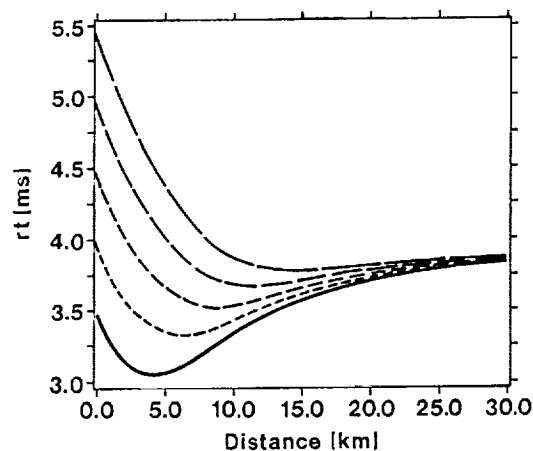


Figure 4. Development of risetime for a 30 Pa overpressure shock wave for $T=295^{\circ}\text{K}$ and a relative humidity of 10%.

The dip in risetime displayed in Figs. 3 and 4 occurs because the steady state rise function does not resemble a hyperbolic tangent function. Figure 5 displays the behavior of the risetime for the case which displayed the largest relative decrease in risetime. The risetime for the 10% relative humidity case at 100 Pa drops from 1.0 ms to 0.5 ms, then rises to 1.0 ms at a distance of 5 km. The development of the rise function with distance for this case is shown in Fig. 6. The 1.0 ms risetime at 5.0 km is determined principally by the foot of the wave. This portion of the wave is due to velocity dispersion caused by molecular relaxation. This time development of the wave shape should be contrasted with Fig. 2, where the final waveform approximates the hyperbolic tangent function.

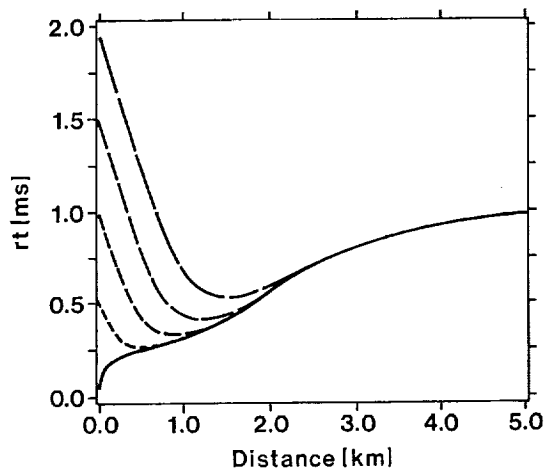


Figure 5. Development of risetime for a 100 Pa overpressure shock wave for $T=295^{\circ}\text{K}$ and a relative humidity of 10%.

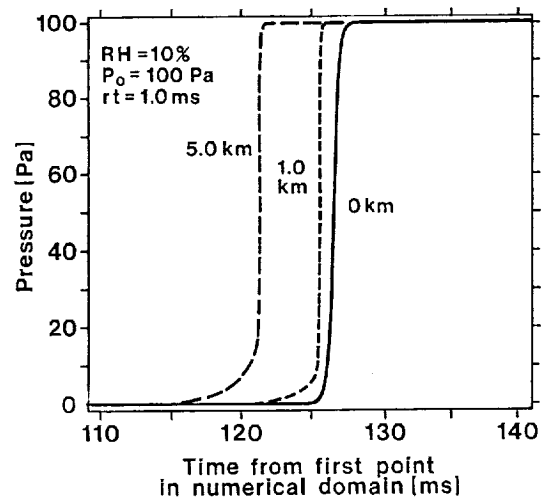


Figure 6. Development of the shock front with distance for a square wave with 100 Pa overpressure at 295°K and a relative humidity of 10%.

Table II contains a chart of the approximate healing distance for a shock risetime perturbed by 0.5 ms to return to within 0.1 ms of a shock started with the correct risetime (but not the final rise shape). These distances are an average of the distance for a pulse started with the equilibrium risetime plus 0.5 ms and a pulse started with the equilibrium risetime minus 0.5 ms.

Table II. Approximate healing distance for different shocks perturbed by .5 ms in risetime

RelativeHumidity	Pressure	Distance (km)
10%	100	0.8
	30	10.0
	10	70.0
30%	100	0.8
	30	3.0
	10	35.0

CONCLUSION

The enhanced Pestorius algorithm applied to square pulses agrees closely with steady shock calculations of risetimes. The use of the square pulse is convenient for comparisons.

The square pulses were also used to examine the finite wave healing of perturbed pulses. This rough calculation shows that if scattering in the planetary boundary layer induces a longer risetime in a sonic boom, the longer risetime will still be present at the ground. Finite wave calculations on the scattered waveforms predicted by Yao¹⁰ will be performed in the near future.

Another implication of the large healing distance is that atmospheric conditions at higher altitudes may determine quiet atmosphere risetimes at the ground.

REFERENCES

1. Richard Raspet and Henry E. Bass, "Comparison of sonic boom risetime prediction techniques," 13th Aeroacoustics Conference of the American Institute of Aeronautics and Astronautics, Tallahassee, FL, October 1990.
2. Henry E. Bass and Richard Raspet, "Vibrational relaxation effects on the atmospheric attenuation and risetimes of explosion waves," *J. Acoust. Soc. Am.* 64, 1208–1210 (1978).
3. Henry E. Bass, Jean Ezell and Richard Raspet, "Effect of vibrational relaxation on risetimes of shock waves in the atmosphere," *J. Acoust. Soc. Am.* 74, 1514–1517 (1983).
4. Henry E. Bass, Bruce A. Layton, Lee N. Bolen, and Richard Raspet, "Propagation of medium strength shock waves through the atmosphere," *J. Acoust. Soc. Am.* 82, 306–310 (1987).
5. Allan D. Pierce, "Weaker sonic booms may be considerably more quiet," *J. Acoust. Soc. Am.* 86, S30 (1989).
6. Jongmin Kang and Allan D. Pierce, "Propagation of nonlinear transients, such as sonic booms, through an absorbing and relaxing atmosphere," *J. Acoust. Soc. Am.* 85, S81 (1989).
7. Jongmin Kang, "Nonlinear acoustic propagation of shock waves through the atmosphere with molecular relaxation," a dissertation in Mechanical Engineering, The Pennsylvania State University, May 1991.

8. Victor W. Sparrow, "Time domain computations in nonlinear acoustics without one way assumptions," 3rd IMACS Symposium on Computational Acoustics, Boston, MA, 26–28 June.
9. K.J. Plotkin and A.R. George, "Propagation of weak shock waves through turbulence," J. Fluid Mech. 54, 449–467 (1972).
10. Lixin Yao, Henry E. Bass and Richard Raspet, "A statistical study of the relaxation between weather conditions and sonic boom waveforms," J. Acoust. Soc. Am. 89, S1 (1991).

**LATERAL SPREAD OF SONIC BOOM MEASUREMENTS FROM US AIR FORCE
BOOMFILE FLIGHT TESTS**

**J. Micah Downing
Armstrong Laboratory
Wright-Patterson Air Force Base, OH**

SUMMARY

A series of sonic boom flight tests were conducted by the US Air Force at Edwards AFB in 1987 with current supersonic DOD aircraft. These tests involved 43 flights by various aircraft at different Mach number and altitude combinations. This paper compares the measured peak overpressures to predicted values as a function of lateral distance. Some of the flights are combined into five groups because of the varying profiles and the limited number of sonic booms obtained during this study. The peak overpressures and the lateral distances are normalized with respect to the Carlson method predicted centerline overpressures and lateral cutoff distances, respectively, to facilitate comparisons between sonic boom data from similar flight profiles. This paper demonstrates that the data obtained in this study agrees with sonic boom theory and previous studies and adds to the existing sonic boom database by including sonic boom signatures, tracking, and weather data in a digital format.

INTRODUCTION

In 1987, the Armstrong Laboratory of the US Air Force conducted a sonic boom measurement study at Edwards Air Force Base. This study had three basic goals. The first goal was to collect reference sonic boom signatures for the current inventory of DOD supersonic aircraft. The second goal was to perform the

first complete field test of the newly developed unmanned Boom Event Analyzer Recorder (BEAR)^{1,2}, which records the full sonic boom waveform in a digital format. The third goal was to measure the lateral spread of the sonic boom carpet and capture full sonic boom signatures near lateral cutoff. This paper involves the third aspect of this study by comparing the lateral spread of the sonic booms to predicted values. Several previous studies have measured the lateral spread of sonic booms ³⁻¹⁰. This study enhances the results of the earlier studies by including weather and tracking data along with full sonic boom waveforms. All of these data are stored in a digital format and are available upon request from the Noise Effects Branch of the Armstrong Laboratory (AL/OEBN Area B Bldg 441, Wright-Patterson AFB, Ohio 45433, (513)255-3664).

TEST DESCRIPTION

The tests consisted of near steady supersonic flights at various Mach number and altitude combinations by various aircraft¹¹. Table 1 lists the flights performed during this study along with the aircraft and the nominal flight conditions (i.e., Mach number and altitude). The sonic booms were measured by a monitor array which consisted of 13 BEAR units and 9 modified dosimeters. Figure 1 displays the layout of the test area along with the target ground track and monitor locations. The lateral portion of the array was 24 miles in length. The target intersection between the flight tracks and the array separated the array into two sections. One section extended 6 miles north of the targeted flight track, and the other section extended 18 miles south. The actual flight track intersections with the array, which are provided in Table 1, were scattered along the array by up to 4 miles from the targeted intersection. The actual Mach number and altitude profiles were also scattered about the targeted conditions. Weather and tracking data were obtained during the study. The weather data include three daily

rawinsonde launches and ground station observations which obtained temperature, pressure, dew point, relative humidity, and wind data. Tracking data, obtained for all but three flights, include ground position, altitude, Mach number, climb angle, and heading angle. These supporting data help to identify the actual conditions under which the sonic booms were generated, propagated, and measured.

Table 1. BOOMFILE Flight Conditions Summary

		FLIGHT TRACK		MACH	ALTITUDE	BOOM AT SITE 00	FLIGHT #	
DATE	AIRCRAFT	INTERSECTION	NUMBER	(Ft MSL)		(Local Time)	AND GROUP	
31 JUL 87	F-4	57.8	1.20	16000		08:41:20	1 C	
03 AUG 87	F-4	60.1	1.24	29200		07:48:33	2 B	
	F-4	60.6	1.29	29300		07:58:33	3 B	
	F-4	53.6	1.10	13000		08:08:04	4	
	F-4	59.2	1.10	14400		10:29:59	5 D	
	F-4	61.3	1.37	44400		10:43:22	6 A	
	T-38	58.6	1.00	13600		10:05:35	7	
	T-38	56.0	1.10	13000		10:12:15	8	
	T-38	59.5	1.11	29600		12:28:18	9	
	T-38	60.5	1.05	21200		12:38:17	10	
04 AUG 87	AT-38	60.0	1.17	41400		07:19:41	11	
	AT-38	60.0	1.12	32300		07:30:09	12	
	AT-38	63.0	1.15	16700		07:36:46	13	
	AT-38	59.6	1.20	30300		09:14:06	14	
	AT-38	59.0	1.10	14000		09:23:15	15	
	F-15	61.5	1.38	41400		07:56:42	16	
	F-15	60.3	1.20	29700		08:04:06	17	
	F-15	60.6	1.10	12500		08:10:13	18 D	
	F-15	60.0	1.13	15200		10:46:15	19 D	
	F-15	59.0	1.28	31000		11:02:18	20 B	
	F-15	64.0	1.42	45000		11:11:28	21 A	
	F-15	60.0	1.40	45500		11:34:21	22 A	
	05 AUG 87	F-16	57.0	1.25	29500		09:06:05	23 B
		F-16	60.0	1.43	46700		09:33:54	24 A
F-16		58.8	1.17	19300		09:44:51	25	
F-16		59.5	1.13	14400		11:44:24	26 D	
F-16		60.6	1.12	13800		11:54:39	27 D	
F-16		60.5	1.25	30000		12:04:46	28 B	
SR-71		60.8	2.50	64800		09:26:12	29 E	
SR-71		59.8	3.00	73000		10:55:12	30 E	
SR-71		59.4	1.23	32400		11:08:38	31	
SR-71		62.0	1.70	52000		12:35:51	32 E	
06 AUG 87	F-18	60.0	1.30	30000		07:44:12	33 B	
	F-18	59.6	1.40	44700		07:57:05	34 A	
	F-18	58.0	1.10	14200		08:10:36	35 D	
	F-18	59.8	1.30	30000		10:22:47	36 B	
	F-18	59.8	1.43	45000		10:34:14	37 A	
	F-18	59.8	1.10	13000		10:48:38	38 D	
	F-14	56.2	1.20	31500		08:28:45	39	
	F-14	62.0	1.27	16500		10:43:43	40 C	
	F-111F	59.8	1.20	14000		11:48:18	41 C	
07 AUG 87	F-111F	59.8	1.40	45000		12:04:44	42 A	
	F-111	58.3	1.25	29900		10:50:26	43 B	

COMPARISON OF THE PEAK OVERPRESSURES

Comparisons of the measured overpressures to Carlson predictions¹² are done in two ways to relate this new database to previous efforts. First, the overall peak overpressures obtained from the BEAR units are compared to predictions. Second, the data is divided into five selected groupings of the flights to facilitate a better comparison of the lateral spread of the measured data to the predicted values.

Overall Comparison of the Peak Overpressures

As in previous studies^{5,7,8,10}, the ratio of measured peak overpressures to predicted is used to derive a probability curve for the data. This curve demonstrates the expected normal variation of sonic boom overpressures due to atmospheric effects which can cause rounded and peaked N-wave signatures¹³⁻¹⁵. This curve estimates the probability that a given sonic boom overpressure will exceed a certain value. The calculated values were evaluated by Carlson's method with a 1972 U.S. Standard Model Atmosphere. This ratio allows the various peak overpressures to be combined without any restriction to aircraft shape, Mach number, and altitude. The peak overpressure data is divided into two groups by their lateral propagation distance. The selected division point is 50% of the calculated lateral cutoff point, dyc. In this database there are 278 valid data points in the < 50% of dyc group and 91 valid points in the > 50% of dyc group. This grouping excludes 24 points where no measured values were obtained and 70 points where signatures were measured beyond the predicted lateral cutoff. Some of these signatures obtained beyond dyc are reduced overpressure N-waves, while others may be classified as rumble waves. Figure 2 shows the probability curves for the two groups along with their histograms in terms of the measured to predicted ratio. The two probability curves and histograms agree with those given for previous sonic boom measurement studies^{5,7,8,10}. The curve for data points <

50% of dyc lies in a straight line in the region about a ratio of 1.0 and flattens as the two extremes are reached. The 50% probability point corresponds to a ratio of 0.83 which means the predictions are, in general, overestimating the peak overpressures. The curve for the > 50% of dyc group is shifted to the left and tends to flatten sooner. This shift indicates that the calculated values are overestimating the actual measurements to a greater extent in this region. In both curves the flattened portion may be attributed to the limited number of data points used to derive the curves. This simple analysis demonstrates that this sonic boom database agrees well with past sonic boom measurements, even though this database is much smaller. In addition, this database confirms the trend that theory tends to overpredict the overpressure as the lateral distance approaches the predicted cutoff point^{5,8}.

Comparison of Peak Overpressure vs Lateral Distance

The following analysis is meant to highlight some of the data contained within the BOOMFILE database. This comparison will examine more closely the lateral spread of the sonic boom overpressures. Some of the flights are combined into groups to collapse the limited data. Twenty-eight of the flights are separated into five groups according to their nominal flight conditions in the following Mach number-altitude combinations: A) 1.4 M at 45 kFt, B) 1.25 M at 30 kFt, C) 1.18 M at 16 kFt, D) 1.1 M at 14 kFt, and E) SR-71 at Mach numbers greater than 1.5. This grouping of flights are also noted in Table 1. The peak overpressure data, measured and predicted, are combined by normalizing the overpressure and the lateral propagation distance. The peak overpressures are normalized by the predicted centerline overpressure, and the lateral distances are normalized with respect to the predicted lateral cutoff. The predictions use the actual flight conditions as listed in Table 1. This procedure allows the limited data from this study to be combined for better comparison of the lateral spread of the boom carpet

and analysis between the various flights performed during this test. From the probability curves, measured values should be overestimated as the lateral distance approaches dyc.

Comparison of Group A Overpressures

Figure 3 displays the peak overpressures as a function of lateral distance for Group A flights, whose nominal flight conditions are around 1.4 M at 45 kFt MSL. For points < 50% of dyc, the measured overpressures are scattered about the predicted value, but for points > 50% of dyc, the measured values fall below predictions as expected from the probability analysis shown in Figure 2. In Figure 3 an amplified peak overpressure is highlighted with a normalized overpressure of 2.4 at the centerline of the boom carpet. This boom was generated by an F-4 operating at 1.37 M at 44.4 kFt MSL (flight #6). Figure 4 shows this sonic boom signature. The signature is not a normal N wave but seems to be a combination NU wave with an increased peak overpressure of over two times the normal N wave peak overpressure. Also, note that the initial shock overpressure of 2 psf from this signature falls within the expected variation about the predicted value of 1.5 psf. Figure 3 also shows a number of points > 50% of dyc where the measured overpressures are much smaller than the predicted value. Figure 5 presents one of these reduced overpressure signatures. This sonic boom signature was generated by an F-15 flying at 1.4 M at 45.5 kFt MSL (flight #22) and measured at a lateral distance of 80% of predicted dyc. This signature retains a basic N-wave shape, but its peak overpressure is much lower than the calculated value. The other signatures in this same region have both normal and rounded N-wave characteristics.

Comparison of Group B Overpressures

The lateral spread of the peak overpressures for flights in Group B with 1.25 M at 30 kFt MSL nominal flight conditions is shown in Figure 6. This figure also demonstrates that near the centerline the overpressures are scattered about the predicted values as expected, but as the lateral distance approaches the cutoff point, the measured overpressures tend to be less than predicted. In this figure, some measured signatures were obtained just beyond dyc, but within an expected variation of dyc, and the overpressures are less than the predicted value at cutoff. Figure 7 displays one of these signatures which was generated by an F-15 flying at 1.28 M at 31 kFt MSL (flight #20). This signature was obtained at an 11 mile lateral distance which was only 6% longer than the predicted dyc. This signature has retained its N-wave shape although it was obtained near the lateral cutoff region. An amplified overpressure of 2.3 is also noted in Figure 6. This amplified boom was generated by an F-18 flying at 1.3 M at 30 kFt MSL (flight #33) and is plotted in Figure 8. This signature contains a double boom signature which has a normal N wave followed by an NU combination wave with an increase in the peak overpressure. The peak overpressure of the first boom agrees with the calculated value, and the second boom appears to be caused by some unsteady aspect of the flight profile. Tracking for this event is provided in Figure 9 and shows that the aircraft had a slight turn as it approached the array which could be the cause of the second, focused boom. This signature was obtained at a lateral offset of 4 miles which was at 40% of the predicted lateral cutoff, yet other measurement sites beyond this point only obtained rumbled signatures even though they were within the predicted dyc. This signature highlights some of the non-normal sonic boom signatures obtained during this study, which need a more thorough analysis to explain and quantify their shapes.

Comparison of Groups C & D Overpressure

For Group C with nominal flight conditions at 1.18 M at 16 kFt MSL, Figure 10 displays the same trend of reduced measurements compared to calculated values as the lateral distances increases, as seen in Figures 3 and 6. Figure 10 also shows that some signatures were collected at points up to 1.8 times the predicted dyc. These signatures beyond dyc are rounded signatures like the one demonstrated in Figure 11. This rumbled signature was produced by an F-111 at 1.2 M at 14 kFt MSL (flight #41) and measured at a lateral distance of 9.8 miles (1.5 dyc). This type of rumbled signature is expected for such long propagation distances beyond dyc. For Group D flights, which have nominal flight conditions at 1.1 M and 14 kFt MSL, more signatures were obtained beyond dyc, as shown in Figure 12. The expected lateral cutoff point for this group is about 4 miles. Most of these signatures are well rounded and barely retained any N-wave characteristics. For these lower and slower flights, the carpet widths are more sensitive to variations in the atmosphere, flight track, and the Mach number. Even with the measured signatures beyond dyc, the trend of overestimating the peak overpressures at the more laterally displaced locations is still present. A more comprehensive analysis on these two groups of flights should lower the uncertainty in predicting lateral cutoff and provide answers to the seemingly long lateral propagation distances evidenced in Figure 12.

Comparison of SR-71 Overpressures

Another comparison is shown for the SR-71 flights which were above 1.5 M. Figure 13 shows that the peak overpressures were consistently overpredicted in this analysis except for one event which is given in Figure 14. This signature was generated at 1.7 M at 52 kFt MSL (flight #32) and exhibits a pronounced peak in the signature. This peak is caused by variations in the

atmosphere since there are corresponding peaks at each shock in the signature. This signature is an example of the peaked signatures that are contained in this database.

CONCLUSION

This paper has set forth to introduce and highlight the sonic boom data obtained by Armstrong Laboratory of the USAF at Edwards AFB in 1987. The sonic boom data is contained in a digital format which can easily be analyzed on a personal computer. Information on the actual local weather conditions and the aircraft tracking are also included in this database. The BOOMFILE database can be requested from the Noise Effects Branch of Armstrong Laboratory (AL/OEBN, Area B Bldg 441, Wright-Patterson AFB, OH 45433, (513)255-3664). Basic analysis of the peak overpressure data demonstrates that they agree with previous sonic boom measurements. Also, this analysis confirms previous findings that the peak overpressure is overestimated as the lateral distance approaches the predicted lateral cutoff point. This overestimation needs to be studied further so that better estimates of peak overpressure and lateral cutoff can be obtained for sideline distances.

REFERENCES

1. R.A. Lee: Air Force Boom Event Analyzer Recorder (BEAR): Comparison with NASA Boom Measurement System. AAMRL-TR-88-039, 1988.
2. R.A. Lee, M. Crabill, D. Mazurek, B. Palmer, and D. Price: Boom Event Analyzer Recorder (BEAR): System Description. AAMRL-TR-89-035, 1989.
3. D.J. Maglieri, T.L. Parrott, D.A. Hilton, and W.L. Copeland: Lateral-Spread Sonic-Boom Ground Pressure Measurements From Airplanes at Altitudes to 75,000 Feet and at Mach Numbers to 2.0. NASA TN D-2021, 1963.
4. D.J. Maglieri, D.A. Hilton, and N.J. McLeod: Experiments on the Effects of Atmospheric Refraction and Airplane Accelerations on Sonic-Boom Ground-Pressure Patterns. NASA TN D-3520, 1966.
5. D.J. Maglieri: Sonic Boom Flight Research--Some Effects of Airplane Operations and the Atmosphere on Sonic Boom Signatures. NASA SP-147, 1967, pp. 25-48.
6. D.J. Maglieri: Sonic Boom Ground Pressure Measurements for Flights at Altitudes in Excess of 70,000 Feet and at Mach Numbers up to 3.0. NASA SP-180, 1968, pp. 29-36.
7. D.J. Maglieri, V. Huckel, H.R. Henderson, and N.J. McLeod: Variability in Sonic-Boom Signatures Measured Along an 8000-Foot Linear Array. NASA TN D-5040, 1969.

8. H.H Hubbard, D.J. Maglieri, and V. Huckel: Variability of Sonic Boom Signatures with Emphasis on the Extremities of the Ground Exposure Patterns. NASA SP-255, 1971, pp. 351-359.
9. G.T. Haglund and E.J. Kane: Flight Test Measurements and Analysis of Sonic Boom Phenomena Near the Shock Wave Extremity. NASA CR D6-40758, 1972.
10. D.J. Maglieri, V. Huckel, and H.R. Henderson: Sonic-Boom Measurements for SR-71 Aircraft Operating at Mach Numbers to 3.0 and Altitudes to 24384 Meters. NASA TN D-6823, 1972.
11. R.A. Lee and J.M. Downing: Sonic Booms Produced by United States Air Force and United States Navy Aircraft: Measured Data. AL-TR-1991-0099, 1991.
12. H.W. Carlson: Simplified Sonic-Boom Prediction. NASA TP-1122, 1978.
13. D.J. Maglieri: Some Effects of Airplane Operations and the Atmosphere on Sonic-Boom Signatures. Proceedings of the Sonic Boom Symposium. JASA, vol. 39, no. 5, part 2, 1966, pp. S36-S42.
14. I.E. Garrick: Atmospheric Effects on the Sonic Boom. NASA SP-180, 1968, pp. 3-18.
15. A.D. Pierce and D.J. Maglieri: Effects of Atmospheric Irregularities on Sonic-Boom Propagation. JASA, vol. 51, no. 2, part 3, 1972, pp. 702-21.

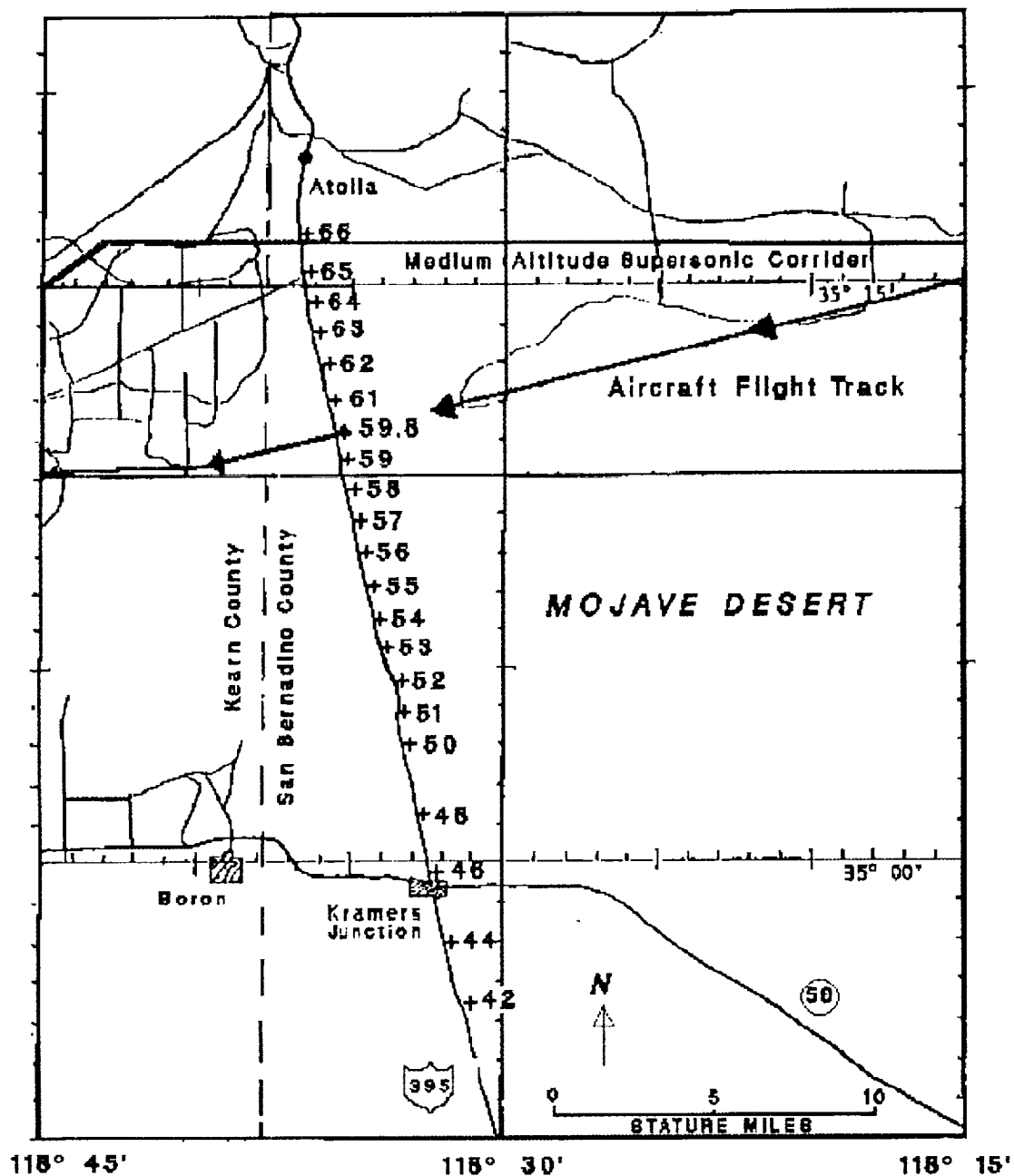


Figure 1. Layout of test area with the target ground track and monitor array.

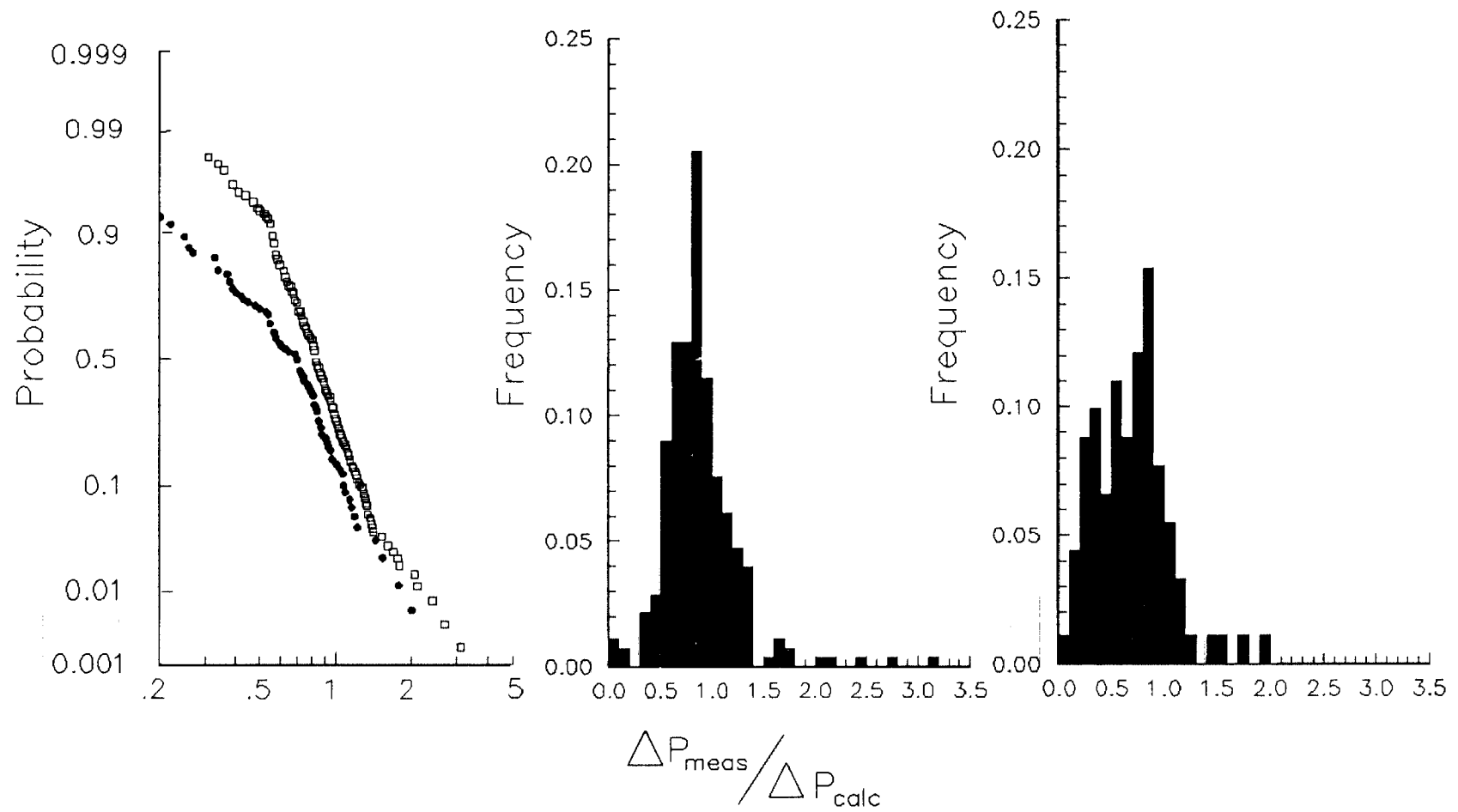


Figure 2. Probability curves and histograms for the ratio of measured to predicted peak overpressures in the BOOMFILE database.

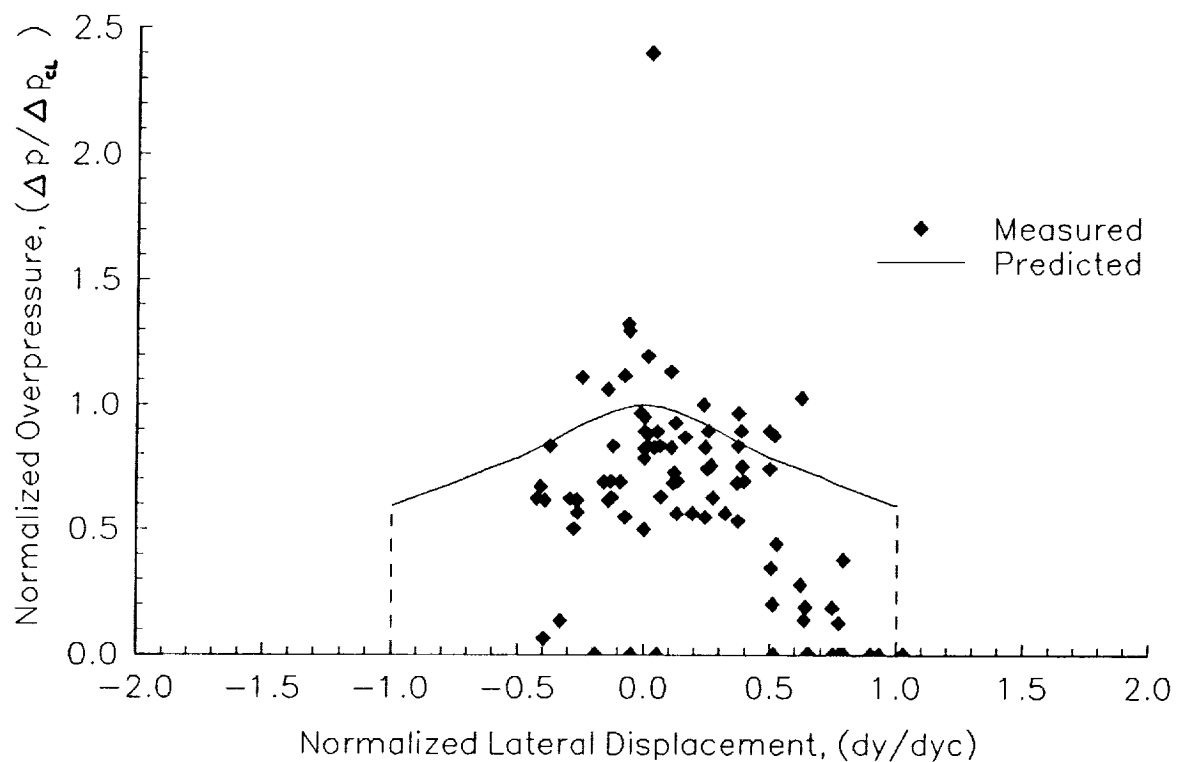


Figure 3. Normalized peak overpressures as a function of the normalized lateral propagation distance for flight with nominal conditions of 1.4 M at 45 kFt MSL.

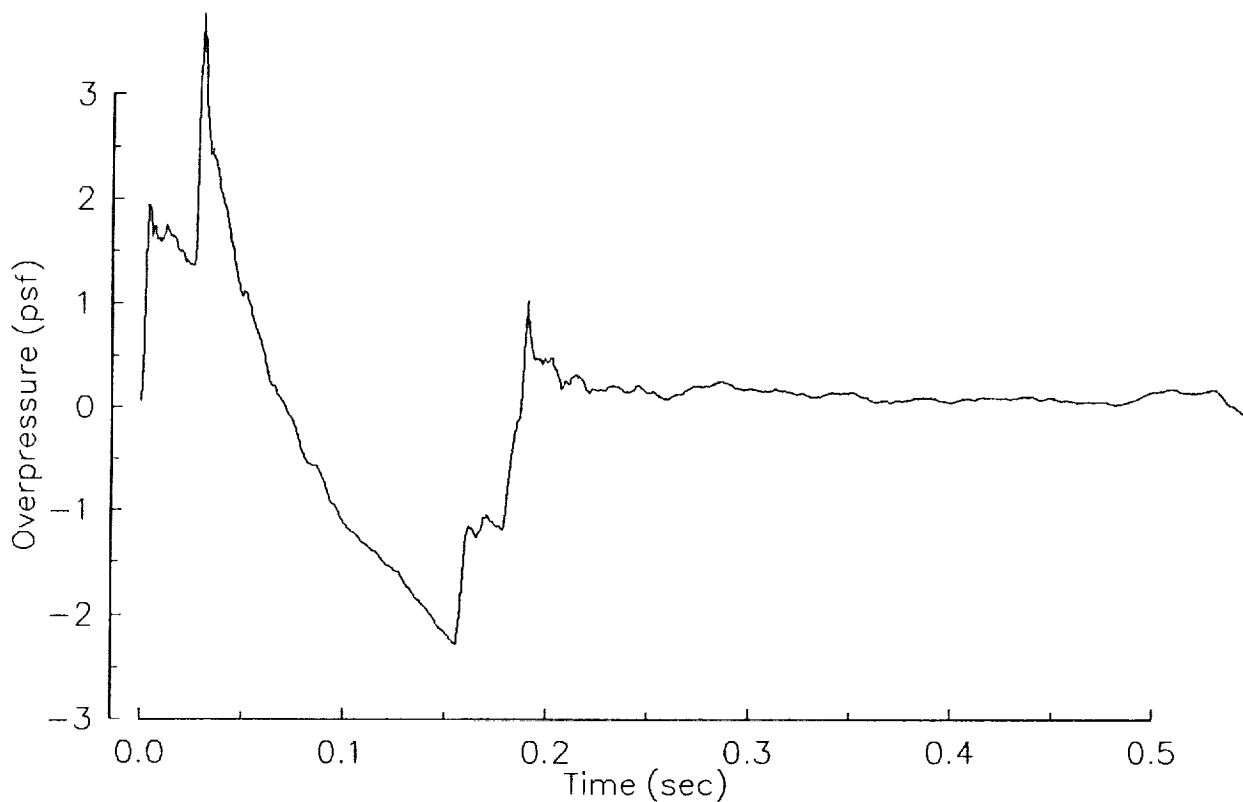


Figure 4. Peaked sonic boom signature generated by an F-4 at 1.37 M at 44.4 kFt MSL (flight #6) measured under the flight track.

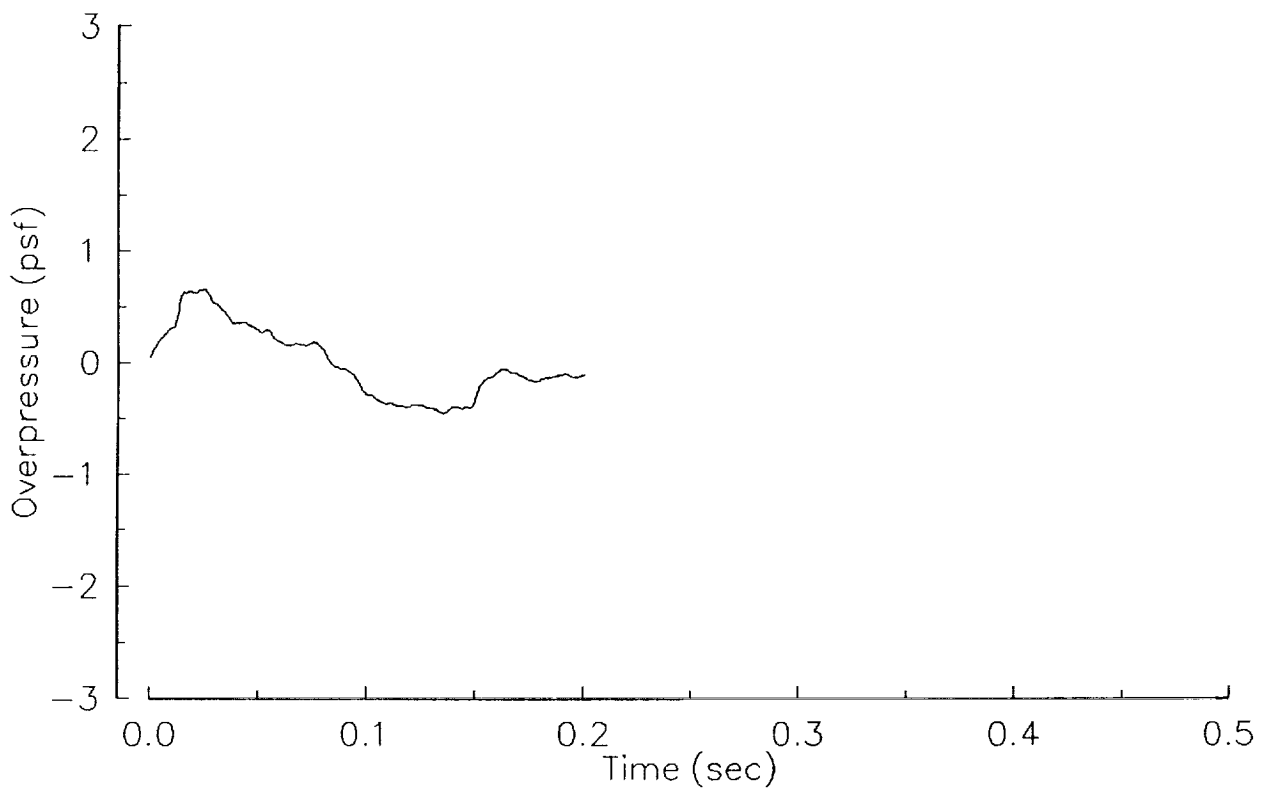


Figure 5. Rounded sonic boom signature generated by an F-15 at 1.4 M at 45.5 kFt MSL (flight #22) measured 12 lateral miles from the flight track.

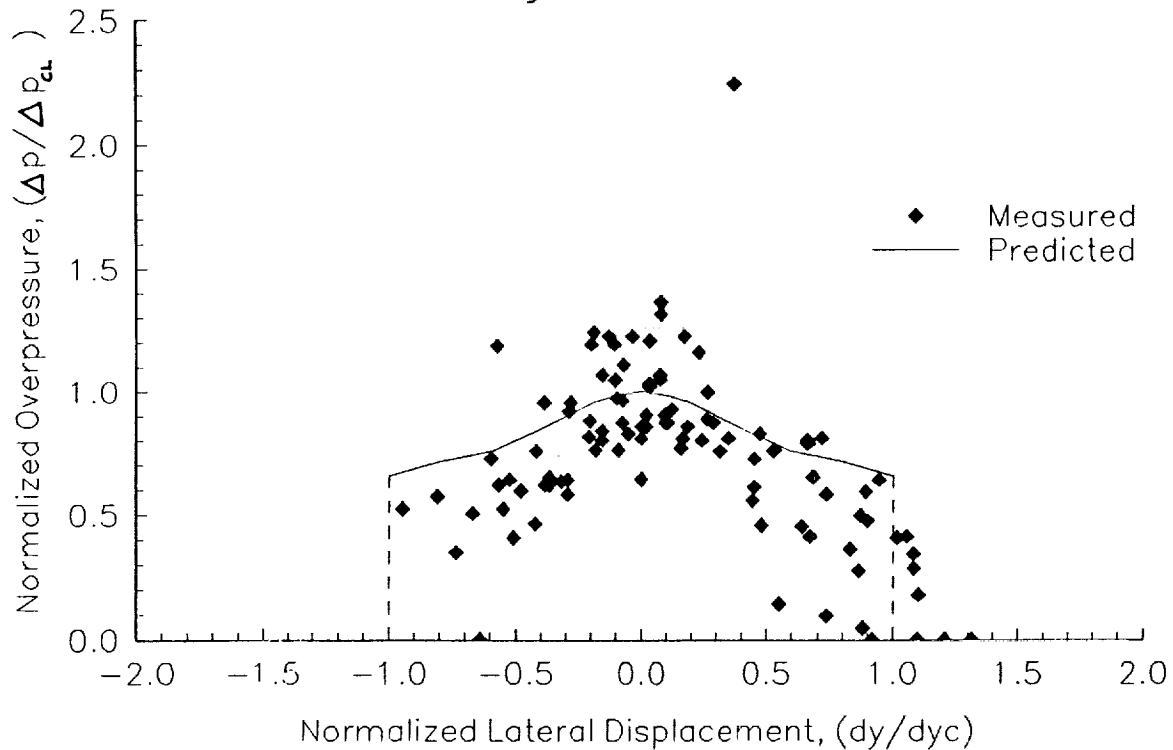


Figure 6. Normalized peak overpressures as a function of the normalized lateral propagation distance for flight with nominal conditions of 1.25 M at 30 kFt MSL.

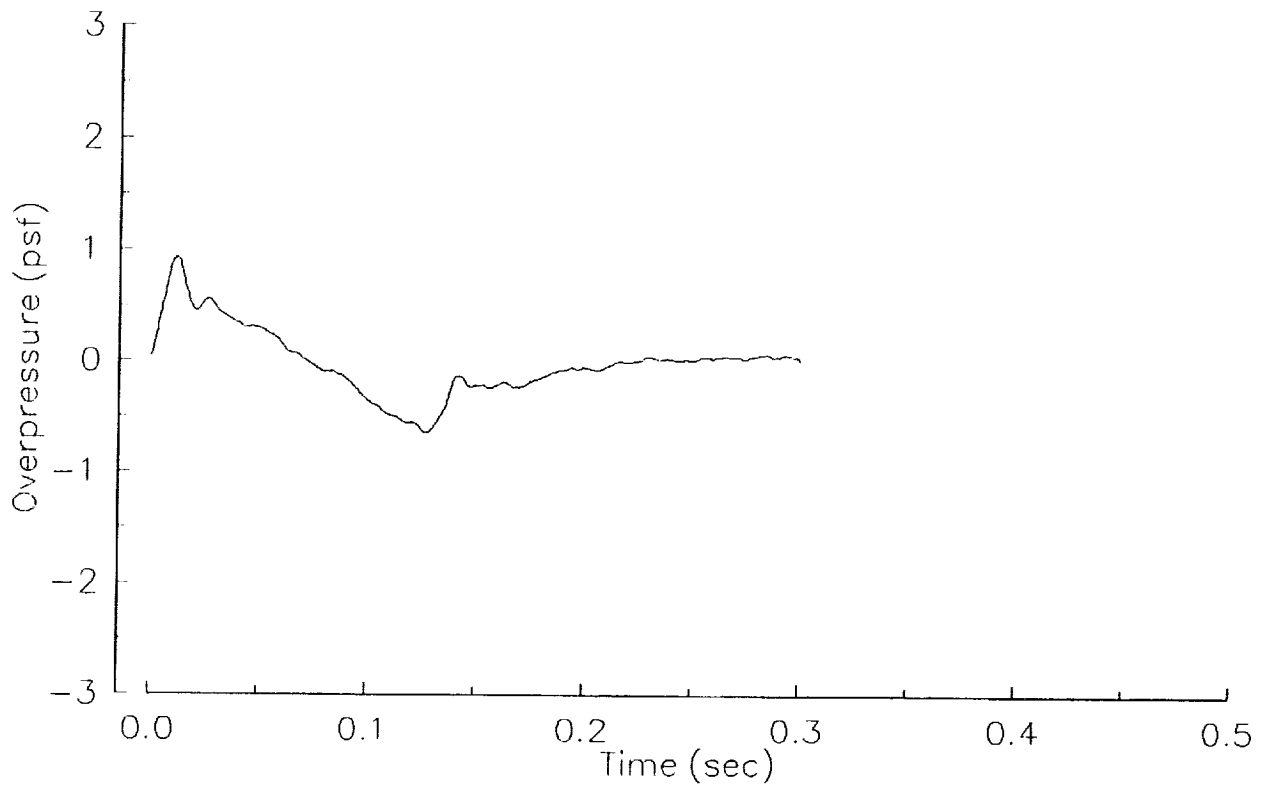


Figure 7. Sonic boom signature near lateral cutoff generated by an F-15 at 1.28 M at 31 kFt MSL (flight #20) measured 11 lateral miles from the flight track.

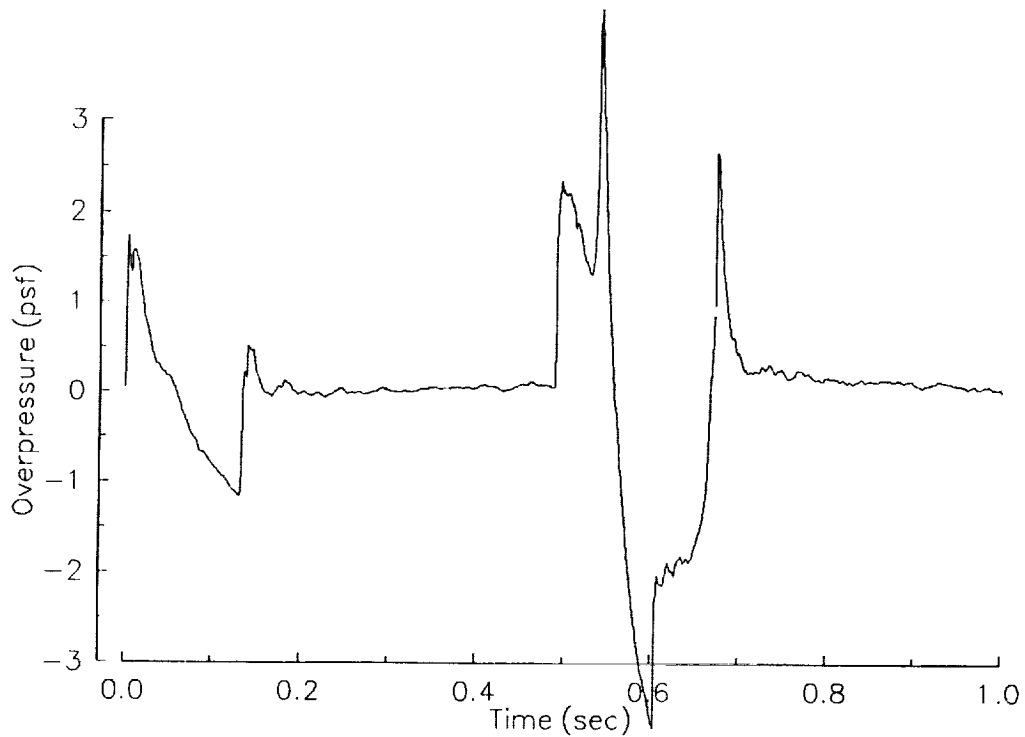


Figure 8. Double sonic boom signature generated by an F-18 at 1.3 M at 30 kFt MSL (flight #33) measured 4 lateral miles from the flight track.

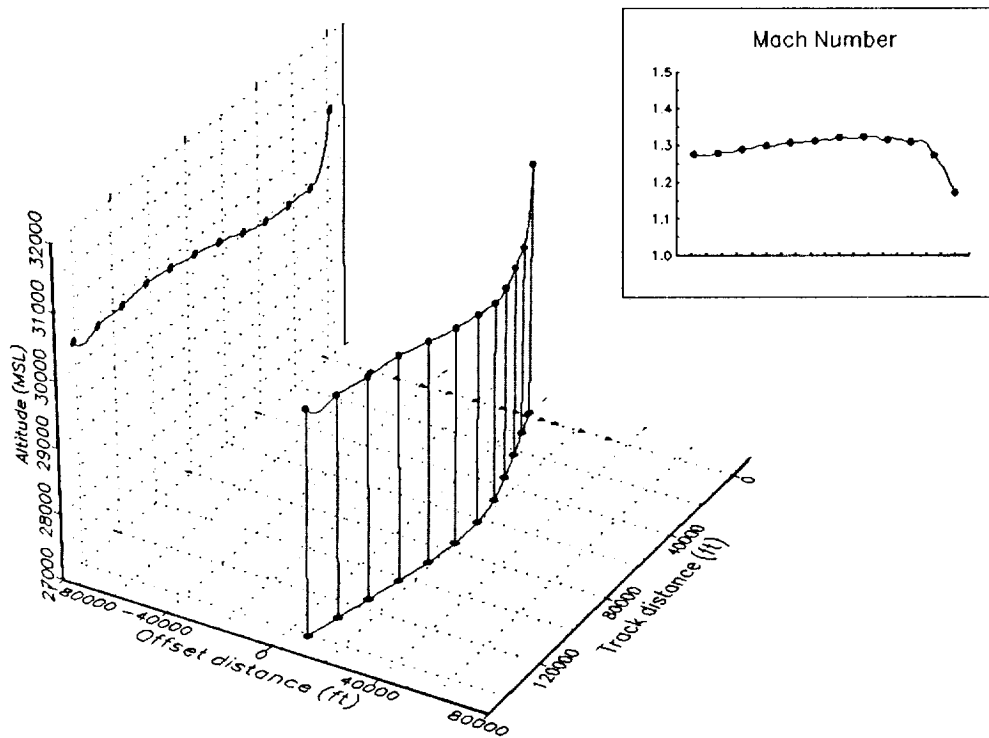


Figure 9. Tracking plot of F-18 flight #33.

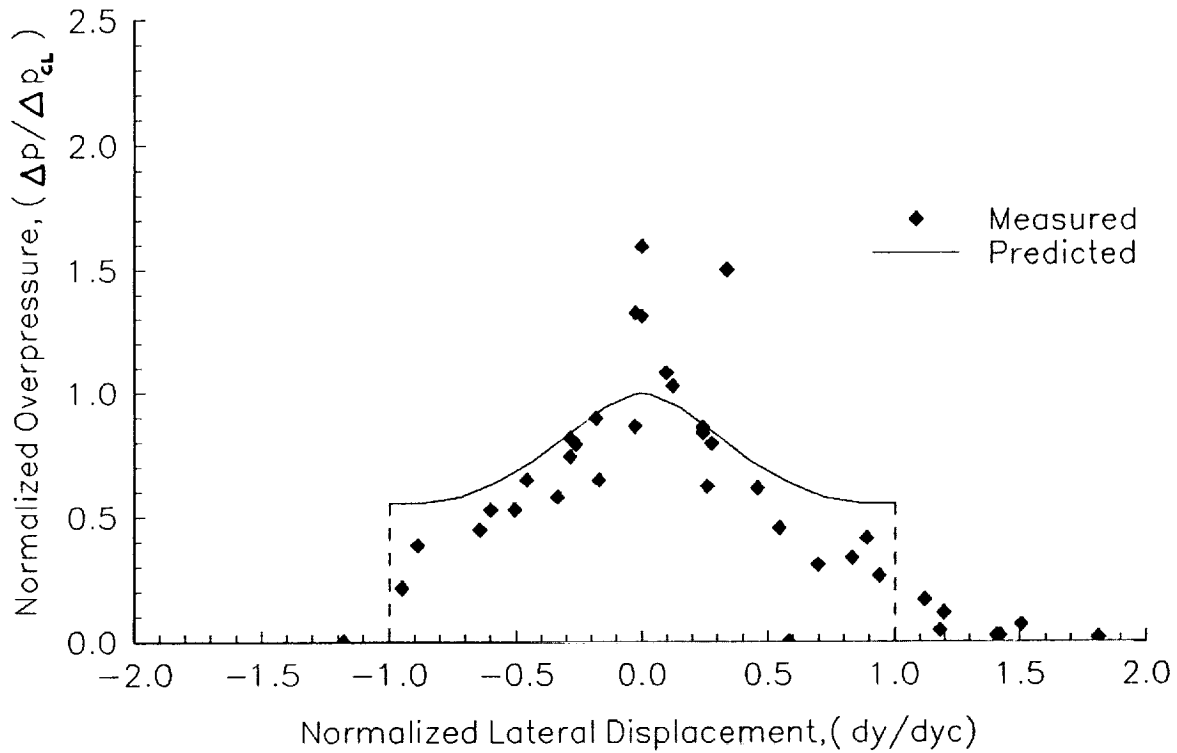


Figure 10. Normalized peak overpressures as a function of the normalized lateral propagation distance for flight with nominal conditions of 1.18 M at 16 kft MSL.

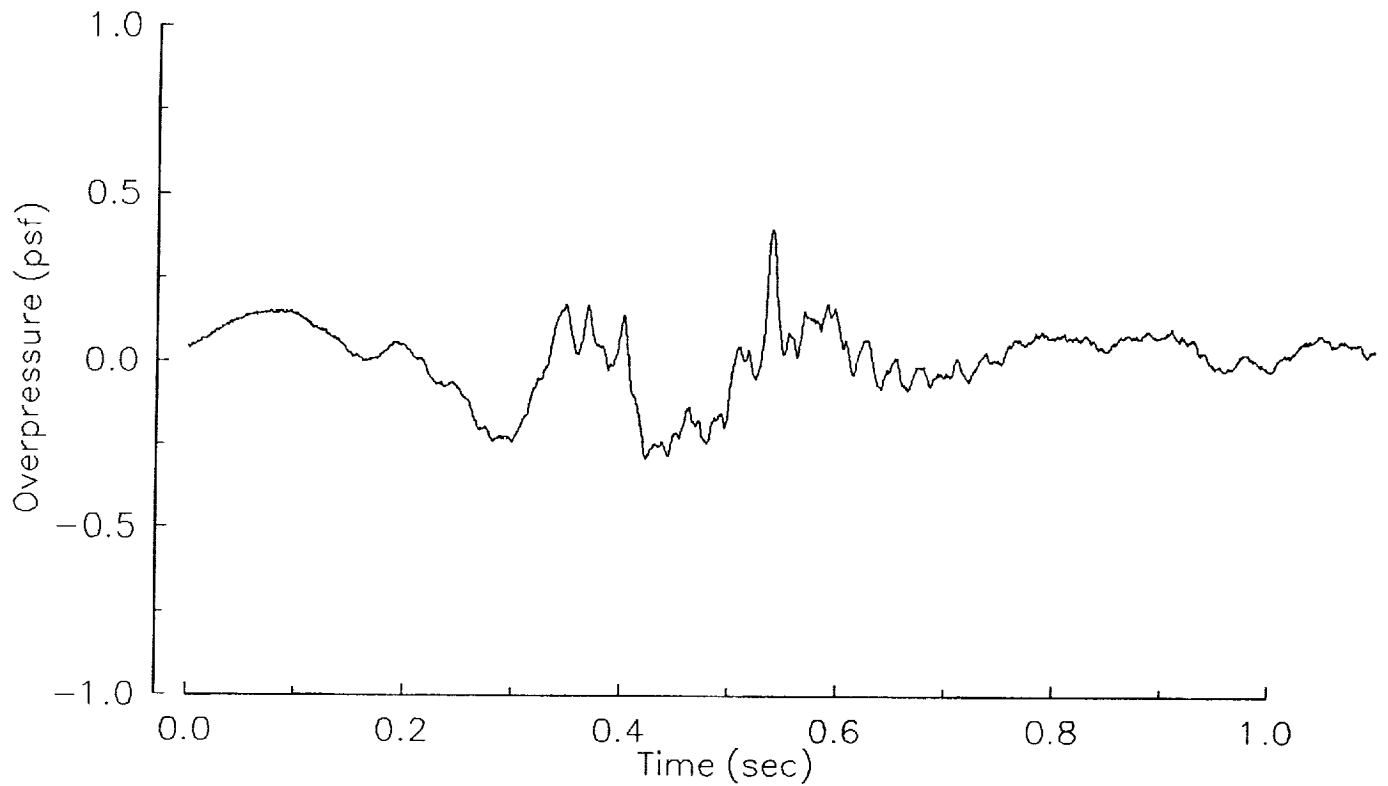


Figure 11. Rumble pressure signature generated by an F-111 at 1.2 M at 14 kFt MSL (flight #41) measured 10 lateral miles from the flight track.

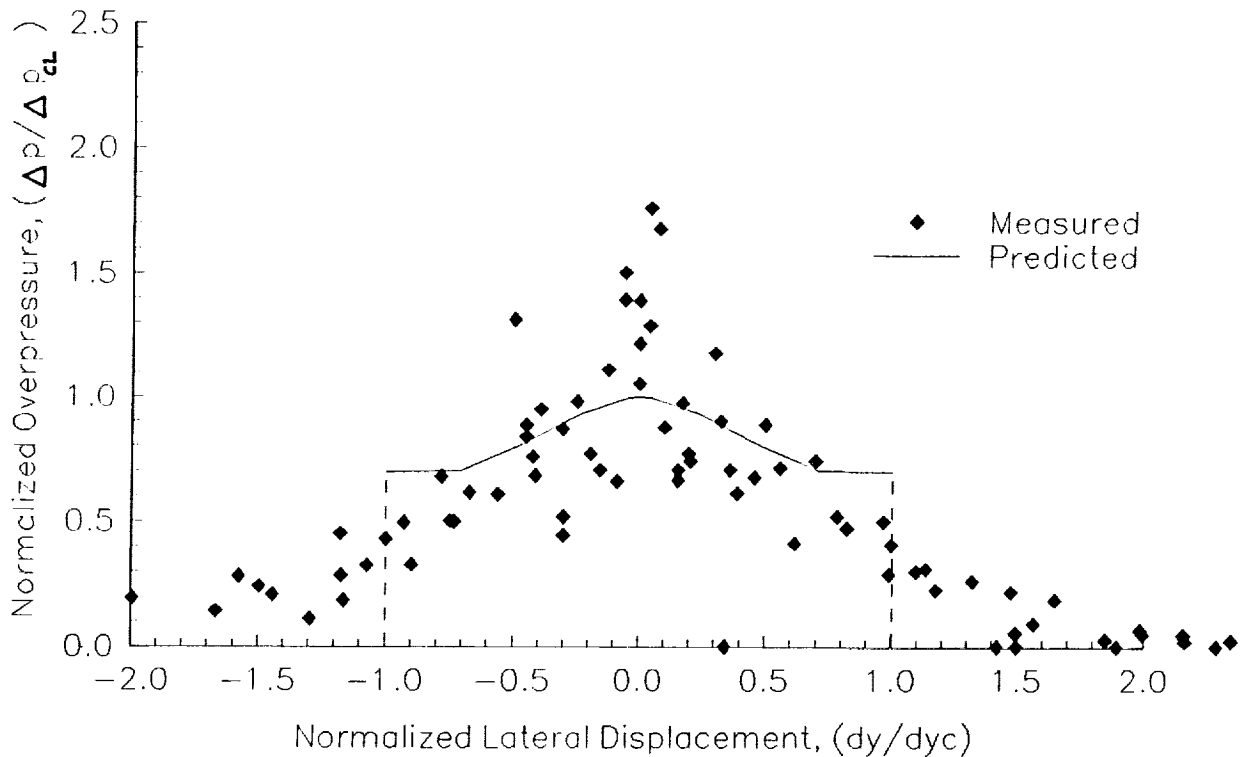


Figure 12. Normalized peak overpressures as a function of the normalized lateral propagation distance for flight with nominal conditions of 1.1 M at 14 kFt MSL.

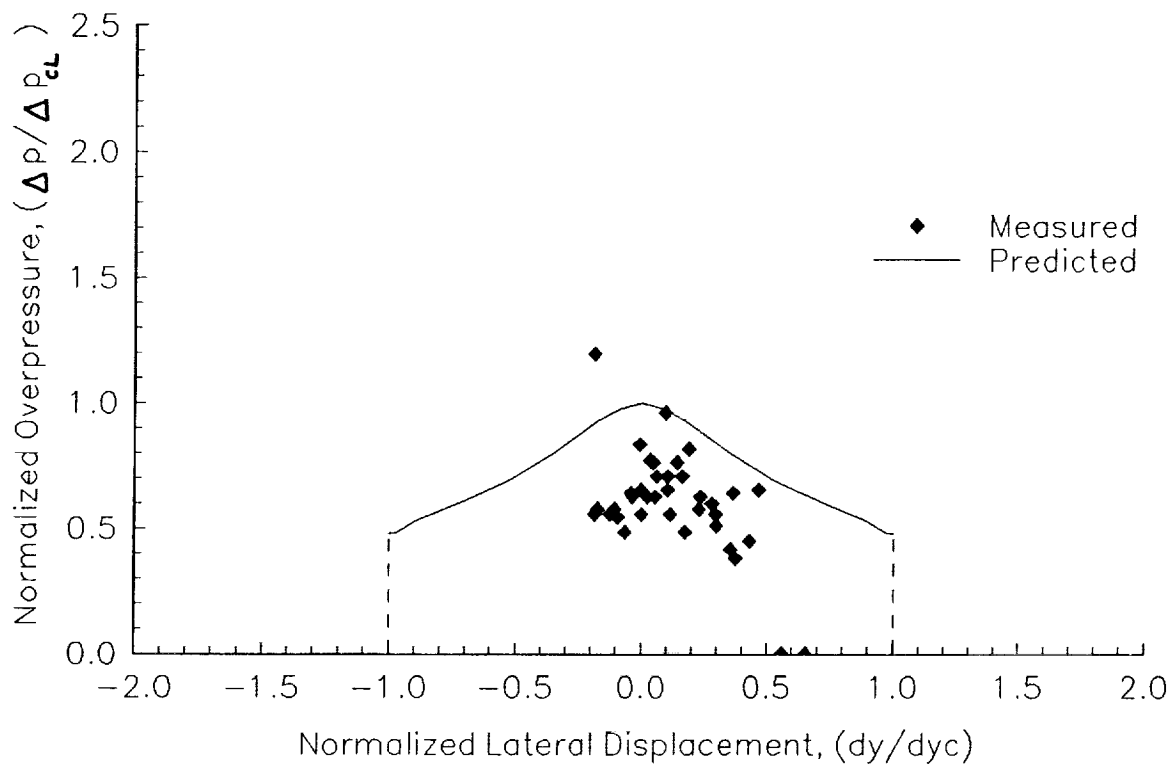


Figure 13. Normalized peak overpressures as a function of the normalized lateral propagation distance for SR-71 flights above 1.5 M.

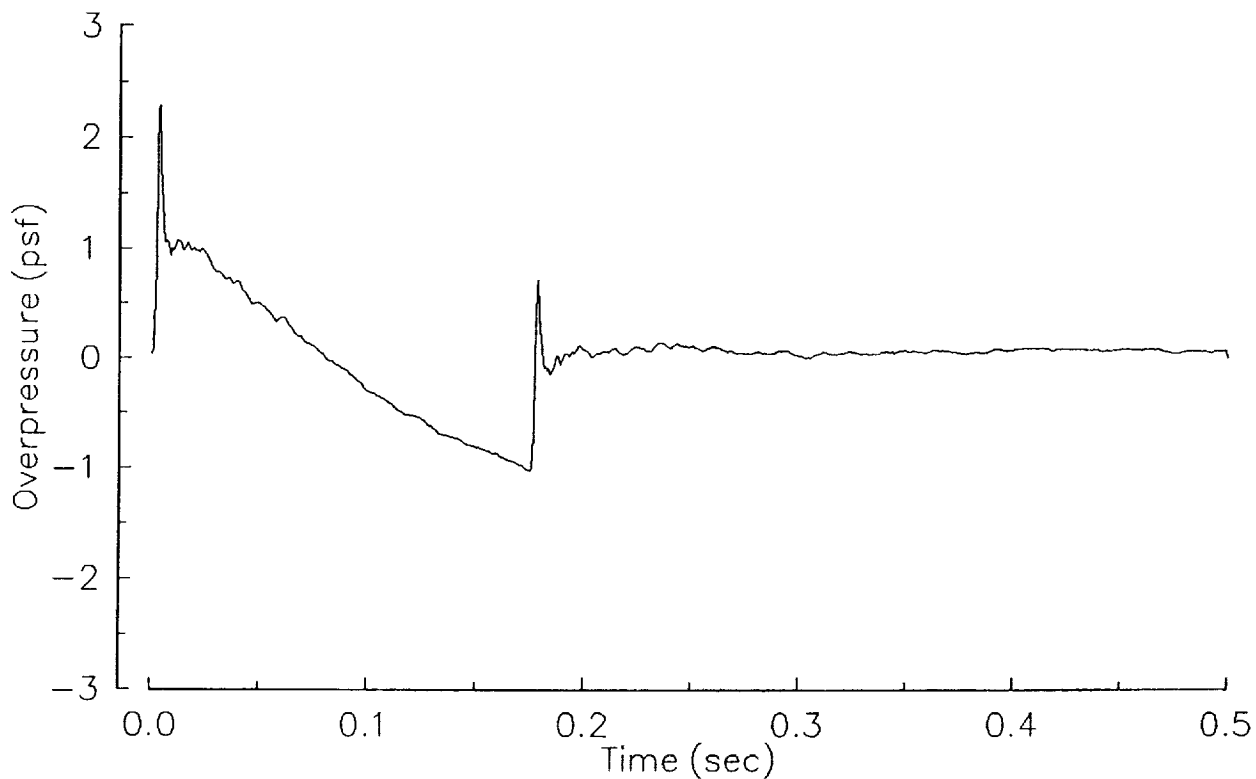


Figure 14. Peaked sonic boom signature generated by an SR-71 at 1.7 M at 52 kFt MSL (flight #32) measured 4 lateral miles from the flight track.

PRELIMINARY RESULTS FROM THE WHITE SANDS MISSILE RANGE SONIC
BOOM PROPAGATION EXPERIMENT

William L. Willshire, Jr.
NASA Langley Research Center
Hampton, VA

David W. DeVilbiss
Lockheed Engineering and Sciences Company
Hampton, VA

SUMMARY

Sonic boom bow shock amplitude and rise time statistics from a recent sonic boom propagation experiment are presented. Distributions of bow shock overpressure and rise time measured under different atmospheric turbulence conditions for the same test aircraft are quite different. The peak overpressure distributions are skewed positively, indicating a tendency for positive deviations from the mean to be larger than negative deviations. Standard deviations of overpressure distributions measured under moderate turbulence were 40% larger than those measured under low turbulence. As turbulence increased, the difference between the median and the mean increased, indicating increased positive overpressure deviations. The effect of turbulence was more readily seen in the rise time distributions. Under moderate turbulence conditions, the rise time distribution means were larger by a factor of 4 and the standard deviations were larger by a factor of 3 from the low turbulence values. These distribution changes resulted in a transition from a peaked appearance of the rise time distribution for the morning to a flattened appearance for the afternoon rise time distributions. The sonic boom propagation experiment consisted of flying three types of aircraft supersonically over a ground-based microphone array with concurrent measurements of turbulence and other meteorological data. The test aircraft were a T-38, an F-15, and an F-111, and were flown at speeds of Mach 1.2 to 1.3, 30,000 feet above a 16 element, linear microphone array with an inter-element spacing of 200 ft. In two weeks of testing, 57 supersonic passes of the test aircraft were flown from early morning to late afternoon.

INTRODUCTION

In 1990, the National Aeronautics and Space Administration together with industry implemented a research program to develop the technology necessary to design and build the next generation of commercial supersonic transport. Early in NASA's technology development program, referred to as the High Speed Research (HSR) program, airport noise, sonic boom and ozone depletion were identified as issues requiring investigation in order to develop the necessary technology for a successful aircraft design.

An element of the HSR program is to develop a High Speed Civil Transport (HSCT) design which has a minimized sonic boom. A typical sonic boom heard on the ground has a pressure signature referred to as an N-wave: an abrupt positive pressure rise from the ambient pressure (the bow shock), followed by a steady decrease to a negative value with an abrupt jump back to the ambient pressure (the tail shock). Rise time is a measure of the

abruptness of the bow shock. The amplitude and rise time of the bow shock strongly influence the subjective response to the sonic boom. Typically, a large bow shock is associated with a short rise time.

A goal of the sonic boom research effort is to modify the bow shock by making the positive pressure jump smaller, more gradual, or shaped differently. One type of shaped boom is the so-called flat top where the bow shock pressure received on the ground rises to a design level, then remains at that level for a short time rather than immediately starting to decrease to the negative tail shock level. An aircraft designed for minimized sonic boom would have a different shape than a purely optimal aerodynamic aircraft design and may suffer performance penalties over that of the aerodynamic design. A key technical question is "Can the turbulence these shaped booms encounter during propagation affect the sonic boom signature shape in such a manner as to negate the subjective benefits of the sonic boom shaping?" The White Sands Missile Range (WSMR) sonic boom propagation experiment was conducted to investigate the influence of turbulence on the propagation of sonic booms.

Although many sonic boom measurement experiments have been done in the past (Ref. 1), the purpose of the WSMR experiment was to obtain multiple measurements of a sonic boom event with concurrent meteorological measurements sufficient to statistically describe the influence of turbulence on the propagation of sonic booms. Multiple measurements of a sonic boom event were achieved through use of 16 microphones at 200 ft intervals and multiple similar aircraft overflying the array within short time periods. The WSMR Sonic Boom Propagation Experiment consisted of flying three test aircraft, operated to simulate the bow shock over pressures of different proposed HSCT designs, over the ground-based microphone array. Meteorological data were measured with free-release and tethered balloons, ten instrumented towers from 6 to 32 meters in height, two acoustic sounding systems (SODAR), and a radio/acoustic sounding system (RASS) system. The data will be used to validate propagation models which incorporate the effects of turbulence. The test aircraft nominally generated N-wave sonic boom signatures. Once the observed effects of turbulence on these N-wave shaped sonic booms are understood and predictable, the validated propagation codes will then be used to predict the effect of turbulence on the propagation of shaped sonic booms.

The purpose of this paper is to describe the WSMR sonic boom propagation test and to present some preliminary data analysis results for a T-38 and an F-15. At the time of writing this paper for the 1992 HSR Workshop, the complete data base, particularly the meteorological data, had not been compiled into a unified data base and was not available for the data analyses reported here. The complete data base, when available, will be utilized in future data analyses. In the next section of this paper, the experimental set-up, instrumentation, and procedures are discussed. In this section, the measured meteorological parameters are discussed. The results of sonic boom bow shock amplitude and rise time statistical analyses are presented in the following section. Final comments, including analysis and plans, are given in the last section of the paper.

EXPERIMENT

General

The sonic boom propagation experiment was conducted during August 1991 at WSMR, New Mexico as a part of the NATO Joint Acoustic Propagation Experiment (JAPE). The sonic boom propagation experiment was added to JAPE to take advantage of the extensive

amount of meteorological instrumentation gathered to perform the JAPE experiment. The researchers performing JAPE, in particular Mr. Bob Olsen of the Atmospheric Science Laboratory of WSMR, were supportive of adding the sonic boom propagation experiment to their already large test matrix.

Acoustic Measurements

The primary acoustic array employed in the sonic boom propagation experiment was a 16 element, ground based, linear array sketched in Figure 1. The array was deployed at Dirt Site which is located in the southeastern corner of the range, west of the Jarilla Mountains. The array consisted of BEAR (Boom Event Analyzer/Recorder) microphone systems specifically designed to measure sonic booms (Ref. 2). The BEAR systems were deployed in a linear array with at least a 200 ft distance between them. The BEAR systems are comprised of a microphone, digitizer, microprocessor, and storage medium, and were used with the supplied ground plates and wind screens. Once calibrated and set-up, a BEAR system continuously digitizes at 8 kHz the signal measured by the microphone. The microprocessor detects a sonic boom when preset criteria, for example overpressure amplitude and rise time, are met. After a sonic boom is detected, the portion of the digitized signal containing the sonic boom is stored in a personal computer (PC) memory module. After a test, the memory module is removed from the BEAR unit and the stored data is transferred from the module to a PC for analysis or storage on other digital media. The BEAR units are battery operated and autonomous. The array was located on a dirt road which ran in a North/South direction between the three main meteorological measuring sites. The location of each BEAR unit was selected to be in a flat area, away from ditches, ruts and the like. The coordinates of the 16 BEAR positions are given in Table 1 in the standard WSMR UTM coordinate system. The BEAR units used in this experiment were borrowed from the Harry G. Armstrong Aerospace Medical Research Laboratory, Wright-Patterson AFB.

From previous sonic boom measurement programs (Ref. 3), it was expected that the 200 ft microphone spacing could result in unique sonic boom signatures at each microphone location. Sonic booms close to the aircraft do not vary much for constant speed and altitude flight. The variability observed on the ground is due to propagation through the atmosphere. In previous work it was found that a spacing of 50 to 200 ft can result in different shaped sonic booms being received for the same supersonic pass. This indicates that the received waveforms at the two different microphone locations propagated along unique atmospheric paths which resulted in different received waveforms. The 200 ft microphone spacing was chosen in this experiment to provide unique source emission times for the waveforms measured at each microphone and to hopefully yield unique waveforms at each microphone, particularly under turbulent conditions.

In addition to the BEAR microphone systems, three standard analog systems were deployed (see Figure 1). The measured signals from these systems were recorded on an FM recorder at a tape speed sufficient to yield a 10 kHz upper frequency limit. The analog systems were 1/2 in. condenser microphones which did not have sufficient low frequency response to accurately measure the waveforms of the sonic booms, but which were able to capture the bow shocks. Two of the analog systems were located between BEAR locations 9 and 10. One microphone was mounted at the top of a 10 m pole. The second microphone was mounted on a ground board at the base of the pole. This microphone pair was deployed to measure the incidence angle of the bow shock to the ground. The third analog microphone system was mounted on a ground board halfway between BEAR systems 8 and 9 and was used to measure the acoustic ambients.

Meteorological Measurements

Meteorological measurements were made at three primary sites, referred to as the south tower, the north tower, and the remote sensing site (see Figure 1). The sites were located along a 1.8 km North-South line formed by the south tower and remote sensing sites. The south and north towers were 33 m high, walk-up towers and were separated by a distance of 1 km. The south tower was instrumented with three dimensional sonic anemometers at the 2, 4, 6, 8, and 10 m heights, with single hot wires orientated in the direction of the mean wind at the 2 and 10 m heights, and instrumentation to measure a spatial temperature average from 2 to 33 m. The north walk-up tower was instrumented at the 2 and 10 m levels with 2 dimensional sonic anemometers. In addition, at the north tower site a 32 m standard weather tower was located which measured wind speed, direction, and temperature at the 2, 4, 8, 16, and 32 m levels, as well as the humidity, atmospheric pressure, and solar radiation at the 10 m level. Also, located at the north tower site was a 6 m weather pole which measured wind speed, direction and temperature profiles. The remote sensing site was equipped with a sodar which measured winds to 3 km, a mini-sodar which measured winds and turbulence to 200 m; a Radio Acoustic Sounding System (RASS) which measured temperature profiles to 600 m; a tethersonde, to measure wind, temperature, pressure, and humidity profiles to 400 m; a rawinsonde, to measure wind, temperature, pressure, and humidity profiles to 18 km and two 10 m weather towers. Surrounding the general test site were 6 additional 10 m weather towers instrumented at the 2 and 10 m levels. In the WSMR sonic boom experiment, the quantity of meteorological data exceeded that of the acoustic data. For the present paper, most of the meteorological data were not available for inclusion in the data analyses reported here. The meteorological data reduction is nearing completion and the results are due to be made available and published as a WSMR document soon.

Test Aircraft and Flight Procedures

The sonic boom propagation experiment consisted of flying three types of aircraft supersonically, straight, and level over a ground based microphone array. The three test aircraft were the T-38, the F-15, and the F-111. The aircraft were flown 30,000 feet above the microphone array at speeds of Mach 1.2 to 1.3. Each aircraft type was chosen and operated to roughly simulate the amplitude of the bow shock of different proposed HSCT designs. The T-38 represented the minimized sonic boom design, the F-111 the aerodynamically optimized design, and the F-15 a compromise between the two. The aircraft were flown above the linear microphone array from the north to the south and were skin tracked. The sonic boom prediction program 'PCBOOM2' (Ref. 4) was used to initially determine the supersonic portions of the test aircraft flight path. After the first test day, data analysis results led to modifications to the flight procedures to maximize the number of aircraft passes over the microphone array within a test period.

Completed Test Matrix

In two weeks of testing, 57 supersonic passes of the test aircraft were flown. Thirty T-38, 21 F-15, and 6 F-111 passes over the microphone were flown and recorded. The dates, type of aircraft, number of passes, and local time of the passes are listed in Table 2. A single T-38 was used throughout the test. The multiple F-15 passes for a particular test period were made by different aircraft. When a flight of multiple F-15's was available, they were flown over the microphone array with a nominal 90 second interval between the aircraft. Each of the two F-111 test periods was flown with a single airplane.

Included in Table 2 is a fly-over of an SR-71. On August 26, NASA Dryden's SR-71 flew over the array at 65,000 above ground level at Mach 3 from the north to the south. On its

way back to the West Coast it flew from the east to the west over the middle of the microphone array. On-board recordings of the SR-71's navigational output were used for determining position. The SR-71 should roughly simulate the minimized boom design but at a greater cruise altitude than the T-38.

DATA REDUCTION

After each day of testing, the recorded, digitized sonic booms were read from the BEAR memory modules and transferred to a mini-computer environment. There the sonic booms were converted to absolute levels and screened for abnormalities. Acceleration booms and sonic boom reflections from a distant ridge were rejected. A tool used in this process is illustrated in Figure 2. In Figure 2, the test aircraft speed, acceleration, and sonic boom emission position are plotted. A two dimensional ray tracing program incorporating a linear estimate of the measured rawinsonde meteorological profiles was used to predict the source emission position. If the aircraft speed or acceleration close to the emission position for a particular pass of the microphone array was off the nominal for a test point, the data from that pass was rejected.

Bow shock overpressure and rise time are the two sonic boom descriptors chosen for the statistical analyses to be presented in this paper. Bow shock overpressure is simply defined as the maximum acoustic pressure in pounds per square foot (psf) associated with the bow shock of the sonic boom event. The definition for rise time used in the results presented here is the time it takes the bow pressure to rise from 10% of the peak overpressure to 90% of the peak overpressure based on the initial slope of the bow shock. Multiple peak characteristics and extreme rounded shaped sonic booms make calculation of the 90% time questionable and can lead to long rise times. The intent of the present work was to concentrate on the initial slope of the bow shock. The initial slope was used to calculate the rise time between 10% and 90% of the bow shock overpressure. Rise time was calculated from

$$Dt = t_{90\%} - t_{10\%} = \frac{0.9 p_{\max} - 0.1 p_{\max}}{\frac{dp}{dt}}$$

where

Dt = rise time

p_{\max} = peak overpressure

dp/dt = initial slope of bow shock

RESULTS

Histograms of the percentage of occurrence of peak bow shock overpressure and rise time will be presented for a T-38 and an F-15 for low and moderate turbulence conditions. As mentioned previously, most of the meteorological data were not available for inclusion in the data analysis reported here. Typically, during the WSMR sonic boom experiment there was little cloud cover. Temperature inversions with light winds were the norm in the morning. By afternoon the desert floor had heated up, the morning inversion had been replaced with a lapse, and the winds had increased in speed. Thus, it is assumed that the morning time period was associated with low turbulence and the afternoon time period with moderate turbulence. The mean value, standard deviation, Skewness (α_3), Kurtosis (α_4), and the number data points for each histogram are listed in the histogram legends.

Skewness is defined as the ratio of the third central moment to the second central moment to the $3/2$ power and is a measure of the degree of symmetry of a distribution. Positive skewness indicates a longer (negative values a shorter) distribution tail toward values larger than the central maximum. A value of zero skewness is associated with a symmetric distribution. Kurtosis can be expressed as the ratio of the fourth central moment to the second central moment squared, minus 3. Kurtosis is a measure of the peakedness of a distribution. Positive values of Kurtosis indicate a distribution which is more peaked than a normal distribution; a value of zero is associated with a normal distribution; and negative values indicate a flat-topped distribution.

T-38 bow shock and rise time distributions for low and moderate turbulence conditions are presented in Figures 3a and 3b, respectively. A summary of the statistical analysis is given in Table 3. The T-38 overpressure distributions illustrate a point common to all the overpressure distributions: that although HSCT designs have target sonic boom overpressures, some people, some of the time, will hear larger, occasionally much larger, overpressures (a factor of 4 larger than the mean overpressure for the T-38). While the mean overpressures for the T-38 are similar for the two assumed turbulence conditions, the standard deviation and distributions are different. These differences are attributed to the effects of turbulence. The moderate turbulence overpressure standard deviation is 40% larger than the low turbulence value. Both overpressure distributions are skewed positively (the median is less than the mean) indicating a tendency for positive deviations to be larger than negative deviations. The moderate turbulence distribution is less peaked (smaller value of Kurtosis) than the low turbulence distribution. The difference between the mean and median is larger for the moderate turbulence overpressure distribution than for the low turbulence distribution. This indicates that an effect of turbulence is to cause larger positive deviations.

The T-38 rise time distributions illustrated in Figure 3b are quite different for the two turbulence conditions. The moderate turbulence mean rise time (1.82 ms) is 3.8 times larger than the low turbulence mean rise time (.48 ms) while the moderate turbulence rise time standard deviation is 3.5 times larger than the low turbulence value. The moderate turbulence rise time distribution is dramatically less peaked than the low turbulence rise time distribution. From a subjective point of view, the increased rise times associated with moderate turbulence should act to diminish the adverse effect of the larger positive deviations.

Low and moderate turbulence overpressure and rise time distributions are presented in Figures 4a and 4b for the F-15 and are summarized in Table 4. The moderate turbulence mean overpressure is 30% larger and the standard deviation is 40% larger than the low turbulence distribution values. The moderate turbulence overpressure distributions are more skewed than the low turbulence distribution. The mean and median are further apart for the moderate turbulence overpressure distribution. The moderate turbulence mean rise time of 2.0 ms is approximately 4 times the low turbulence value of .48 ms with an accompanying factor of 3 increase in rise time standard deviation. The rise time distributions are very different for the two turbulence conditions, with the moderate turbulence distributions much less peaked than the low turbulence rise time distribution.

CONCLUDING REMARKS

A flight test was designed and conducted to investigate effects of turbulence on sonic boom propagation. The experiment was conducted at White Sands Missile Range, New Mexico to take advantage of a NATO acoustic propagation test site that was heavily instrumented with meteorological sensors. The flight experiment was designed so that the data collected could be used in a statistical analysis of the effects of turbulence on sonic boom propagation. In two weeks of testing, 59 supersonic passes over a linear microphone array

were made by T-38, F-15, F-111, and SR-71 aircraft. The aircraft were chosen and operated to simulate the range of ground bow shock overpressures expected from the envisioned HSCT designs.

Little of the extensive meteorological data collected were available for inclusion in this paper. Bow shock overpressure and rise time statistical analysis were performed based on turbulence levels with the underlying assumption that turbulence was low in the early morning and moderate in the afternoon. The bow shock overpressure distributions illustrated that even though HSCT designs have target sonic boom overpressures, some people, some of the time, will hear much larger overpressures. These overpressure and rise time distributions should be factored into predictions of subjective assessments for HSCT designs.

The bow shock overpressure distributions were skewed positively indicating large positive deviations. The majority of measured data indicated that the mean and standard deviation of the bow shock overpressure distributions increased from the low turbulence condition to the moderate turbulence condition. As turbulence increased, the difference between the median and the mean increased indicating larger positive overpressure deviations. The fact that the bow shock overpressure distributions are skewed toward larger values of overpressure is evidence to the nature of the interaction of propagating sonic booms with turbulence. A single scatter scattering model would cause overpressure distributions to be skewed toward smaller values of overpressure. The measured overpressure distributions suggest a refractive, focusing effect which would cause the observed shift in the moderate turbulence distributions to large positive deviations from the mean.

The effect of turbulence was more readily seen in the rise time distributions. In general, the moderate turbulence rise time distribution means were larger by a factor of 4 and the standard deviations were larger by a factor of 3 from the low turbulence distribution values. These distribution changes resulted in a transition from a peaked appearance of the rise time distribution for the low turbulence to a flattened appearance for the moderate turbulence rise time distributions. Taken by itself, the increase in rise time with increasing turbulence should have a beneficial subjective effect. However, the combined subjective impact of longer rise times coupled with the larger bow shock overpressure positive deviations is not clear and needs to be assessed.

Not having the meteorological data to factor into the data analysis limited the results presented here. In the future, the statistical analysis will include direct measurement of the turbulence scale and amplitude, along with temperature, wind and solar radiation conditions associated with each measured sonic boom. After these analyses the measured data will be used to validate propagation models which include the effects of turbulence. The validated propagation models will be used to predict the influence of turbulence on the propagation of HSCT generated sonic booms, including HSCT shaped sonic booms.

REFERENCES

1. Domenic J. Maglieri and Kenneth J. Plotkin: Sonic Booms. Aeroacoustics of Flight Vehicles: Theory and Practice, Volume I: Noise Sources, Harvey H. Hubbard, ed., NASA RP-1258, WRDC TR 90-3052, 1991.
2. Robert A. Lee, Doug Mazurek, Dale Price, Monty Crabill, and Barbara Palmer: Boom Event Analyzer Recorder (BEAR): System Description, AAMRL-TR-89-035 (AD-A218 048), August 1989.

3. David A. Hilton, Vera Huckel, Roy Steiner, and Domenic J. Maglieri: Sonic-boom Exposures During FAA Community- Response Studies Over a 6-month Period in the Oklahoma City Area, NASA TN D-2539, December 1964.
4. Melissa Burn, and Kenneth J. Plotkin: PCBOOM2: Enhancement of PCBOOM Sonic Boom Analysis Program, Wyle Research Technical Note TN 89-13 (Work performed under Air Force Contract N0. F08635-89-C-0044), October 1989.

Table 1. White Sands Missile Range UTM BEAR coordinates.

LOCATION	EASTING (m)	NORTHING (m)	ALTITUDE (m)
BEAR 1	391425.26	3589920.77	1255.31
BEAR 2	391440.02	3589861.40	1256.18
BEAR 3	391453.91	3589801.67	1256.69
BEAR 4	391468.44	3589743.43	1257.33
BEAR 5	391483.37	3589683.73	1257.76
BEAR 6	391498.36	3589624.83	1258.29
BEAR 7	391513.83	3589565.79	1258.73
BEAR 8	391528.53	3589506.84	1259.34
BEAR 9	391543.28	3589447.56	1259.98
BEAR 10	391558.05	3589388.47	1260.62
BEAR 11	391572.22	3589329.12	1261.48
BEAR 12	391587.54	3589270.41	1262.13
BEAR 13	391605.72	3589211.49	1263.02
BEAR 14	391633.79	3589093.50	1264.16
BEAR 15	391662.03	3588975.07	1265.65
BEAR 16	391677.72	3588916.04	1266.52

Table 2. Test period dates, aircraft, and times.

DATE	AIRCRAFT	TIME, Local
8/19/91	4 F-15's	11:30-12:30
8/20/91	2 F-15's 2 T-38's	8:30-9:00
8/21/91	4 F-15's 3 T-38's	13:00-14:00
8/22/91	4 F-15's 3 T-38's	8:00-9:00
8/23/91	4 T-38's 1 F-15's 2 F-111's 4 T-38's	6:30-7:00 10:00-11:00
8/24/91	4 T-38's	12:00-12:30
8/26/91	2 SR-71's	13:00-13:30
8/28/91	3 T-38's 2 F-15's 3 T-38's	8:00-8:30 14:30-15:30
8/29/91	4 T-38's 4 F-15's 4 F-111's	14:00-15:30

Table 3. T-38 statistical analysis summary.

Overpressure	
LOW TURBULENCE	MODERATE TURBULENCE
Maximum = 2.78 psf	Maximum = 2.38 psf
Minimum = 0.47 psf	Minimum = 0.30 psf
Average = 0.82 psf	Average = 0.83 psf
Median = 0.74 psf	Median = 0.73 psf
Standard Deviation = 0.28 psf	Standard Deviation = 0.38 psf
Skewness = 3.25	Skewness = 1.47
Kurtosis = 15.0	Kurtosis = 2.48
Count = 170	Count = 133

Rise Time	
LOW TURBULENCE	MODERATE TURBULENCE
Maximum = 2.37 ms	Maximum = 6.47 ms
Minimum = 0.13 ms	Minimum = 0.54 ms
Average = 0.48 ms	Average = 2.47 ms
Median = 0.38 psf	Median = 2.31 ms
Standard Deviation = 0.33 ms	Standard Deviation = 1.02 ms
Skewness = 2.10	Skewness = 1.24
Kurtosis = 6.49	Kurtosis = 2.43
Count = 170	Count = 133

Table 4. F-15 statistical analysis summary.

Overpressure	
LOW TURBULENCE	MODERATE TURBULENCE
Maximum = 2.83 psf	Maximum = 4.80 psf
Minimum = 0.40 psf	Minimum = 0.25 psf
Average = 1.34 psf	Average = 1.79 psf
Median = 1.35 psf	Median = 1.63 psf
Standard Deviation = 0.55 psf	Standard Deviation = 0.77 psf
Skewness = 0.30	Skewness = 1.22
Kurtosis = -0.34	Kurtosis = 1.99
Count = 67	Count = 157

Rise Time	
LOW TURBULENCE	MODERATE TURBULENCE
Maximum = 2.46 ms	Maximum = 7.41 ms
Minimum = 0.11 ms	Minimum = 0.30 ms
Average = 0.51 ms	Average = 2.05 ms
Median = 0.32 ms	Median = 1.72 ms
Standard Deviation = 0.45 ms	Standard Deviation = 1.38 ms
Skewness = 2.13	Skewness = 1.15
Kurtosis = 4.88	Kurtosis = 1.42
Count = 67	Count = 157

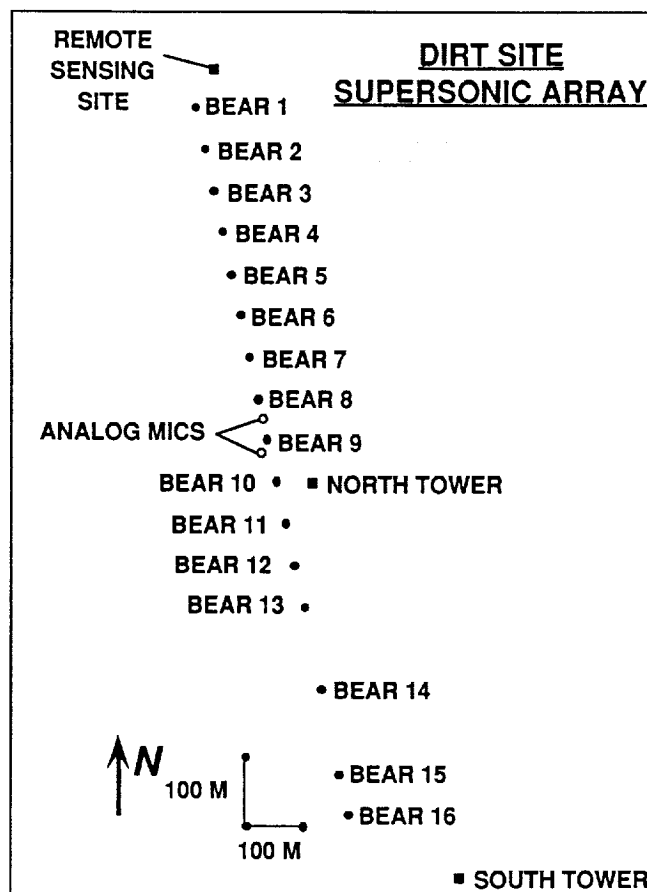


Figure 1. Sketch of test site.

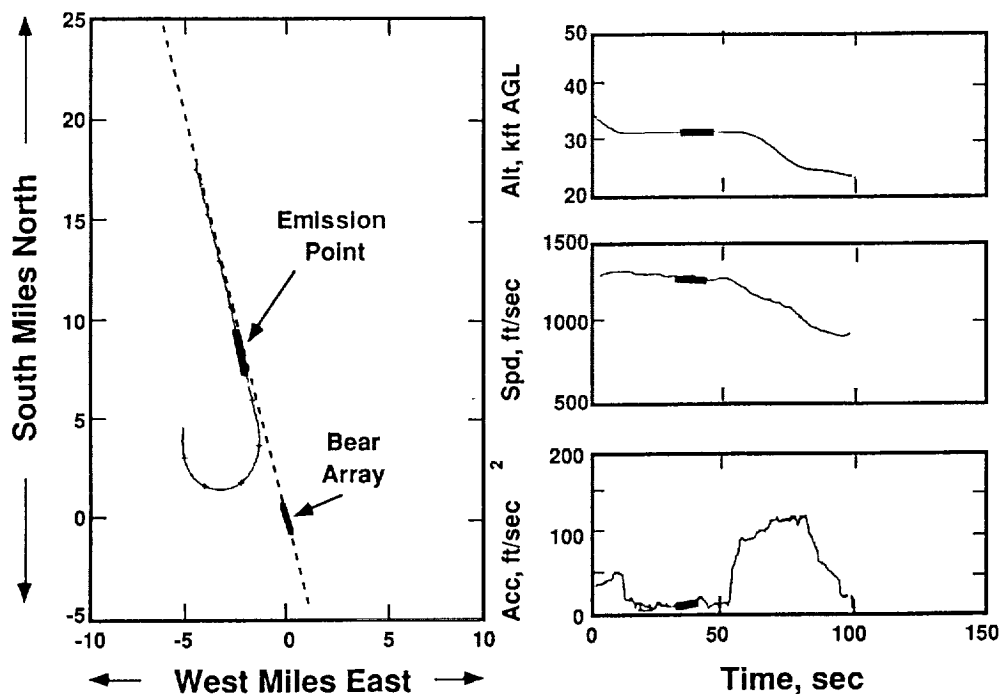


Figure 2. Representative radar tracking data for a T-38 Aircraft.

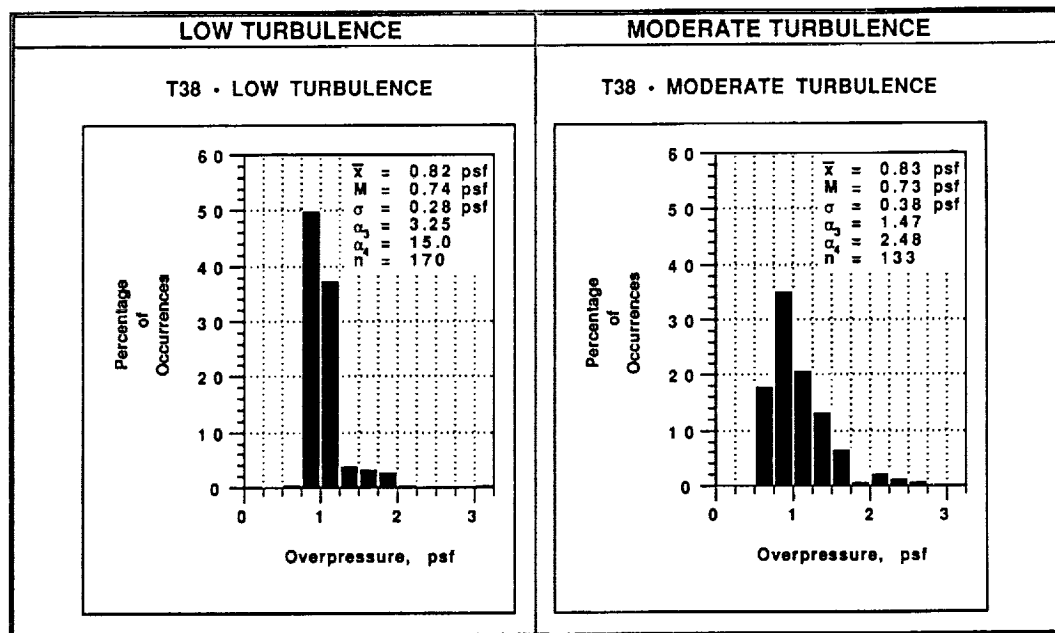


Figure 3.a. Low and moderate turbulence T-38 bow shock overpressure distributions.

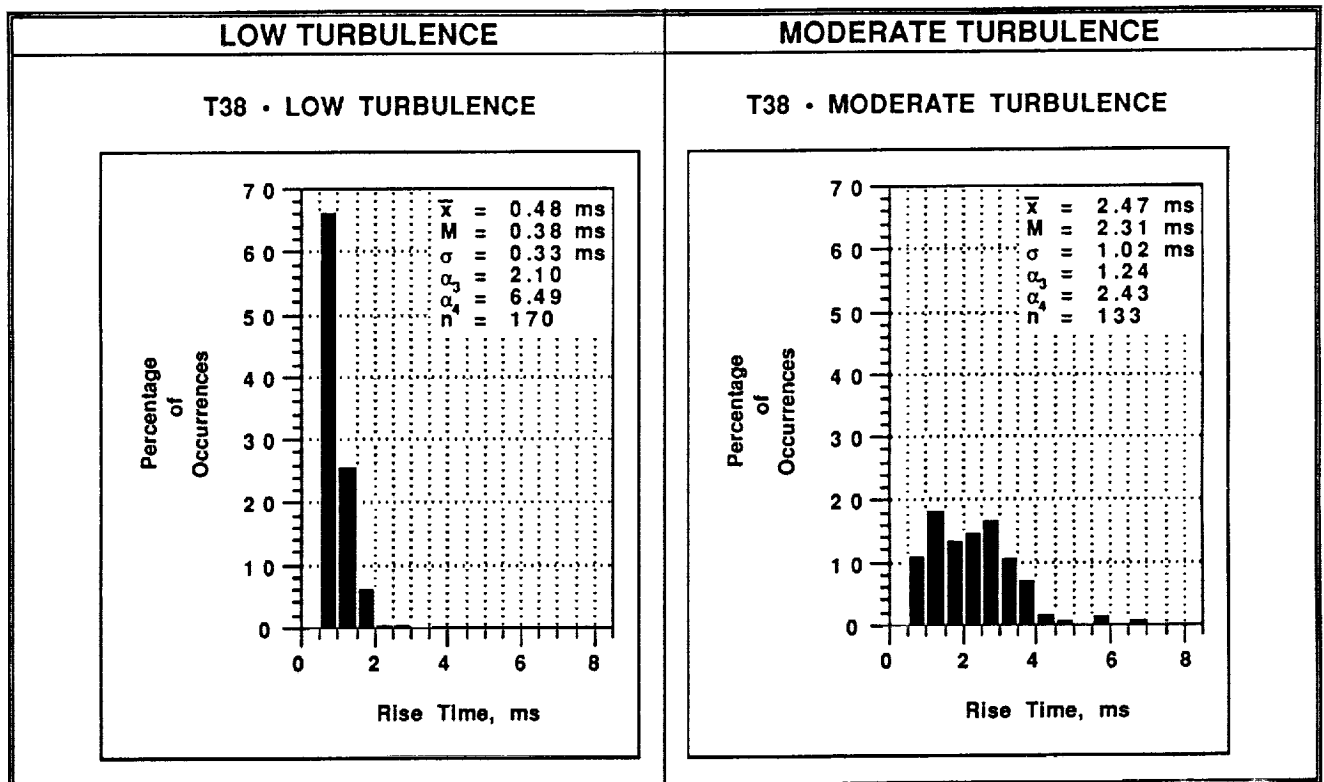


Figure 3.b. Low and moderate turbulence T-38 rise time distributions.

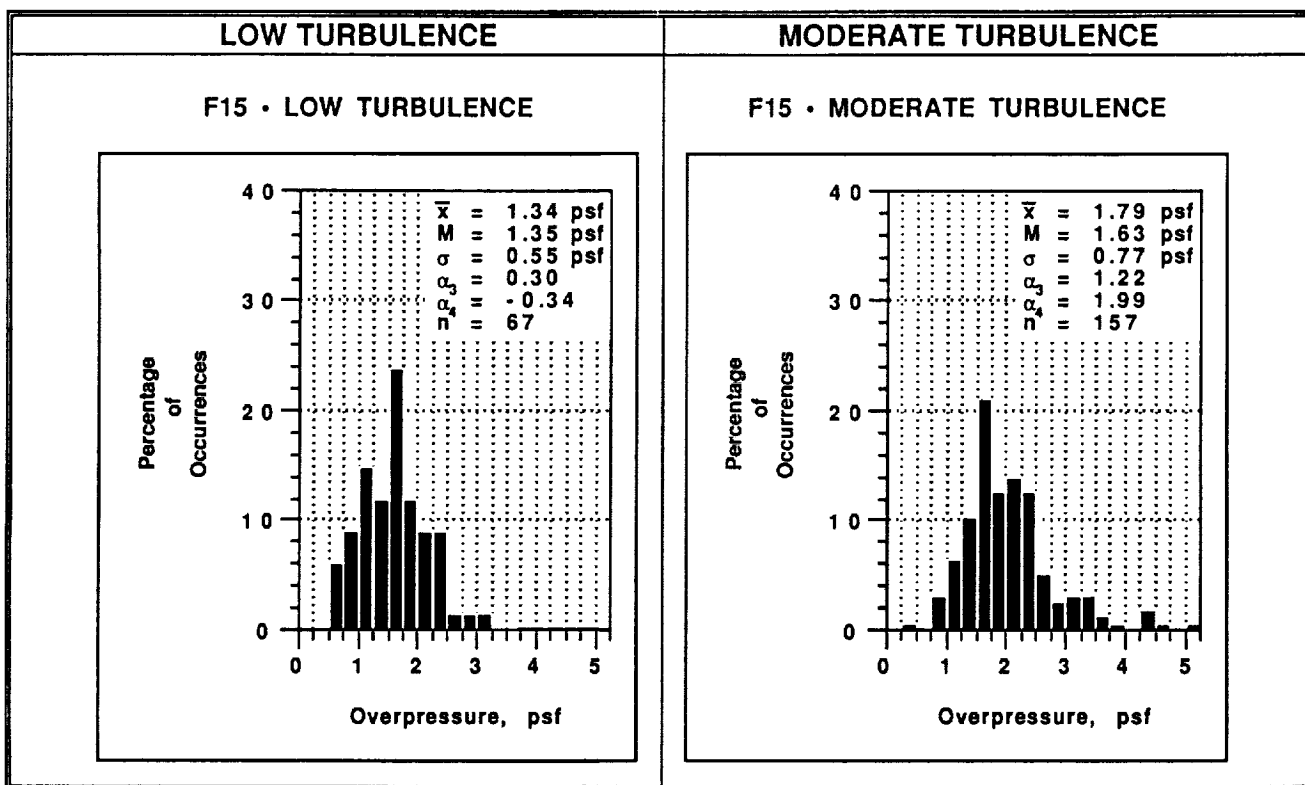


Figure 4.a. Low and moderate turbulence F-15 bow shock overpressure distributions.

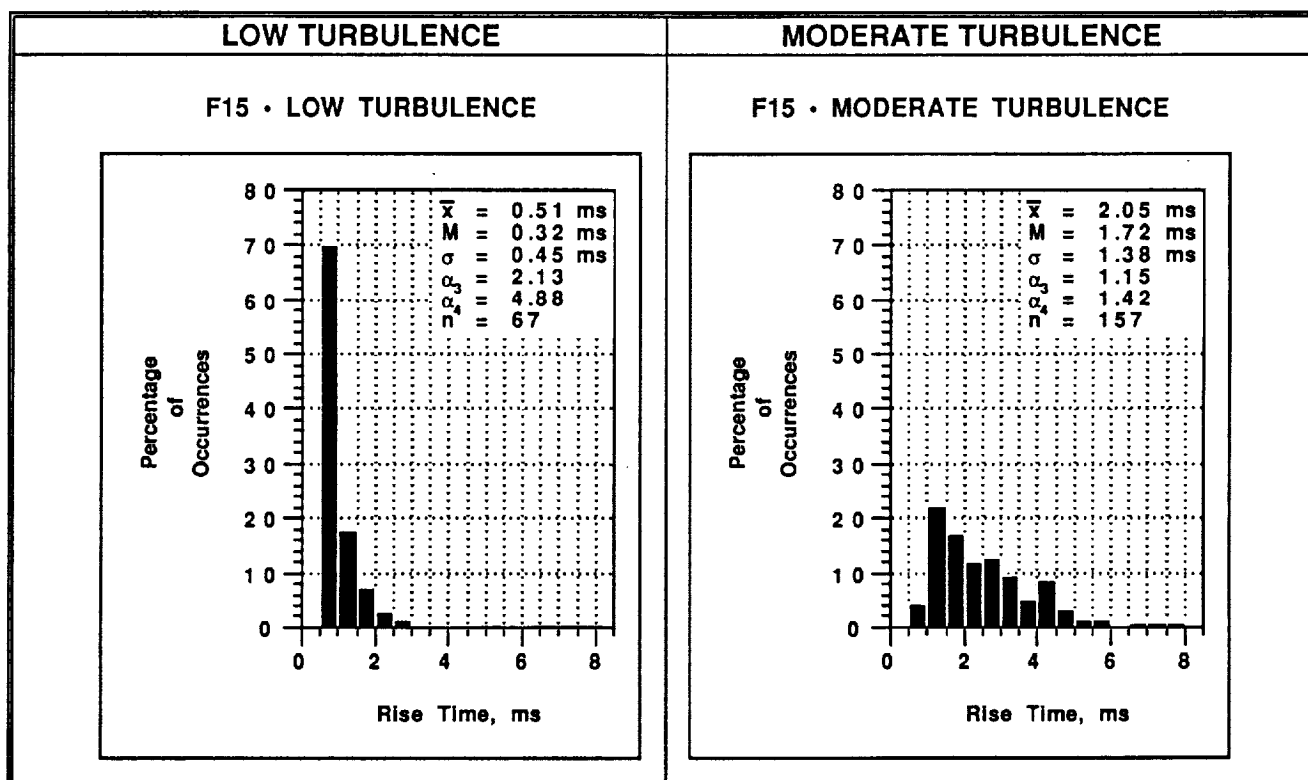


Figure 4.b. Low and moderate turbulence F-15 rise time distributions.

SUBJECTIVE LOUDNESS RESPONSE TO SIMULATED SONIC BOOMS

Jack D. Leatherwood
NASA Langley Research Center
Hampton, VA

Brenda M. Sullivan
Lockheed Engineering and Sciences Company
Hampton, VA

SUMMARY

A series of laboratory studies were conducted at NASA Langley Research Center to: (1) quantify the effects of sonic boom signature shaping on subjective loudness; (2) evaluate candidate loudness metrics; (3) quantify the effects of signature asymmetry on loudness; and (4) document sonic boom acceptability within the laboratory. A total of 212 test subjects evaluated a wide range of signatures using the NASA Langley Research Center's sonic boom simulator. Results indicated that signature shaping via front-shock minimization was particularly effective in reducing subjective loudness without requiring reductions in peak overpressure. Metric evaluations showed that A-weighted sound exposure level, Perceived Level (Stevens Mark VII), and Zwicker's Loudness Level were effective descriptors of the loudness of symmetrical shaped signatures. The asymmetrical signatures were generally rated as being quieter than symmetrical signatures of equal calculated metric level. The magnitude of the loudness reductions were observed to increase as the degree of asymmetry increased and to be greatest when the rear half of the signature was loudest. This effect was not accounted for by the loudness metrics. Sonic boom acceptability criteria were determined within the laboratory. These agreed well with results previously obtained in more realistic situations.

INTRODUCTION

The aircraft community is considering the feasibility of developing a commercial high speed civil transport that will be quiet enough to fly over land at supersonic speeds. To be successful in this effort, the sonic booms created by such an aircraft must not be objectionable to the general populace. This will require that the loudness and startle effects of sonic booms be kept to a minimum. In support of this effort, the NASA Langley Research Center is conducting experiments, using a new sonic boom simulator, to obtain human

subjective loudness responses to a wide range of candidate sonic boom signatures. The goals of these efforts include identification of preferred signature shapes for minimum sonic boom loudness and development of a sonic boom loudness prediction model.

The potential benefits of boom shaping for N-wave signatures have been discussed in references 1 and 2, which describe the results of paired comparison tests to assess the relative loudness of signatures defined by various combinations of rise time, duration, and peak overpressure. Results from these studies showed that substantial reductions in subjective loudness of N-waves, for constant peak overpressure, could be achieved by decreasing the rise time of the front and rear shocks. Other studies (references 3 and 4) suggested that boom loudness can be reduced by more detailed shaping employing front shock minimization (FSM). This approach involved replacing the N-wave signatures with signatures that achieved peak overpressure in two pressure steps instead of one. It entailed decreasing the strength of the initial pressure rise (first step) and then allowing a slower pressure rise to maximum overpressure (second step). For symmetrical FSM signatures this procedure was also followed for the rear shock.

This paper summarizes the results of recent laboratory studies conducted in the NASA Langley Research Center's sonic boom simulator to further quantify the effects of detailed boom shaping on human subjective loudness response. Specific topics addressed include: (1) loudness reductions due to front shock minimization; (2) evaluation of the performance of candidate loudness metrics; (3) the effects of sonic boom signature asymmetry on subjective loudness; and (4) sonic boom acceptability criteria within the laboratory and comparisons with criteria developed/proposed by others.

EXPERIMENTAL METHOD

Sonic Boom Simulator

The experimental apparatus used in these studies was the Langley Research Center's sonic boom simulator, which is described in reference 2. The simulator, shown in figure 1, is a man-rated, airtight, loudspeaker-driven booth capable of accurately reproducing user-specified sonic boom waveforms at peak sound pressure levels up to 138-139 dB. Input waveforms were computer-generated and "pre-distorted" to compensate for the non-uniform frequency response characteristics of the booth. Pre-distortion was accomplished by use of a digital broadband equalization filter (see reference 5). Boom simulator construction details, performance capabilities, and operating procedures are given in reference 2.

Experimental Designs

The results presented in this paper are based upon the results of four separate experiments that utilized a total of 212 test subjects. The majority of the results presented herein, however, were derived from two of these experiments. Thus only the experimental designs associated with these two studies are discussed. These studies will be referred to as Experiment 1 and Experiment 2. The two studies not discussed include one that validated simulator capability and performance and was reported in reference 2. The remaining study (unpublished) validated the application of the magnitude estimation method for evaluation of sonic boom loudness and addressed several related methodology issues.

Experiment 1

The first experiment was designed to study loudness reductions due to front (and rear) shock minimization (FSM) and to quantify boom acceptability within the laboratory. This experiment used 60 test subjects. The set of test stimuli consisted of 180 signatures comprised of factorial combinations of four FSM boom shaping parameters. These parameters are illustrated in figure 2 and consisted of: (1) peak overpressure, ΔP_{\max} ; (2) front shock rise time, τ_1 ; (3) secondary rise time, τ_2 ; and (4) the ratio of front shock overpressure to peak overpressure, $\Delta P_f/\Delta P_{\max}$, denoted as overpressure ratio. The factorial combinations consisted of five peak overpressure levels (ranging from 1.0 to 2.25 psf), three front shock rise times (1, 2, and 4 msec), three secondary rise times (20, 30, and 50 msec), and four overpressure ratios (0.25, 0.50, 0.75, and 1.0). Duration for all FSM signatures was 300 milliseconds. These signatures were organized into five sessions with the booms randomly assigned to the sessions. To minimize order effects the booms within each session were presented in both forward and reverse sequence. In this experiment subjective loudness ratings were obtained using a continuous 11-point unipolar loudness scale. The scale was anchored at one end (scale value of 0) by the words **NOT LOUD AT ALL** and at the opposite end (scale value of 10) by the words **EXTREMELY LOUD**.

Boom acceptability was studied using three signatures selected from the set of FSM signatures described above and a fourth signature consisting of an N-wave with a rise time of 3 milliseconds and a duration of 300 milliseconds. The three FSM signatures differed only with respect to front shock rise time (1, 2 and 4 msec). Secondary rise time and overpressure ratio were 30 msec and 0.50, respectively, for each FSM signature. Each signature was presented at seven peak overpressure levels for a total of 28 stimuli. These 28 booms comprised one test session. During this session the subjects were simply asked whether each signature would be acceptable if heard three or four times a day (none at night) as they pursued their daily activities.

Experiment 2

Earlier studies (unpublished), using a very limited number of asymmetrical signatures, indicated that asymmetrical signatures may be rated quieter than symmetrical signatures having identical calculated metric levels. This effect was investigated in detail under controlled conditions in Experiment 2. This experiment used 40 test subjects.

The test stimuli for Experiment 2 consisted of N-wave signatures in which the rise times and peak overpressures of the front and back shocks were systematically varied. The specific factors included in the study were front shock rise time, back shock rise time, front shock overpressure, and back shock overpressure. A typical asymmetrical signature is shown in figure 3. Front and back rise times selected for evaluation were 2, 3, and 6 milliseconds. Front and rear peak overpressures were set at five levels each. Actual peak overpressure values varied from signature to signature, but ranged from approximately 0.2 to 1.7 psf. Factorial combinations of these factors resulted in a total of 225 test stimuli. These were randomly assigned to five sessions of 45 stimuli each. As in Experiment 1 the sessions were presented in forward and reverse sequence to minimize order effects.

The scaling method used in Experiment 2 was magnitude estimation. The standard stimulus used was a symmetrical N-wave with rise time of 3 milliseconds, duration of 300 milliseconds, and peak overpressure of approximately 0.70 psf. The standard was assigned a loudness value of 100 and was presented as every fourth stimulus during the test sessions.

To understand the asymmetry results presented later, it is useful to consider how asymmetry is defined in this paper. The procedure was as follows: Each asymmetrical signature was played in the booth and measured with the booth empty. These measured signatures were then used to calculate the Perceived Level (PL) loudness metric for the front part (PL_f), back part (PL_b), and total signature (PL). The difference (in dB) between PL_f and PL_b was defined as the signature asymmetry in terms of loudness. Thus asymmetry was not defined by peak overpressure, but by loudness level.

DISCUSSION OF RESULTS

FSM Boom Parameter Effects

Overall effects on subjective loudness of front shock rise time, secondary rise time, and overpressure ratio obtained in Experiment 1 are presented in figures 4 and 5. The loudness ratings of figure 4 were averaged over overpressure ratio and boom level, and those of figure 5 were averaged over front shock rise time and boom level. Both

figures present results for each of the three secondary rise times. They show that boom loudness decreased with increasing front shock rise time (figure 4) and decreased as overpressure ratio decreased (figure 5). These effects are consistent with the results of prior studies (references 3 and 4, for example) and illustrate the nature of the loudness reductions attainable through boom shaping. The data in figures 4 and 5 also indicate that subjective loudness did not depend upon the length of the secondary rise time for the range of secondary rise times used in this study.

Specific examples of loudness reduction tradeoffs attainable by front shock minimization are illustrated in figures 6 and 7 for boom signatures having peak overpressures of 1.0 and 2.0 psf. These figures show that the quietest booms, for a given peak overpressure, were those with the largest front shock rise time and lowest overpressure ratios. They also show that, for the range of front shock rise times in this study, the reduction of front shock overpressure was particularly effective in reducing loudness.

Using the acceptability data (to be discussed later) it was determined that a mean loudness rating of 4.54 and 2.64 corresponded to the loudness levels that were rated acceptable by 50 and 80 percent of the subjects, respectively. These levels are indicated by the horizontal dashed lines in figures 6 and 7. Mean loudness ratings less than 2.64 were considered to be highly acceptable and those between 2.64 and 4.54 were considered marginally acceptable. (Note that these estimates apply strictly to the laboratory environment.)

Based upon the above assumptions, several comments are appropriate. First, consider the FSM signatures with peak overpressure of 1.0 psf (figure 6). These signatures were all highly acceptable for overpressure ratios of 0.25 for all three rise times. All of the signatures having a 2- or 4-millisecond rise time were at least marginally acceptable at all overpressure ratios. However, the 1-millisecond rise time signatures were unacceptable at overpressure ratios of 0.75 and 1.0 and only marginally acceptable for an overpressure ratio of 0.5.

Consider next the FSM signatures with peak overpressure of 2.0 psf. Inspection of figure 7 indicates that none of these signatures were acceptable for overpressure ratios of 0.75 or larger. The only signature that was highly acceptable was the one with a 4-millisecond rise time and overpressure ratio of 0.25. The remaining signatures were marginally acceptable, except for the 1-millisecond rise time signature with an overpressure ratio of 0.50. This signature was also unacceptable.

The above results illustrate the loudness tradeoffs achievable by boom shaping. Generally, for the FSM signatures within the range of parameters selected for this study, it would be desirable to design for as low a peak overpressure as possible and then further reduce loudness by reducing overpressure ratio and increasing rise time.

Longer rise times (that is, greater than 4 milliseconds) would provide additional loudness reductions.

Metric Considerations

Sonic boom signatures of Experiment 1 were measured with the simulator empty using a special low-frequency microphone located roughly at ear level for a seated subject. These measurements were computer-processed to calculate sound exposure level in terms of three metric weightings and to calculate two loudness metrics. The sound exposure level metrics were unweighted sound exposure level (L_{UE}), A-weighted sound exposure level (L_{AE}), and C-weighted sound exposure level (L_{CE}). The loudness metrics used were Stevens Mark VII Perceived Level (PL) and Zwicker Loudness Level (LLZ). The calculation procedure for PL and LLZ was based on the method described in reference 4. The final metric considered was peak overpressure. Estimates of peak front (positive) and peak back (negative) overpressures of the symmetrical FSM booms were obtained from the measured boom signatures. Since these generally differed slightly from one another, the average of the absolute values of the two were calculated and used to represent peak overpressure of a signature.

Scatterplots showing the mean loudness ratings as a function of level for the metrics ΔP_{max} , L_{CE} , L_{AE} , and PL are presented in figure 8. The L_{UE} and LLZ metrics are not shown since they were very similar to ΔP_{max} and PL, respectively. cursory inspection of this figure shows very large scatter associated with ΔP_{max} (or equivalently, L_{UE}), implying that it was not a good metric for quantifying subjective loudness. Significant reduction in scatter was evident for L_{CE} , and the least scatter occurred for L_{AE} and PL (and LLZ). This indicates that L_{AE} , PL, and LLZ accounted for the loudness effects of the FSM boom shaping parameters.

Correlation coefficients between levels for each metric and the mean loudness ratings were calculated. These were 0.4937 for ΔP_{max} , 0.8430 for L_{CE} , 0.9581 for L_{AE} , and 0.9561 for PL. All were statistically significant ($p < 0.01$). The correlation coefficients for ΔP_{max} and L_{CE} were both significantly different from those for L_{AE} and PL. However, L_{AE} and PL did not differ significantly.

The above correlation results indicated that L_{AE} and PL correlated highest with the subjective loudness ratings. Consideration of the correlation coefficients alone, however, is not sufficient justification for selecting one or more of the metrics as being better predictor(s) of loudness. To further justify and select a metric, the prediction ability, or accuracy, of each metric was evaluated.

The method used to assess metric prediction accuracy involved application of residual analysis to the data for each metric. Specifically, polynomial regression analysis was used to determine the

best-fit curve describing the relationship between mean loudness ratings and level of each metric. The regression curve for each metric was then used to obtain estimated or "predicted" loudness ratings for each measured level of that metric. The difference between the predicted and obtained loudness ratings was defined as the residual or, equivalently, the prediction error. The standard deviation of the residual for each metric was a measurement of how accurately the metric predicted loudness. The residual standard deviations are shown in figure 9 for all metrics except ΔP_{\max} . These data show that the least accurate predictors were L_{UE} and L_{CE} , which had standard deviations of approximately 1.66 and 0.97 scale units. The most accurate predictor was L_{AE} (standard deviation = 0.35 scale units), followed closely by LLZ and PL (standard deviations of 0.46 and 0.47, respectively). Thus, the L_{AE} metric displayed a slight advantage over PL and LLZ in terms of loudness prediction accuracy. However, the differences between the prediction accuracies of these three metrics were not statistically significant. Consequently, any one of these metrics could be used as loudness predictors without compromising prediction accuracy.

Asymmetry Effects

Loudness effects due to boom signature asymmetry were studied in Experiment 2 using the method of magnitude estimation. These effects are displayed in figures 10(a)-10(d) for signature loudness asymmetries of approximately ± 4 , ± 8 , ± 12 , and ± 16 dB. (Recall that asymmetry was defined earlier as the difference between the PL of the front and back parts of a signature, that is, $PL_f - PL_b$). Shown on each plot are the linear regression lines relating the logarithms of the mean magnitude estimates and total PL for (a) the signatures which have zero or very small loudness asymmetry (heavy solid lines); (b) the signatures for which front loudness is greatest (dashed lines); and (c) those signatures for which the back loudness is greatest (thin solid lines). The regression lines representing the signatures with zero or very small loudness asymmetry are labelled as symmetrical and are identical in each plot.

The results in figures 10(a)-10(d) show that the asymmetrical signatures were generally rated quieter than symmetrical signatures of equivalent total PL. Also, the magnitude of the loudness reductions increased as the degree of asymmetry increased. This is evidenced by consecutive inspection of figures 10(a)-10(d). Of particular interest is the fact that the loudness reductions due to asymmetry also depended upon which half of the signature was loudest. For example, figure 10(d) [for $PL_f - PL_b = \pm 16$ dB] shows that the asymmetrical signatures in which the back half was loudest were rated significantly quieter than those for which the front was loudest. This effect diminished with decreasing asymmetry.

The effect of signature asymmetry is summarized in figure 11 in terms of reductions, or corrections, in calculated total PL as a function of the degree of asymmetry, $PL_f - PL_b$. This curve was obtained from a multiple regression analysis, with loudness ratings the dependent variable and total PL and degree of asymmetry as independent variables. In the analysis asymmetry was included up to third order. The loudness reductions due to asymmetry alone were then obtained by subtracting from the model the effect due to total PL. These loudness reductions were converted to equivalent reductions in total PL by use of the individual linear regression equation slopes (separately obtained) relating loudness to total PL for the loudness data within each asymmetry band.

Figure 11 shows that loudness reductions increased as the degree of asymmetry became increasingly negative ($PL_b \gg PL_f$). Loudness reductions equivalent to about 3 dB in total PL were observed at asymmetries of approximately -16 dB. Only minor reductions in loudness occurred for positive asymmetry values. These effects were not accounted for by any of the loudness metrics. Further, they do not appear to be accounted for by temporal masking, since the delay between the front and back shocks of these signatures was about 300 milliseconds, and significant temporal masking effects generally are limited to delay times of less than 200 milliseconds (reference 6). It is possible that some type of "psychological" masking occurred in which the loudness, or presence, of a quieter front shock tended to divert, or mask, the attention of the subjects such that back shocks were not perceived to be as loud as they would have been in the absence of a front shock. This is speculative, however, and further investigation of asymmetry effects may be warranted in order to gain additional understanding of these results.

Boom Acceptability Considerations

Earlier discussion of boom shaping in Experiment 1 defined subjective loudness on the basis of numerical category scale ratings. This scale provided data in a format appropriate for statistical analysis and loudness estimation but it provided no information on the absolute acceptability of the various booms. Although substantial differences in loudness responses were observed as boom parameters were varied, it was not known whether all, none, or some of the booms were unacceptable in an absolute sense. Consequently, Experiment 1 also collected data for use in quantifying boom acceptability within the laboratory environment. The data were used to approximately anchor the category scale data of Experiment 1 and to compare laboratory acceptability results to acceptance results obtained by other investigators.

The subjective acceptability parameter of interest was the percentage of subjects that rated a given shape as unacceptable. This

parameter is shown in figure 12 as a function of L_{AE} metric level. L_{AE} was selected since it was a slightly better predictor of loudness than PL or LLZ. From figure 12 it was determined that an L_{AE} level of 80 dB corresponds to the level that about 50 percent of the subjects found unacceptable. Also shown in figure 12 by the vertical dashed lines are L_{AE} acceptability levels obtained and/or derived from other sources (references 7 and 8). The vertical dashed line to the right of the figure was derived from the results of reference 7 in which noise simulation systems were placed in the homes of 12 families. As part of the study, the families were asked on a weekly basis to indicate whether or not the booms they were exposed to in the previous week would be acceptable if they were to continue indefinitely. Using results presented in Tables 5-7 of reference 7, the present authors determined that an L_{AE} level of approximately 79 dB (heard 30 times a day) corresponded to 50 percent "YES" responses to the above question. The results of Experiment 1 indicated that an L_{AE} level of 80 dB would be acceptable if heard three or four times a day. A recent study (reference 8) that assessed loudness and other environmental impacts of a high-speed civil transport selected as tentative sonic boom loudness acceptability goals L_{AE} levels of 72 dB for corridors and 65 dB for unconstrained flight. These levels are indicated by the two leftmost vertical dashed lines in figure 12. In terms of the data of Experiment 1, an L_{AE} level of 72 dB was acceptable to about 88 percent of the test subjects and a level of 65 dB to approximately 98 percent of the subjects. Thus, the laboratory results compare reasonably well with the recommendations and results of references 7 and 8.

CONCLUDING REMARKS

The NASA Langley Research Center's sonic boom apparatus was used to quantify human subjective loudness response to a wide range of shaped sonic boom signatures. In addition, loudness acceptability judgments were obtained for a subset of the signatures. The loudness and acceptability results validated the potential of boom shaping to significantly improve public acceptance of sonic booms. Front (and rear) shock minimization was shown to be an effective method for reducing boom loudness with no peak overpressure penalty. That is, significant loudness reductions were achieved by modifying front (and rear) shock parameters (rise time, overpressure ratio) without the necessity of reducing peak overpressure of the signatures. Investigation of sonic boom asymmetry demonstrated that signatures which were asymmetrical in terms of loudness were generally rated quieter than symmetrical signatures of equal total calculated perceived level. Also sonic boom acceptability determined within the laboratory environment compared favorably with acceptability criteria proposed and/or obtained by other investigators for the in-home environment.

Specific conclusions and comments pertinent to the results of the

NASA Langley experimental studies are summarized as follows:

- (1) The effects of varying boom shaping parameters were consistent with results reported by other investigators. Generally, increasing front shock rise time and/or decreasing front shock overpressure were very effective in reducing subjective loudness without the necessity of reducing peak overpressure.
- (2) Secondary rise times of FSM signatures did not affect subjective loudness ratings for the range of values (20 to 50 milliseconds) used in Experiment 2. This result, however, would not apply if secondary rise time is made sufficiently small or is comparable to the rise time of the front shock.
- (3) Correlation and prediction error analysis of the noise metrics indicated that L_{AE} , PL, and LLZ performed well and effectively accounted for the effects of the FSM shaping parameters. Although L_{AE} had a very slight advantage in terms of prediction accuracy, this fact alone is probably not sufficient evidence to justify selecting it as the "best" metric for estimating loudness. It is reasonable to conclude, based upon the results of these studies, that any one of the three metrics could be used to estimate boom loudness effects.
- (4) Loudness reductions due to sonic boom signature asymmetry were strongly dependent upon the "direction" of the asymmetry, that is, upon which part of a signature was loudest. When the rear part was loudest, the reductions in rated loudness were as much as 3 dB for loudness asymmetries approaching -16 dB. The asymmetry effects were not accounted for by any of the loudness metrics.
- (5) The reasonably good agreement of the laboratory acceptability results with results and criteria proposed by others implies that data obtained within the laboratory environment may extend, at least to a limited extent, to more realistic situations. This, however, must be confirmed by results from non-laboratory situations.

References

1. Niedzwiecki, A.; and Ribner, H.S.: Subjective Loudness of N-wave Sonic Booms. J. Acoustical Soc. Am., vol. 64, no. 6, December 1978.
2. Leatherwood, J.D.; Shepherd, K.P.; and Sullivan, B.M.: A New Simulator for Assessing Subjective Effects of Sonic Booms. NASA TM-16912, December 1991.
3. Niedzwiecki, A.; and Ribner, H.S.: Subjective Loudness of "Minimized" Sonic Boom Waveforms. J. Acoustical Soc. Am., vol. 64, no. 6, December 1978.

4. Shepherd, K.P.; and Sullivan, B.M.: Loudness Calculation Procedure Applied to Shaped Sonic Booms. NASA TP-3134, December 1991.
5. Brown, D.E.; and Sullivan, B.M.: Adaptive Equalization of the Acoustic Response in the NASA Langley Sonic Boom Simulator. Proc. Conf. on Advances in Active Control of Sound and Vibration, VPI & SU, Blacksburg, Va, April 15-17, 1991.
6. Zwicker, E.; and Fasti, H.: Psychoacoustics, Springer-Verlag, pp. 72-73, 1990.
7. Mabry, J.E.; and Oncley, P.B.: Establishing Certification/Design Criteria for Advanced Supersonic Aircraft Utilizing Acceptance, Interference, and Annoyance Response to Simulated Sonic Booms by Persons in Their Homes. Report No. FAA-RD-75-44, March 1975.
8. Brown, J.G.; and Haglund, G.T.: Sonic Boom Loudness Study and Airplane Configuration Development. AIAA Paper No. 88-4467, September 1988.

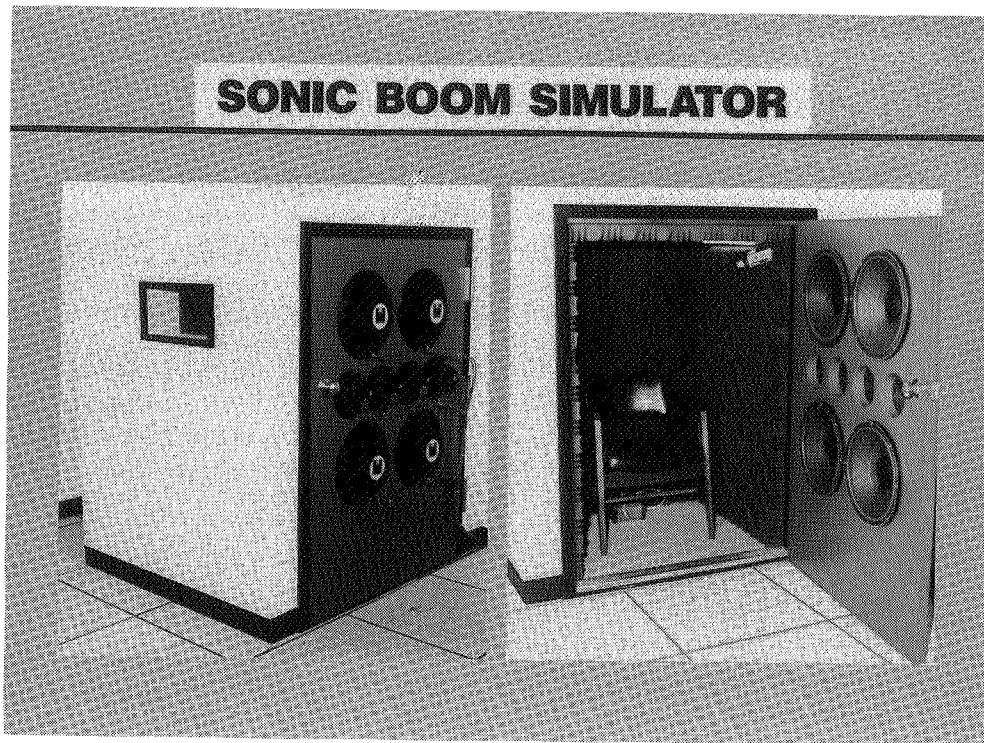


Figure 1.- Sonic Boom Simulator.

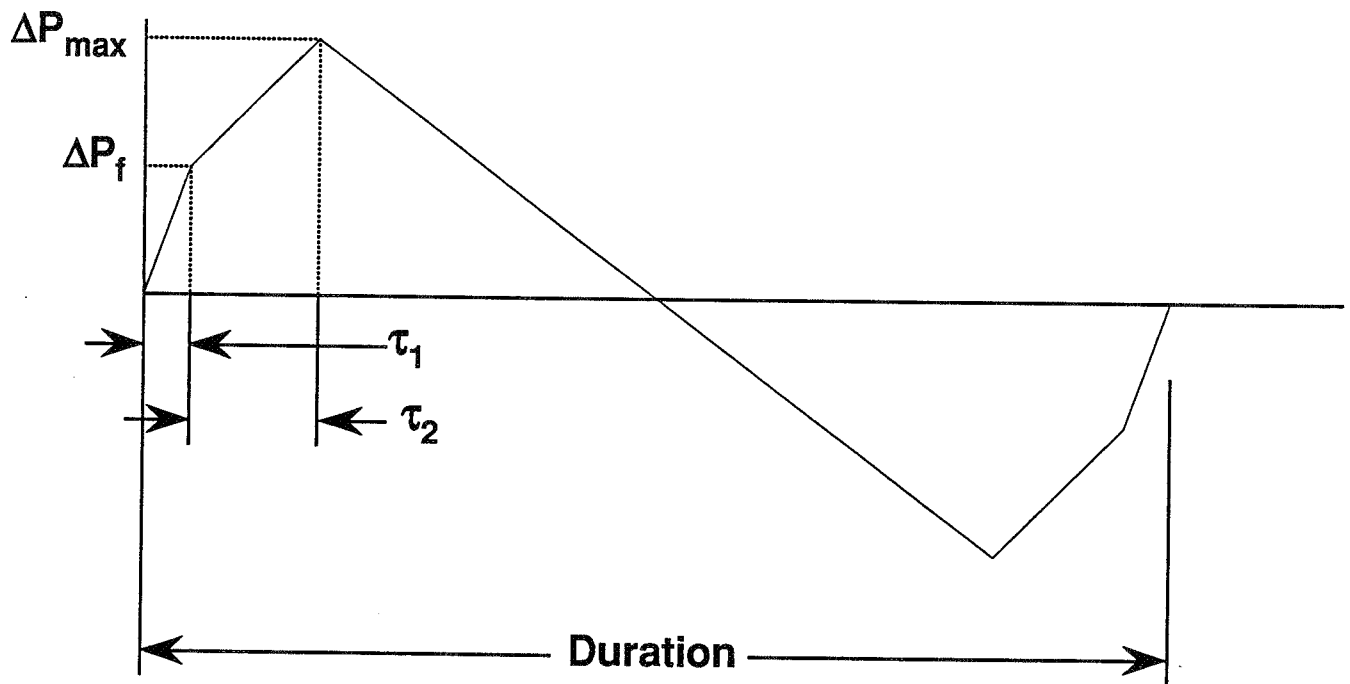


Figure 2.- Shape Parameters for Symmetrical Front Shock Minimized Signatures.

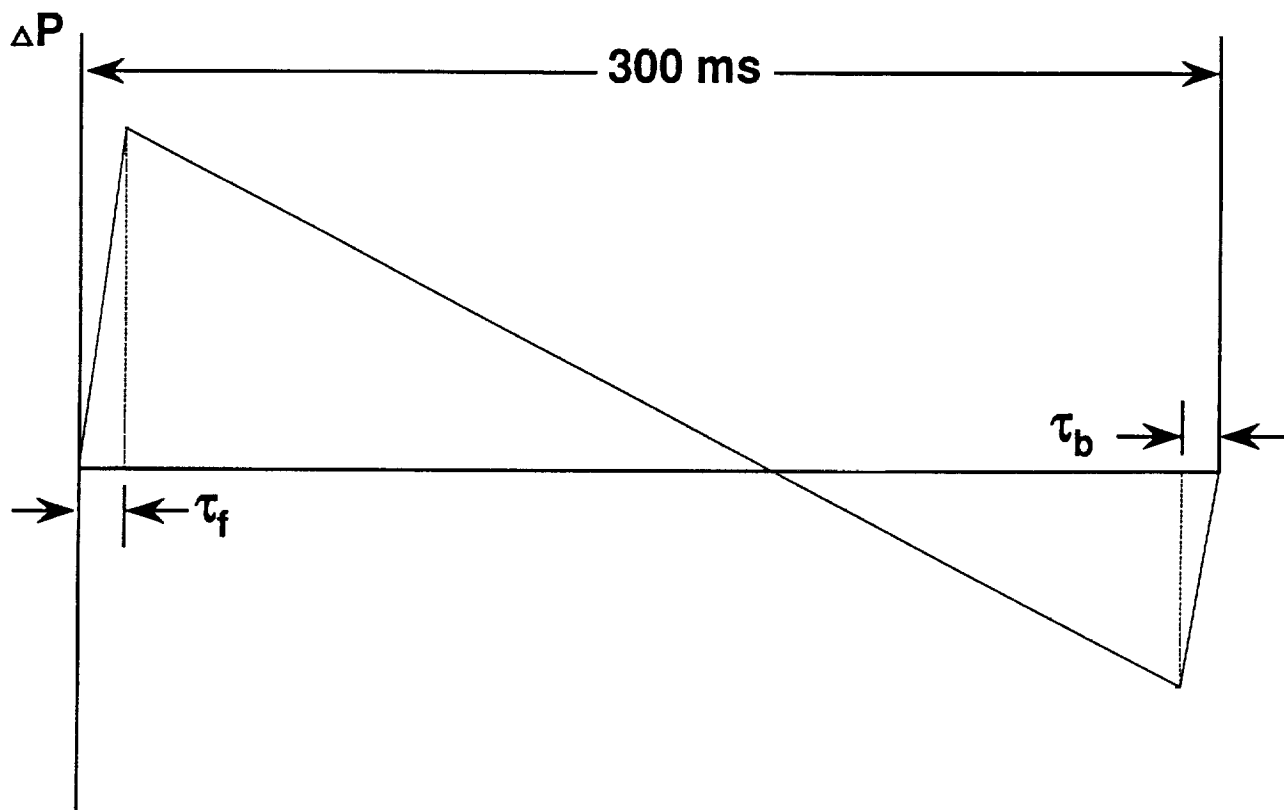


Figure 3.- Shape Parameters for Asymmetrical N-wave Signatures.

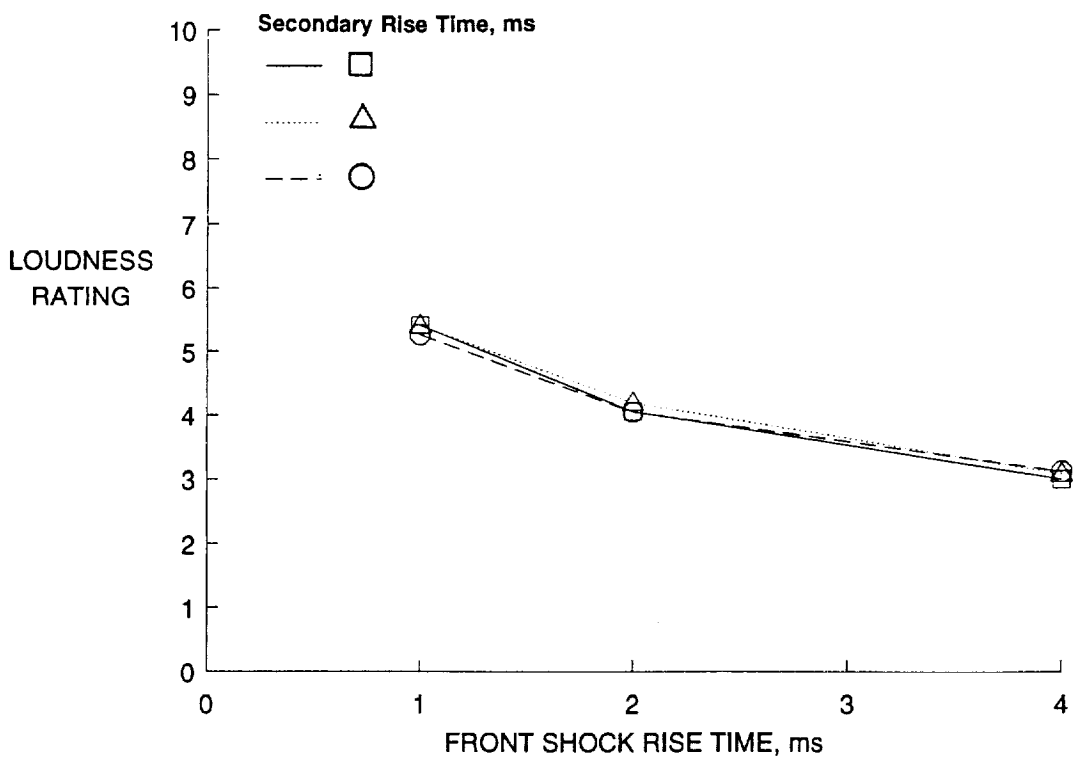


Figure 4.- Overall Effect of Front Shock Rise Time for Symmetrical Front Shock Minimized Signatures and for Secondary Rise Times of 20, 30, and 50 milliseconds.

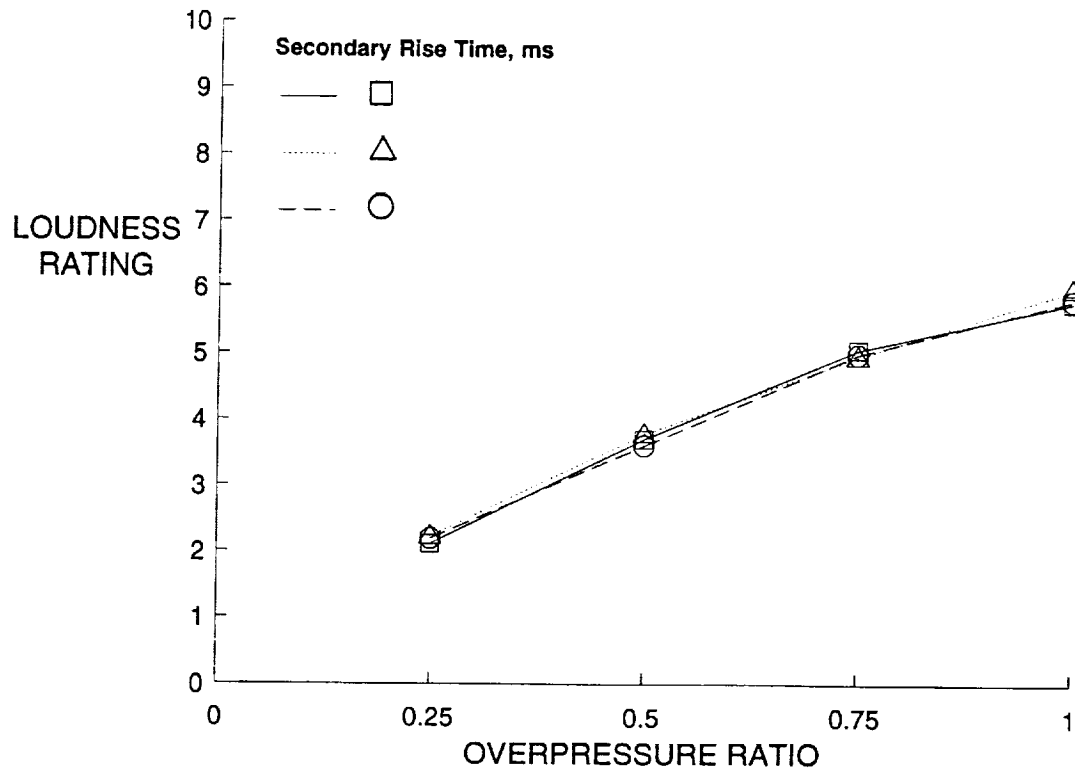


Figure 5.- Overall Effect of Overpressure Ratio for Symmetrical Front Shock Minimized Signatures and for Secondary Rise Times of 20, 30, and 50 milliseconds.

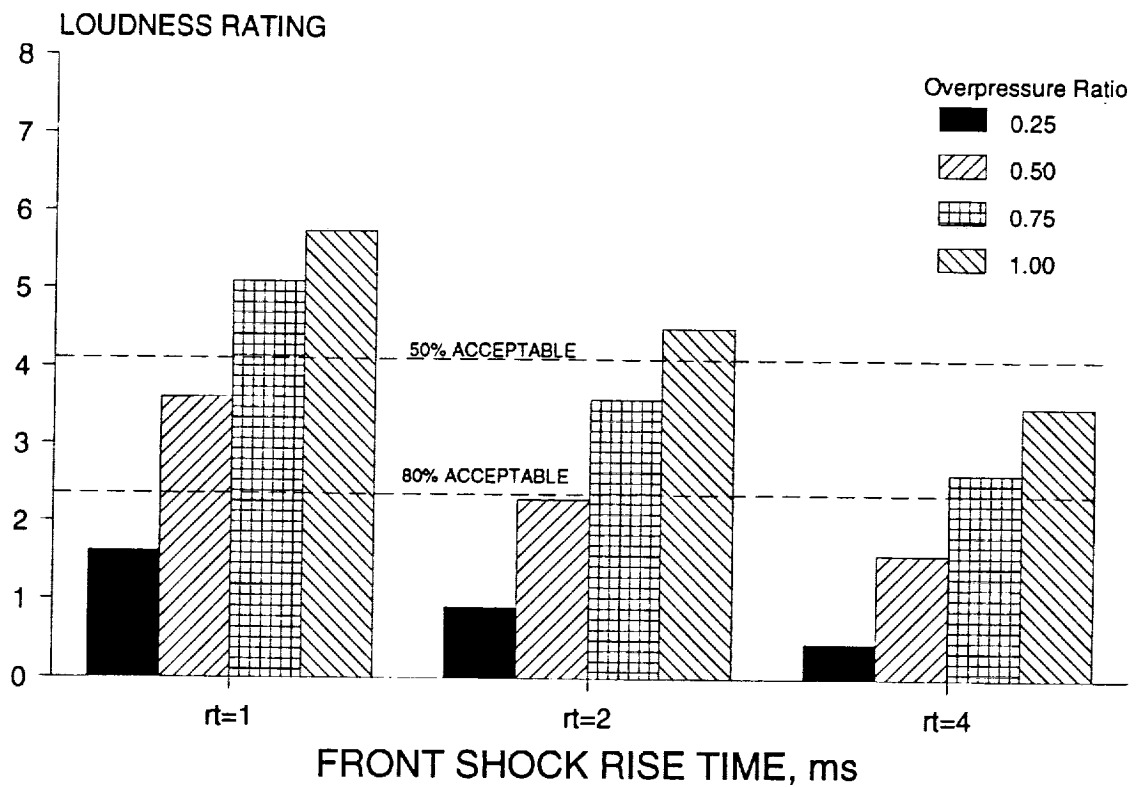


Figure 6.- Front Shock Rise Time and Peak Overpressure Ratio Loudness Tradeoffs for a Peak Overpressure of 1.0 psf.

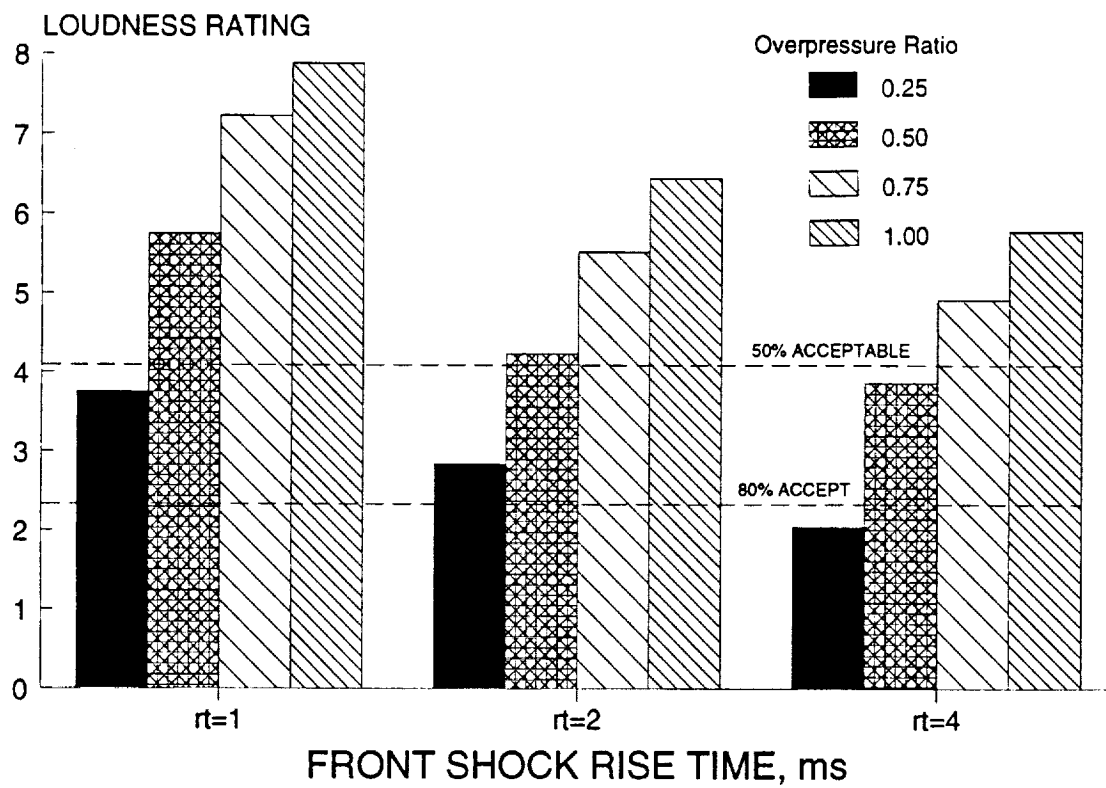
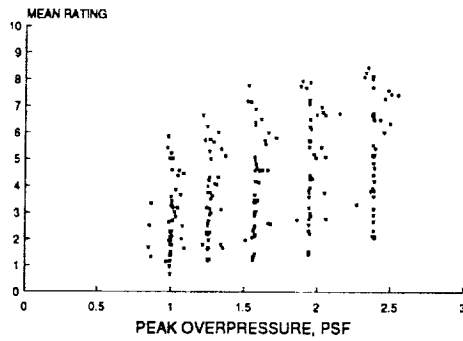
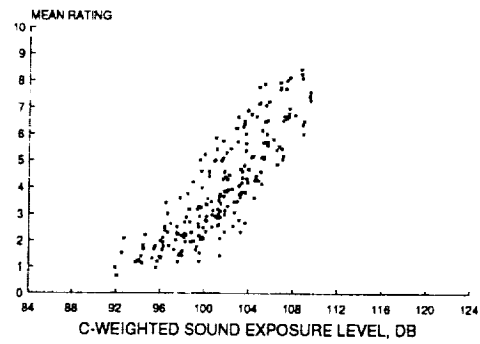


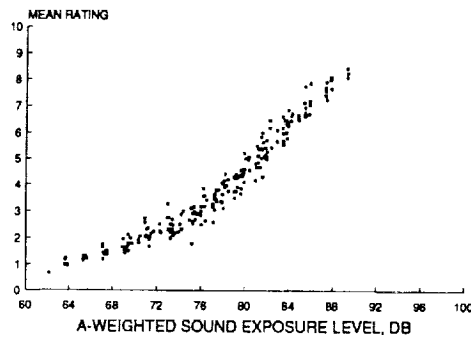
Figure 7.- Front Shock Rise Time and Peak Overpressure Ratio Loudness Tradeoffs for a Peak Overpressure of 2.0 psf.



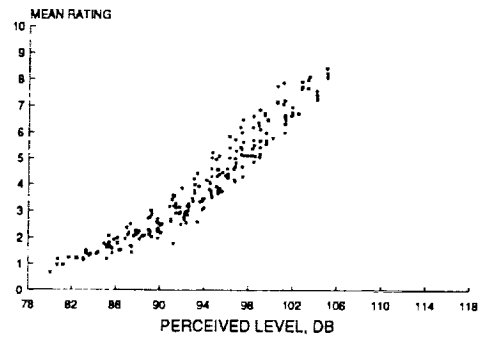
(a) Peak Overpressure, psf



(b) C-Weighted Sound Exposure Level, dB



(c) A-Weighted Sound Exposure Level, dB



(d) Perceived Level, dB

Figure 8.- Loudness metric scatterplots.

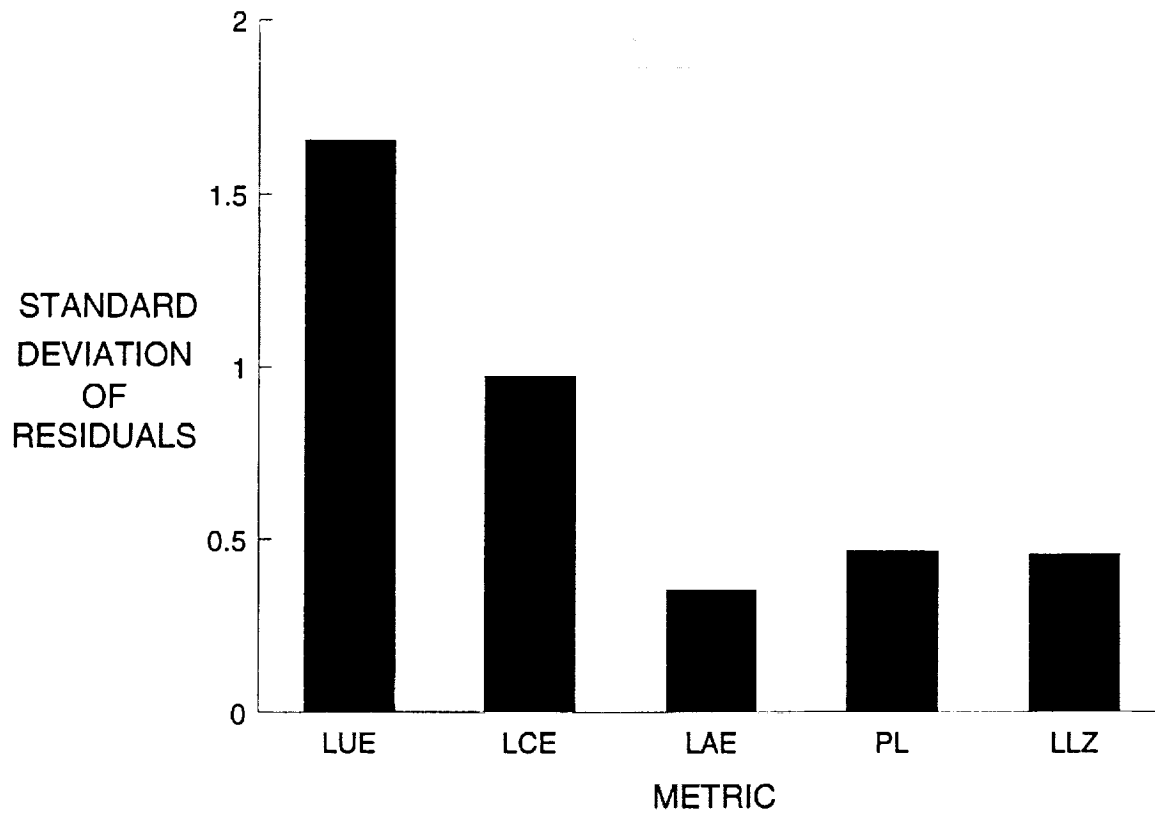
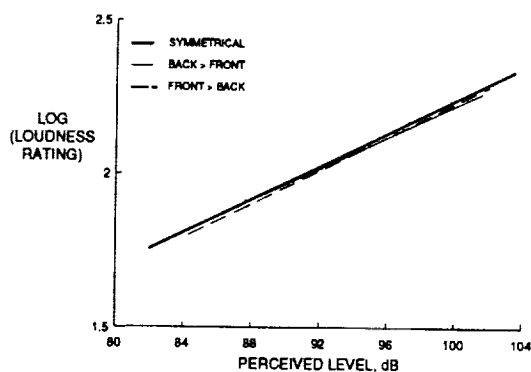
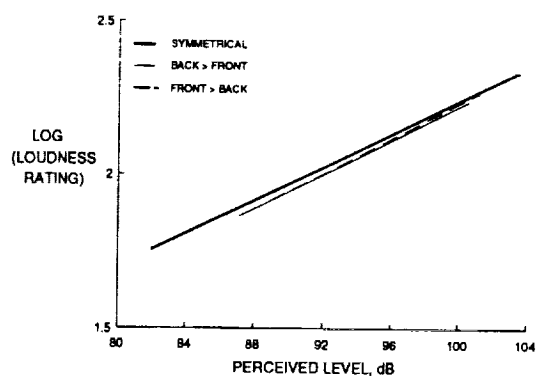


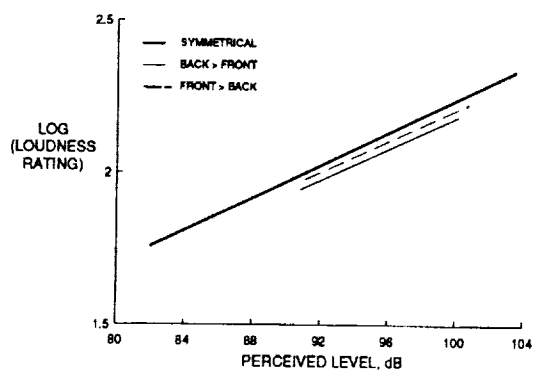
Figure 9.- Standard Deviation of Residuals for Loudness Metrics L_{AE} , L_{CE} , L_{AE} , PL, and LLZ.



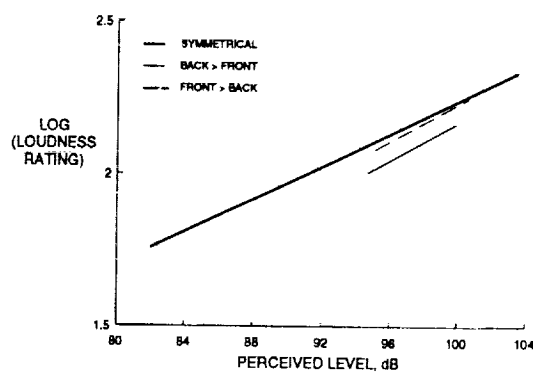
(a) $|PL_f - PL_b| \approx 4 \text{ dB}$



(b) $|PL_f - PL_b| \approx 8 \text{ dB}$



(c) $|PL_f - PL_b| \approx 12 \text{ dB}$



(d) $|PL_f - PL_b| \approx 16 \text{ dB}$

Figure 10.- Loudness Effects of N-wave Signature Asymmetry.

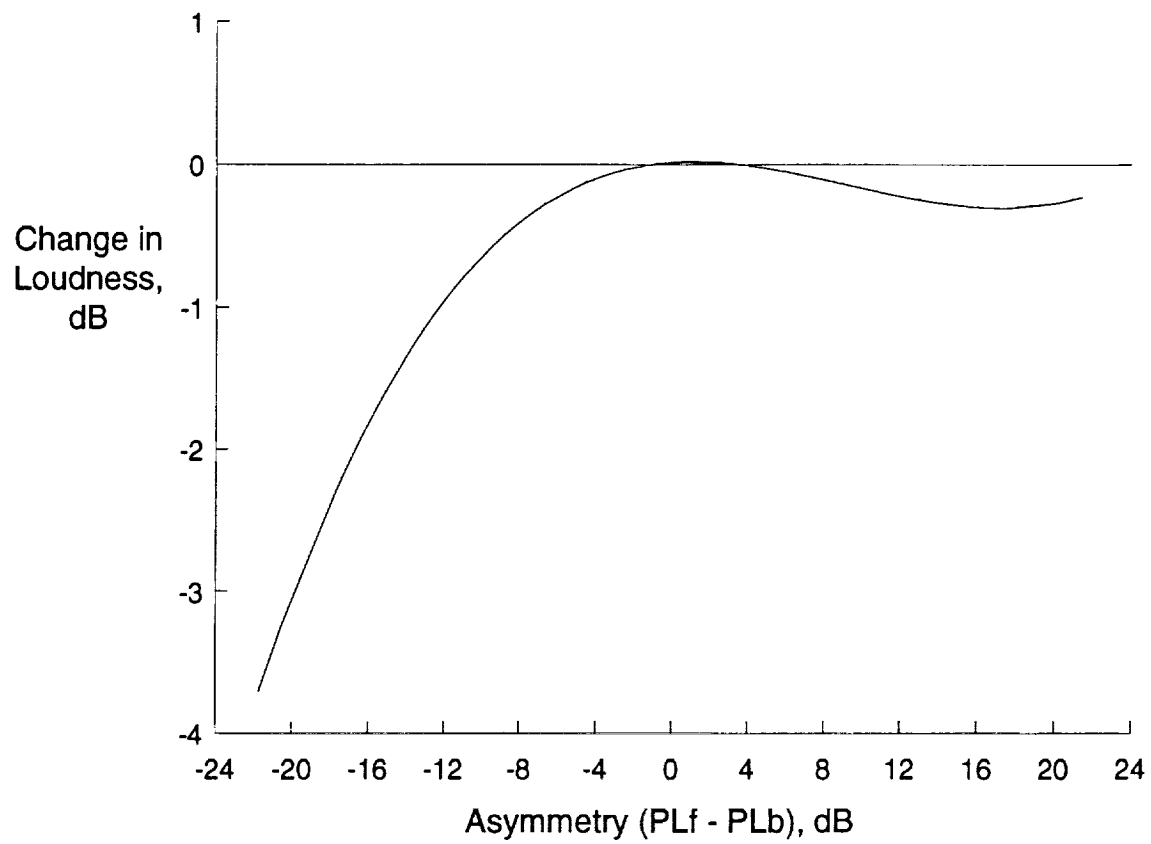


Figure 11.- Predicted N-wave Asymmetry Effect.

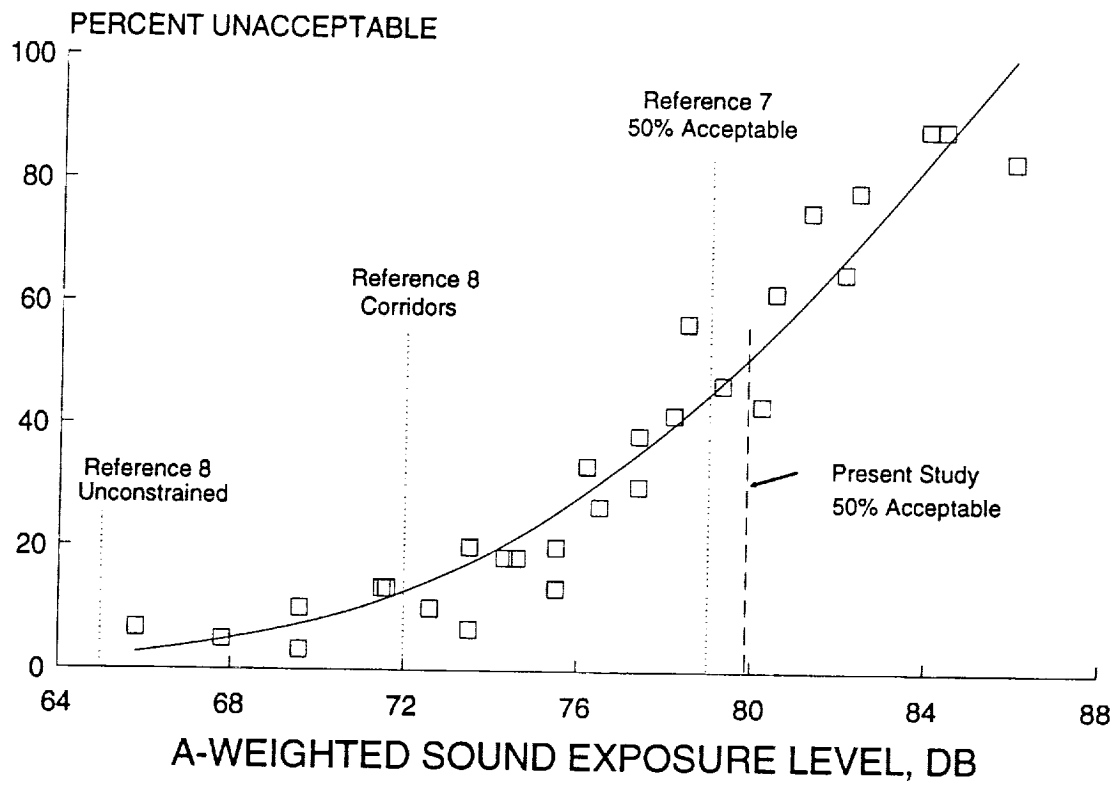


Figure 12.- Percent Unacceptable as a Function of Perceived Level With Comparison to Results/Recommendations of References 7 and 8.

EVALUATION OF HUMAN RESPONSE TO STRUCTURAL VIBRATION INDUCED BY SONIC BOOM

L. C. Sutherland, J. Czech
Consultants to WYLE RESEARCH
El Segundo, California

1.0 INTRODUCTION

This paper addresses the topic of building vibration response to sonic boom and the evaluation of the associated human response to this vibration. The paper reexamines some of the issues addressed in the previous extensive coverage of the topic, primarily by NASA, and attempts to offer a fresh viewpoint for some of the problems that may assist in reassessing the potential impact of sonic boom over populated areas.

The topics addressed are: 1) human response to vibration; 2) criteria for, and acoustic signature of rattle; 3) structural response to shaped booms, including definition of two new descriptors for assessing the structural response to sonic boom; and 4) a detailed review of the previous NASA/FAA Sonic Boom Test Program involving structural response measurements at Edwards AFB and an initial estimate of structural response to sonic booms from possible HSCT configurations. Finally, these estimated vibration responses are shown to be substantially greater than the human response and rattle criteria developed earlier.

The results presented herein would not have been possible without the vast amount of research in the area published previously by NASA (e.g., Mayes and Edge, 1964; Findley, Huckle and Hubbard, 1975; Hubbard and Mayes, 1967; Cardon and Mayes, 1970; Clarkson and Mayes, 1972; Clevenson, 1978; Hubbard, 1982).

2.0 CRITERIA FOR HUMAN VIBRATION AND THE ONSET OF RATTLE

For purposes of this study, the revised composite whole-body and tactile vibration perception criteria curve shown in Figure 1 as a function of frequency is developed. It represents a composite average of previously published criteria curves for whole body vibration (ISO, 1985, 1989; Goldman and von Gierke, 1961) and published studies on tactile vibration (Goldman, 1957; Verillo, 1962).

The difference between response to steady-state vs impulsive vibration suggests, as indicated in Figure 2, a "vibration exposure" or vibration energy descriptor as one possible way to evaluate duration effects on response to transient vibration from sonic booms. However, further experimental evaluation of this concept is needed (e.g., Clevenson, et al., 1978).

New data on the acoustic signature of rattling objects are shown in Figure 3 corresponding to the type of high frequency rattle noise shown in Figure 4 first reported by NASA from sonic boom tests (Hubbard and Mayes, 1967). These data indicate that once rattle occurs, it will almost certainly be audible in normal ambient noise background noise. Results of subsequent research by NASA on rattle thresholds (see Figure 5 & 6) and other research (Tokita and Nakamura, 1981) summarized in Figure 7, combined with simple theoretical models for the occurrence of rattle, indicate a consistent pattern for the acceleration required to induce rattle – a peak acceleration of 0.045 ± 0.012 g's.

3.0 PREDICTING STRUCTURAL RESPONSE TO SONIC BOOM

Typical measurements of structural response to sonic boom, such as shown in Figure 8, tend to support the use of relatively simple Single Degree of Freedom (SDOF) models for approximate evaluation of the dominant vibration response of structures to sonic boom. Such response is typically dominated by response in the fundamental vibration mode of the structure.

A well known method to predict response of structure treated as SDOF systems to sonic booms is the classical Shock Response Spectrum method illustrated in Figure 8 by the Displacement Shock response to a sonic boom and Figure 9 by the Acceleration Shock

response to ideal N-waves. The Shock Spectra indicate the peak response of a SDOF model of a structure to a transient (i.e., sonic boom) load, relative to its response to a static load of the same magnitude. This spectra varies as a non-dimensional frequency, $f_0 \cdot T$, where f_0 is the fundamental resonance frequency and T is the boom duration.

This method was applied to evaluate the response of various shaped sonic booms as shown in Figures 10 and 11. For boom signatures which do not include any effects of diffraction around a finite size wall, the shock response spectra for the various shaped booms is not markedly different as expected due to the relatively little change in their pressure spectra at the low frequency range coincident with their structural resonance frequencies (Sutherland, Brown and Goerner, 1990). When diffraction of the incident boom is taken into account, the shock response spectra decreases significantly (See Figure 11). Methods to evaluate diffracted sonic boom loading on buildings, first developed from well established blast loading concepts for ideal sonic booms, are illustrated in Figure 12. They depend on the use of diffraction loading adjustment to the incident wave form that corresponds to a pressure doubling of the incident pressure at the moment of incidence and reducing by 50% to just the incident pressure after a "clearing time" τ equal to $3S/V$, where S is a characteristic front face dimension of a finite wall and V is the wave front velocity (ARDE Associates, 1959). This same principle can be applied to shaped booms, with the use of a convolution integral concept illustrated in Figure 13, by treating the shaped boom as the sum of a series of step pulses whose magnitude is proportional to the slope of the pressure time history. However, as indicated by the results in Figure 11, including diffraction can be expected to normally reduce the structural response below that without diffraction.

A new method for analyzing structural response to sonic boom employs a measure of the total energy, or Acceleration Exposure, E_A , in the transient vibration response signal. The Acceleration Exposure can be conveniently determined from the absolute value of the Fourier Spectra of a sonic boom and the absolute value of a frequency response function for a SDOF system. A related quantity, an (energy) Equivalent Peak Acceleration illustrated in Figure 14, can also be readily computed from this Acceleration Exposure. This Equivalent Peak Acceleration is the peak acceleration of a simple damped-sine acceleration signal with the same energy (i.e., same E_A) as the actual acceleration signal. Representative values for this Equivalent Peak Acceleration are shown in Figure 15 as a function of resonance frequency for a damped SDOF system with an effective surface weight of 5 psf (typical for residential walls) responding to an ideal (N-wave) sonic boom with a pressure of 1 psf. The effect of damping is also shown, however, unlike response to steady-state vibration, damping has a less significant effect on the peak response magnitude to transient excitation. As shown in Figure 16, this Equivalent Peak Acceleration has very nearly the same value as the Peak Acceleration obtained from the Shock Response Spectrum. Note, however, the Equivalent Peak Acceleration shows a much stronger peak at a small value of $f_0 T$ due to the fact that this measure is sensitive to the duration of the transient response as well as its magnitude. In both cases, with the exception of this initial peak, significant only for structures with very low resonance frequencies, the peak acceleration varies in roughly the same manner with the non-dimensional frequency parameter $f_0 T$.

4.0 REVIEW OF EDWARDS AFB SONIC BOOM TEST DATA ON STRUCTURAL RESPONSE

In support of these analytical methods, a detailed review was made of NASA-sponsored measurements on two residential dwellings (indicated in the layout of the test geometry in Figure 17) in one of the largest sonic boom structural response programs ever conducted (Phase I of the Edwards AFB Tests in 1967). A detailed regression analysis of the relationship between peak acceleration and peak sonic boom pressure data from these tests, such as illustrated in Figure 18, provided the basis for empirical corrections to the preceding

simple SDOF structural response models to account for the more complex vibration response patterns of internal elements (i.e., floor, ceiling) of residential structures. The scatter in the data in Figure 18 is due, in part, to the differences between the sonic boom loading generated by the two different aircraft included in this evaluation (data from a limited number of B-70 measurements were also available from the test results (SRI, 1967) and to variations in pressure loading due to atmospheric effects.

Figures 19 and 20 illustrate the comparison between the average measured and predicted peak acceleration responses for walls, floors and ceilings from these data. The peak acceleration is shown in the non-dimensional form indicated by the analytical models as [peak acceleration x surface weight/peak pressure]. As indicated in Figure 19, the predicted response for the walls are, on average, roughly comparable to the measured values. This is to be expected since the actual wall vibration response corresponds most closely to the simple SDOF model. Figure 20 indicates that the simple prediction model generally under-predicts the average ceiling response and over-predicts the average floor response. These deviations can be used to provide approximate adjustment factors to make initial approximate predictions of the response of floor and ceiling elements of structure to sonic booms, as well as walls.

5.0 ESTIMATED VIBRATION RESPONSES FOR HSCT BOOMS VS CRITERIA

The result of applying such experimentally-based corrections to estimates of the Equivalent Peak Acceleration, $A(eq)_{pk}$, is indicated in Table 1 by the example estimated values for the structural response of walls and floors of typical wood-frame residential buildings to a reference HSCT sonic boom with a peak pressure of 1 psf, a rise/fall time of 8 ms and duration of 350 ms. The estimated response values are shown in Table 1 in terms of both peak acceleration and acceleration exposure level. The latter is the acceleration exposure expressed in a logarithmic form, in decibels, relative to a reference acceleration exposure equal to $(1\mu g)^2 \cdot \text{sec}$.

The significance of these estimates of boom-induced structural vibration is also provided in Table 1 by a comparison between the estimated vibration responses and the criteria for human response and, for peak acceleration, rattle thresholds. For convenience, the ratio between the estimated environment levels and the criteria is expressed in decibels. It is apparent that the estimated sonic-boom induced responses would be expected to be substantially greater than the human response criteria or the rattle threshold criteria. The difference between the estimated environment and vibration criteria range from a high of 36 dB (a factor of 63 to 1 in magnitude) for the peak acceleration of walls and human response (e.g., tactile) vibration criteria to a low of 16 dB (factor of 6.2 to 1) for the rattle threshold.

When a comparison is made in terms of acceleration exposure, while the criteria are only rough estimates, the difference between estimated environment and criterion levels is reduced substantially. However, further research on human response criteria for short transient vibration is suggested.

Although there are many approximations in the analysis carried out here, it seems unlikely that a refined analysis of structural vibration response to the boom wave forms would modify these general results.

Estimates presented in the paper of structural response for shaped sonic booms of the same peak pressure, while limited, do not indicate a major change in the preceding results.

REFERENCES

- ARDE Associates, (1959) "Response of structure to aircraft generated shock waves," WADC Technical Report 58-169, April 1959.
- Cardon H.D. and Mayes, W.H. (1970) "Measured vibration response characteristics of four residential structures excited by mechanical and acoustical loadings," NASA Langley Research Center, NASA TN-D-5776, April 1970.
- Clarkson, B.L. and Mayes, W.H. (1972) "Sonic-boom induced building structure responses including damage", J. Acoust.Soc. Am. 51: 742-757.
- Clevenson, S.A. (1978) "Experimental determination of the rattle of simple models," NASA Langley Research Center, NASA TM 78756, July, 1978.
- Clevenson, S.A., et al. (1978) "Effect of vibration duration on human discomfort," NASA TP-1283, September 1978.
- Findley, D.S., Huckle, V. and Hubbard, H.H. (1975) "Vibration responses of Test Structure No. 2 during the Edwards Air Force Base Phase of the National Sonic Boom Program," NASA TM X-72704, NASA Langley Research Center, 1975.
- Goldman, D.E. (1957), "Effects of vibration on man," "Handbook of Noise Control," C.M Harris (ed), McGraw-Hill Book Co., N.Y., 1957.
- Goldman, D.E. and von Gierke, H.E. (1961), "Effects of shock and vibration on man," Chapter 44, "Shock and Vibration Handbook," C.M Harris and C.E. Crede (eds), McGraw-Hill Book Co. N.Y., 1961.
- Hubbard, H.H. (1982) "Noise induced house vibrations and human perception," Noise Control Engr. 19, 49-55, Sept.-Oct.1982.
- Hubbard, H.H. and Mayes, W.H.(1967) "Sonic boom effects on people and structures," in "Sonic Boom Effects," Seebass, A.R. (ed), NASA Langley Research Center, NASA SP-147, 65-76, 1967.
- International Organization for Standardization (1985) "Evaluation of human exposure to whole-body vibration - Part 1: General requirements," ISO 2631-1:1985.
- International Organization for Standardization (1989) "Evaluation of human exposure to whole-body vibration - Part 2: Continuous and shock-induced vibration in buildings (1 to 80 Hz)," ISO 2631-2:1989.
- Mayes, W.H. and Edge, P.M. (1964) "Response of ground buildings to sonic booms," Symposium on effect of sonic blast on buildings, Chicago, June 25, 1964.
- Stanford Research Institute (1967) "Sonic boom experiments at Edwards Air Force Base," Interim Report for National Sonic Boom Evaluation Office, July 1967.
- Sutherland, L.C. (ed) (1968) "Sonic and vibration environments for ground facilities - a design manual," Wyle Research Report WR 68-2, 1968.

Sutherland, L.C., Brown, R. and Goerner, D. (1990) "Evaluation of potential damage to unconventional structures by sonic booms," Wyle Research Report for Tyndall AFB, HSD-TR-90-021, June 1990.

Tokita, Y. and Nakamura, S. (1981) "Frequency weighting characteristics for evaluation of low frequency sounds," Proc. INTERNOISE-81, The Netherlands, pp 739-742, October 1981.

Verillo, R.T. (1962) "Investigation of some parameters of the cutaneous threshold for vibration," J. Acoust.Soc. Am. 34, 1768-1773, 1962.

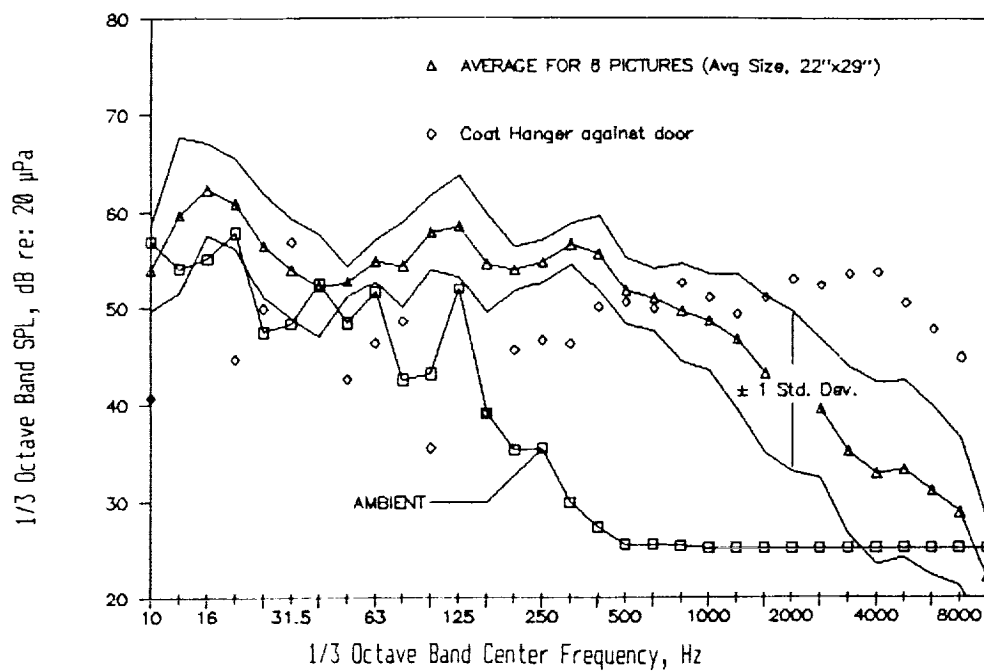


FIGURE 3. 1/3rd OCTAVE BAND LEVEL SPECTRA OF WALL-RATTLING OBJECTS

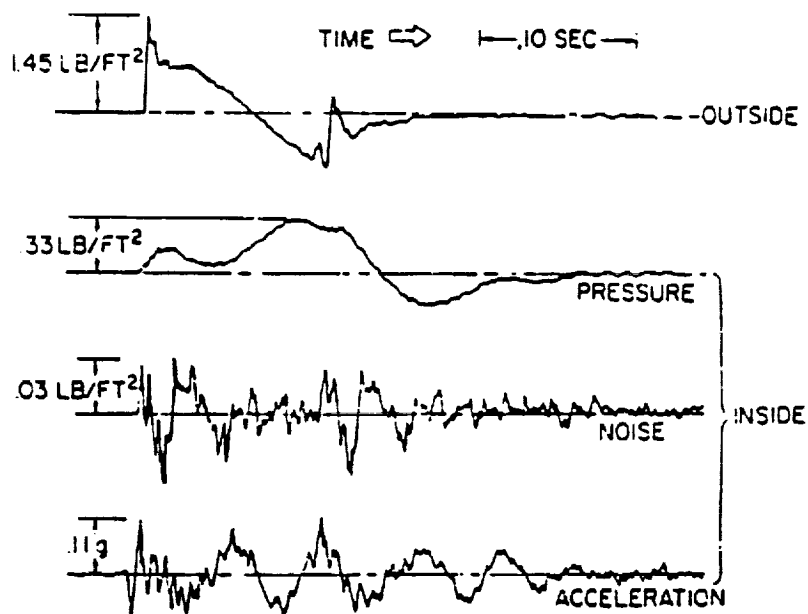


FIGURE 4. OUTSIDE & INSIDE NOISE AND STRUCTURAL VIBRATION FROM
EARLY NASA SONIC BOOM TESTS DEMONSTRATING PROBABLE
RATTLE SOUNDS (Hubbard and Mayes, 1967)

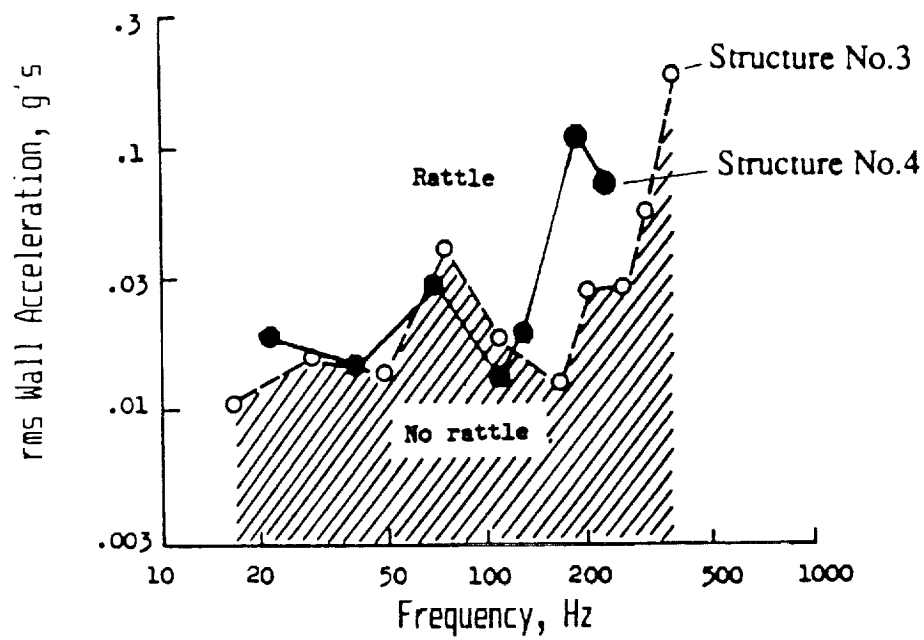


FIGURE 5. RATTLE THRESHOLD FOR WALL-MOUNTED PLAQUES (Cardon & Mayes, 1971)

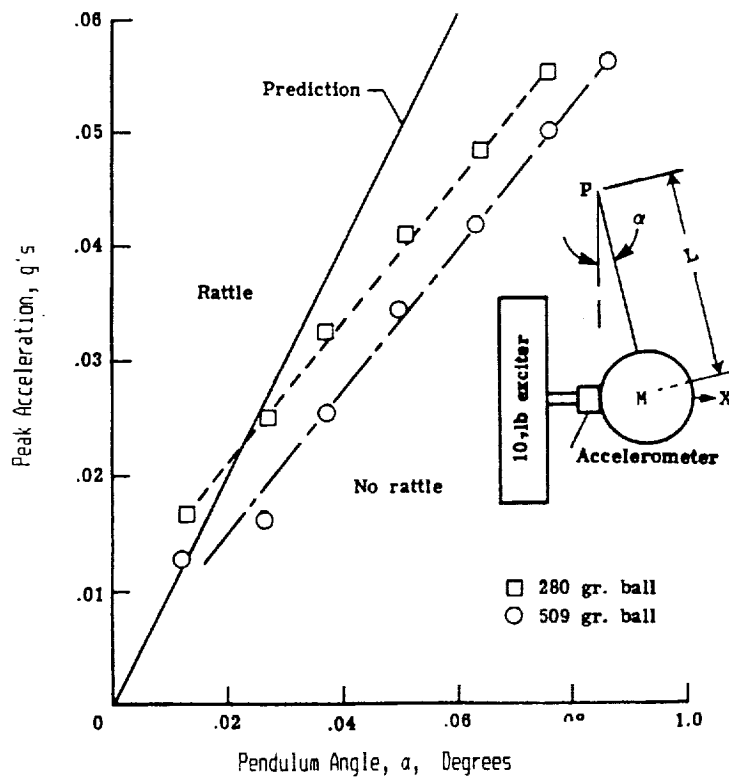


FIGURE 6. RATTLE THRESHOLD OF VERTICAL PENDULUM (Clevenson, 1978)

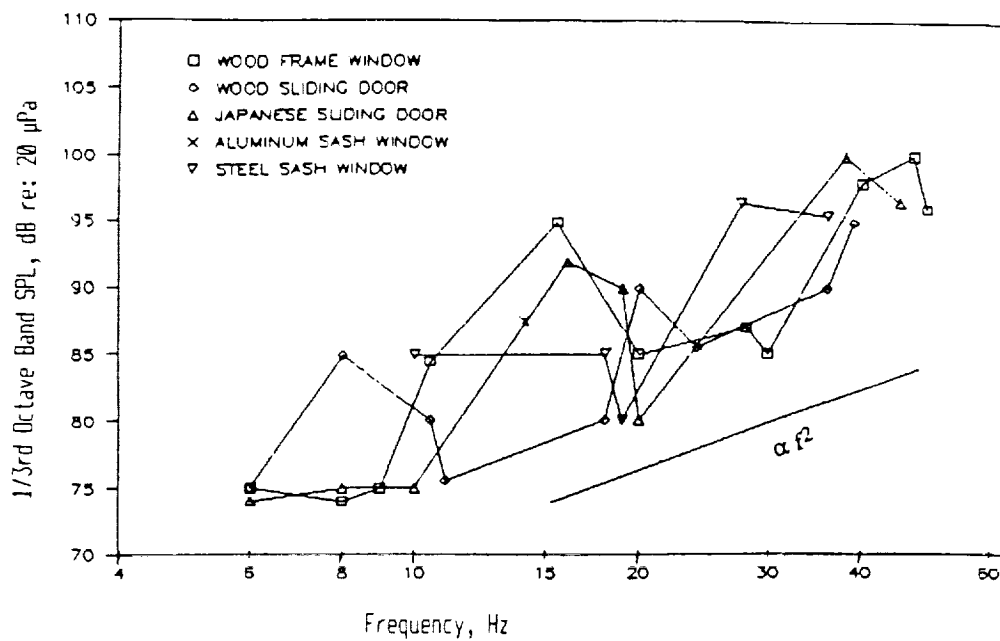


FIGURE 7. RATTLE THRESHOLD FOR BUILDING ELEMENTS INDUCED BY WIDE-BAND RANDOM NOISE (Tokita and Nakamura, 1981)

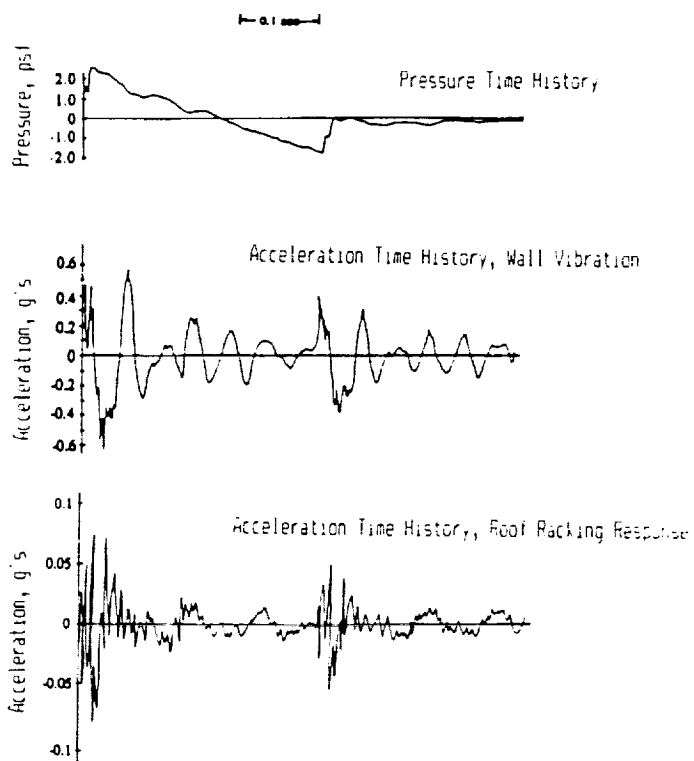
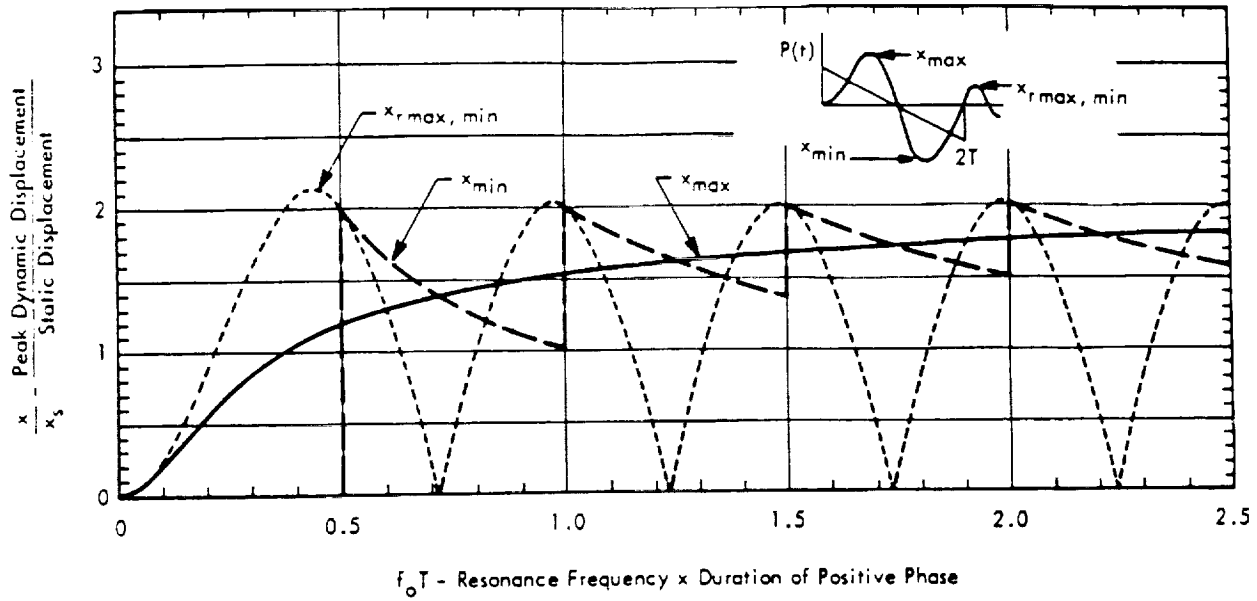


FIGURE 8. TYPICAL STRUCTURAL RESPONSE OF RESIDENTIAL BUILDINGS TO SONIC BOOM (Edwards AFB Sonic Boom Tests, 1966)

a) Displacement Shock Response Spectrum (Undamped System)



b) Acceleration Shock Response Spectrum (Damped System)

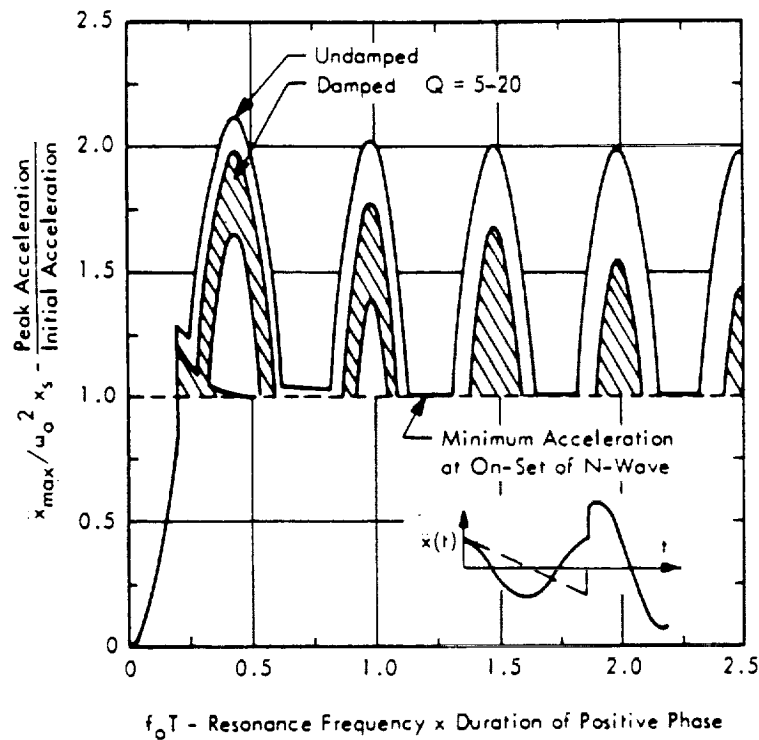


Figure 9. Displacement and Acceleration Shock Response Spectra for Simple Mass-Spring (SDOF) System Responding to Ideal N-Wave (from Sutherland, ed., 1968)

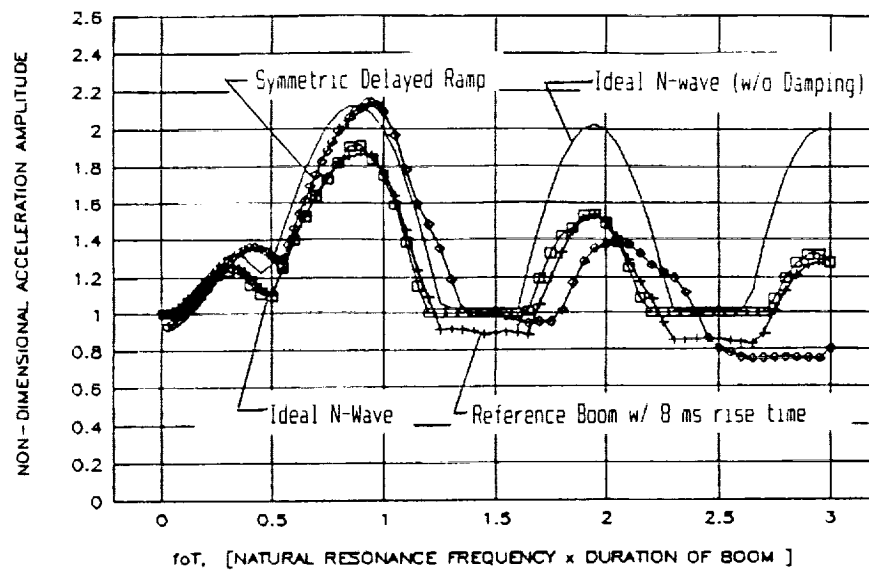


FIGURE 10. ACCELERATION SHOCK RESPONSE SPECTRA FOR RESPONSE OF DAMPED SDOF SYSTEM with $Q = 10$ TO VARIOUS BOOM WAVE SHAPES

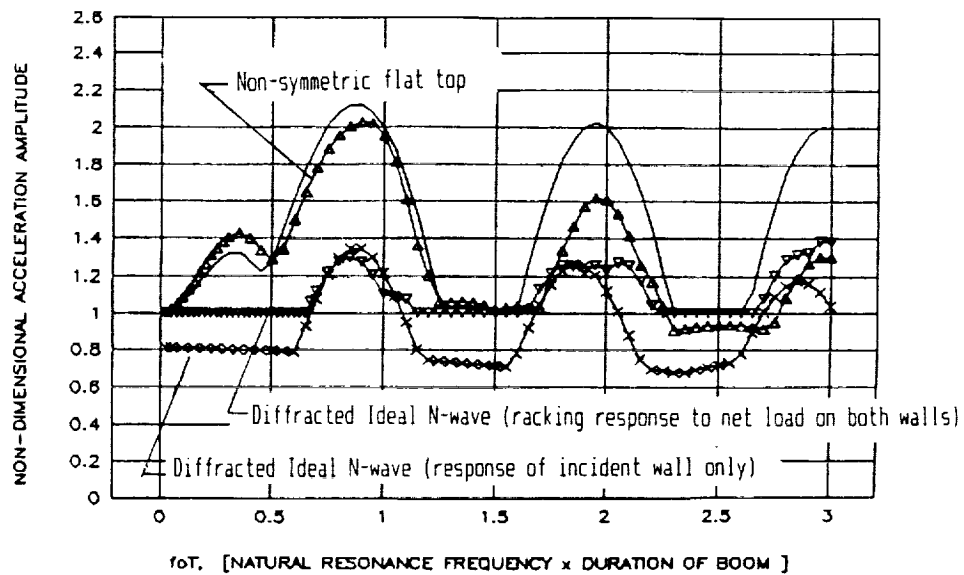


FIGURE 11. ACCELERATION SHOCK RESPONSE SPECTRA FOR DAMPED SDOF RESPONSE TO VARIOUS BOOM WAVE SHAPES SYSTEM with $Q = 10$

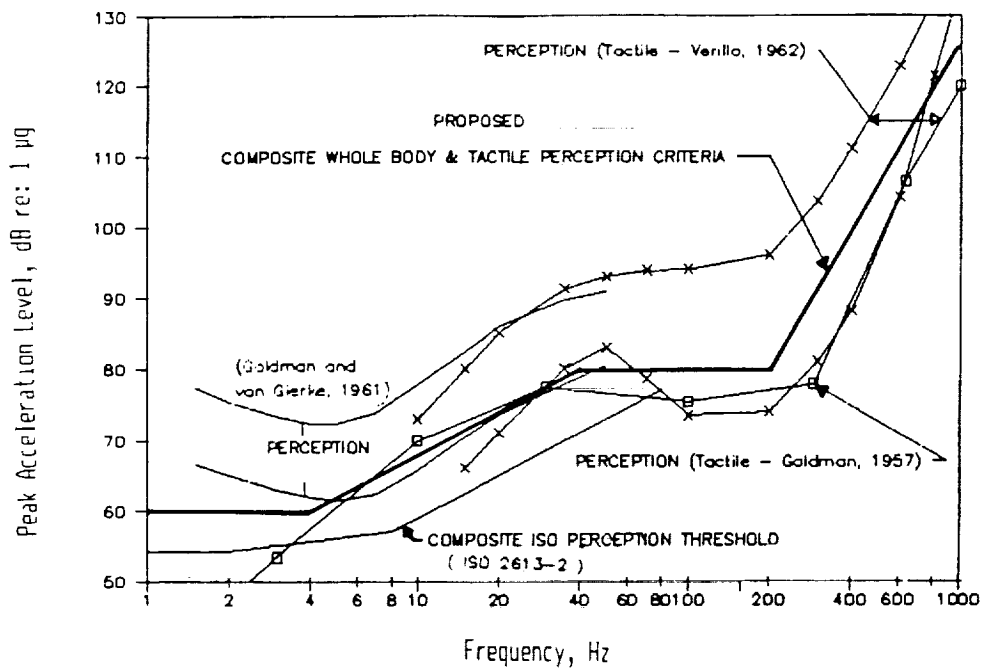


Figure 1. COMPOSITE WHOLE-BODY and TACTILE VIBRATION CRITERIA

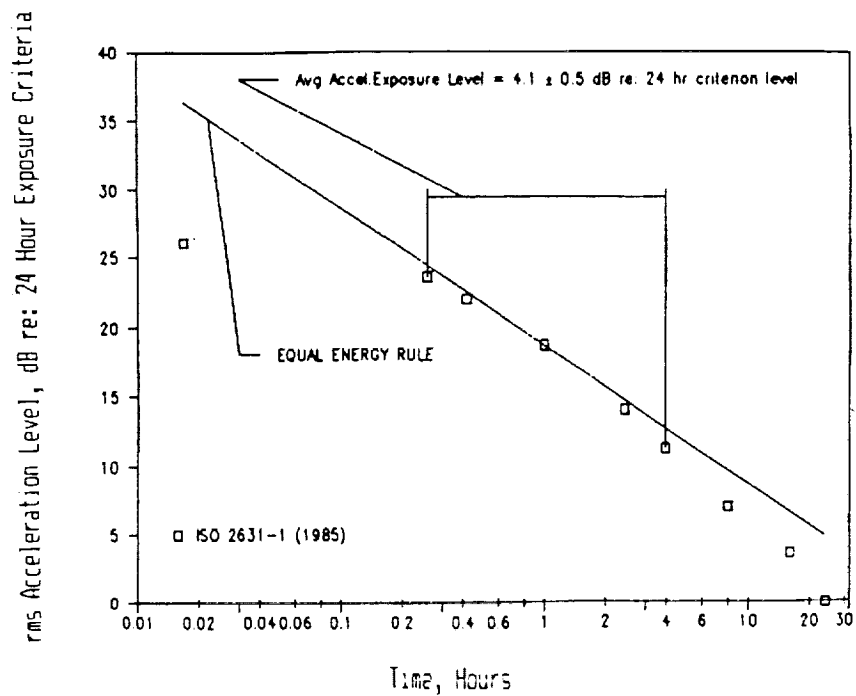


Figure 2. EQUAL ENERGY RULE SUGGESTED BY STANDARD (ISO-9613-1)
ON HUMAN RESPONSE TO VIBRATION OF VARYING DURATION

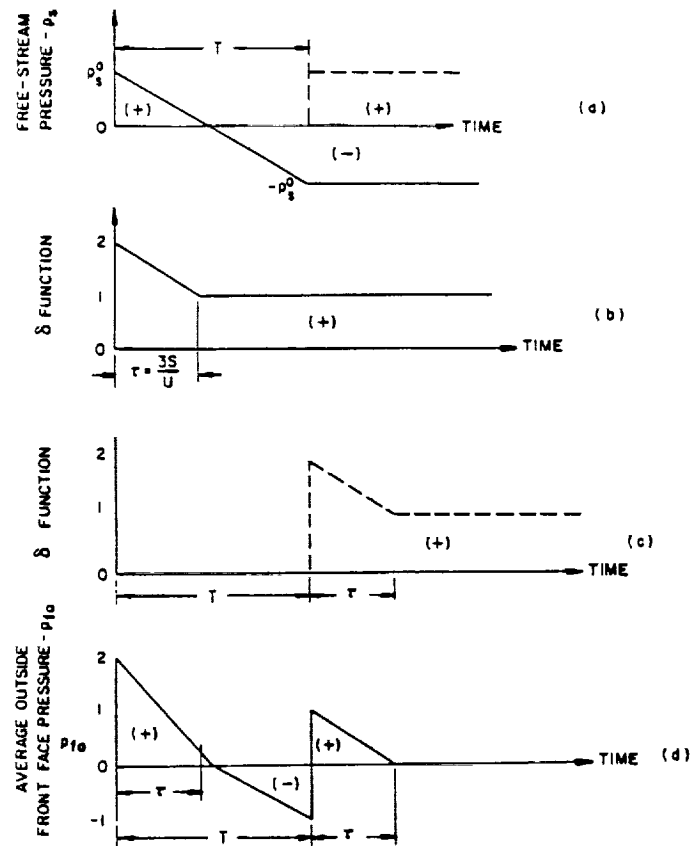
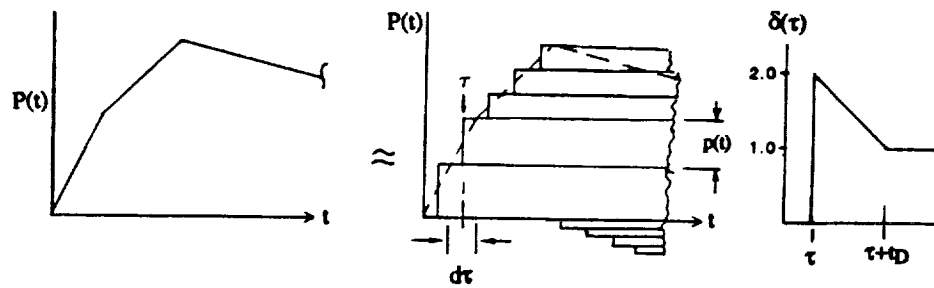


FIGURE 12. DIFFRACTED SONIC BOOM LOAD ON FINITE SIZE WALL FOR IDEAL N-WAVE LOADING (ARDE Assoc., 1959)



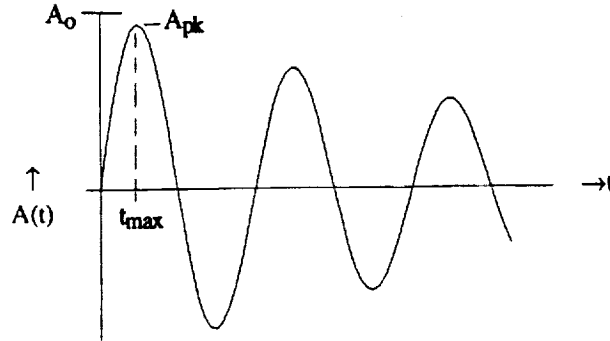
$$P_o(t) = \int_{\tau=0}^t \delta(t-\tau) \frac{dP(\tau)}{d\tau} \cdot d\tau$$

FIGURE 13. CONVOLUTION METHOD FOR COMPUTING DIFFRACTED LOADING FOR SHAPED, NON-IDEAL SONIC BOOMS BY SUMMING UP SERIES OF RAMPS

ACCELERATION EXPOSURE, E_A = Energy in Acceleration Time History, $A(t)$

= Energy in Acceleration Spectra, $|A(f)|$ or

$$E_A = \int_0^T A^2(t) dt = 2 \int_0^\infty |A(f)|^2 df \approx [A_0^2 / (4\pi f_0)] \cdot [Q - 1/4Q]$$



EQUIVALENT PEAK ACCELERATION = Peak Acceleration of Damped Sine

w/ SAME ENERGY (Same E_A) as actual acceleration response or

$$A(eq)_{pk} = [4\pi f_0 \cdot E_A \cdot e^{-\pi/2Q}]^{1/2} \cdot [Q - 1/4Q]^{-1/2}$$

FIGURE 14. ACCELERATION EXPOSURE AND EQUIVALENT PEAK ACCELERATION

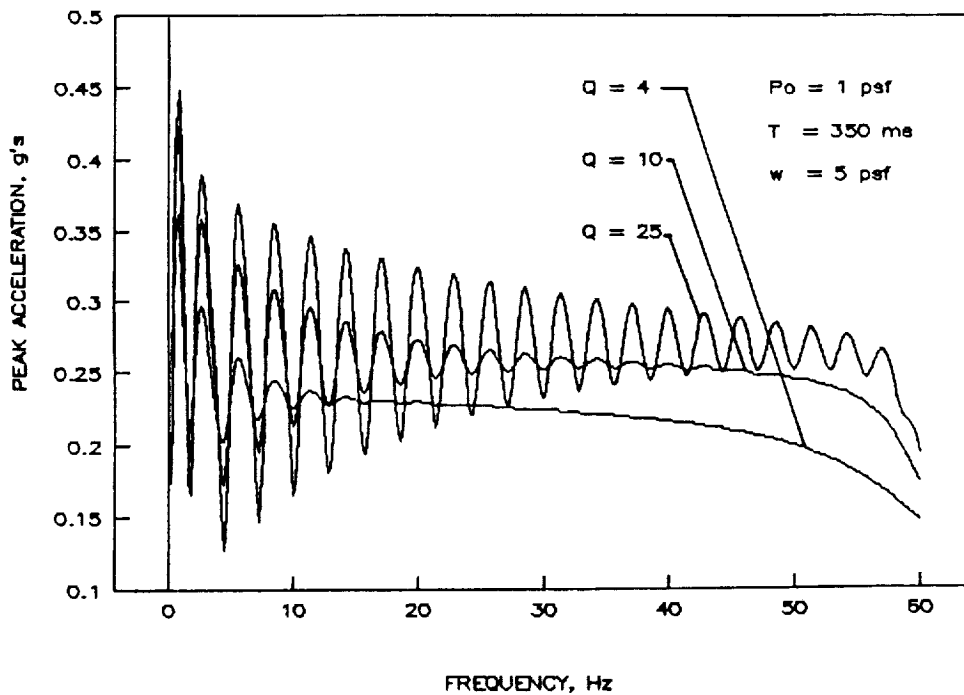


FIGURE 15. EQUIVALENT PEAK ACCELERATION RESPONSE OF DAMPED SDOF SYSTEM WITH EFFECTIVE SURFACE WEIGHT, w OF 5 psf AND Q OF 4, 10 or 25 TO IDEAL, 1 psf, 350 ms DURATION SONIC BOOM

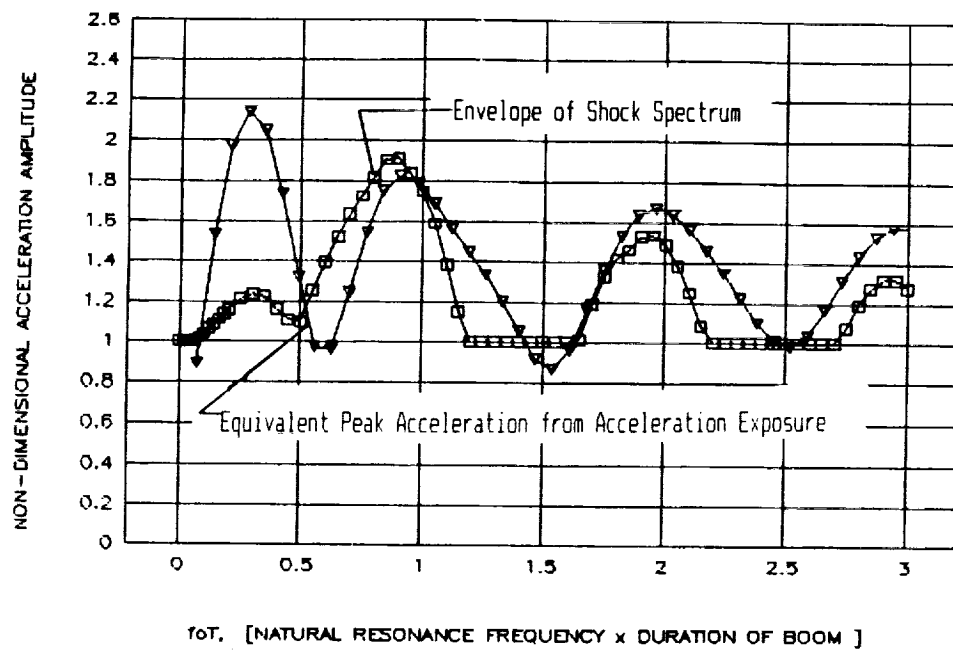
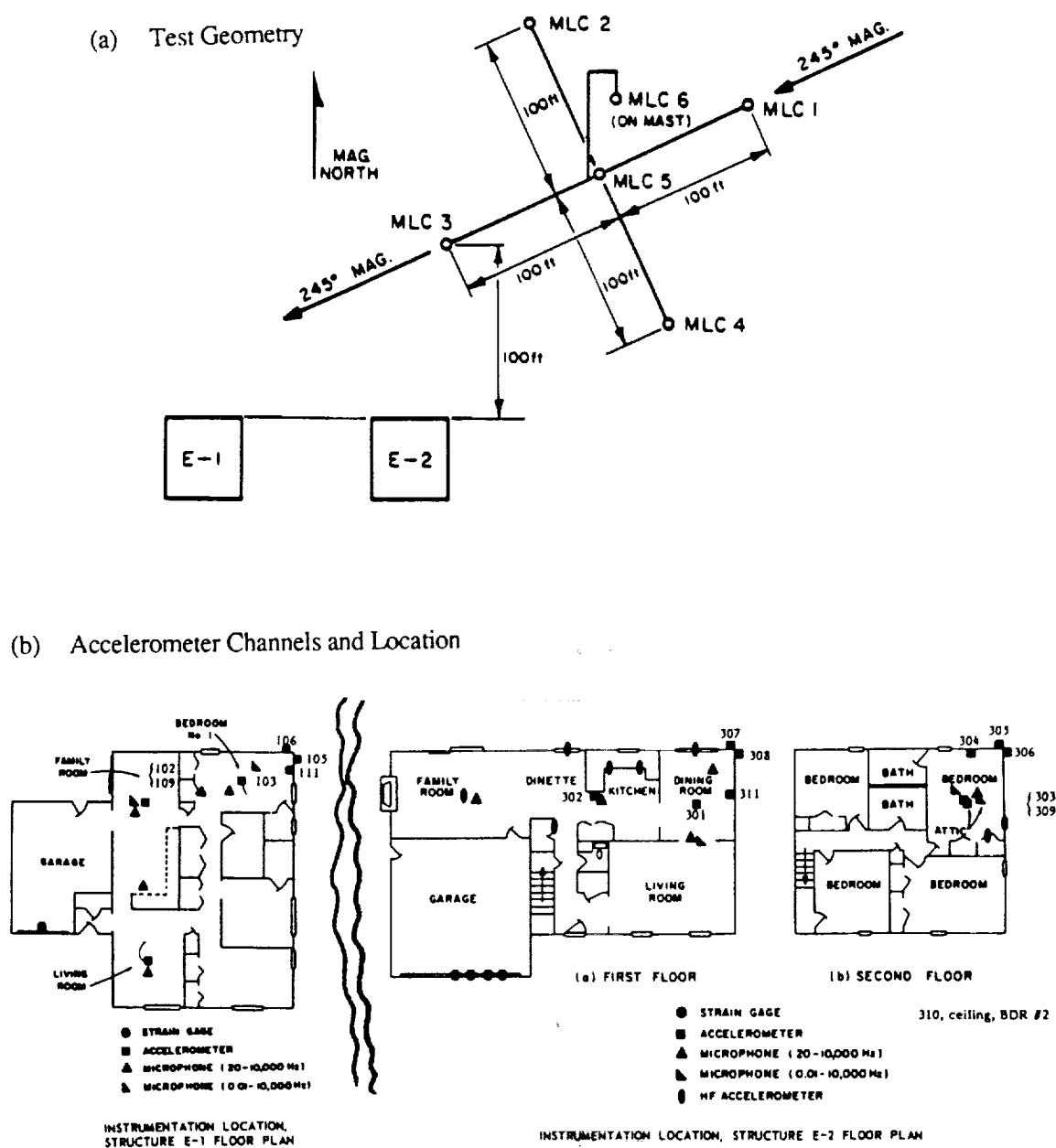


FIGURE 16. COMPARISON OF EQUIVALENT PEAK ACCELERATION RESPONSE
AND CORRESPONDING ENVELOPE OF THE ACCELERATION SHOCK
RESPONSE SPECTRUM FOR A DAMPED SDOF SYSTEM
($Q = 10$) AND AN IDEAL N-WAVE. [Note added Peak in
Equivalent Accel. Spectrum for $fo \cdot T \approx 0.3$.]



Element	Wall		Floor	Ceiling	Roof Line		Kitchen
	East	North			East	North	
House #1	111		101,102 103	109,110	105	106	
House #2	311	304	301,303	309,310	306,308	305,307	302

Figure 17. Test Geometry (a), and Accelerometer Positions and Data Channel Location (b) for Edwards AFB Sonic Boom Tests (Phase I) (from Stanford, 1967).

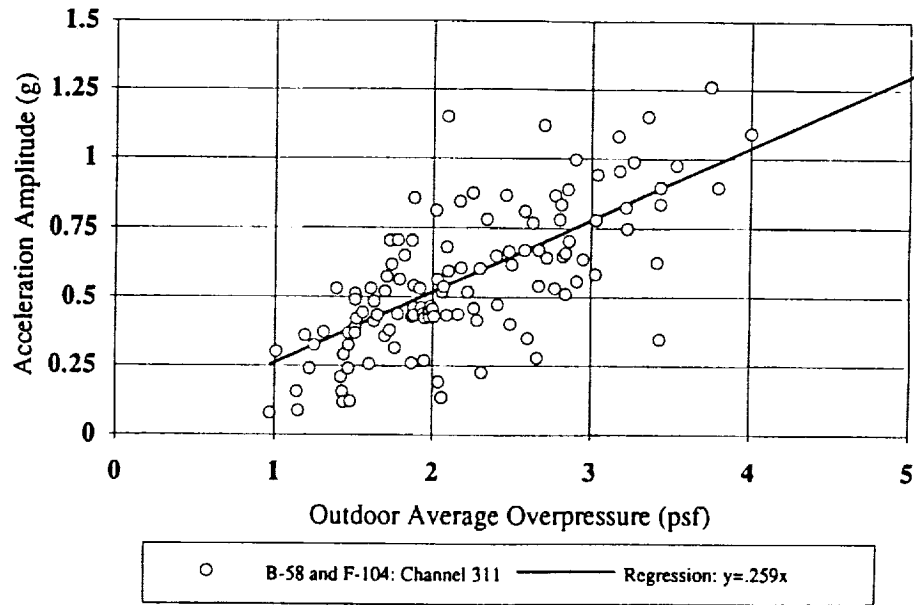


FIGURE 18. TYPICAL CORRELATION BETWEEN PEAK ACCELERATION RESPONSE OF EAST DINING ROOM WALL, HOUSE E-2 AND PEAK PRESSURE FROM EDWARDS AFB SONIC BOOM TESTS (SRI, 1967)

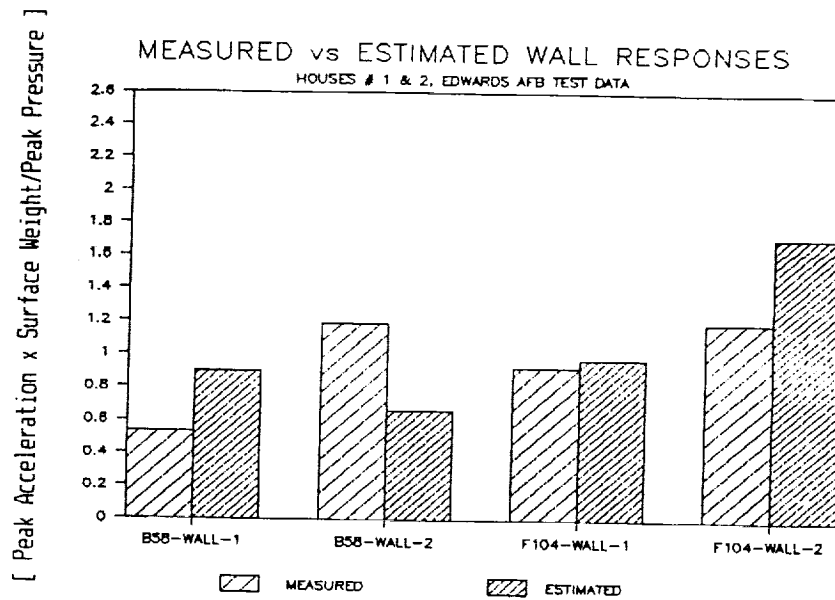


FIGURE 19. COMPARISON BETWEEN MEASURED AND PREDICTED STRUCTURAL RESPONSES OF WALLS, EDWARDS AFB SONIC BOOM TESTS

[Peak Acceleration x Surface Weight/Peak Pressure]

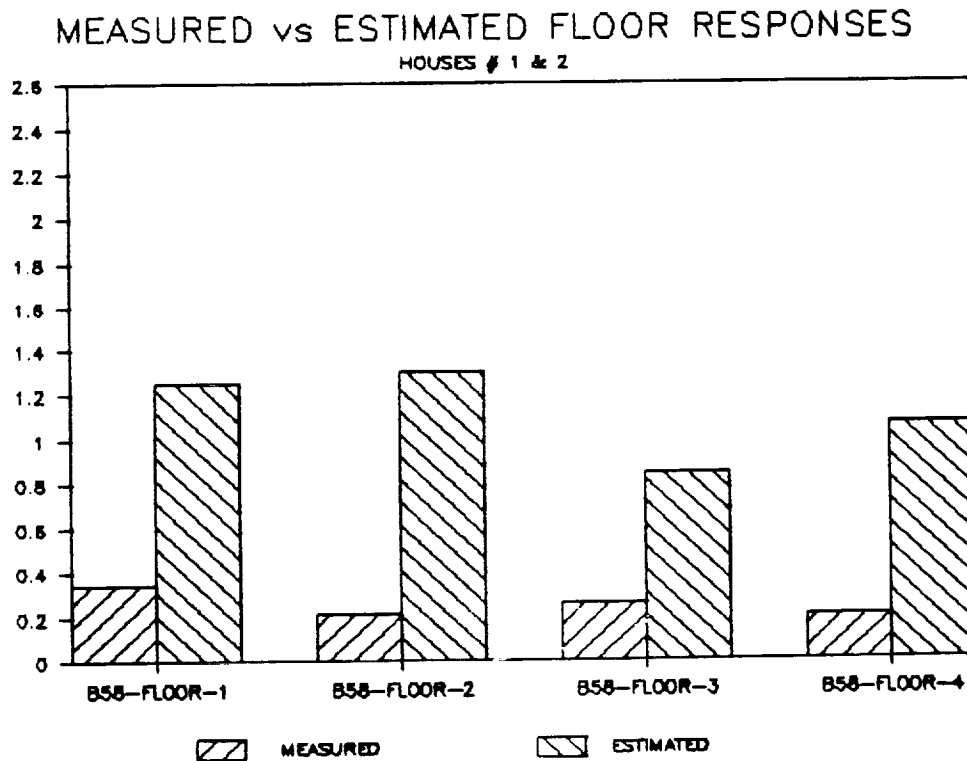
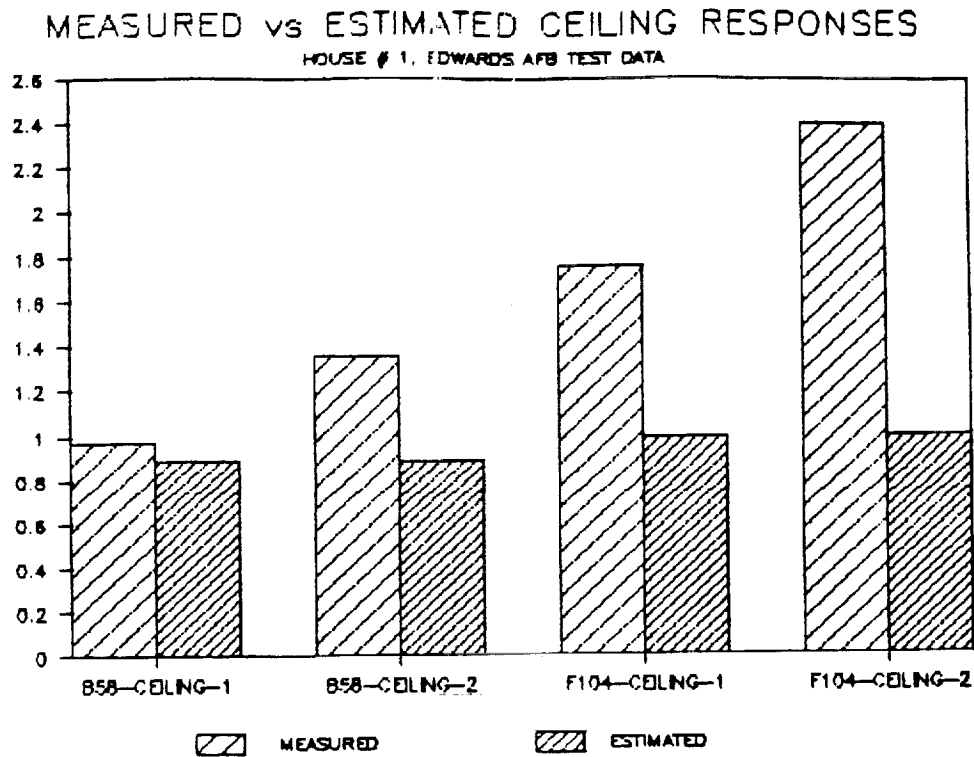


FIGURE 20. COMPARISON BETWEEN MEASURED AND PREDICTED STRUCTURAL RESPONSES OF CEILINGS AND FLOORS, EDWARDS AFB TESTS

Table 1

Predicted Structural Vibration Responses of Residential Building Elements
to Reference Sonic Boom from High Speed Civil Transport
(Peak Pressure = 1 psf, Duration = 350 ms, 8 ms Rise Time)

Structural Element	Peak Acceleration						
	Predicted Peak Acceleration (SDOF Model) g's	Adjustment Per EAFB Test Data -	Corrected Peak Acceleration g's	Human Detection Criteria g's	Rattle Threshold Criteria g's	Ratio of Environment to Criteria	
						Detection dB	Rattle dB
Walls Floors	0.28 0.27	1.0 0.25	0.28 0.068	0.0043 0.005	0.045 ± 0.021 ?	+ 36 +23	+16 ?

Structural Element	Acceleration Exposure (in decibels)		
	Predicted Acceleration Exposure Level dB re: [1μg ² •sec]	Estimated Human Response Criteria dB re: [1μg ² •sec]	Ratio of Environment to Criteria dB
Walls Floors	96 83	75-85 75-85	+11 to +21 -2 to +8

1992 Sonic Boom Workshop Attendees/Participants--Unrestricted Session

Name & Address	Phone No.	Dates in Attendance
----------------	-----------	---------------------

K. K. Ahuja GTRI/AERO Georgia Tech Research Institute Atlanta, GA 30332-0800	(404) 528-7054	Feb. 25-26
---	------------------------	------------

Daniel G. Baize Mail Stop 412 NASA Langley Research Center Hampton, VA 23665-5225	(804) 864-1071	Feb. 25-27*
--	------------------------	-------------

Raymond Barger Mail Stop 128 NASA Langley Research Center Hampton, VA 23665-5225	(804) 864-2315	Feb. 25-27*
---	------------------------	-------------

David T. Blackstock Applied Research Labs University of Texas at Austin P.O. Box 8029 Austin, TX 78713-8029	(512) 835-3374	Feb. 25-26
---	------------------------	------------

Percy Bobbitt Eagle Engineering, Inc. Tower Box 77 2101 Executive Drive Hampton, VA 23666	(804) 827-1100	Feb. 25-27*
---	------------------------	-------------

David Chestnutt Mail Stop 460 NASA Langley Research Center Hampton, VA 23665-5225	(804) 864-5259	Feb. 25
--	------------------------	---------

Samson Cheung MCAT Institute Mail Stop 258-1 NASA Ames Research Center Moffett Field, CA 94035	(415) 604-4462	Feb. 25-27*
--	------------------------	-------------

Susan Cliff Mail Stop 227-2 NASA Ames Research Center Moffett Field, CA 94035	(415) 604-5656	Feb. 25-27*
--	------------------------	-------------

David DeVilbiss Lockheed Engineering & Sciences Co. 144 Research Drive Hampton, VA 23666	(804) 766-9722	Feb. 25-26
---	------------------------	------------

* Persons who also attended restricted sessions on Feb. 27, 1992

** Persons are Foreign Nationals and were allowed to only attend on Feb. 25, 1992

Name & Address	Phone No.	Dates in Attendance
----------------	-----------	---------------------

Samuel M. Dollyhigh Mail Stop 412 NASA Langley Research Center Hampton, VA 23665-5225	(804) 864-6503	Feb. 26
--	--------------------------	---------

Christopher S. Domack Lockheed Engineering & Sciences Co. Mail Stop 412 NASA Langley Research Center Hampton, VA 23665-5225	(804) 864-6504	Feb. 26
---	--------------------------	---------

Micah Downing AL/OEBN Wright-Patterson, AFB OH 45433	(513) 255-3664	Feb. 25-27*
--	--------------------------	-------------

Cornelius Driver Eagle Engineering, Inc. Tower Box 77 2101 Executive Drive Hampton, VA 23666	(804) 827-1100	Feb. 26
--	--------------------------	---------

Tom Edwards Mail Stop 258-1 NASA Ames Research Center Moffett Field, CA 94035	(415) 604-4465	Feb. 25-27*
--	--------------------------	-------------

Dr. Sanford Fidell BBN Systems and Technologies 21120 Vanowen Street Canoga Park, CA 91303	(818) 347-8360	Feb. 26
---	--------------------------	---------

Willard E. Foss, Jr. Lockheed Engineering & Sciences Co. Mail Stop 406 NASA Langley Research Center Hampton, VA 23665-5225	(804) 864-5990	Feb. 25-27*
--	--------------------------	-------------

Dr. Kamran Fouladi Lockheed Engineering & Sciences Co. Mail Stop 412 NASA Langley Research Center Hampton, VA 23665-5225	(804) 864-5993	Feb. 25-27*
--	--------------------------	-------------

Don Garber Lockheed Engineering & Sciences Co. 144 Research Drive Hampton, VA 23666	(804) 766-9675	Feb. 25-26
--	--------------------------	------------

* Persons who also attended restricted sessions on Feb. 27, 1992

** Persons are Foreign Nationals and were allowed to only attend on Feb. 25, 1992

Name & Address	Phone No.	Dates in Attendance
----------------	-----------	---------------------

Thomas Gionfriddo Pennsylvania State University 117 Applied Science Building University Park, PA 16802	(814) 863-3214	Feb. 25-26
---	--------------------------	------------

George T. Haglund Mail Stop 9R-84 Boeing Commercial Airplane Group P.O. Box 3707 Seattle, WA 98124-2207	(206) 965-3773	Feb. 25-27*
---	--------------------------	-------------

Herbert R. Henderson Eagle Engineering, Inc. Tower Box 77 2101 Executive Drive Hampton, VA 23666	(804) 827-1100	Feb. 25-26
--	--------------------------	------------

H. H. Hubbard Lockheed Engineering & Sciences Co. Mail Stop 463 NASA Langley Research Center Hampton, VA 23665-5225	(804) 864-3610	Feb. 25-26
---	--------------------------	------------

Mahendra C. Joshi Mail Code 36-60 McDonnell Douglas Aircraft Co. 3855 Lakewood Boulevard Long Beach, CA 90846	(310) 593-8583	Feb. 25-27*
---	--------------------------	-------------

Jack Leatherwood Mail Stop 463 NASA Langley Research Center Hampton, VA 23665-5225	(804) 864-3591	Feb. 25-26
---	--------------------------	------------

Bart Lipkens University of Texas at Austin P.O. Box 8029 Austin, TX 78713-8029	(512) 835-3155	Feb. 25
---	--------------------------	---------

Robert J. Mack Mail Stop 412 NASA Langley Research Center Hampton, VA 23665-5225	(804) 864-5988	Feb. 25-27*
---	--------------------------	-------------

Mike Madson Mail Stop 227-2 NASA Ames Research Center Moffett Field, CA 94035	(415) 604-3621	Feb. 25-27*
--	--------------------------	-------------

* Persons who also attended restricted sessions on Feb. 27, 1992

** Persons are Foreign Nationals and were allowed to only attend on Feb. 25, 1992

Name & Address	Phone No.	Dates in Attendance
----------------	-----------	---------------------

Domenic J. Maglieri Eagle Engineering, Inc. Tower Box 77 2101 Executive Drive Hampton, VA 23666	(804) 827-1100	Feb. 25-27*
---	--------------------------	-------------

Gerry L. McAninch. Mail Stop 460 NASA Langley Research Center Hampton, VA 23665-5225	(804) 864-5269	Feb. 25
---	--------------------------	---------

David A. McCurdy Mail Stop 463 NASA Langley Research Center Hampton, VA 23665-5225	(804) 864-3596	Feb. 25-26
---	--------------------------	------------

Munir Metwally Mail Code 35-29 McDonnell Douglas Corp. 3855 Lakewood Boulevard Long Beach, CA 90846	(310) 593-3935	Feb. 25-26
---	--------------------------	------------

John Morgenstern Mail Code 35-59 McDonnell Douglas Aircraft Co. 3855 Lakewood Boulevard Long Beach, CA 90846	(310) 496-9151	Feb. 26-27*
--	--------------------------	-------------

Alan K. Mortlock Mail Code 35-29 McDonnell Douglas Aircraft Co. 3855 Lakewood Boulevard Long Beach, CA 90846	(310) 593-3937	Feb. 25-27*
--	--------------------------	-------------

Kathy E. Needleman Lockheed Engineering & Sciences Co. Mail Stop 412 NASA Langley Research Center Hampton, VA 23665-5225	(804) 864-5987	Feb. 25-27*
--	--------------------------	-------------

Benjamin Neumann Mail Code OAST/RF NASA Headquarters Washington, DC 20546	(202) 453-2828	Feb. 25 & 27*
--	--------------------------	---------------

* Persons who also attended restricted sessions on Feb. 27, 1992

** Persons are Foreign Nationals and were allowed to only attend on Feb. 25, 1992

<u>Name & Address</u>	<u>Phone No.</u>	<u>Dates in Attendance</u>
---------------------------	------------------	----------------------------

Gene L. Nihart	(206) 237-7620	Feb. 25 & 27*
Mail Stop 6H-FR		
Boeing Commercial Airplane Group		
P.O. Box 3707		
Seattle, WA 98124-2207		

Steven S. Ogg	(206) 965-3774	Feb. 26-27*
Mail Stop 6H-FK		
Boeing Commercial Airplane Group		
P.O. Box 3707		
Seattle, WA 98124-2207		

S. Paul Pao	(804) 864-3044	Feb. 25-26
Mail Stop 280		
NASA Langley Research Center		
Hampton, VA 23665-5225		

Andrew Piacsek	(814) 865-2859	Feb. 25-26
Pennsylvania State University		
P.O. Box 30		
State College		
University Park, PA 16804		

Allan D. Pierce	(814) 865-3161	Feb. 25-26
Pennsylvania State University		
157 Hammond Building		
University Park, PA 16802		

Kenneth J. Plotkin	(703) 415-4550	Feb. 25-27*
Wyle Laboratories		
Suite 701		
2001 Jefferson Davis Highway		
Arlington, VA 22202		

Joe W. Posey	(804) 864-7686	Feb. 25
Mail Stop 460		
NASA Langley Research Center		
Hampton, VA 23665-5225		

Clemans A. Powell	(804) 864-3575	Feb. 25-26
Mail Stop 463		
NASA Langley Research Center		
Hampton, VA 23665-5225		

Richard Raspet.	(601) 232-5888	Feb. 25-26
Department of Physics		
University of Mississippi		
University, MS 38677		

* Persons who also attended restricted sessions on Feb. 27, 1992

** Persons are Foreign Nationals and were allowed to only attend on Feb. 25, 1992

Name & Address	Phone No.	Dates in Attendance
----------------	-----------	---------------------

Capt. Helmut H. Reda. Code ASD/NAXP U. S. Air Force Wright-Patterson AFB, OH 45433	(513) 255-1857	Feb. 25-27*
---	--------------------------	-------------

H. S. Ribner Mail Stop 460 NASA Langley Research Center Hampton, VA 23665-5225	(804) 864-7618	Feb. 25
---	--------------------------	---------

Leick D. Robinson Applied Research Labs University of Texas at Austin P.O. Box 8029 Austin, TX 78713	(512) 835-3134	Feb. 25-26
--	--------------------------	------------

Zvi Rusak Mechanical & Aeronautical Engineering and Mechanics Department Rensselaer Polytechnic Institute Troy, NY 12180-3590	(518) 276-3036	Feb. 25**
---	--------------------------	-----------

Dale R. Satran Mail Stop 227-2 NASA Ames Research Center Moffett Field, CA 94035	(415) 604-5879	Feb. 25-27*
---	--------------------------	-------------

Wallace C. Sawyer Mail Stop 410 NASA Langley Research Center Hampton, VA 23665-5225	(804) 864-6515	Feb. 25
--	--------------------------	---------

Kevin P. Shepherd Mail Stop 463 NASA Langley Research Center Hampton, VA 23665-5225	(804) 864-3583	Feb. 25-27*
--	--------------------------	-------------

Michael J. Siclari Mail Stop A08-35 Grumman Corporate Research Center Bethpage, NY 11714	(516) 575-8067	Feb. 26
---	--------------------------	---------

Wel-Chung Sim Grumman 294 Mechanical & Aerospace Engineering Dept. Cornell University Ithaca, NY 14853	(607) 255-9118	Feb. 25**
--	--------------------------	-----------

* Persons who also attended restricted sessions on Feb. 27, 1992

** Persons are Foreign Nationals and were allowed to only attend on Feb. 25, 1992

Name & Address	Phone No.	Dates in Attendance
----------------	-----------	---------------------

Norbert F. Smith McDonnell Douglas Aircraft Co. Suite 120 22 Enterprise Parkway Hampton, VA 23666	(804) 838-2551	Feb. 25-27*
---	--------------------------	-------------

Victor Sothcott Eagle Engineering, Inc. Tower Box 77 2101 Executive Drive Hampton, VA 23666	(804) 827-1100	Feb. 25-27*
---	--------------------------	-------------

Victor Sparrow Pennsylvania State University 157 Hammond Building University Park, PA 16802	(814) 865-3162	Feb. 25-26
--	--------------------------	------------

David G. Stephens Mail Stop 462 NASA Langley Research Center Hampton, VA 23665-5225	(804) 864-3640	Feb. 25
--	--------------------------	---------

Brenda M. Sullivan Mail Stop 463 NASA Langley Research Center Hampton, VA 23665-5225	(804) 864-3585	Feb. 25-27*
---	--------------------------	-------------

Louis C. Sutherland Consultant to Wyle Labs 27803 Longhill Drive Rancho Palos Verdes, CA 90274	(310) 541-1655	Feb. 25-27*
---	--------------------------	-------------

Bill Willshire Mail Stop 460 NASA Langley Research Center Hampton, VA 23665-5225	(804) 864-5270	Feb. 25-26
---	--------------------------	------------

Matthew M. Winston Mail Stop 403 NASA Langley Research Center Hampton, VA 23665-5225	(804) 864-5256	Feb. 26
---	--------------------------	---------

* Persons who also attended restricted sessions on Feb. 27, 1992

** Persons are Foreign Nationals and were allowed to only attend on Feb. 25, 1992

REPORT DOCUMENTATION PAGE			Form Approved OMB No. 0704-0188	
Public reporting burden for this collection of information is estimated to average 1 hour per response, including the time for reviewing instructions, searching existing data sources, gathering and maintaining the data needed, and completing and reviewing the collection of information. Send comments regarding this burden estimate or any other aspect of this collection of information, including suggestions for reducing this burden, to Washington Headquarters Services, Directorate for Information Operations and Reports, 1215 Jefferson Davis Highway, Suite 1204, Arlington, VA 22202-4302, and to the Office of Management and Budget, Paperwork Reduction Project (0704-0188), Washington, DC 20503.				
1. AGENCY USE ONLY (Leave blank)	2. REPORT DATE October 1992	3. REPORT TYPE AND DATES COVERED Conference Publication		
4. TITLE AND SUBTITLE High-Speed Research: Sonic Boom Volume I		5. FUNDING NUMBERS 537-03-21-01		
6. AUTHOR(S) Christine M. Darden, Compiler				
7. PERFORMING ORGANIZATION NAME(S) AND ADDRESS(ES) NASA Langley Research Center Hampton, VA 23681-0001		8. PERFORMING ORGANIZATION REPORT NUMBER L-17145		
9. SPONSORING/MONITORING AGENCY NAME(S) AND ADDRESS(ES) National Aeronautics and Space Administration Washington, DC 20546-0001		10. SPONSORING/MONITORING AGENCY REPORT NUMBER NASA CP-3172		
11. SUPPLEMENTARY NOTES Christine M. Darden: Langley Research Center, Hampton, Virginia.				
12a. DISTRIBUTION/AVAILABILITY STATEMENT Unclassified—Unlimited Subject Category 05		12b. DISTRIBUTION CODE		
13. ABSTRACT (Maximum 200 words) A High-Speed Sonic Boom Workshop was held at NASA Langley Research Center on February 25-27, 1992. The purpose of the workshop was to make presentations on current research activities and accomplishments and to assess progress in the area of sonic boom since the program was initiated in FY-90. Twenty-nine papers were presented during the 2-1/2 day workshop. Attendees included representatives from academia, industry, and government who are actively involved in sonic-boom research. Volume I contains papers related to atmospheric effects on the sonic-boom signature during propagation and on acceptability studies.				
14. SUBJECT TERMS Atmospheric effects on sonic boom; Turbulence effects on sonic boom; Molecular absorption effects on sonic boom; Sonic boom acceptability			15. NUMBER OF PAGES 201	
			16. PRICE CODE A10	
17. SECURITY CLASSIFICATION OF REPORT Unclassified	18. SECURITY CLASSIFICATION OF THIS PAGE Unclassified	19. SECURITY CLASSIFICATION OF ABSTRACT Unclassified	20. LIMITATION OF ABSTRACT Unlimited	